Nadeem Akhtar

Investigation of Hyperfine Structures of Spectral Lines of Singly Ionized Praseodymium Using Fourier Transform Spectrum, Saturation Spectroscopy and Collinear Laser Ion Beam Spectroscopy

DOCTORAL THESIS

For obtaining the academic degree of

Doktor der technischen Wissenschaften

Doctoral Programme of Technical Sciences
Technical Physics

TU
Graz
Graz University of Technology

Graz University of Technology

Supervisor:

Univ.-Prof. Dipl.-Ing. Dr.techn. Laurentius Windholz

Institute of Experimental Physics, Graz, Austria

May 2012

Senat

Deutsche Fassung:
Beschluss der Curricula-Kommission für Bachelor-, Master- und Diplomstudien vom 10.11.2008
Genehmigung des Senates am 1.12.2008

EIDESSTATTLICHE ERKLÄRUNG

Ich erkläre an Eides statt, dass ich die vorliegende Arbeit selbstständig verfasst, andere als die angegebenen Quellen/Hilfsmittel nicht benutzt, und die den benutzten Quellen wörtlich und inhaltlich entnommene Stellen als solche kenntlich gemacht habe.

Graz, am ....
(Unterschrift)

Englische Fassung:

STATUTORY DECLARATION

I declare that I have authored this thesis independently, that I have not used other than the declared sources / resources, and that I have explicitly marked all material which has been quoted either literally or by content from the used sources.

....
date (signature)

To

Prof. Dr. L. Windholz, Prof. Dr. H. Hühnermann
my beloved parents
my wife Uzma and little angles Fatima and Ahmed

Acknowledgment

First of all I would like to pay my gratitude to the Almighty ALLAH for His Support and Blessings which made me able to complete this research work. I pay deep respect and sincere praise to the Holy Prophet Muhammad (peace be upon him) who is like a beacon in every aspect of life.

I would like to thank my supervisor Prof. Dr. Laurentius Windholz, whose facilitative attitude, technical support and encouragement have always been a source of hope and inspiration for me during research work. I appreciate his vast knowledge and skill in the field of experimental and theoretical physics. I am also very much thankful to Prof. Dr. Harry Hühnermann for his great help and guidance during this work. During my research work, I found him very knowledgeable, cooperative, polite, sincere and caring person. It was a really nice experience to work with him. I would like to thank Prof. Dr. Theo Neger, who initially accepted me for PhD studies. During my stay in Graz, I found him very kind, caring and cooperative.

I am thankful to the head of the institute Prof. W. E. Ernst for providing me an opportunity to work here. Many thanks to the members of the institute and people from electronic/machine workshop for their cooperation. Especial thanks to C. Neureiter, J. Friedrich, R. Dämon, J. Pichler, U. Seidl, W. Luttenberger and R. Maierhofer for their cooperation during establishing the laboratory.

I am thankful to my colleague Naveed Anjum for companionship and a nice working atmosphere in the laboratory. I am also thankful to Pakistani colleagues, Syed Tanveer Iqbal, Imran Siddiqui, Shamim Khan and Shahid Mehmood in the Institute of Experimental Physics at the Graz University of Technology for providing a friendly atmosphere.

I would like to thank my loving and caring parents and all family members (sisters, brothers and in law relatives) for their support and prayers. They continuously encouraged me to achieve my goals. This will not be complete without mentioning my wife Uzma for her immense support during the whole life and especially during my PhD studies.

Finally, I would like to thank the Higher Education Commission (HEC) of Pakistan for providing financial support during my stay in Austria. Also thanks to the Optics laboratories for granting me the studies leave to complete my PhD studies.

Abstract

The hyperfine structure splitting of a fine structure energy level is caused by the interaction of the electromagnetic nuclear moments with the electromagnetic moments of the electron shell. The hyperfine structure splitting is three orders of magnitudes smaller than the fine structure splitting. The splitting of the hyperfine structure is determined by the magnetic dipole interaction constant *A* and an additional small shift in the hyperfine levels is determined by the quadrupole interaction constant *B*.

Praseodymium (Pr) has five electrons in the outermost shells. The coupling of five (Pr I) or four (Pr II) electrons produces a large number of fine structure levels resulting in a dense and complicate optical spectrum of Pr I and Pr II emission lines. For the classification of spectral lines, precise values of hyperfine constants and energy values of the levels involved in the transitions are required.

This work is divided into three parts, regarding the investigation of hyperfine structures of Pr II spectral lines. In the first part, the spectral lines of Pr II are analyzed using a high resolution Fourier transform spectrum in the spectral range from 3260 to 11700 Å and a classification program. Transition wavelengths of Pr II spectral lines are re-determined and then, using these accurate transition wavelengths, the energy values of the levels involved in the transitions are improved. During this work, wavelengths for 441 spectral lines and energy values for 227 known levels of Pr II are improved along with the classifications for 36 Pr II lines. The correction to previous energy values range from -0.051 to 0.194 cm^{-1}.

Investigation of narrow hyperfine structures needs a reduction of the Doppler broadening of the investigated lines. The hyperfine structures are experimentally investigated using two methods of Doppler reduced spectroscopy. In the second part of this work, the hyperfine structures of the Pr II spectral lines are investigated in a hollow cathode discharge lamp using inter-modulated laser induced fluorescence spectroscopy. Using this method 6 Pr II transitions are investigated and a spectral width of about ca. 200 MHz was achieved.

The main research work is carried out in the third part. The Pr II spectral lines are investigated using the high resolution method of Collinear Laser Ion Beam Spectroscopy

(CLIBS). The CLIBS measurements are performed using the Marburg mass separator MARS-II, originally installed at the university of Marburg/Germany. This MARS-II system has been transferred to the Institute of Experimental Physics of the Technical University Graz and is now fully working. The MARS-II is first calibrated by investigating the ^{137}Ba II line 5857.7 Å ($5d\,^2D_{3/2} \rightarrow 6p\,^2P^\circ_{3/2}$). Then the hyperfine structures of Pr II spectral lines are investigated in order to determine the hyperfine constants A and B of Pr II levels involved in the transitions. In this method, the Doppler width is reduced by accelerating the ions to a high velocity as compared with the thermal velocity. A line width of spectral lines was observed between 35 MHz to 80 MHz. The ions are produced using a hot surface ion source, accelerated to 20 kV and focused using an ion optics system, consisting of electrostatic lenses and an 80° magnet. After passing the magnet, the ion beam is superposed with a laser beam in the interaction chambers (light collecting chambers). A ring dye laser pumped by an Argon ion laser is used as light source. The dyes Rhodamine 6G and Kiton red are used to operate the laser in the wavelength region 5750 - 6432 Å. In the first light collecting chamber, Doppler tuning is carried out to investigate the hyperfine structures. With help of the second light collecting chamber the laser frequency is stabilized to one of the hyperfine components to overcome the fluctuations in the accelerating voltage as well as a frequency drift of the laser. The laser induced fluorescence is recorded using a photon counting method. Using a fit program, the hyperfine constants A and B of the involved energy levels are determined.

Using CLIBS, 99 spectral lines of singly ionized praseodymium are investigated. The hyperfine constants A and B of 70 involved energy levels are determined. Many levels are investigated for the first time using this technique thereby improving the accuracy of the hyperfine constants of these levels.

Kurzfassung

Die Hyperfeinstrukturaufspaltung eines Feinstruktur-Energieniveaus wird durch die Wechselwirkung von elektromagnetischen Kernmomenten mit den elektromagnet-ischen Momenten der Elektronenhülle verursacht. Die Hyperfeinstrukturaufspaltung ist drei Größenordnungen kleiner als die Feinstrukturaufspaltung. Die Aufspaltung wird durch die magnetische Dipol-Wechselwirkungskonstante A bestimmt. Eine zusätzliche kleine Verschiebung der Hyperfeinstrukturniveaus wird durch die Quadrupol-Wechselwirkungskonstante B beschrieben. Praseodym (Pr) verfügt über fünf Elektronen in der äußersten Schale. Die Kopplung von fünf (Pr I) oder vier (Pr II) Elektronen erzeugt eine große Anzahl von Feinstruktur-Werten und damit ein dichtes und kompliziertes optisches Spektrum von Pr I und Pr II Emissionslinien. Für die Klassifizierung von Spektrallinien sind genaue Werte der Hyperfein-Konstanten und Energiewerte von den an den Übergängen beteiligten Niveaus erforderlich.

In Bezug auf die Untersuchung der Hyperfeinstruktur von Pr II Spektrallinien ist diese Arbeit in drei Teile gegliedert. Im ersten Teil werden die Spektrallinien des Pr II analysiert mit Hilfe eines Fourier-Transformations-Spektrums hoher Auflösung im Spektralbereich von 3260 - 11700 Å und eines Klassifizierungsprogramms. Übergangs-Wellenlängen der Pr II Spektrallinien werden neu ermittelt und dann werden unter Verwendung dieser genauen Übergangs-Wellenlängen die Energiewerte der an den Übergängen beteiligten Niveaus verbessert. Während dieser Arbeiten sind für 441 Spektrallinien die Wellenlängen und für 227 bekannten Niveaus des Pr II Energiewerte verbessert worden. Die Korrekturen von den vorherigen Energiewerten reichen von -0,051 bis 0,194 cm^{-1}. Außerdem wurden 36 Pr II Linien klassifziert.

Untersuchung enger Hyperfeinstrukturen erfordert eine Verringerung der Doppler-Verbreiterung der untersuchten Linien. Die Hyperfeinstrukturen werden experimentell untersucht mit Hilfe von zwei Methoden. Im zweiten Teil dieser Arbeit werden die Hyperfeinstruktur der Pr II Spektrallinien in einer Hohlkathoden Entladungslampe mit inter-modulierter Laser induzierter Fluoreszenz-Spektroskopie untersucht. Mit dieser Methode wurden 6 Pr II Übergänge untersucht und eine spektrale Breite von etwa ca. 200 MHz erreicht.

Schwerpunkt der Forschungs-Arbeiten werden im dritten Teil durchgeführt. Die Pr II Spektrallinien werden untersucht mit der hochauflösenden Methode der kollinearen Laser Ionenstrahl-Spektroskopie (CLIBS). Die CLIBS Messungen werden unter Verwendung des Marburger Massenseparator MARS-II, der ursprünglich an der Universität Marburg / Deutschland installiert war durchgeführt. Das MARS-II-System war im Institut für Experimentelle Physik der Technischen Universität Graz neu aufgebaut worden und ist nun voll funktionsfähig. MARS-II wird zunächst durch die Untersuchung der ^{137}Ba II Linie 5857,7 Å ($5d^2D_{3/2} \rightarrow 6p^2P^{\circ}_{3/2}$) kalibriert. Dann werden die Hyperfeinstrukturen von Pr II Spektrallinien untersucht um die Hyperfein-Konstanten A und B der beteiligten Pr II Niveaus in den Übergängen zu bestimmen. Bei diesem Verfahren wird die Doppler-Breite durch die Beschleunigung der Ionen auf eine Geschwindigkeit, die hoch ist verglichen mit der thermischen Geschwindigkeit, reduziert. Damit wurden Linienbreiten zwischen 35 MHz und 80 MHz beobachtet. Die Ionen werden mit einer Oberflächen-Ionenquelle hergestellt, beschleunigt auf 20 kV und fokussiert unter Verwendung eines Ionen-Optik, bestehend aus elektrostatischen Linsen und einem 80° Magneten. Nach dem Passieren des Magneten wird der Ionenstrahl mit einem Laserstrahl in den Interaktionskammern (Licht-Sammelkammern) überlagert. Ein von einem Argon-Ionen-Laser gepumpter Farbstoff-Ringlaser wird als Lichtquelle benützt. Die Farbstoffe Rhodamin 6G und Kiton rot werden verwendet, um den Laser im Wellenlängenbereich 5750 - 6432 Å zu betreiben. Im ersten Licht-Sammler wird Doppler Tuning durchgeführt, um die Hyperfeinstrukturen zu untersuchen. Mit Hilfe der zweiten Licht-Sammler wird die Laserfrequenz auf eine der Hyperfeinkomponenten stabilisiert, um die Schwankungen in der Beschleunigungs-spannung sowie eine Frequenzdrift des Lasers zu überwinden. Die Laser-induzierte Fluoreszenz wird mittels eines Photon-Counting-Verfahren aufgezeichnet. Mit Hilfe eines Fit-Programms werden die Hyperfein-Konstanten A und B der beteiligten Energieniveaus bestimmt.

Mit CLIBS sind 99 Spektrallinien des einfach ionisierten Praseodym untersucht worden. Die Hyperfein-Konstanten A und B von 70 beteiligten Energieniveaus wurden bestimmt. Viele Niveaus wurden erstmalig mit dieser Technik und damit mit erhöhter Genauigkeit vermessen.

Declaration

This dissertation is submitted to the Institute of Experimental Physics, Graz University of Technology, Graz, Austria, in partial fulfillment of the requirement for the degree of Doctor of Technical Sciences.

The thesis is entitled:

Investigation of Hyperfine Structures of Spectral Lines of Singly Ionized Praseodymium Using Fourier Transform Spectrum, Saturation Spectroscopy and Collinear Laser Ion Beam Spectroscopy

written by Nadeem Akhtar and has been approved by the Institute of Experimental Physics, Graz University of Technology, Graz, Austria.

The final copy of this thesis has been examined by the under signed authority, and find that both the content and the form meet acceptable presentation standards of scholarly work in the above mentioned discipline.

____

Univ.-Prof. Dipl.-Ing. Dr.techn. Laurentius Windholz

Date _______________

Contents

1 INTRODUCTION

The hyperfine splitting of an atomic fine structure level is caused by the electromagnetic interaction of orbiting and spinning electrons with the nucleus [1]. The study of hyperfine structures provides information about the nuclear structure and electronic properties of atoms. Usually, the hyperfine structure splitting is three orders of magnitude smaller than the fine structure splitting but can be not neglected if data are determined from the profile of an observed spectral line, e.g. in astrophysics [2]. A fine structure energy level splits into $2I + 1$ if $J > I$ or $2J + 1$ if $J < I$ hyperfine levels, where J is the quantum number of total angular momentum of the electron and I is the nuclear spin quantum number. The hyperfine pattern of a spectral line is characterized by the magnetic dipole interaction constants A, the electric quadrupole interaction constants B and the total angular momenta J of the combining energy levels.

In this work, the spectral lines of singly ionized praseodymium (Pr II) are investigated. Since praseodymium has a high density of energy levels, consequently the spectrum of Pr I and Pr II lines is very dense and complicated. The study of the hyperfine structures of Pr II lines is valuable in understanding the spectra of astrophysical objects as well as optical spectra of chemical peculiar (CP) stars [3, 4].

This work is divided into three parts:

1) Energy correction of the fine structure Pr II levels: Using a high resolution Fourier transform (FT) spectrum of Pr spectral lines [5], the transition wavelengths of many Pr II spectral lines are improved. From these wavelengths, energy values of numerous Pr II levels are re-determined [6].

2) Saturation spectroscopic studies of Pr II spectral lines: Using a Doppler reduced method “saturation spectroscopy” the hyperfine structures of the Pr II spectral lines are investigated.

3) Investigation of Pr II spectral lines using collinear laser ion beam spectroscopy (CLIBS): The main work of this thesis is concerned with the investigation of Pr II spectral lines using a high resolution spectroscopic technique known as CLIBS. Using this method, the hyperfine constants A and B of many Pr II fine structure energy levels are determined with an accuracy improved by one order of magnitude.

CLIBS is known as a high resolution spectroscopic method in atomic physics. CLIBS provides a resolution improved by a factor of 10 - 20 compared to Doppler broadened emission lines from glowing gas, electric arc discharge (e.g. hollow cathode). A line width of ca. 60 MHz (or even less) of the spectral components is obtained which allows precise measurements of the hyperfine constants and the isotope shift of spectral lines.

In CLIBS investigations, the velocity spread of the ions is reduced by increasing the velocity of the ions to a value much larger compared with the thermal velocity, by applying an accelerating potential. Then the ions are mass separated and are superposed collinearly with the excitation light (laser light). The ions are produced in an ion source where low lying metastable states are populated due to collisions. The ions are extracted from the ion source by applying a high acceleration voltage and are focused using a system of electrostatic lenses. Then an ion beam of a single isotope is selected using a mass separator (“sector magnet”). Finally, the ion beam interacts collinearly with the laser beam in an interaction chamber. The hyperfine structures are observed by detecting the fluorescence light. The hyperfine structures are recorded by applying a post acceleration voltage to the interaction chamber. This method of scanning of the spectral lines is known as “Doppler tuning”.

1.1 Praseodymium (Pr)

Praseodymium (Pr) is the 3rd element of the lanthanide group with the atomic number Z = 59. Its atomic weight is 140.9076 a.m.u. In 1841, the Swedish scientist C. G. Mosander discovered a rare earth oxide which he named “didymium”. In 1885, the Austrian chemist Baron Carl Auer von Welsbach separated didymium into two salts, which he named praseodymium and neodymium. The name praseodymium comes from the Greek word “prasios” meaning green and “didymos” meaning twin. It is a silvery, soft, malleable and ductile metal. It is rapidly developed into a green oxide when exposed to air, though its oxidation rate is less than that of neodymium, europium or lanthanum. A centimeter sized piece of Pr is completely oxidizes within a year [7]. Therefore Pr is stored under a light mineral oil or sealed under a noble gas, e.g. argon (Ar).

Naturally, Pr is composed of only one stable isotope with the mass number 141 (^{141}Pr). 38 radioisotopes of Pr, ranging in mass number from 121 to 159, have been characterized.

The most stable isotopes of Pr are: ^{143}Pr with a half-life 13.57 days and ^{142}Pr with a half-life 19.12 hours. All of the remaining radioactive isotopes have half-lives less than six hours and most of these have half-lives less than 10 minutes. The radioactive isotopes with mass numbers less than 141, most commonly decay to cerium isotopes through a β^+ decay and the remaining radioactive isotopes (mass number greater than 141) decay to neodymium isotopes through a β^- decay.

The crystalline structure of Pr is hexagonal (hex) and its melting point is 931 ˚C. Before going into the liquid phase, the hexagonal structure of Pr is changed to body centered cubic structure (bcc) [8] at 798 ˚C. Some physical and chemical properties of praseodymium are listed in table 1.1.

Table1.1: Some physical and chemical properties of praseodymium (Pr).

Symbol	Pr	Element category	Metal - Lanthanide
Atomic number (Z)	59	Color	Silvery white
Mass number (A)	141	Crystal structure	Hexagonal (hex)
Density	6.8 g/cm^3	Electron-negativity	1.13 (Pauling scale)
Melting temperature	931 ˚C	Oxidation states	3 (mildly basic oxide)
Boiling temperature	3520 ˚C	Thermal conductivity	13 W/m-K
Electrical resistivity	7.1×10^{-7} Ω-m	Ionization energy	523 kJ/mol
Nuclear magnetic moment	$\mu_I = 4.2754(5)\ \mu_N$	Electric quadrupole moment	-0.066 barn

Some applications of praseodymium:

- Praseodymium is mixed with magnesium to create a high strength alloy that is used in aircraft engines [9, 10].
- Praseodymium is used in the fabrication of yellow filters. Didymium (praseodymium and neodymium) glasses are used to fabricate certain types of welder’s and glass blower’s goggles [11].
- Praseodymium doped silicate crystals have been used to slow a light pulse down to few hundred meters per second [12].
- Praseodymium doped fluoride glass is used as a single mode fiber optical amplifier [13].

- Praseodymium oxides, if mixed with cerium oxide (CeO_2) or with cerium-zirconium-oxide ($Ce_{1-x}Zr_xO_2$), can be used as oxidation catalyst [14].

From the spectroscopic point of view, praseodymium is of a great importance because of the 5 electrons in the outermost shells. The ground-state of atomic Pr is ($1s^22s^22p^63s^23p^63d^{10}4s^24p^64d^{10}5s^25p^6$) $4f^36s^2$ ($^4I°_{9/2}$) and of the singly ionized Pr it is ($1s^22s^22p^63s^23p^63d^{10}4s^24p^64d^{10}5s^25p^6$) $4f^3(^4I°_{9/2})$ $6s$ $(9/2,1/2)°_4$. The coupling of five (Pr I) or four (Pr II) electrons produces a large number of energy levels resulting in a very dense and complicated optical emission spectrum of Pr I and Pr II. The nuclear spin quantum number is $I = 5/2$ for ^{141}Pr. For most of the levels the total angular momentum J is larger than I; such a fine structure level splits into 6 hyperfine levels. There are 15 (for $\Delta J = \pm 1$) or 16 (for $\Delta J = 0$) hyperfine components when a transition takes place between two fine structure levels with ($J > I$), which include 6 strong (diagonal) hyperfine components and two groups of weak (off diagonal) hyperfine components. Thus, the complexity of the Pr spectrum is further enhanced when the hyperfine splitting is taken into account, which ranges from 10 GHz to 60 GHz and when hyperfine components of different transitions, having almost the same center of gravity wavelengths, overlap with each other. In the Fourier transform spectrum, the hyperfine components of a transition appear close to their theoretical relative intensities, thus the hyperfine patterns can be used for the identification of different transitions. Accurate knowledge of energy and hyperfine constants along with a high resolution of the available spectrum is required to identify different closely lying transitions. There are few ten thousand spectral lines in the optical spectrum of Pr and most of them are unclassified. It is of great importance to classify as many of these lines as possible for gaining a better understanding of the electronic configurations of the Pr atom.

1.2 A short review of the investigation of Pr I spectral lines

In 1928, A. S. King [15] first time reported 1018 Pr I and Pr II lines in the wavelength range 1741-5839 Å. In 1929, H. E. White [16] investigated the hyperfine structures of 200 spectral lines of Pr II using a grating spectrograph. During his work, he observed that the hyperfine structure of 100 lines were completely resolved into six strong components, so he determined the nuclear spin quantum number $I = 5/2$ of ^{141}Pr. N. Rosen et al. (1941)

[17] determined the energy values, the total angular momentum *J* and the Landé g factors for 74 Pr II fine structure energy levels using Zeeman effect measurements. He found $f^3(^4I°)\ s$ - $^4I°_4$ to be the lowest term of Pr II. In 1953, H. Lew [18] used the method of atomic magnetic resonance to investigate the hyperfine structure of the ground state $4f^36s^2$ ($^4I°_{9/2}$) of Pr I. In the same year, P. Brix [19] determined the magnetic hyperfine interaction constant for the 6s electrons in the configuration $4f^3(4I)6s$ and also calculated the magnetic moment ($\mu_I = 3.9 \pm 0.3$ nuclear magnetons) of Pr. In 1955, J. M. Baker and B. Bleany [20] classified three lines of Pr I and determined the hyperfine constants of the involved levels in the transitions.

In 1962, Y. C. Amado et al. [21] investigated the hyperfine structure of the ground state $^4I_{9/2}$ of the 19-hr ^{142}Pr isotope using the atomic magnetic resonance method. They determined the hyperfine constant, nuclear moment and the nuclear quadrupole moment of ^{142}Pr.

In 1965, R. Zalubas and M. Wilson [22] published 3532 Pr I lines in the wavelength range 1741-5839 Å. In 1973, R. Zalubas and B. R. Borchardt [23] reported the discovery of 60 even energy levels of Pr I and three odd levels of the ground term $4\ f^36s^2\ ^4I°$. In 1980, A. Ginibre [24] discovered 54 new fine structure levels of Pr I and determined their magnetic dipole interaction constants. Her work was based on the analysis of high resolution recordings in the visible and IR regions. In addition to her published work, she classified lot of new lines in Pr I and Pr II optical spectrum. This work is now part of her PhD thesis [25]. R. M. Macfarlane et al. (1982) [26] calculated a new value of the nuclear magnetic moment ($\mu_I = 4.2754(5)\ \mu_N$) and improvement the precision by two orders of magnitude compared to the previous measurement. In 1985, K. T. Chen and W. J. Childs [27] determined the electric quadrupole of praseodymium (Q = -0.066b).

M. N. Reddy and G. N. Rao [28] (1987) employed laser optogalvanic spectroscopy in a hollow cathode discharge lamp and identified altogether 121 Pr I and Pr II lines. In 1996 T. Kuwamoto et al. [29] investigated the hyperfine structures of 34 lines of neutral praseodymium in the region 5440 - 5960 Å. They used the high resolution method of laser atomic beam fluorescence spectroscopy. In 1998, M. Song et al. [30] determined the lifetimes of low lying states of Pr I using atomic beam laser spectroscopy.

Using laser induced fluorescence spectroscopy on an atomic beam, A. Krzykowski et al. [31], determined (1997) the hyperfine constants of many Pr I levels. J. Ruczkowski et al. [32] applied (2003) a semi empirical method and analyzed the hyperfine structures in the even configuration system $4f^25d6s^2$ + $4f^25d^26s$ + $4f^36s6p$ + $4f^35d6p$ + $4f^25d^3$ of Pr I. In 2006, B. Furmann et al. [33] used the method of laser induced fluorescence spectroscopy and discovered 57 new electron levels in the spectral range 560 - 590 nm Pr I.

In 2010, S. G. Oppel et al. [34] reported the active frequency stabilization of a diode laser on Pr I lines. They achieved the stabilization of laser frequency within 1.4 (1) MHz for an average time greater than 0.2 second.

In 2011, B. Gamper et al. [5] presented a high resolution Fourier transform spectrum of Pr recorded at the Institute of Quantum Optics at the Leibniz University in Hannover. They discovered 24 new Pr I levels and classified more than 1200 lines in the FT spectrum of praseodymium. Recently, K. Shamim et al. [35] and T. I. Syed et al. [36] have discovered altogether 94 new levels and classified more than 500 spectral lines of Pr I during their systematic investigations carried out in our research group, based on laser induced fluorescence spectroscopy in a hollow cathode discharge lamp.

1.3 A short review of the investigation of Pr II spectral lines

As mentioned in the previous section, A. S. King [15], H. E. White [16] and N. Rosen et al. [17] did the initial work for the classification of the spectral lines of Pr II and discovered numerous Pr II energy levels. In 1960, K. Murakawa [37] classified three spectral lines of Pr II at wavelengths 4951.4, 4914.0 and 4552.2 Å. He used a liquid air cooled hollow cathode discharge tube as a light source. In 1973, J. Blaise et al. [38] discovered many energy levels of Pr II in the configurations $4f^3(^4\mathrm{I})(5d+6s)$, $4f^2(5d+6s)^2$ and $4f^25d6p$ using high resolution experimental data (spectral plates of grating spectrographs and Fourier Transform spectra). In 1974, J. F. Wyart et al. [39] applied Racah’s method [40] to already known experimental data to determine energies of some energy levels of configurations $4f^N(5d+6s)$ for Pr II and Pr III. In 1989, A. Ginibre [25, 41, 42] used high resolution Fourier transform (FT) spectra and classified a number of unidentified lines in the Pr II spectrum in the wave number range between 2783 - 27920 cm^{-1}. Along with the discovery of new levels, she also improved the energy, *J* values and *A* values for some already known levels.

H. Iimura et al. (1990, 1994) [43, 44] investigated the hyperfine structures of the spectral lines of singly ionized praseodymium using CLIBS measurements. In 2001, S. Ivarsson et al. [45] presented improved wavelengths of 49 Pr II and 15 Pr III lines along with improved energies for 36 Pr II fine structure levels. M. Hongliang's group (2000-2002) [46, 47] has reported some Doppler reduced measurements of Pr II transitions using CLIBS. Using the same technique, R. C. Rivest et al. (2002) [48] investigated the hyperfine structure of 36 transitions of Pr II in the blue wavelength region and improved the accuracy of the hyperfine constants of 40 energy levels. In the same year, T. J. Scholl et al. [49] measured the radiative lifetimes of 33 Pr II levels and 13 Nd II levels using the collinear and 90° beam-laser methods. The measured lifetimes were in the range 6-170 ns with experimental errors less than 11%.

B. Furmann et al. (2001-2007) [50-52] investigated many hyperfine structures of Pr II and discovered altogether 45 new electronic levels of Pr II performing systematic investigations of hyperfine structures of singly ionized praseodymium based on laser induced fluorescence (LIF) technique in a hollow cathode discharge lamp. In 2007, R. Li et al. [53] measured the spontaneous-emission branching fractions of 32 levels of Pr II levels using fast-ion-beam laser-induced-fluorescence technique. Recently, further investigations in respect of Pr II energy levels are reported in this thesis. Wavelengths for 441 spectral lines, classifications for 36 lines and energy values of 227 Pr II fine structure energy levels are improved using a high resolution FT spectrum [5]. A preliminary presentation was given in 2012 by N. Akhtar and L. Windholz [6]. Furthermore this thesis describes the measurement of the hyperfine structures of numerous spectral lines with the help of CLIBS by which the hyperfine structure constant of 70 Pr II energy levels could be significantly improved. For preliminary results see N. Akhtar et al. [54, 55].

1.4 A short review of the investigation of Pr III spectral lines

The spectra of ionized atoms, especially doubly ionized atoms, are hard to produce. It might happen that strong lines lie in spectral regions where the excitation and detection is limited by the apparatus. In 1964 N. J. Spector [56] calculated the energy parameters for the $4f^2 6s$ and $4f^2 6p$ configurations of Pr III (Pr^{2+}). An average agreement of better than 0.5% of the total configuration spread was obtained between the predicted and the observed fine structure energy levels. J. Reader and J. Sugar [57] (1964) investigated the hyperfine structures of ^{141}Pr III lines by means of a sliding spark discharge and a concave-grating spectrograph. They calculated the nuclear moment 4.06(6) nm and the splitting factor of the $6s$ electron of $a_{6s} = +0.639 \pm 0.007\,\mathrm{cm}^{-1}$. They also determined the probability density of the $6s$ electron at the nucleus using interpolated values of the energy difference and quantum defect difference for $4f^2 7s$ and $4f^2 6s$ configurations. In 1968, S. Feneuille and N. A. Pelletier derived energy parameters for the Pr III ($4f^2 5d + 4f^2 6s$) and $4f^2 6p$ configurations which included the effective interactions corresponding to “all two-particle operators, acting only upon the orbit of the electrons” [58]. Later in 1974, J. F. Wyart et al. [39] used the data of ref. [58] and discovered two missing levels of the multiplet $4f^2(^3F)5d\ ^4D$. Along with the investigations of Pr II lines (as mentioned earlier) S. Ivarsson et al. [45] also presented improved wavelengths of 15 strong Pr III lines. In 2002, M. W. Glenn [59] analyzed the effective temperature dependence for the strong lines of Pr I λ = 5227.967 Å, Pr II λ = 5220.108 Å, and Pr III λ = 5299.969 Å in the stellar and laboratory spectra. He used the synthetic spectrum program SYNTHE and a program ATLAS9 to generate model atmospheres.

1.5 A short review of CLIBS

In 1973, H. J. Andrä et al. [60] reported life time measurements by laser excitation of a fast Ba^+ beam and in 1975 [61] he introduced the laser induced quantum beat method in fast ion beams. In 1976, S. L. Kaufman [62] proposed to use the velocity bunching phenomenon in fast ion beams to obtain narrow absorption lines of neutral Cs. In the same year, W. H. Wing et al. [63] observed a vibration-rotation spectrum of molecules in a HD^+

ion beam using the velocity bunching effect. They employed Doppler tuning for the detection of the fluorescence light. M. Dufay et al. (1976) [64] used a 30 kV mass separator for high resolution studies of barium-138 and barium-137 isotopes. At the University of Marburg, Th. Meier et al. (1977) [65] used the experimental setup MARS-II (Marburg separator) to performed high resolution laser induced fluorescence spectroscopy on a fast beam of mass separated Xe ions. They investigated the hyperfine structure of the transition at 605 nm.

More than 60 papers were published using MARS-II setup at the University of Marburg between 1966 and 1996. The hyperfine structures and isotope shift of different spectral lines of different materials were determined: such as barium [66], xenon [65, 67], lanthanum [68, 69], samarium [70, 71], europium [72-75], cadmium [76], promethium [77, 78].

Different experimental arrangements have been developed and significant progress has been made in the high resolution spectroscopic method of collinear laser ion beam spectroscopy all over the world. A mass separator which is similar to MARS-II is working in Russia, known as IRIS (Investigation of Radioactive Isotopes on Synchrocyclotron) and is recently modified [79]. There are many other groups, for example in Japan [43, 44], Canada [48, 49], China [46, 47, 80], Sweden [81, 82] etc., working using the CLIBS technique to study the optical properties of different elements.

1.6 Thesis outline

The whole thesis is composed of eleven chapters including this chapter. In chapter 2, the theoretical background of fine structure levels is given. Chapter 3 gives a theoretical overview on the hyperfine structure splitting of an atomic fine structure level. Different broadening mechanisms of the spectral lines are discussed in the 4th chapter. Then different spectroscopic techniques which can be used for the investigation of hyperfine or fine structure patterns are discussed in chapter 5.

The research work carried out during these studies is discussed in chapters 6 to 10. The energy correction of the fine structure Pr II levels, by investigating the hyperfine structures appearing in the FT spectrum, is described in chapter 6. In chapter 7, the experimental setup of a Doppler reduced spectroscopic technique, namely inter-modulated laser induced fluorescence saturation spectroscopy, along with the results obtained is discussed.

A description of CLIBS is given in chapter 8. The detailed description of the experimental setup of MARS-II and its operating procedure is given in chapter 9. The results of CLIBS measurements are given in chapter 10. Finally, chapter 11 gives the conclusion.

2 A SUMMARY OF ATOMIC STRUCTURE

In spectroscopy, the radiation emitted or absorbed by atoms and molecules is investigated experimentally and theoretically to determine the identity, the structure and the environment of atoms and molecules. This field of physics has not only contributed much to our knowledge concerning our own earth but also of the sun, of interstellar space and of distant stars. The pioneer work in this field can be assigned to Newton's simple experiment (1666) in which he observed the band of different colors of the sunlight when he allowed white light to pass through a prism. He named this band of colors as "spectrum". In the beginning of the 19th century, W. Wollaston [83] and J. Fraunhofer [84] discovered several hundreds of dark absorption lines in the solar spectrum. Fraunhofer labeled eight of the strongest lines with the first eight letters of the alphabets. These lines are now known as Fraunhofer lines.

In 1860, L. Foucault [85] observed from a sodium flame two dark lines exactly at the same position of the D lines of the solar spectrum. This confirmed the presence of sodium in the sun. In the same year, G. Kirchhoff [86] presented a mathematical and experimental proof of the law (now known as Kirchhoff's law) "the ratios between the powers of emission and the powers of absorption for rays of the same wavelength is constant for all bodies at the same temperature". In 1868, A. Ångström et al. [87] published an investigation of the solar spectrum with accurate measurements of wavelengths to ten-millionths of a millimeter. This is known as Ångström's map and stood as a standard source of wavelengths for a number of years.

From 1885 onwards, the spectroscopic foundations were developed in some meaningful fashion on the basis of observed spectral lines by Balmer, Rydberg and many other renowned scientists. In 1913, N. Bohr [88] developed an atomic model for the hydrogen atom that really established a link between the experimental and theoretical work. Between 1920s and 1930s, spectroscopy grew rapidly in the scope of atomic physics with the introduction of quantum mechanics and the discovery of the electron and nuclear spins.

In order to understand the theory of atomic spectra, the hydrogen atom or hydrogen-like ions are treated in this chapter, because the Schrödinger and Dirac equations can be solved analytically for the hydrogen atom.

2.1 Bohr's formulation for hydrogen atom

It is well known that the energy levels of the hydrogen atom (neglecting fine structure) are given by simple formula of Bohr

$$T = -{}^{R}\!/_{n^2} \tag{2.1}$$

where R is the Rydberg constant and n is a positive integer. While deriving this formula, Bohr assumed the electron to follow a circular motion in an orbit around the nucleus with two additions: firstly, the orbital angular momentum is quantized and it is an integral multiple of $\hbar$ ($=h/2\pi$) and secondly, the electron does not radiate in such an allowed orbit. For a two body system (electron plus nucleus), the energy of a state with angular momentum $n\hbar$ is given by

$$E_n = -\frac{\mu e^4}{2(4\pi\varepsilon_0)^2\hbar^2}\frac{Z^2}{n^2} \tag{2.2}$$

where $\mu = mM/(m+M)$, is the reduced mass of the electron, m the mass of electron, M is the mass of the nucleus and Z is its charge (1 for H, 2 for He^{+}, 3 for Li^{++} and so on).

The Rydberg constant (in cm^{-1}) is given by

$$R = -\frac{2\pi^2\mu e^4}{100ch^3(4\pi\varepsilon_0)^2} \quad . \tag{2.3}$$

For hydrogen, R = 109678.00 cm^{-1} and for an infinitely heavy nucleus $\mu \to m$ it is R_∞ = 109737.31 cm^{-1}.

The radii of the Bohr orbits are given by

$$a_n = -\frac{(4\pi\varepsilon_0)\hbar^2}{me^2}\frac{n^2}{Z} \equiv \frac{n^2}{Z}a_0 \tag{2.4}$$

where a_0 is the radius of Bohr's first orbit and is treated as the atomic unit of length. Its numerical value is 0.529 Å.

2.2 Schrödinger equation for hydrogen/hydrogen like ions

The model of Bohr is valid only for hydrogen atom and does not explain the fine structure splitting. In order to describe the atomic structures of hydrogen/hydrogen like ions, scientists succeeded to develop the quantum mechanics and formulated a most unified theory, based on the de Broglie principle, Heisenberg's uncertainty principle, Schrödinger equation, Dirac's theory etc.

The starting point is the time independent Schrödinger equation

$$\hat{H}\Psi(r,\vartheta,\varphi) = E\Psi(r,\vartheta,\varphi) \ . \tag{2.5}$$

This is also known as eigenvalue equation. $\hat{H}$ is called the total energy operator or Hamiltonian. For simple hydrogen like systems it can be written as

$$\hat{H} = -\frac{\hbar^2}{2m}\,\nabla^2 + V(r) \ . \tag{2.6}$$

In above equation, the first term (∇^2) is the kinetic energy operator or the Laplacian operator and the second term is the potential energy of the electron given by

$$V(r) = -\frac{Ze}{4\pi\varepsilon_0 r} \ . \tag{2.7}$$

In equation 2.5, $\Psi(r,\vartheta,\varphi)$ is known as wave function or eigenfunction and is to be interpreted as a complex "probability amplitude", such that $\Psi * \Psi = |\Psi|^2$ is the probability of finding the electron at the point in space defined by the co-ordinates (r,ϑ,φ) (the nucleus is considered as the origin of the co-ordinates). The Hamiltonian operator operates on the wavefunction and gives the energy eigenvalue E and the eigenfunction. If more than one eigenfunctions are obtained corresponding to one eigenvalue of energy, then the eigenvalue E is said to be degenerate.

With ∇^2 expressed in spherical polar co-ordinates, it is possible to separate the wave function $\Psi(r,\vartheta,\varphi)$ into separate radial function $R(r)$ and angular function $Y(\vartheta,\varphi)$ as follows

$$\Psi(r,\vartheta,\varphi) = R(r)Y(\vartheta,\varphi) \ . \tag{2.8}$$

Now the Schrödinger equation can be split into radial and angular parts. The radial part of the Schrödinger equation is given by

$$\left(-\frac{1}{r}\frac{\partial^2}{\partial r^2}r + \frac{l(l+1)}{r^2} + \frac{Ze^2}{r}\right)R(r) = ER(r) \ . \tag{2.9}$$

The angular part of the Schrödinger equation is given by

$$\widehat{L^2}Y(\vartheta,\varphi) = l(l+1)Y(\vartheta,\varphi) \tag{2.10}$$

where L^2 is the operator of the total orbital angular momentum squared. The angular part of the wave function can further be separated into two parts, one in ϑ and the second in φ.

The solution of Schrödinger equation of radial and angular parts gives

$$E_n = -\frac{1}{2}\frac{me^4}{(4\pi\varepsilon_0)^2\hbar^2}\frac{Z^2}{n^2} \ . \tag{2.11}$$

Since an electron is bound with the nucleus therefore energy is negative. Equation 2.11 is same as result of model of Bohr (equation 2.2) for $\mu \to m$. In above equation n is an integer with $n \geq (l+1)$ and is known as the principle quantum number. l is the orbital angular momentum and can have values 0, 1, 2, 3, 4, 5, ….. corresponding to s, p, d, f, g, h ….. orbitals. The solution of Schrödinger equation for the angular part φ results in another quantum number m_l, known as magnetic quantum number which can have values from $+l$, l-1, . . .0, . . $-l$+1, $-l$ ($2l$ + 1 values).

The fine structure energy levels are produced due to the spin-orbit interaction of electrons (section 2.3.5). In the case of hydrogen like atoms, the total wave function of an atom in terms of spin wavefunction $\chi(m_s)$ and orbital wavefunction $\Psi(r,\vartheta,\varphi)$ is given by

$$\mathbf{\Psi} = \Psi_{nlsm_lm_s}(r,\vartheta,\varphi,m_s) = R_{nl}(r)Y_{lm_l}(\vartheta,\varphi)\chi(m_s) \tag{2.12}$$

where *n*, *l*, *s* are the principle, orbital and spin quantum numbers of an electron respectively. m_l is the projection of *l* and m_s is the projection of *s* with respect to the z-axis.

In hydrogen like atoms as well as in many electrons system, effects of some more perturbations such as relativistic term, Darwin term and Lamb shift are observed which are discussed in the upcoming section.

2.3 Hamiltonian for many electron systems

As the atomic number increases the number of electrons around the nucleus increases and the interactions between the electrons has to be taken into account, which become more and more complex. This needs a modification of the Hamiltonian of the whole system: Therefore some correction terms are introduced to obtain more realistic values for the allowed energies. For an N-electron system the Hamiltonian can be written as

$$H = \sum_{j=1\ to\ N} \left(-\frac{\hbar^2}{2\mathrm{m}} \nabla_{\mathrm{j}}^2 + V(r_i) \right) + correction\ terms\ . \qquad (2.13)$$

The correction terms mainly arise due to the electron-electron interactions, electron-nucleus interactions, interaction of orbital motion of the electron with their spin motion etc. These interactions can be considered as perturbations to the sum of kinetic and potential energies of all electrons. These correction terms are also known as fine structure corrections. The total Hamiltonian can be written as

$$H = H_0 + H_{ee} + H_r + H_D + H_{SO} \qquad (2.14)$$

where

H_0 is the core Hamiltonian given by $\sum_{j=1\ to\ N} \left(-\frac{\hbar^2}{2\mathrm{m}} \nabla_{\mathrm{j}}^2 + V(r_i) \right)$ and represents the electrostatic attraction between electrons and the nucleus

H_{ee} is the Hamiltonian representing the repulsive interaction between electrons

H_r is the Hamiltonian representing the relativistic term

H_D is known as the Darwin Hamiltonian

and

H_{SO} is the Hamiltonian representing the spin-orbit interaction of the electrons.

2.3.1 Electron-electron interaction H_{ee}

In many electron systems, the electron-electron repulsive interaction plays a major role in perturbing the electronic structure around the nucleus. In this case the energy operator of electron-electron interaction is given by

$$H_{ee} = \sum_{i<j} \frac{Ze^2}{r_{ij}} \tag{2.15}$$

where r_{ij} is the mean distance between a pair of electrons. The evaluation of the matrix element of the operator 2.15 involves a lengthy mathematics.

The interaction energy between a pair of electrons is given by

$$E_{ee} = \langle \Psi(1)\Psi(2) \left| \frac{Ze^2}{r_{ij}} \right| \Psi(1)\Psi(2) \rangle \ . \tag{2.16}$$

The solution of above matrix element can be expressed in two further matrices, Coulomb or direct integral *"*$\mathrm{J}(i,j)$*"* and the exchange integral *"*$K(i,j)$". The Coulomb integral represents the Coulomb interaction energy due to the charge distribution of the electrons and is given by

$$J(i,j) = \sum_k a^k(i,j) F^k(i,j) \ . \tag{2.17}$$

In above equation, a^k is the product of matrix elements of spherical harmonics and $F^k(i,j)$ is given by

$$F^k(i,j) = \int_0^\infty \int_0^\infty \frac{e^2 r_<^k}{r_>^{k+1}} |P_i(r_1)|^2 \left|P_j(r_2)\right|^2 dr_1 dr_2 \ . \tag{2.18}$$

The exchange integral represents the exchange part of the interaction energy between pairs of electrons and is given by

$$K(i,j) = \sum_k b^k(i,j) G^k(i,j) \tag{2.19}$$

where b^k are similar constants like a^k and

$$G^k(i,j) = \int_0^\infty \int_0^\infty \frac{e^2 r_<^k}{r_>^{k+1}} P_i(r_1)P_j(r_2)P_i(r_2)P_j(r_1)dr_1dr_2 \ . \qquad (2.20)$$

In equation 2.18 and 2.20, $r_<$ and $r_>$ are the smaller and the greater of the distances r_1 and r_2 of the electrons from the nucleus, respectively.

- $F^k(i,j)$ and $G^k(i,j)$ are positive radial integrals and are known as Slater-Condon parameters.
- For equivalent electrons $F^k(i,j) = G^k(i,j)$
- Only for few values of k the coefficients $a^k$and b^k have non-zero values therefore, equations 2.17 and 2.19 contain not too many terms.

2.3.2 The relativistic term H_r

The relativistic kinetic energy correction in the total Hamiltonian is given by

$$E = \sqrt{(m^2c^2)^2 + p^2c^2}$$

$$= m^2c^4 + \frac{p^2}{2m} - \frac{p^4}{8m^3c^2} + \ \ldots.$$

The third term in the above expansion is the first order relativistic correction to the energy i.e.

$$H_r = -\frac{p^4}{8m^3c^2} \ . \qquad (2.21)$$

As compared to the second term H_r is smaller by a factor of $(p/2mc)^2$, which is of the order of 0.1 cm^{-1}.

2.3.3 The Darwin term H_D

The Darwin term affects only the *s* states (l = 0) and makes the *s* and *p* states of roughly the same energy. This term arises due to the changes in the effective potential at the nucleus. It can be understood as a smearing out of the electrostatic interaction between the electron and nucleus due to rapid quantum oscillations of the electron. The shift in the *s* state is of the order of less than 0.1 cm^{-1} and is given by the relation

$$H_D = \left(\frac{e\hbar^2}{8m^2c^2}\right)\nabla \cdot E \ . \tag{2.22}$$

2.3.4 The Lamb shift

Another mechanism, same in nature as the Darwin term, affects the *s* state and is known as Lamb shift and makes the *s* state higher in energy than the *p* state. This shift occurs due to vacuum or zero point fluctuations of the quantized electromagnetic field. For hydrogen levels 2 $s_{1/2}$ and 2 $p_{1/2}$ the Lamb shift is about 0.034 cm^{-1} and for hydrogen like ions the shift is proportional to Z^4.

2.3.5 Spin-orbit interaction term H_{SO}

The interaction of the magnetic moment of the electron(s) with the magnetic field produced by the orbiting electron(s) is known as spin-orbit interaction. This interaction leads to the splitting of a term (energy level) into further levels known as fine structure energy levels. The separation of fine structure levels is of the order of 10-1000 cm^{-1} and is proportional to *Z*. For multi-electron systems H_{SO} can be written as

$$H_{SO} = \sum_{i=1\ to\ N} \xi(r_i)\vec{l}_i \cdot \vec{s}_i = \xi(r)\vec{L} \cdot \vec{S} \tag{2.23}$$

where $\xi(r)$ is the fine structure splitting constant. It depends on the electronic configuration, $\vec{S}\ (= \sum_i s_i)$ and $\vec{L}\ (= \sum_i l_i)$. Its expectation value is given by

$$\langle \xi(r) \rangle \propto \langle \Psi \left| \frac{1}{r^3} \right| \Psi \rangle \ . \tag{2.24}$$

The total angular momentum vector $\vec{J}$ is the vector sum of $\vec{L}$ and $\vec{S}$

$$\vec{J} = \vec{L} + \vec{S} \ . \tag{2.25}$$

Squaring equation 2.25 and solving for $\vec{L} \cdot \vec{S}$ gives

$$\vec{L} \cdot \vec{S} = \frac{(J^2 - L^2 - S^2)}{2} \ . \tag{2.26}$$

Equation 2.23 becomes

$$H_{SO} = \xi(r)\frac{(J^2 - L^2 - S^2)}{2} \quad . \tag{2.27}$$

The energy splitting due to the spin orbit interaction is given by

$$\Delta E_{SO} = \langle \Psi \xi(r)\ \frac{(J^2 - L^2 - S^2)}{2} \Psi \rangle$$

$$\Delta E_{SO} = \langle \xi(r) \rangle\ \frac{1}{2}[J(J+1) - L(L+1) - S(S+1)] \quad . \tag{2.28}$$

- Possible values of the total angular momentum quantum number J are $L + S$, $L + S - 1$, ..., $|L - S| + 1$, $|L - S|$.
- The selection rules for dipole transitions are $\Delta J = 0, \pm 1$.
- Each term splits into $(2S + 1)$ terms if $S < L$ or into $(2L + 1)$ if $L < S$.
- The total width of the fine structure splitting between $L + S$ and $L - S$ for $L > S$ is $\langle \xi(r) \rangle 2S(2L + 1)$ and for $L < S$ it is $\langle \xi(r) \rangle\ 2L(2S + 1)$.
- If $\langle \xi(r) \rangle > 0$, the fine structure multiplets are normal and if $\langle \xi(r) \rangle < 0$, the multiplets are inverted.

The energy difference between adjacent fine structure levels in a multiplet is given by the following relation

$$\Delta E(J) = E(J) - E(J-1) = \langle \xi(r) \rangle\, J\,. \tag{2.29}$$

From above equation it is clear that the energy difference between two fine structure levels with J and J-1 is proportional to the larger J value. This is known as Landé interval rule.

The energy difference does not depend on the orientation of the J vector in space, this implies that

$$\sum_{(L+S) \geq J \geq |L-S|} (2J+1)\Delta E_J = 0\,. \tag{2.30}$$

The mean value of terms which represents the center of gravity of the fine structure multiplet can be written as

$$\langle E \rangle = \frac{\sum_J (2J+1)E_J}{\sum_J (2J+1)} \quad . \tag{2.31}$$

The center of gravity coincides with the energy of the unsplitted term.

Since the relativistic term and the Darwin term are very small as compared to other interactions, the Hamiltonian for a system of N electrons can be reduced to

$$H = H_0 + H_1 + H_2 \tag{2.32}$$

where H_1 represents the electron-electron interaction and H_2 represents the spin orbit interaction. The relativistic effects of these two terms depend on the atomic number *Z*. For lighter atoms H_2 is smaller than H_1 and can be considered as perturbation, whereas in heavy atoms the spin-orbit interaction is stronger than the electron-electron interaction and therefore H_1 can be treated as perturbation.

2.4 The central field model

For atoms containing more than one electron, Schrödinger equation includes in the potential energy not only the attractive interaction between electron and the nucleus but also the repulsive interactions between each pair of electrons. Therefore, it is not possible to separate Schrödinger equation into the involved co-ordinates and hence it is almost impossible to solve it, neither directly, analytically nor by numerical methods. But the problem can be handled by assuming that all interactions (electron-electron repulsive interaction and electron-nucleus attractive interactions) are combined to produce an effective field and any arbitrary electron moves in this combined potential V_c. Furthermore, V_c is assumed to be a function of r only and not of the angle co-ordinates. This is known as the central field model or the central field approximation. This enables to separate the radial and angular parts of the Schrödinger equation as in the case of hydrogen. The potential V_c is different for each electron and depends on the radial wave functions of all the other electrons. The effective field V_c is computed by some sort of self-consistent field approach. Using Poisson equation, V_c is computed for a guessed wave function for each electron and a new set of *R(r)* is obtained. The cycle is repeated unless V_c and *R(r)* become consistent.

2.5 Coupling of angular momenta

In many electron systems, various angular momenta couple together and result in a total angular momentum of the atoms. There are different ways of angular momenta coupling. For the electron systems having stronger interaction between electrons than the spin-orbit interaction the electrons couple through LS-coupling. The electrons couple according to jj-coupling in an electron system where spin-orbit interactions are strong. There are also intermediate-coupling schemes which are employed if neither of the two interactions dominates.

2.5.1 LS-coupling

For many electrons system, where the electrostatic interaction between electrons is larger than the spin-orbit interaction, the LS-coupling or Russell-Saunders coupling [89] is employed. The orbital angular momenta of individual electrons couple together to give a total orbital quantum number $\vec{L}$ and similarly the spins of individual electrons combine together to give a resultant spin $\vec{S}$ i.e.

$$\vec{L} = \sum_i l_i \text{ and } \vec{S} = \sum_i s_i$$

with

$$|\vec{L}| = \sqrt{L(L+1)}\hbar \text{ and } |\vec{S}| = \sqrt{S(S+1)}\hbar \quad .$$

The total orbital angular momentum $\vec{J}$ is the vector sum of $\vec{L}$ and $\vec{S}$ and is given by

$$\vec{J} = \vec{L} + \vec{S} \text{ with } |\vec{J}| = \sqrt{J(J+1)}\hbar \quad .$$

The possible values of J are $|L + S|$, ... , $|L - S|$.

The LS-coupling is dominant in low lying states of light atoms and is often used to determine the ground states of the atoms. The capital letters of the Latin alphabet are used for denoting states, as follows:

$L = 0$,	1,	2,	3,	4,	5,	6,	7,	………..
S	*P*	*D*	*F*	*G*	*H*	*I*	*K*	………..

The state of an electron is described in the form $^{2S+1}L_J$. For example the state with $L = 0$, $S = 3/2$ and $J = 3/2$ is denoted as $^4S_{3/2}$.

2.5.2 jj-coupling

jj-coupling scheme is the most suitable coupling scheme in the multi electrons systems when the spin-orbit interaction is stronger than the electrostatic Coulomb interaction between the electrons. In this case $\vec{l}_i$ and $\vec{s}_i$ of individual electrons combine together to form the resultant angular momentum $\vec{J}_i$ i.e.

$$\vec{j}_i = \vec{l}_i + \vec{s}_i \ .$$

The total angular momentum J is the vector sum of $\vec{j}_i$ vectors, given by

$$\vec{J} = \sum_i \vec{j}_i \ .$$

The possible J values lie between

$|\sum_i \vec{j}_i|_{\text{Max}}, |\sum_i \vec{j}_i|_{\text{Max}} - 1, \ldots \ |\sum_i \vec{j}_i|_{\text{Min}} + 1, |\sum_i \vec{j}_i|_{\text{Min}}$

In the jj-coupling scheme the state of each electron is described by $(j_1\ j_2)_J$. For example, for a d-electron, $j = 3/2, 5/2$, $j_1 = 1/2$, $j_2 = 3/2$ and $J = 1, 2$. The electron states become $(1/2,\ 3/2)_1$ and $(1/2,\ 3/2)_2$.

The spin-orbit interaction is strong for the high lying states. This interaction depends on the nuclear charge *Z*, therefore jj-coupling occurs in the heavier atoms.

2.6 Parity

The wave functions $\Psi(r,\vartheta,\varphi)$ corresponding to different values of the angular momentum of an electron behaves differently when an inversion transform [($x \rightarrow -x; y \rightarrow -y; z \rightarrow -z$) or in spherical co-ordinates ($r \rightarrow r;\ \vartheta \rightarrow \pi - \vartheta;\ \varphi \rightarrow \varphi + \pi$)] is applied.

Consequently $\Psi = \Psi\,(-1)^l$. The functions Ψ correspond to the even states with even values of l and do not change the sign. Similarly, for odd values of l the wave function changes the sign on an inversion transform and the states are called odd states.

The Hamiltonian is invariant under inversion. This means that the parity of the wave function of a stationary state is conserved. So, each state in a centrally symmetric field is characterized by a definite parity. The wave function of the state of non-interacting particles can be written as a product of different functions, therefore the parity of a wave function is determined by $\sum_i l_i$. The parity of a system of particles is even if the sum of the angular momenta of the particles has even value and odd for odd values of this sum.

2.7 Electron configuration

The electrons in an atom occupy individual energy levels E_{nl} with respect to the quantum numbers n and l. This is known as the electron configuration. In spectroscopic notations, n is written as number and l as letter. The configuration of the ground state is called the ground configuration and the configurations of higher states are called the excited configurations. First the orbitals with lowest energy are filled. The order of filling the orbitals is known as Madelung rule. According to this rule the orbitals with the lower value of (n + l) are filled before those with the higher (n + l) value. The number of electrons in an orbital is limited by Pauli's exclusion principle.

The electron configuration of praseodymium (Pr) is:

$[1s^2 2s^2 2p^6 3s^2 3p^6 3d^{10} 4s^2 4p^6 4d^{10} 5s^2 5p^6]\ 4f^3 6s^2 (^4\mathrm{I}^\circ_{9/2})$

The electrons inside the bracket [ ] are in fully occupied orbits. Therefore, all spin and orbital momenta compensate fully and the configuration of the core is $^1\mathrm{S}_0$ (noble gas ground state). In case of a many electrons system like Pr, the coupling of angular momenta gives rise to a number of energy levels and the higher excited states overlap with each other. In such kind of situations the configuration is given by the mixture of all overlapping configurations, this situation is called configuration mixing or configuration interaction which takes place only within configuration of same parity.

3 HYPERFINE STRUCTURE

The hyperfine structure in the optical spectra was discovered independently, in 1891 by A. Michelson [90] and in 1897 by C. Fabry and A. Pérot [91], and was explained by W. Pauli [1] in 1924. In this chapter, the splitting of a fine structure electronic level into hyperfine structure levels is discussed. The hyperfine splitting is caused by the interaction of spinning and orbiting electrons with the nuclear moments. The hyperfine splitting is smaller than the fine structure splitting and is of the order 0.001 to 1 cm^{-1} depending on the atomic number of the element.

The hyperfine splitting is explained by associating a small magnetic moment to the nucleus. The nucleus is composed of a compound structure of nucleons (protons and neutrons). Each of these nucleons has an intrinsic spin ½ which may involve in the orbital motion of the nucleus. The nuclear spin I, also called nuclear spin quantum number is the resultant of spins and angular momenta of all these nucleons. Consequently, a nucleus has a nuclear magnetic moment μ_I in the direction of I. The nuclear spin quantum number can have either integral of half integral values. Its value ranges from 0 to 15/2 for the stable atomic nuclei. The nuclear spin interacts with the total angular momentum of the electron which causes the splitting of a fine structure level into hyperfine levels. Then the total angular moment $\vec{F}$ of the atom is the vector sum of the nuclear spin $\vec{I}$ and the total angular momentum of the electrons $\vec{J}$ (figure 3.1) i.e.

$$\vec{F} = \vec{I} + \vec{J} \quad . \tag{3.1}$$

Atoms having an even number of protons as well as even number of neutrons have nuclear spin quantum number 0 and thus show no splitting of fine structure levels.

Due to the strong nuclear interactions, a distribution and motion of nucleons is established inside the nucleus in a particular manner, giving rise to the production of electromagnetic multipole moments of the nucleus. Amongst possible numbers of multipole moments (2^m pole moments), the non-vanishing nuclear multipoles are: The magnetic moments for odd value of m and electric moments for even value of m (where $m > 0$). A nucleus with spin I can not possess a multipole moment of order $2m$ where $m > 2I$. Usually, two lowest order interactions with $m = 1$ and $m = 2$ are taken into account. $m = 1$ corresponds to the magnetic dipole interaction and m = 2 corresponds to the electric quadrupole interaction. The magnetic dipole moment depicts the structure of the individual nucleons in the nucleus and the electric quadrupole moment gives so the information about the shape and charge distribution within the nucleus. The splitting of a fine structure level is caused mainly by the interaction of the magnetic dipole moment with the electromagnetic moment of the electrons. The total width of the splitting of a fine structure level is given by a constant known as magnetic dipole interaction constant A. The interaction of the nuclear electric quadrupole moment with the electromagnetic moment of electrons causes a shift of the hyperfine structure levels but does not further split the levels. This is also named as the electric hyperfine structure and is described by a constant known as electric quadrupole interaction constant B.

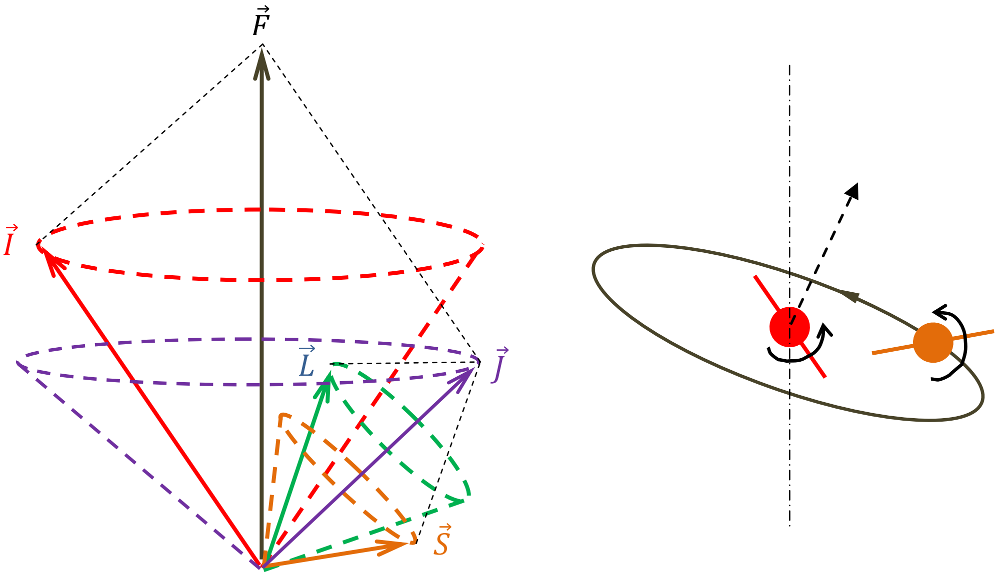

Figure 3.1: Orbital and vector models illustrating the coupling of nuclear moment $\vec{I}$ with the electronic angular moment $\vec{J}$ to form a resultant angular moment of atom $\vec{F}$.

3.1 Magnetic dipole interaction

The nucleus has a spin angular moment I which leads to the nuclear magnetic moment μ_I given by

$$\mu_I = g_i \mu_N I \tag{3.2}$$

where μ_N is known as nuclear magneton and is related with Bohr's magneton μ_B as

$$\mu_N = \frac{\mu_B}{1836} = 5.05082 \times\ 10^{-27}\ J/T. \tag{3.3}$$

In equation 3.2, g_i is called nuclear g factor or nuclear Landé factor. The magnitude of $\vec{I}$ is given by $|\vec{I}| =\ \sqrt{I(I+1)}\hbar$.

The nuclear moment μ_N interacts with the magnetic field $\vec{B}$ produced by the spin and the orbital motion of the electrons and is treated as small perturbation to the energy of the atom. The Hamiltonian of this interaction is given by

$$\widehat{H}_\mu = -\, \vec{\mu}_N \cdot \vec{B}\ . \tag{3.4}$$

The magnetic field produced by the electrons is proportion to the total angular momentum $\vec{J}$ i.e.

$$\vec{B} \propto \vec{J}\ \ .$$

Equation 3.4 becomes

$$\begin{aligned} \widehat{H}_\mu &\propto -\,\vec{I}\cdot\vec{J} \\ &= A\,\vec{I}\cdot\vec{J}\ \ . \end{aligned} \tag{3.5}$$

"*A*" is known as the magnetic dipole interaction constant.

The interaction energy is obtained by

$$\begin{aligned} E_\mu &= \langle \Psi(r,\vartheta,\varphi) \big| \widehat{H}_\mu \big| \Psi(r,\vartheta,\varphi)\ \rangle \\ &= \langle \Psi(r,\vartheta,\varphi) \big| A\,\vec{I}\cdot\vec{J} \big| \Psi(r,\vartheta,\varphi)\ \rangle\ . \end{aligned} \tag{3.6}$$

The total angular momentum of the atom is given by equation 3.1. The value of $\vec{I}\cdot\vec{J}$ can be obtained by squaring equation 3.1 and solve for $\vec{I}\cdot\vec{J}$

$$\vec{I}\cdot\vec{J} = \frac{F^2 - I^2 - J^2}{2}\ . \tag{3.7}$$

Solution of equation 3.6 gives

$$E_\mu = \frac{A}{2}[F(F+1) - I(I+1) - J(J+1)] \tag{3.8}$$

or

$$E_\mu = \frac{CA}{2} \tag{3.9}$$

with

$$C \equiv F(F+1) - I(I+1) - J(J+1) \quad . \tag{3.10}$$

The Landé interval rule is also applicable for magnetic hyperfine structure splitting, so the energy spacing between successive hyperfine levels is given by

$$\begin{aligned} \Delta E_\mu(F, F-1) &= E_\mu(F) - E_\mu(F-1) \\ &= \frac{A[F(F+1) - (F-1)F]}{2} \\ &= AF \quad . \end{aligned} \tag{3.11}$$

The magnet dipole interaction constant *A* is the product of nuclear and electronic quantities. For a particular atom, *A* is a function of the total angular momentum *J* and is given by

$$A(J) = \frac{\mu_I < \vec{B} >}{IJ} \tag{3.12}$$

or

$$A(J) = \frac{g_I \mu_B < \vec{B} >}{1836 J} \quad . \tag{3.13}$$

3.1.1 Some characteristics of magnetic hyperfine structure multiplets

- The number of hyperfine levels are equal to 2*J* + 1 if $J \leq I$ or 2*I* + 1 if $J > I$.
- The possible values of *F* are *I* + *J*, *I* + *J* - 1. . . . . . , |*I* – *J* + 1|, |*I* - *J*|.
- The total width of the splitting between |*I* - *J*| and *I* + *J* is

$$\Delta W = AI(2J + 1) \text{ if } I \leq J$$

and it is $\Delta W = AJ(2I + 1)$ if $I \geq J$

- From equation 3.13, it is clear that for constant B values, the magnetic dipole interaction constant A would be maximum for minimum J values. The minimum possible J value is ½ for an unpaired s electron, so the A value is largest for an unpaired s electron.
- The electric dipole transitions rules for F are $\Delta F = 0, \pm 1$.
- The transition from $F = 0$ to $F = 0$ is not allowed.
- The separation between adjacent hyperfine levels is proportional to the larger F values of the two levels.
- For positive values of A ($A > 0$), the hyperfine multiplets are known as normal hyperfine multiplets (as shown in figure 3.2) and the level with the largest F values has the highest energy. For $A < 0$, the level with largest F values has the minimum energy and the hyperfine multiplets are known as inverted hyperfine multiplets.

  The classical explanation of the normal and inverted hyperfine structures is: If the spinning electron and the nucleus are considered as small magnets acting on each other at same distance from each other, the stable of the two will be that for which the mechanical moments are in the same direction and the magnetic moments are in opposite direction. In this case the hyperfine multiplet is known to be normal. If the nuclear and electron magnetic moments are in the same direction then the hyperfine multiplet is inverted.

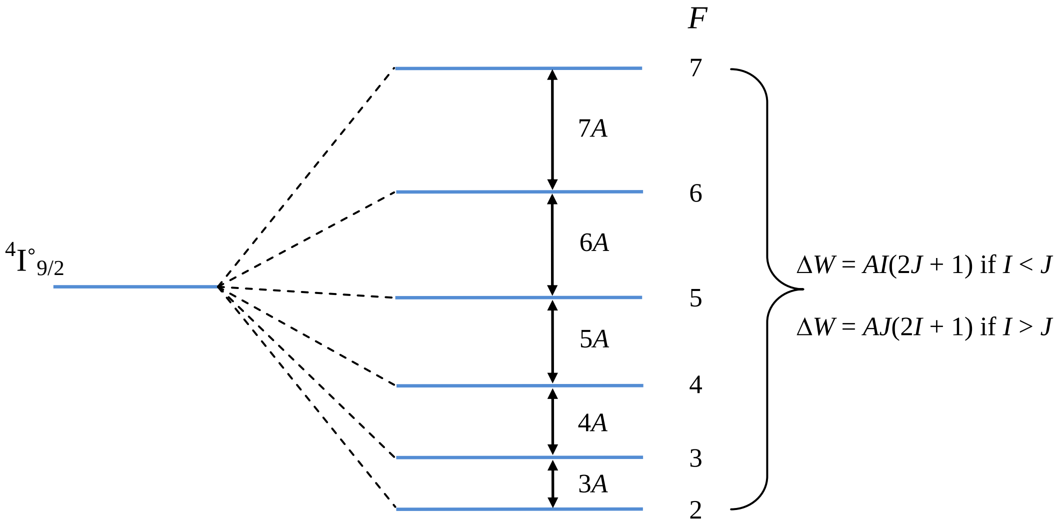

Figure 3.2: Splitting of the ground state of praseodymium into 6 hyperfine levels.

3.2 Electric quadrupole interaction

In 1935 Schüler and Schmidt [92] observed that the optical spectra of the europium isotopes could not be explained by the magnetic hyperfine structure but by the existence of electric quadrupole moments Q of the nuclei. The quadrupole moment is a measure of the deviation of the charge distribution in the nucleus from spherical symmetry. A non-spherically symmetric charge distribution interacts with the electric field produced by the electrons and consequently gives rise to an electric hyperfine structure.

$Q = 0$: Spherical charge distribution

$Q < 0$: Oblate charge distribution

$Q > 0$: Prolongated charge distribution

Q is measured in barn and 1barn is equal to 10^{-24} cm^2.

Q is a tensor: By choosing a proper coordinate system the off-diagonal elements can be made zero, consequently the mathematics involved can be made simple. Q is given by

$$Q = \langle I,I \left| r^2(3cos^2\theta_{IJ} - 1) \right| I,I \rangle \tag{3.14}$$

where θ_{IJ} is the angle between I and J (which are the principle axes for nuclear and electric systems).

The averaged gradient V_Q of the electric field produced by the electrons at the nucleus is given by

$$V_Q = \frac{1}{2}\langle J,J \left| \frac{\partial^2 V_c}{\partial z^2} \right| J,J \rangle \quad . \tag{3.15}$$

V_c is the electrostatic potential created by all electrons at the nucleus. The shift in the hyperfine levels due to the quadrupole interaction is given by

$$E_Q = \frac{eQ}{4}\langle \left| \frac{\partial^2 V_c}{\partial z^2} \right| \rangle \left[\frac{6(I \cdot J)^2 + 3(I \cdot J) - 2IJ(I+1)(J+1)}{IJ(2I-1)(2J-1)} \right] \; . \tag{3.17}$$

The classical analogue of above equation is

$$E_Q = \frac{eQ}{4}\langle\left|\frac{\partial^2 V_c}{\partial z^2}\right|\rangle\left[\frac{(3cos^2\theta_{IJ}-1)}{2}\right] \ . \tag{3.18}$$

Substituting the value of *C* (equation 3.10) in equation 3.17

one gets

$$E_Q = \frac{eQ}{4}\langle\left|\frac{\partial^2 V_c}{\partial z^2}\right|\rangle\left[\frac{\frac{3}{2}C(C+1)-2IJ(I+1)(J+1)}{IJ(2I-1)(2J-1)}\right]$$

$$= \frac{B}{4}\left[\frac{\frac{3}{2}C(C+1)-2IJ(I+1)(J+1)}{IJ(2I-1)(2J-1)}\right] \ . \tag{3.19}$$

B is known as the electric quadrupole interaction constant and is defined by

$$B = eQ\,\langle\frac{\partial^2 V_c}{\partial z^2}\rangle \ . \tag{3.20}$$

For *s* terms the electron charge distribution is spherical therefore $\langle\frac{\partial^2 V_c}{\partial z^2}\rangle = 0$. So *B* is 0 for *s* terms. *B* is also 0 for *I* < 1.

The total splitting of the hyperfine levels is obtained by combining equations 3.9 and equation 3.19 i.e.

$$E_{hfs} = \frac{CA}{2}+\frac{B}{4}\left[\frac{\frac{3}{2}C(C+1)-2IJ(I+1)(J+1)}{IJ(2I-1)(2J-1)}\right] \ . \tag{3.21}$$

Here *A*(*J*) and *B*(*J*) both are functions of *J*. The magnetic dipole interaction causes a splitting of the fine structure levels into the hyperfine levels whereas the electric quadrupole interaction causes an additional shift of the hyperfine levels. The quadrupole interaction gives rise to a deviation from the interval rule because its dependency on *F* is different from that of the magnetic dipole interaction and becomes more prominent whenever the magnitude of *B* is comparable with the *A* value. The hyperfine levels are independent of the quantum number M_F and have (2*F* + 1) degenerate levels. The degeneracy can be removed by studying the Zeeman Effect.

3.3 Experimental determination of the hyperfine interaction constants

Equation 3.21 contains two parts one part is the magnetic interaction and the second part is the electrostatic interaction i.e.

$$\Delta E_{hfs} = \alpha(F,J,I)A(J) + \beta(F,J,I)B(J)\ . \tag{3.22}$$

Where $\alpha(F,J,I)$ and $\beta(F,J,I)$ are called Casimir factors and are given by

$$\alpha(F,J,I) \equiv \frac{C}{2} = \frac{1}{2}[F(F+1) - I(I+1) - J(J+1)] \tag{3.23}$$

and

$$\beta(F,J,I) = \frac{1}{4}\left[\frac{\frac{3}{2}C(C+1) - 2IJ(I+1)(J+1)}{IJ(2I-1)(2J-1)}\right]. \tag{3.24}$$

The transitions between two different hyperfine levels (of different fine levels) are allowed for the selection rules $\Delta F = 0, \pm 1$ and $\Delta J = 0, \pm 1$. The transition between $F = 0 \rightarrow F = 0$ is not allowed. Also the parities of the levels involved in a transition must be different. The hyperfine components of a hyperfine pattern of a transition are determined by the following relation.

$$\nu(F_{\mathrm{o}}, F_{\mathrm{u}}) = \nu_{\mathrm{c}} + \alpha_{\mathrm{o}}(F_{\mathrm{o}}, J_{\mathrm{o}}, I_{\mathrm{o}})A_{\mathrm{o}} + \beta_{\mathrm{o}}(F_{\mathrm{o}}, J_{\mathrm{o}}, I_{\mathrm{o}})B_{\mathrm{o}} - \alpha_{\mathrm{u}}(F_{\mathrm{u}}, J_{\mathrm{u}}, I_{\mathrm{u}})A_{\mathrm{u}} - \beta_{\mathrm{u}}(F_{\mathrm{u}}, J_{\mathrm{u}}, I_{\mathrm{u}})B_{\mathrm{u}}\ . \tag{3.25}$$

In this equation, ν_c is known as the center of gravity of the transition and is equal to the energy difference of the fine structure levels involved in the transition. A_{o}, B_{o}, A_{u}, and B_{u} are the hyperfine constants of the upper and the lower levels, respectively (the letters in the subscript “o” and “u” are denoted for the upper (oben in German) and for the lower (unten in German) levels, respectively. For the determination of these unknown constants from an experimentally recorded hyperfine structure, it is necessary to identify the quantum numbers of at least 5 hyperfine components and then to solve 5 linear equations. If more than 5 components are indentified then the relative or absolute position of the hyperfine components can be determined by solving these equations using a least square method.

The relative intensity of the individual hyperfine components can be determined using the following expression

$$I(F_\text{o} \to F_\text{u}) = \frac{(2F_\text{o}+1)(2F_\text{u}+1)}{2I+1}\begin{Bmatrix} J_\text{o} & F_\text{o} & I \\ F_\text{u} & J_\text{u} & 1 \end{Bmatrix}^2 . \qquad (3.26)$$

The term in the curly brackets is known as 6j tensor operator. The expression 3.26 is valid for the cases where interactions between neighboring fine structure electronic levels are weak. The strongest hyperfine components in a hyperfine structure are those for which $\Delta F = \Delta J$ i.e., J and F are oriented in the same direction. These components lie on the diagonal of the matrix 3.26 and therefore are also called diagonal components. The off diagonal entries in 3.26 give the relative intensities of the weak components of a hyperfine structure for $\Delta F \neq \Delta J$, therefore are called off diagonal components.

3.4 Intensity sum rule

In 1920s, H. Dorgelo [93] and L. Orstein and H. Burger [94] proposed independently an intensity rule which is also called the sum rule for the transitions between fine structure levels. It is stated as “1) the sum of the intensities of all lines of a multiplet which start from a common initial level is proportional to the quantum weight $(2J_\text{o} + 1)$ of the initial level, 2) the sum of the intensities of all lines of a multiplet which end on a common final level is proportional to the quantum weight $(2J_\text{u} + 1)$ of the final level”. The statistical weight of a fine structure level is given by $2J + 1$ (or $2F + 1$ in case of a hyperfine structure level). We consider an example of transitions between ^2D and ^2P multiplets (figure 3.3).

According to the sum rule:

$$\frac{I_b}{I_a + I_c} = \frac{2 \times \frac{5}{2} + 1}{2 \times \frac{3}{2} + 1} = \frac{3}{2}$$

and

$$\frac{I_c}{I_a + I_b} = \frac{2 \times \frac{1}{2} + 1}{2 \times \frac{3}{2} + 1} = \frac{1}{2} \ .$$

The relative intensities of these lines can be calculated from these two equations as

$$I_a : I_b : I_c = 1 : 9 : 5 \ . \tag{3.27}$$

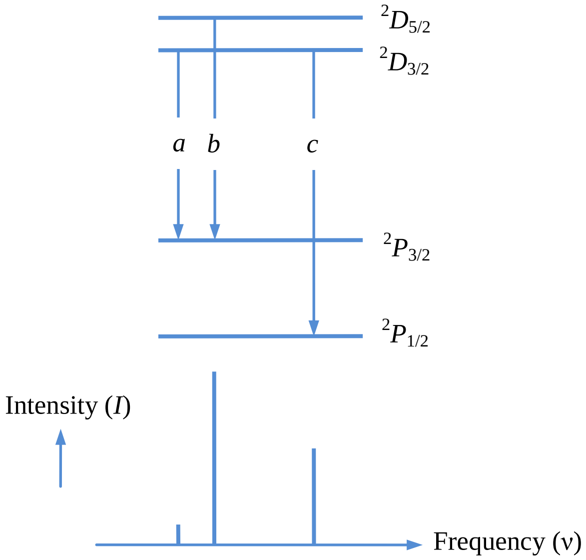

Figure 3.3: Illustration of intensity sum rule in the transition between ^{2}D and ^{2}P multiplets.

Normally, the intensity sum rules alone are not sufficient to determine the relative intensities within a multiplet. H. Russel and F. Saunders [95] developed an angular momenta coupling, known as Russel-Saunders coupling, using the quantum mechanical treatment of P. Dirac [96]. For complex spectra the transition intensities between fine structure multiplets are given by

For transitions $L - 1 \rightarrow L$

$$\begin{cases} J - 1 \rightarrow J, I_{int} = \dfrac{a(L+J+S+1)(L+J+S)(L+J-S)(L+J-S-1)}{J} \\ J \rightarrow J, I_{int} = -\dfrac{a(L+J+S+1)(L+J-S)(L-J+S)(L-J-S-1)(2J+1)}{J(J+1)} \\ J + 1 \rightarrow J, I_{int} = \dfrac{a(L-J+S)(L-J+S-1)(L-J-S-1)(L-J-S-2)}{(J+1)} \end{cases} \tag{3.28}$$

For transitions $L \rightarrow L$

$$\begin{cases} J-1 \rightarrow J, I_{int} = -\dfrac{b(L+J+S+1)(L+J-S)(L-J+S+1)(L-J-S)}{J} \\ J \rightarrow J, I_{int} = \dfrac{b[L(L+1)J(J+1)-S(S+1)]^2(2J+1)}{J(J+1)}. \\ J+1 \rightarrow J, I_{int} = -\dfrac{b(L+J+S+2)(L+J-S+1)(L-J+S)(L-J-S-1)}{(J+1)} \end{cases}$$

(3.29)

Where "a" and "b" are constants and need not to be determined for the calculation of relative intensities. The expression in equations 3.28 and 3.29 are valid for all kind of interactions of the angular momenta. Therefore, the relative intensities of the hyperfine components can be calculated by replacing *F* with *J*, *S* with *I*, and *L* with *J* in above equations. This leads to

For transitions $J - 1 \rightarrow J$

$$\begin{cases} F-1 \rightarrow F, I_{int} = \dfrac{a(J+F+I+1)(J+F+I)(J+F-I)(J+F-I-1)}{F} \\ F \rightarrow F, I_{int} = -\dfrac{a(J+F+I+1)(J+F-I)(J-F+I)(J-F-I-1)(2F+1)}{F(F+1)} \\ F+1 \rightarrow F, I_{int} = \dfrac{a(J-F+I)(J-F+I-1)(J-F-I-1)(J-F-I-2)}{(F+1)} \end{cases}$$

(3.30)

For transitions $J \rightarrow J$

$$\begin{cases} F-1 \rightarrow F, I_{int} = -\dfrac{b(J+F+I+1)(J+F-I)(J-F+I+1)(J-F-I)}{F} \\ F \rightarrow F, I_{int} = \dfrac{b[J(J+1)F(F+1)-I(I+1)]^2(2F+1)}{F(F+1)}. \\ F+1 \rightarrow F, I_{int} = -\dfrac{b(J+F+I+2)(J+F-I+1)(J-F+I)(J-F-I-1)}{(F+1)} \end{cases}$$

(3.31)

The relations 3.26, 3.28 and 3.29 are applicable for energy levels which have very weak interactions with neighboring energy levels. When there are levels very close to each others with either with the same parity, same *F* values or their *J* values differ by 0 or ±1, these levels can perturb each other and change the transition probabilities and transitions with $\Delta J = \pm 2$ may also occur. For complex excited states, there is a strong mixing of the energy states and the interactions between the various states produce distortion in the hyperfine patterns. This phenomenon is known as anomalous intensity of hyperfine components.

4 BROADENING OF A SPECTRAL LINE

The spectral lines observed due to the emission or absorption of radiation are never monochromatic but always have a spectral distribution $I(\nu)$ around the center frequency $\nu_o = (E_i - E_f)/h$ corresponding to a transition with the energy difference $\Delta E = E_i - E_f$ between upper and lower energy levels. The spectral distribution function $I(\nu)$ around the central frequency ν_o is known as the line profile of a spectral line. A spectral line is always described by a parameter known as full width at half maximum (FWHM), commonly called half width or line width.

The line width is determined by the frequency interval $\delta\nu = |\nu_2 - \nu_1|$ for which $I(\nu_1) = I(\nu_2) = I(\nu_o)/2$. In terms of angular frequency ($\omega = 2\pi\nu$) it is given by $\delta\omega = 2\pi\delta\nu$ and in terms of wavelength ($\lambda = c/\nu$) it is determined by $\delta\lambda = -(c/\nu^2)\delta\nu$. However, the relative line widths are same in all schemes i.e.

$$\left|\frac{\delta\nu}{\nu}\right| = \left|\frac{\delta\omega}{\omega}\right| = \left|\frac{\delta\lambda}{\lambda}\right| \tag{4.1}$$

The region inside the line width is called the ***kernel*** of the line and the regions outside line width are called the ***line wings*** (figure 4.1).

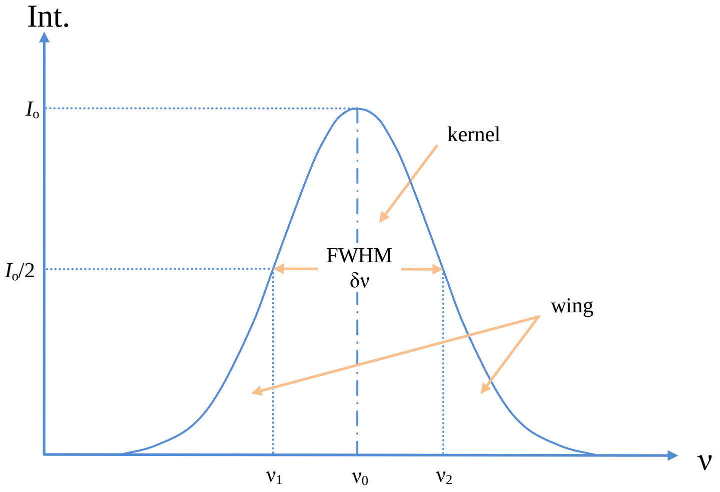

Figure 4.1: The line profile of a spectral line.

The line width of a spectral line is limited not only by the spectral resolution of the measuring instruments but also by several physical broadening mechanisms taking place in the sample (e.g. discharge cell). Some important line broadening mechanisms are: Natural broadening, Doppler broadening, pressure broadening, saturation broadening etc.

If all atoms/molecules in a sample have equal probability of emission or absorption of radiation the broadening mechanism is classified as a homogenous broadening. If the probability of emission or absorption of radiation is different for all atoms/molecules then the broadening is known as an inhomogeneous line broadening. The natural broadening and the pressure broadening are examples for homogenous broadening and the Doppler broadening is an example of inhomogeneous broadening.

In the upcoming sections, some important line broadening mechanisms are discussed.

4.1 Natural broadening

According to the Heisenberg's uncertainty principle in the form of energy and time, $\Delta E_i \Delta t_i \geq \hbar$, an uncertainty in the energy (broadening) of a particular state (level) is associated with the time ($\equiv \tau_i$) which an atom spends in that state (life time). This type of broadening which always exist is known as natural line width of that state and is given by

$$\Delta E_i = \hbar/\tau_i$$

and in terms of frequency

$$\Delta\omega_i = \frac{1}{\tau_i} \ . \tag{4.2}$$

It is just the reciprocal of the mean life time of that state. For metastable states or for ground states, the life time is long enough (for ground state infinitely long) to neglect $\Delta\omega_\mathrm{i}$ in most experiments.

If a transition is taking place between two states $E_\mathrm{i} \rightarrow E_\mathrm{f}$ which have certain spread in their energies ΔE_i and ΔE_f respectively, then both states will contribute to the line broadening. In this case the natural line width of the spectral line is given by

$$\Delta\omega_n = \Delta\omega_{if} = \frac{1}{\tau_i} + \frac{1}{\tau_f} \ . \tag{4.3}$$

Natural broadening of a spectral line is a homogenous broadening with a Lorentzian line profile, given by

$$I(\nu) = \frac{1}{4\pi\tau} \cdot \frac{1}{(\nu - \nu_0)^2 + \left(\frac{1}{4\pi\tau}\right)^2} \; . \tag{4.4}$$

The life time of the high lying states is of the order of 10^{-6} to 10^{-9} sec, therefore natural line width of a transition between such levels is of the order of 0.1 MHz to 100 MHz.

4.2 Doppler Broadening

Usually, the natural line width $\Delta\omega_n$ cannot be observed without using special techniques, because it is completely covered by many broadening effects. The major contribution to the spectral line width at low pressure of a gas is the Doppler broadening. The Doppler broadening is caused by the random thermal motion of the emitting or absorbing atoms/molecules.

For an excited atom/molecule moving with a velocity $\vec{u} = \hat{\imath}u_x + \hat{\jmath}u_y + \hat{k}u_z$ relative to the rest frame of the detector, the central frequency (ω_0) of the emission line is Doppler shifted in the frame of reference of atoms/molecules by an amount

$$\omega_e = \omega_0 + \vec{k} \cdot \vec{u} \; . \tag{4.5}$$

$\vec{k}$ (k = 2π/λ) is the wave vector of the emitted radiation. The frequency of the emitted radiation depends upon the direction of motion of the moving atom with respect to the detector. Detector sees blue shifted radiation ($\omega_e > \omega_0$) from an atom moving towards the detector and red shifted ($\omega_e < \omega_0$) from an atom moving away from the detector. If the direction of motion of an atom and the emitted radiation is chosen as the z-axis, then equation 4.5 can be written as

$$\omega_e = \omega_0 \left(1 + \frac{u_z}{c}\right) \; . \tag{4.6}$$

The Doppler broadening is an example of inhomogeneous broadening. The intensity profile of a Doppler-broadened spectral line is a Gaussian profile with a line width given by the following relation

$$\delta\nu_D = 7.16 \times 10^{-7}\nu_0\sqrt{\frac{T}{M}(\frac{g}{K\cdot mol})} \ . \qquad (4.7)$$

In equation 4.7 $\delta\nu_D$ is the Doppler width, ν_0 is the central frequency of the emission/absorption line. From above equation, it can be concluded that:

- The Doppler width is directly proportional to the frequency, therefore the Doppler width is larger in the visible and UV regions than in the IR.
- Doppler width decreases with increasing atomic mass as $\sqrt{M}$.
- Since $\delta\nu_D \propto \sqrt{T}$, the Doppler width increases with increasing temperature of a gas. Therefore by reducing the temperature of the gas, e.g. by cooling a discharge cell with liquid nitrogen, the Doppler width can be reduced.

There are different experimental arrangements of laser spectroscopy to reduce the Doppler broadening of the spectral lines. Some examples are: Atomic/ionic beam spectroscopy, saturation spectroscopy, two photon spectroscopy etc.

4.3 Saturation broadening

At sufficiently high laser intensities, the optical pumping rate of an absorbing transition becomes larger than the relaxation rates. Therefore, the population in the lower absorbing level decreases resulting in the saturation of the transition. The saturation is most pronounced at the center of the transition and decreases as the frequency moves away from the center. At the line center the fluorescence signal is not proportional to the laser intensity but at wings the fluorescence signal is proportional to the intensity of the laser: Consequently, the spectral line broadens. This kind of line broadening is known as saturation broadening. The line profile of the spectral lines is Lorentzian for saturation broadening of homogenous line profiles.

4.4 Self absorption broadening

The fluorescence light emitted during a transition can partly be re-absorbed by an atom/molecule present in the sample. Since the absorption coefficient is maximum at the line center than elsewhere therefore, the intensity of the emission line decreases more at the center. This kind of decrement in the fluorescence light broadens the spectral line profile and is known as the self absorption broadening.

4.5 Stark broadening

An atomic/molecular energy level is split into J+1sublevels in the presence of an electric field. These sublevels are additionally shifted; this kind of splitting of an energy level is known as the Stark effect (this effect was first observed by J. Stark in 1913). In ion beams or in gas discharges, an energy level can be influenced by the electric fields exerted by the neighboring ions/electrons and hence the optical transitions between such fine structure have broader linewidths: This kind of broadening of the spectral lines is known as Stark broadening. In case of collinear laser ion beam spectroscopy (CLIBS), a residual Stark broadening may occur in the interaction chamber if the electric field at the entrance or at the exit of the interaction chamber is not uniform.

4.6 Time of flight broadening

If the interaction time (flight time) of an atom with the radiation field is shorter as compared with the life time of the excited state, then the line width of a Doppler free transition is limited by the interaction time of an atom instead of the spontaneous life time of that state. This kind of broadening can become much larger in case of transverse atomic and laser beam spectroscopy (sometimes the interaction time is less than 10^{-9} sec which results in a line broadening of few GHz). It can be reduced by either increasing the laser beam diameter or by reducing the velocity of the atoms.

4.7 Collisional broadening

When working at a high pressure of a gas i.e. at high density of atoms, the collision rate between the gas atoms/molecules becomes higher. Sometimes a collision takes place before the spontaneous emission of the fluorescence light, this means that the collision time is shorter than the life time of the excited state and the atom decays to the lower levels before spontaneous emission. Effectively, the life time of the excited state is now limited by the collision time giving rise to the broadening of the spectral lines. This kind of broadening is known as collisional broadening or pressure broadening. This is a homogenous broadening and has a Lorentzian line profile.

In case of elastic collisions between the atoms and ions, the intensity of the fluorescence light remains constant but a frequency shift occurs and the phase of the damped oscillator is changed. This is known as phase-perturbing collisions. In the case of inelastic collisions the intensity of the fluorescence light is reduced.

If the collisions take place between the same kinds of atoms, the broadening mechanism is called Lorentzian broadening and if different kinds of atoms are involved during a collision, then the broadening is known as Holtsmark broadening. The collisional broadening is prominent in gas discharges (plasma) because of the long range Coulomb interaction between the charged particles. By reducing the pressure of the discharge gas, the collisional broadening can be reduced.

4.8 Combined line profile (Voigt profile)

The total line width is now the sum of all broadenings. The resultant line profile can be presented by a single profile *I*(ν) which is the convolution of all types of line profiles;

$$I(\nu) = I_N(\nu) \cdot I_D(\nu) \cdot I_S(\nu) \cdot I_{TOF}(\nu) \cdot I_P(\nu) \cdots \tag{4.8}$$

where

$I_N(\nu)$ ≡ Natural broadened line profile

$I_D(\nu)$ ≡ Doppler broadened line profile

$I_S(\nu)$ ≡ Saturation broadened line profile

$I_{TOF}(\nu)$ ≡ Time of flight broadened line profile

$I_P(\nu)$ ≡ Pressure/collisional broadened line profile

……..

In equation 4.8, some line profiles are homogenous (Lorentzian) and some are inhomogeneous (Gaussian) profiles. Therefore, the combined line profile is neither

Lorentzian nor Gaussian but is a convolution of these two line profiles and is known as Voigt profile.

Figure 4.2 describes the Voigt profile as a convolution of a sum of the individual Lorentzian profiles with different velocity groups u_z and the Gaussian profile due to thermal motion i.e.

$$I_V(\nu) = I_L(\nu) \cdot I_G(\nu) \tag{4.9}$$

where

$I_V(\nu) \equiv$ Voigt profile

$I_L(\nu) \equiv$ Lorentzian profile

and

$I_G(\nu) \equiv$ Gaussian profile.

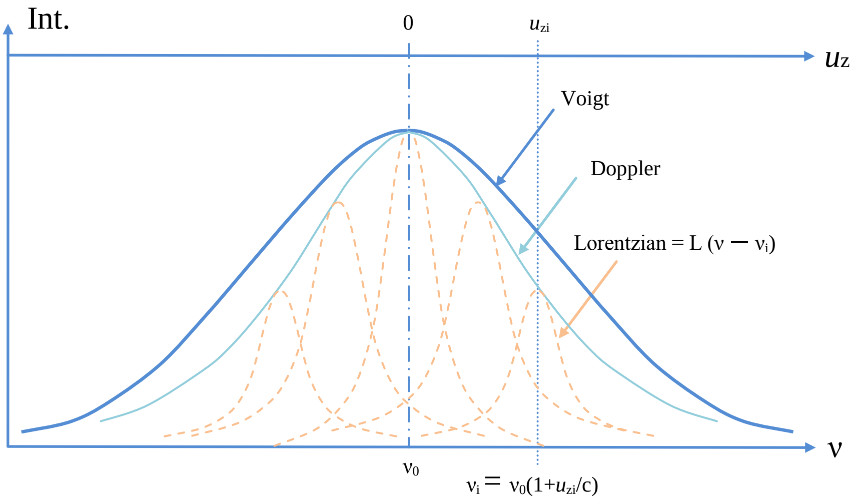

Figure 4.2: Voigt line profile as a convolution of Lorentzian line profiles and Gaussian line profile.

Different broadening mechanisms can be minimized by employing different techniques. The Doppler width can be reduced to 800 MHz (in case of praseodymium spectral lines in a hollow cathode discharge lamp) by cooling the sample gas with liquid nitrogen. Pressure broadening can be reduced by operating the discharge cell at low pressures. Saturation broadening can be avoided by reducing the intensity of the excitation laser light. Amongst all these broadenings, most dominating is the Doppler broadening. There are different techniques to reduce the Doppler broadening and some are discussed in the next chapter.

5 LASER SPECTROSCOPY

In this chapter, different spectroscopic techniques are discussed using lasers as an excitation light source. The invention of lasers has revolutionized the research in all fields of science, especially in the field of atomic and molecular physics. Lasers can act as a light source with very high intensity, coherence and with extremely narrow bandwidth: Therefore are widely used in spectroscopy and have almost replaced conventional light sources and spectral apparatuses. Lasers also provide a better spectral resolution as compared to conventional spectrometers. In table 5.1 a comparison is made between a CW single mode laser and a conventional line light source.

Table 5.1: Comparison between a continuous wave (CW) single mode dye laser and a conventional light source (RF discharge lamp).

	CW single mode dye laser	RF discharge lamp
Linewidth	1 MHz	1000 MHz
Total output of a line	10^{-1} W	10^{-1} W
Power within a useful solid angle	10^{-1} W	10^{-2} W
Power density per unit frequency *	10^{3} W/(cm^{2} MHz)	10^{-6} W/(cm^{2} MHz)
Irradiated area (depends on focusing)	10^{-4} cm^{2}	10 cm^{2}

* using a pulsed laser, a power density of 10^{9} W/(cm^{2}-MHz) or even more can be obtained.

A laser consists of three main components:

1. The active medium: Here population inversion takes place and electromagnetic radiation is amplified through stimulated emission of light.
2. The pump energy: Selected levels are populated to achieve population inversion by supplying the pump energy to the active medium.
3. The optical resonator or laser cavity: Must be able to store light energy in a few number of “Modes” of the electromagnetic field. In this way the induced transitions become more probable than spontaneous transitions and the light field is amplified coherently. Most times this is released by mirrors causing back and forth reflections through the lasing medium inside the cavity.

The pump energy can be provided using: Flash lamps, gas discharges or sometimes other lasers in order to achieve population inversion in the laser medium, which strongly deviates from the Boltzmann distribution.

Different configurations of mirrors are employed for the amplification of light in a laser cavity: For example, plane-parallel, confocal resonators, ring resonators etc. Some special optical elements (e.g. birefringent filters, thick etalon, thin etalon etc.) are inserted inside the laser resonator in order to select a particular laser mode and to suppress other oscillating modes of laser light in the resonator.

Different active laser mediums are being used depending upon the design and requirements, few example are: He-Ne gas (in He-Ne laser), argon gas (Ar^+ laser), chemical dye solutions (dye lasers), ruby crystal, Nd:YAG crystal, semi-conductors etc.

5.1 Ring dye laser

In this work, a CW-ring dye laser is used as an excitation light source. The lasing media are organic molecules e.g. Rhodamine 6G, Ketone red etc. dissolved in a liquid solvent (ethylene glycol). When the pump light is irradiating the dye solution, dye molecules are pumped from the ro-vibronic levels of the ground state S_0 to the higher ro-vibronic levels (excited singlet states S_1) as shown in figure 5.1. Collisions between dye molecules and the solvent molecules induce fast radiation-less decays to the lowest level of S_1 (V_0). This level can be depopulated through an undesired radiation-less decay to the triplet state T_1 or through induced emission into the different levels of the ground state S_0. The transition from S_1 to S_0 determines the laser frequency. Due to collisions between the dye and solvent molecules, these ro-vibronic levels are strongly collision-broadened. Therefore, the emission spectra of the dye molecules are continuous rather than discrete, which provides a wide range of continuous tunable laser frequencies.

The transition from S_1 to T_1 reduces the number of molecules available to achieve population inversion between S_0 and S_1, but also allows the absorption of the radiation by transition from the triplet states T_1 to into the higher triplet states T_2. This effect can be minimized if the molecules with populated triplet state T_1 are removed from the laser resonator in a time scale shorter than the life time of the state T_1. This is done by circulating the dye solution with a high enough pressure to shorten the time of flight of the dye through the active region. A flat stream of the dye solution called “dye jet” is formed with the help of a nozzle. The free jet is inserted inside the laser resonator so that the focused pump laser beam and the path of the ring cavity overlap.

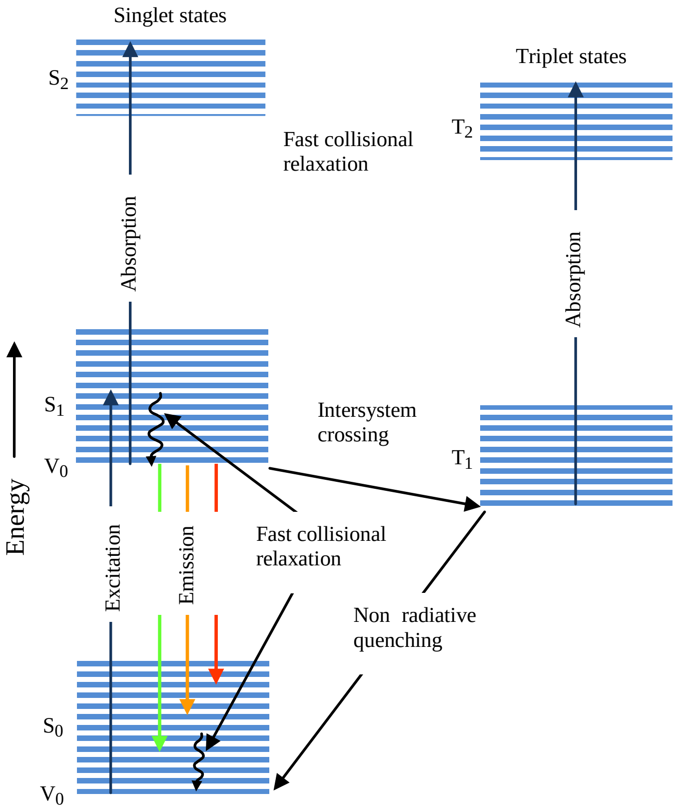

Figure 5.1: Energy level diagram of a common dye molecule.

The mechanical layout of the CW-ring dye laser used at the Institute of Experimental Physics, Technical University of Graz is shown in figure 5.2. The optical layout of the CW-ring dye laser is drawn in figure 5.3. A thin jet of the dye solution is the active medium in a ring dye laser. The dye jet is oriented at Brewster angle to minimize the reflection losses. To achieve the population inversion, an intense pump laser (Ar^+ or Kr^+ laser) is focused by a spherical pump mirror Mp onto the dye jet and excites the dye molecules. A laser resonator of a closed ring is formed with the combination of mirrors M1, M2, M3 and M4. The reflectivity of these mirrors (M1, M2, and M3) and the transmissivity of the output coupler (M4) is selected depending upon the dye being used. The spontaneous fluorescence from the dye jet is emitted symmetrically in all directions in space: When the resonator path is closed, induced emission occurs and two laser beams travel in opposite directions around the ring cavity. In order to increase the output laser power, one of the beams is attenuated and the amplification of the laser light is achieved in one direction. An optical diode, built as a combination of a thin quartz plate and a Faraday rotator, is incorporated to run the laser in one direction inside the laser cavity. An optical diode consists of a Faraday rotator, a rhomb cut at Brewster angle, surrounded by strong prominent magnets which produce a homogenous magnetic field inside the rhomb and change the polarization of the laser beam and a thin quartz plate which turns the polarization of the laser light back to the input polarization.

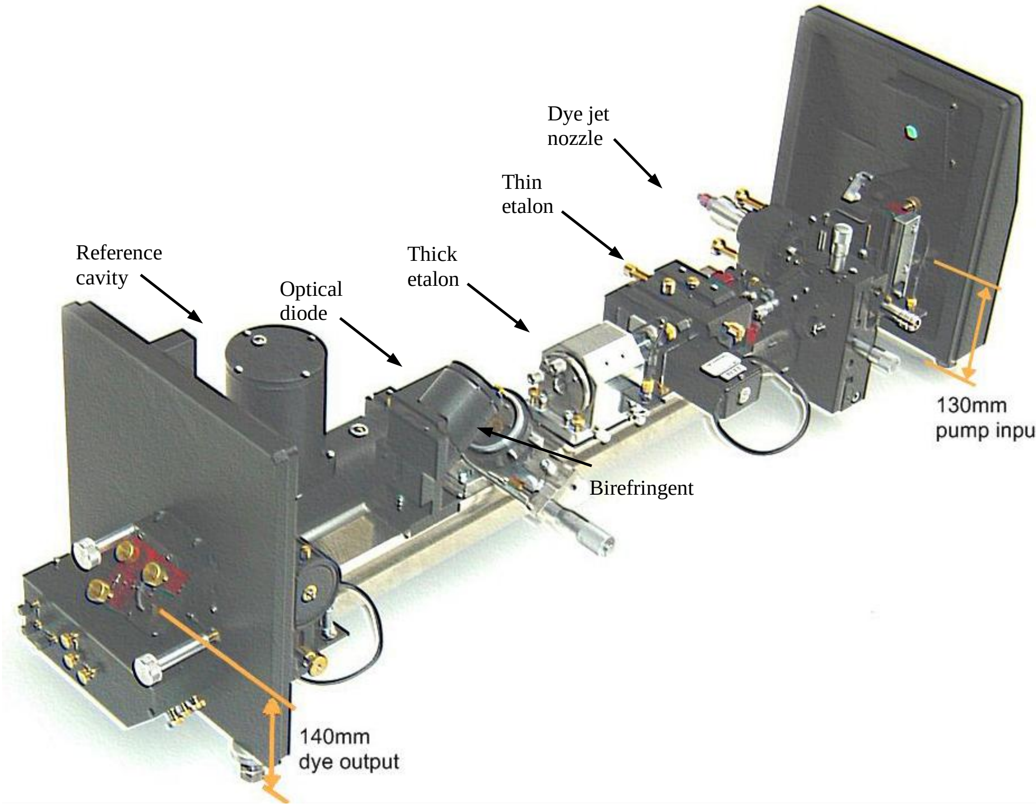

Figure 5.2: Mechanical layout of a CW-ring dye laser system [97].

In order to amplify a single mode of the laser cavity, a number of frequency selective optical components, such as birefringent filter, thick etalon and thin etalon are placed in the path of the laser cavity ring.

The first wavelength selection is made by the birefringent filter. It consists of three plan-parallel birefringent quartz plates, each being 4-times the thickness of the previous one and mounted in a series at Brewster angle. The free spectral range (FSR) of the birefringent is of the order of THz. Due to low finesse of the birefringent filter it is not possible to select one single mode of the laser cavity, therefore two additional optical elements, the thin etalon and the thick etalon, are inserted in the laser cavity. The thin etalon consist of a 0.5 mm plate (reflectivity ≈ 20%, FSR = 200 GHz) is mounted on a galvanometer drive and is inserted at close-normal-to incidence.

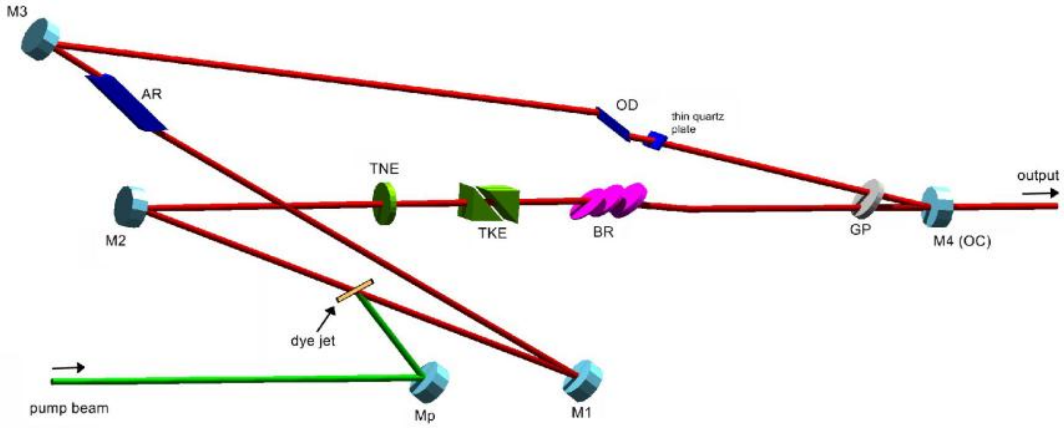

Figure 5.3: Optical layout of a CW-ring dye laser [97]. *MP: Pump mirror, M1, M3: Folding mirrors, M2: Tweeter mirror (PZT mounted), AR: Astigmatism compensation rhomb, TNE: Thin etalon, TKE: Thick etalon, BR: Birefringent, OD: Optical diode (with thin quartz plate), GP: Galvo (Brewster) plate and M4 (OC): Output coupler.*

The thick etalon consist of a 10 mm thick prism-etalon (reflectivity ≈ 20%) with a FSR about 14 GHz and inserted normal to the laser beam axis in the laser cavity. This is mounted on a piezo-electric transducer (PZT).

A temperature stabilized confocal external reference cavity is employed in order to overcome the instability in the laser frequency due to the, vibrations of mirrors, change in the refractive index of the ring cavity due to sound waves, instability in the dye jet etc. A fraction of the output laser beam is obtained using a beam splitter (mounted outside the laser cavity) which is then fed into the reference cavity. The transmitted intensity of the reference cavity is detected by a photodiode (reference photodiode). Another part of the output laser beam is reflected onto a second photodiode (power photodiode). A side-locking technique is employed in order to stabilize the laser frequency. In this technique, the laser frequency is directly locked to one side of the transmission signal of the reference cavity. Therefore the signal from the reference cavity acts as an error signal and is used in a feed-forward servo loop. The signal from the reference cavity is divided by the total power level (using the signal from power photodiode) so that the locking point is independent of laser power. This error signal is then divided into low- and high-frequency parts. The low-frequency part is integrated and is used to drive the laser cavity Galvo plate, while the high-frequency part is amplified and fed to the tweeter PZT (M2). Both these elements (the tweeter PZT and Galvo plate) allow adjusting the length of the laser cavity for the stabilization of the laser frequency. The laser cavity length can be varied by precisely rotating the Galvo plate inside the laser cavity.

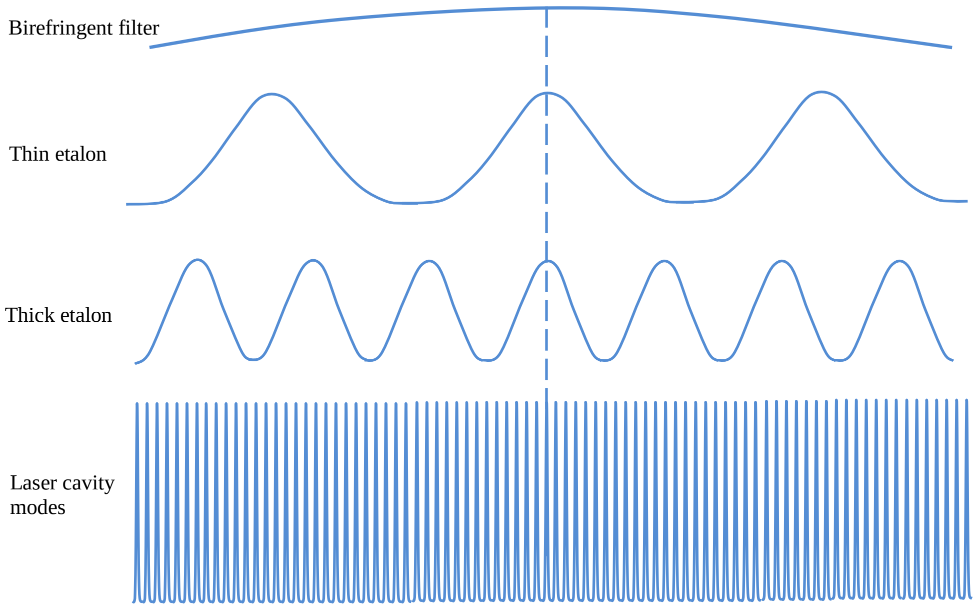

Figure 5.4: Transmission spectra of the mode selective elements inside the CW-ring dye laser cavity (the figure is not to scale).

In figure 5.4, the transmission curves of birefringent, thick and thin etalon are shown. If the transmission curves of all optical elements are tuned to same wavelength, a single mode laser radiation with a line width jitter within 1 MHz can be produced. The length of the reference cavity can be slowly varied by rotating the Galvo plate inside the reference cavity. When laser frequency is locked to the transmission signal of reference cavity, the length of the reference cavity is changed (the transmission maximum changes), the Galvo plate inside the laser cavity follows these changes and adjust the laser cavity: Consequently, the resonance laser frequency is changed accordingly. Using this laser frequency locking scheme, continuous laser frequency scans can be performed over more than 30 GHz.

5.2 Different methods in laser spectroscopy

The study of optical properties of matter by the interaction of electromagnetic radiation is known as spectroscopy. The spectroscopy can be divided into three types:

- Absorption spectroscopy: Electromagnetic radiation of different frequency is absorbed by atoms/molecules.
- Emission spectroscopy: The atoms or molecules are excited to the higher levels by means of e.g. discharge or by radiations etc., the light emitted by the exited atoms/molecules is studied.
- Scattering Spectroscopy: This is also known as Raman spectroscopy: Here the scattering of the electromagnetic radiations by the atoms/molecules is studied.

The availability of single mode tunable lasers provides light sources with extremely narrow line width over a large spectral range. Due to many advantages over conventional light sources, as discussed earlier, lasers are being widely used as an excitation light source in the optical spectroscopy.

The laser spectroscopy can be divided into two main categories: Doppler limited or Doppler broadened laser spectroscopy and Doppler reduced or sub-Doppler laser spectroscopy.

In Doppler limited spectroscopy, the linewidth of the optical transitions is limited by the Doppler broadening which is caused by the thermal movement of the atoms/molecules. Some examples of Doppler limited laser spectroscopy are: Absorption spectroscopy, optogalvanic spectroscopy, laser induced fluorescence spectroscopy, two step excitation spectroscopy etc.

In the sub-Doppler or Doppler reduced spectroscopy, the linewidth of the spectral lines is reduced compared to the Doppler broadened linewidth. Highly stabilized lasers are needed to observe the highly resolved spectra of optical transitions. Few examples of Doppler reduced spectroscopy are saturation spectroscopy, two photon Doppler free absorption spectroscopy, collimated atomic/ionic beam spectroscopy, collinear laser ion beam spectroscopy etc.

5.2.1 Doppler limited laser spectroscopy

In this section few experimental techniques are discussed in which the spectral resolution is limited by the Doppler width of the absorption lines. The main source of Doppler broadening is the thermal motion of the atoms/molecules. Therefore by cooling the sample, Doppler broadening can be reduced significantly. For example, a Doppler width of 800 MHz of spectral lines in a hollow cathode discharge lamp (light source) can be obtained by cooling the discharge lamp with liquid nitrogen. Optogalvanic spectroscopy, two photon absorption spectroscopy, Cavity Ring-down spectroscopy Photoacoustic spectroscopy, Optical Double Resonance spectroscopy, Laser induced Fluorescence spectroscopy etc. are few examples of Doppler limited laser absorption spectroscopy. A couple of examples of Doppler limited spectroscopy are discussed below.

5.2.1.1 Optogalvanic spectroscopy

In 1928, Penning [98] first time observed laser induced changes in the electric properties of a plasma (optogalvanic effect). He observed a change in the electrical properties of a neon gas discharge caused by the light of another adjacent discharge of neon. Similar observations were reported by Kenty [99] in 1950 and then by Meissner and Miller [100] in 1953. In 1976, the first optogalvanic effect using a tunable dye laser was reported by Green et al. [101].

In this kind of laser absorption spectroscopy, a hollow cathode discharge lamp is used as a light source. The plasma produced in the hollow cathode discharge lamp is irradiated by a laser beam. The laser frequency is tuned to resonance with an atomic/ionic optical transition $E_\mathrm{i} \rightarrow E_\mathrm{f}$, which changes the population densities of the lower and the excited levels. Consequently, a change of discharge current ΔI is observed due to the change in population density because different stationary states have different ionization probabilities. This change in discharge current ΔI is detected as a voltage change $\Delta V = R\Delta I$ across the ballast resistor (R). A good signal to noise ratio can be obtained using phase sensitive detection by a lock-in amplifier. The intensity of the laser beam is chopped resulting in periodic changes of the voltage signal across the ballast resistor. The lock-in amplifier is tuned to the laser chopping frequency (reference frequency) and amplifies only the AC signal at the reference frequency.

So the laser absorption is detected by the optically induced current change of the discharge, therefore this technique is named as optogalvanic spectroscopy. The schematic layout of the experimental setup is shown in figure 5.5. There is no need of a monochromator and a photomultiplier tube or a photodiode detector because the discharge itself acts as a detector. Only the knowledge of excitation wavelength is required to study the hyperfine structure of a particular transition. Besides its simplicity, few difficulties are also associated with this method, for example: Minor instabilities of the discharges can produce a large noise in the output signal. Therefore, the discharge must be stable throughout the recordings. The laser induced fluorescence light is not detected in this technique (as no monochromator and PMT are required), therefore no information about the levels involved in the transitions is available.

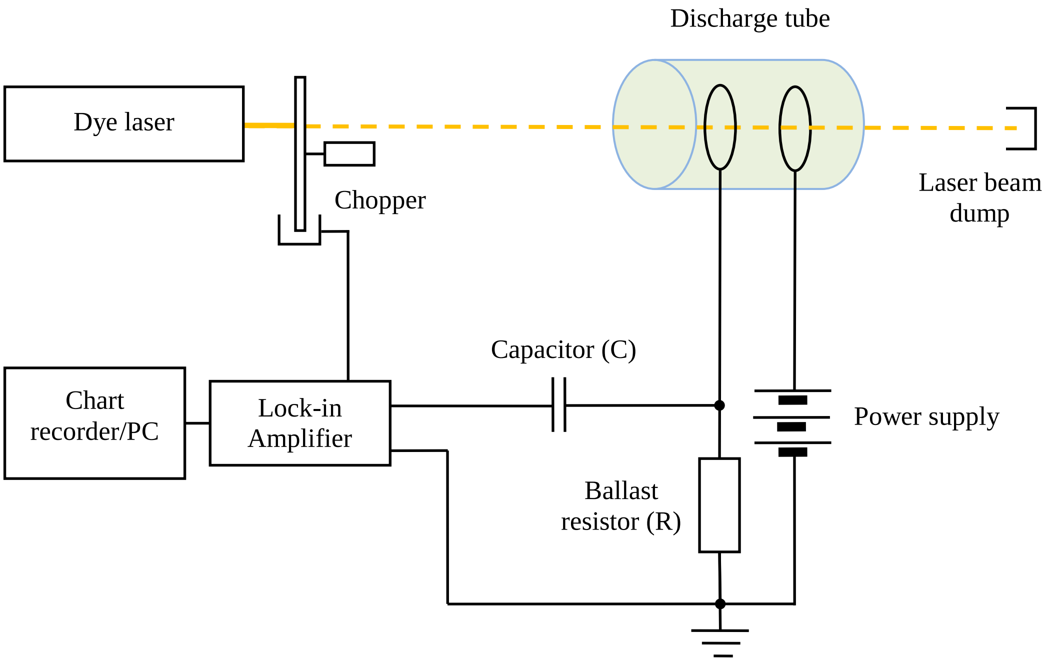

Figure 5.5: Schematic diagram of experimental set up for optogalvanic spectroscopy.

There are several processes which contribute to the ionization of an atom. These include:

1. Direct ionization by electron impact (this process is most probable at low pressure)

$$A + e^- \rightarrow A^+ + 2e^- \ .$$

2. Direct photo-ionization by the electromagnetic radiation

$$A + h\nu \rightarrow A^+ + e^- \ .$$

3. Collisional ionization by metastable atoms: Two atoms in their excited states collide with each other and one of the atom get sufficient energy to be ionized
$$A^* + B^* \rightarrow A^+ + B + e^- \quad .$$
4. Two step or multistep ionization (usually dominant in the higher excited states)
$$A + e^- \rightarrow A^* + e^- \rightarrow A^+ + 2e^- \quad .$$

Using optogalvanic spectroscopy, many processes in flames and gas discharges can be studied [102]. Some more applications of this method are: Investigation of high lying Rydberg states [103], Doppler free saturation spectroscopy [104], laser frequency stabilization [105, 106] etc.

5.2.1.2 Laser induced fluorescence spectroscopy

It is commonly known that an atom in a lower level E_i is excited to the upper level E_f when it absorbs electromagnetic radiation with a frequency (E_f - E_i)/h. This gives rise to an increase of the population of the upper level. The atoms in the upper level are de-excited to the lower levels through different processes. One of them is the spontaneous emission of light of different wavelengths known as fluorescence light. The information gained from fluorescence lines and the excitation wave length is used to study different characteristics of the levels E_i and E_f, for example their energy, parity, angular momentum (J value), hyperfine splitting etc.

In laser induced fluorescence (LIF) spectroscopy the laser light is shined on the atoms/ions (e.g. plasma in a hollow cathode gas discharge lamp). The atoms in the lower state are excited to the upper level if the transition and laser frequency are in resonance. Then the upper level is de-excited to the lower levels by emitting fluorescence light. The different fluorescence wavelengths are resolved using a monochromator and are detected by a photomultiplier tube at the exit of the monochromator. A schematic diagram of the experimental setup used for the LIF spectroscopy at the Institute of Experimental Physics, Technical University Graz is shown in figure 5.6.

In order to get rid of the constant back ground of the fluorescence light from the hollow cathode discharge lamp, a phase sensitive detection of fluorescence light is employed using a phase sensitive lock-in amplifier. The laser intensity is modulated by a mechanical chopper, this modulates the population of the involved levels. Consequently, the fluorescence signal is also modulated with the chopping frequency. When the laser light frequency is in resonance with the transition frequency between two atomic/ionic levels, the lock-in amplifier is tuned to the same chopping frequency and the phase for the detection of fluorescence signal from photomultiplier tube is also matched. In this way, only those fluorescence signals which are in-phase with the modulation frequency are detected.

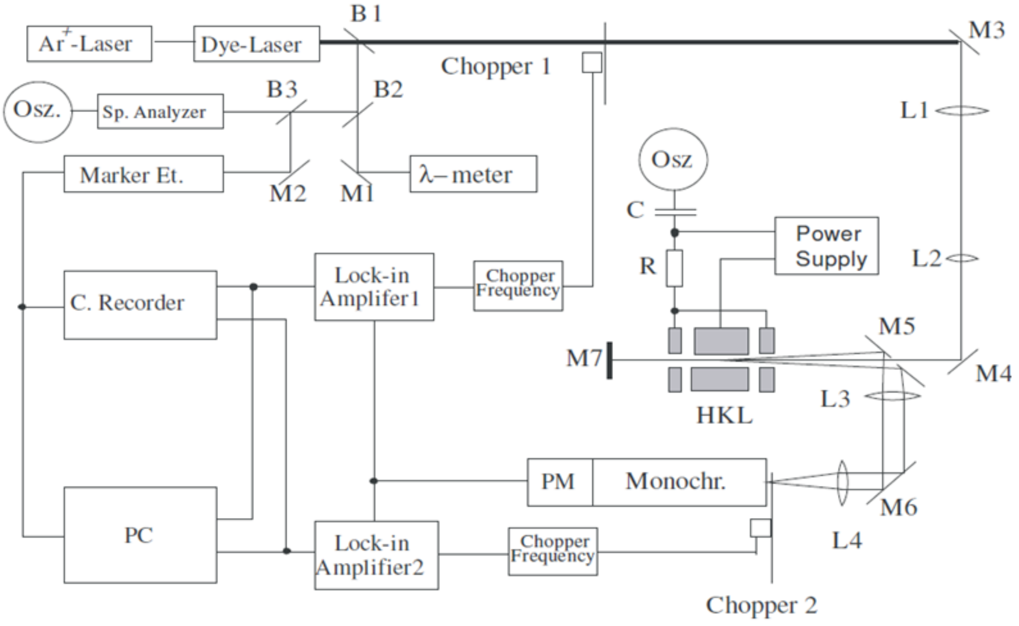

Figure 10.6: Schematic diagram of experimental setup of laser induced fluorescence spectroscopy at the Institute of Experimental Physics Technical University Graz [107].

The observed fluorescence lines can be divided into three types:

i. **Positive fluorescence:**

A fluorescence line which is observed as decay from the upper level of the excited line is called direct fluorescence. As described before, the signal is detected when the LIF light is in phase with the laser intensity. In figure 5.7, a level diagram of LIF is drawn. The excitation is taking place from the lower level E_2 to the upper level E_3 at the resonance wavelength λ_{23}. The upper level E_3 decays to the lower levels E_4 and E_5 by emitting fluorescence light of wavelengths λ_{34} and λ_{35}. If the laser intensity is modulated by a mechanical chopper wheel and the phase sensitive detection is used using a lock-in amplifier, the LIF maximum signal is observed when the LIF signal and the modulation frequency are in phase. As the LIF signal increases when the laser in on, this is called a positive phase or a positive fluorescence.

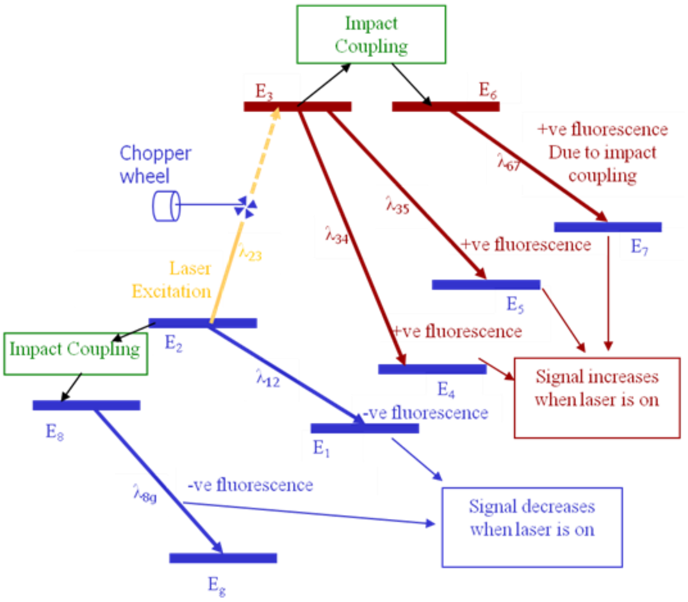

Figure 5.7: The levels scheme of LIF showing the positive and negative fluorescence and impact coupling [107].

ii. Negative fluorescence:

If the lower level involved in a transition is lying higher than other lower levels, it can decay to these lower levels by emitting the fluorescence light. When the laser frequency is in resonance from E_2 to E_3, some of the atoms decay from E_2 to E_1 by emitting λ_{12}. The population of E_2 is decreased when the laser is on and this fluorescence is observed at 180˚ phase shift as compared to the positive fluorescence, therefore this type of fluorescence signal is called negative fluorescence.

iii. Impact or collisional coupling:

Sometimes, two or more energy levels lie close to the levels populated or depopulated by the laser light. Due to thermal collisions, the atoms transfer their energy to the closely lying energy levels during collisions. This is known as impact or collisional coupling. These atoms then decay to the lower level by emitting fluorescence light which carries the signatures of the excited transition. In figure 5.7, the excited energy level E_3 is lying close to the energy level E_6 and the excitation energy of E_3 is transferred to E_6. The energy level

E_6 decays to E_7 and emits λ_{67}. Population transfer is also possible between lower levels e.g. E_2 and E_8.

In all three cases discussed above, the observed hyperfine structure is the hyperfine structure of the excited transition between E_2 and E_3.

Advantages of LIF:

There are numerous applications of the LIF technique:

- One main advantage of LIF technique is the analysis of blend lines. In a blend situation more than one transitions lying very close to each other are observed in a small range of the laser frequency (few examples are discussed in the section 10.4). Using LIF spectroscopy, the individual fluorescence channels corresponding to different upper levels are separated, which helps in the identifications of the levels involved in the blend situation.
- In LIF technique, the signal to noise ratio is usually high, which increases the sensitivity of this method.
- More than one species can be distinguished using the LIF method.

One disadvantage of LIF is: If an upper level involved in a transition has very few numbers of fluorescence lines which lie within the range of the dye laser frequency. Then the fluorescence light is suppressed under the high background from the laser light and cannot be detected. In such cases, the optogalvanic spectroscopy can deliver better results.

5.2.2 Doppler reduced laser spectroscopy

In order to get better understanding of the optical spectra of atomic/ionic transitions, the spectral lines must be completely resolved. Since the development of single mode lasers with extremely narrow line width, several experimental arrangements are developed for Doppler reduced measurements. Some examples of Doppler reduced laser spectroscopy are: Saturation spectroscopy, two photon spectroscopy, collimated atomic beam spectroscopy, collinear laser ion beam spectroscopy etc. Few experimental techniques of Doppler reduced spectroscopy are discussed here, whereas the principle, experimental setup and some results of collinear laser ion beam spectroscopy (CLIBS) are discussed in detail in chapters 8-10.

5.2.2.1 Saturation spectroscopy

Saturation spectroscopy or Lamb dip spectroscopy [108] is based on the velocity-selective saturation of Doppler broadened atomic/molecular transitions. In this method the line width of the spectral lines is narrowed to the linewidth of Lamb dips.

When an intense monochromatic laser beam with frequency corresponding to a transition between two levels is passing through a gaseous medium (sample) of atoms/molecules with a Maxwell velocity distribution, it saturates a particular velocity group, let say u_z. Due to saturation the population density $N_1(u_z)\mathrm{d}u_z$ of the lower level is decreased within the velocity interval $\mathrm{d}u_z$ and correspondingly the population density of the upper level $N_2(u_z)\mathrm{d}u_z$ is increased (figure 5.8). The velocity selective minimum in the Maxwell velocity distribution $\Delta N(u_z)$ at u_z is called Bennet hole [109]. When another laser beam of same intensity and frequency is passing through the sample from opposite direction, another Bennet hole is burnt at the velocity component $-u_z$ into the population distribution $\Delta N(u_z)$ (figure 5.8b).

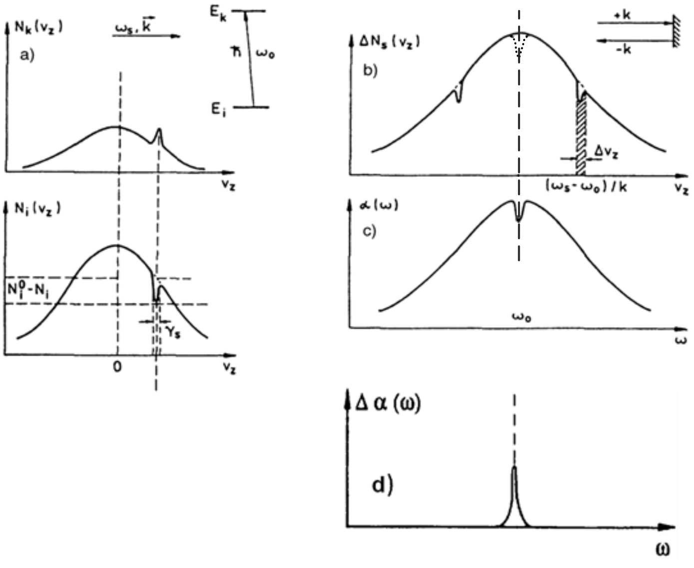

Figure 5.8: Saturation of an inhomogeneous line profile: a) Bennet hole and dip produced by a single laser beam with $\omega \neq \omega_0$. b) Bennet holes caused by the two counter propagating laser beams for $\omega \neq \omega_0$ and for $\omega = \omega_0$ (dotted curve). c) Lamb dip in the absorption profile $\alpha(\omega)$. d) the signal from Lamb dip when fluorescence signal is recorded at sum of the laser beams modulation frequencies f_1+f_2 (chapter 7). In this figure v *stands for velocity [this figure is taken from "Laser spectroscopy"by W. Demtöder].*

Usually, a laser beam is divided into two equal intensity beams which are shinned on the sample from opposite directions. When the laser frequency is tuned to the centre frequency ω_0, a dip (Lamb dip) is observed at the line center in the Doppler broadened absorption profile (figure 5.8c). At the line center, both laser beams interact with same velocity group $u_z = 0$ (which essentially moves perpendicular to the laser beams). For this group of atoms, the intensity per atom is twice as compared with the other velocity groups, therefore the saturation is higher.

A possible arrangement for saturation spectroscopy is shown in figure 5.9. The output beam from a dye laser is split by a beam splitter into a strong pump beam and a weak probe beam with $I_{\text{probe}} << I_{\text{pump}}$. The pump and probe beam pass through the absorbing sample in opposite directions. When the laser frequency is tuned across the transition, a Doppler broadened absorption profile with Lamb dip at the centre is observed in the transmission of the probe laser beam (figure 5.9). The Doppler broadened background can be eliminated if the pump laser beam is chopped and the transmitted probe intensity is recorded using a lock-in amplifier which is tuned to the chopping frequency.

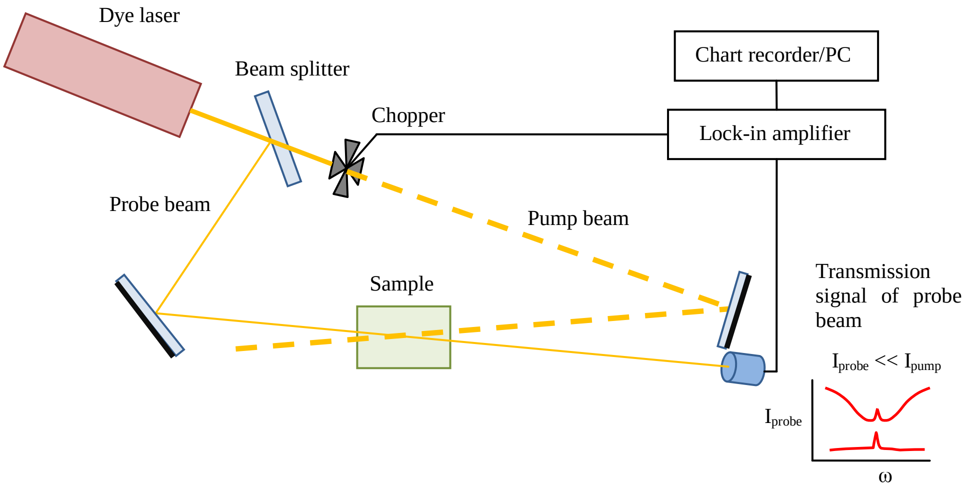

Figure 5.9: Experimental setup for saturation spectroscopy.

Another method to get rid of the Doppler broadened background is: The dye laser beams is split into two equal intensity beams which are passing through the absorbing sample in opposite directions. Both laser beams are chopped at different frequencies f_1 and f_2 and the fluorescence signal is monitored through a lock-in amplifier tuned to the sum frequency $f_1 + f_2$. The Doppler broadened background is suppressed and the signal from Lamp dip is detected (figure 5.8d). This method is known as Inter-modulated Laser Induced Fluorescence technique and is particularly advantageous when the density of the atoms is low, consequently the absorption is small. During this research work, some hyperfine structures are investigated by employing this technique. The experimental setup and results obtained using this technique are discussed in chapter 7.

5.2.2.2 Polarization spectroscopy

This is another type of saturation spectroscopy. A monochromatic laser beam is split into a strong pump beam and a weak probe beam. The pump beam is passing through a λ/4 quartz plate, which produces a circular polarization, and then through the sample. From the opposite direction, after passing through a linearly polarizer P_1, the weak probe beam is passing through the sample cell. Before falling on a detector, the probe beam passes through a second polarizer P_2 which is crossed with P_1.

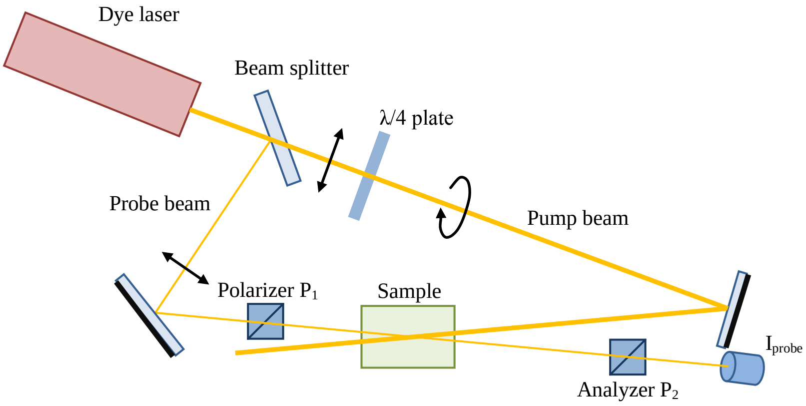

Figure 5.10: Experimental setup for polarization spectroscopy.

When the laser frequency is tuned to an atomic/molecular transition, only the transitions $M'' \rightarrow M'$ are induced by the circularly polarized pump beam (σ^+) for which $\Delta M = +1$ i.e. $M'' \rightarrow M' = M'' + 1$ (M is the quantum number that describes the projection of J onto the direction of propagation of light). Because of saturation, the degenerate M'' sublevels are partially or completely depleted. This implies that using one kind of circularly polarized pump laser beam, an unequal saturation and with it a nonuniform population of the M sublevels is produced. Consequently an anisotropic distribution for the orientations of the angular momentum J vector is produced. Such an anisotropic sample becomes birefringent for the incident linearly polarized probe laser beam and its plane of polarization is slightly rotated when passed through the sample.

Every time the laser frequency is tuned across the center of an atomic/molecular absorption line, the plane of polarization of the probe beam is slightly rotated by some angle, the probe beam pass through the second polarizer and the detector receives a Doppler reduced signal.

5.2.2.3 Doppler reduced two photon laser spectroscopy

In saturation spectroscopy, the Doppler width is reduced by proper selection of a velocity group with the zero velocity component in the direction of propagation of laser beams. In Doppler reduced two photon spectroscopy, no velocity selection is required because all atoms/molecules, regardless of their velocities contribute to the laser induced fluorescence signal.

For an atom, moving with velocity u in the laboratory frame of reference, in the frame of reference of the moving atom the laser frequency ω is Doppler shifted to

$$\omega' = \omega_0 - \vec{k} \cdot \vec{u} \ .$$

The resonance condition for the simultaneous absorption of two photons is

$$(E_f - E_i)/\hbar = (\omega'_1 + \omega'_2) = \omega_1 + \omega_2 - \vec{u} \cdot (\vec{k}_1 + \vec{k}_2) \ . \qquad (5.1)$$

From above equation it is clear that if the two photons of same frequency are absorbed moving in opposite direction i.e. $\vec{k}_1 = -\vec{k}_2$ then the Doppler shift of the two photon absorption is completely cancelled out. Therefore, all atoms irrespective of their velocities absorb the same laser frequency $\omega_1 + \omega_2 = 2\omega$.

The same experimental setup can be used as shown in figure 5.9. The difference is only that both laser beams are split into equal intensities and are chopped with the same frequency. Of course, one cannot investigate the same transition as in saturation spectroscopy due to the requirement of fulfilling certain transition rules. In figure 5.11, a Doppler reduced two photon transition is shown. Two photon transition for E_i to E_f can take place through an intermediate virtual level. The probability of absorption of two photons from opposite laser beams is twice as large as the probability of absorption of two photons from one laser beam. The probability of a two photon transition is much lower than that of a single photon transition and an intense radiation field is required for a two photon transition. A narrow peak at the resonance frequency of a transition ($2\omega_0$) is observed (resulting from the absorption of two photons from opposite laser beams) with a broad Doppler background (resulting from the absorption of two photons from one laser beam) as shown in figure 5.11.

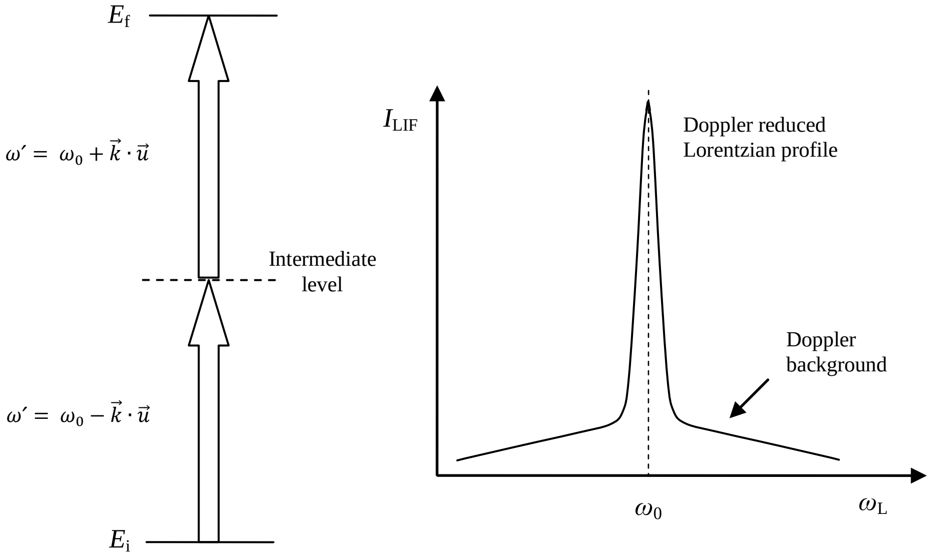

Figure 5.11: Schematic line profile of two photon LIF signal.

With the help of two photon Doppler reduced spectroscopy, parity forbidden transitions can be studied. High lying electronic energy levels in far UV range can be investigated using incident laser frequency being in the visible region.

5.2.2.4 Collimated atomic beam laser spectroscopy

In this method, the Doppler width of the spectral lines is reduced using a collimated atomic/molecular beam with reduced transversal velocity spread. A single mode laser beam is irradiating on a well collimated atomic beam at right angle as shown in figure 5.12.

The reduced Doppler width $(\Delta\nu_D)_{res}$ is given by

$$(\Delta\nu_D)_{res} = \frac{\Delta\nu_D}{C\sqrt{2}} \ . \qquad (5.2)$$

Where $\Delta\nu_D$ is the normal Doppler broadening inside the oven and C is the collimation ratio.

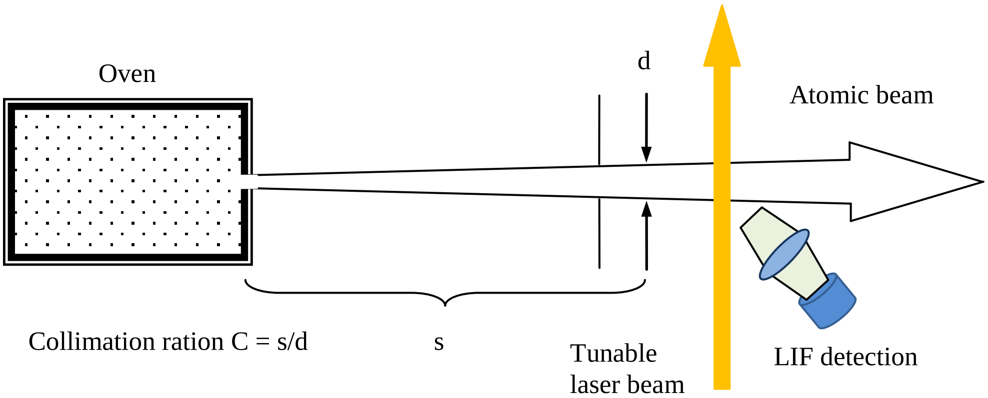

Figure 5.12: Schematic diagram of LIF spectroscopy with a collimated atomic beam.

An atomic beam can be produced for nearly every element. Collisional effects are significantly reduced as compared with discharge cells. The Doppler width is reduced by the collimation ratio.

There are few drawbacks of this technique: The interaction region between laser beam and the atomic beam is very small, a very low fluorescence light intensity is produced which radiates in 4π steradians. Therefore, the atomic/molecular lines with weak transition probabilities cannot be investigated. Using this method only the ground state or low-lying metastable states are populated therefore, very limited number of upper levels can be excited.

6 ENERGY CORRECTION OF PR II FINE STRUCTURE LEVELS

Praseodymium has a large level density which makes the optical spectrum of Pr I and Pr II very complicated. With the help of a highly resolved FT spectrum it is possible to determine accurately the centers of gravity of the optical transitions appearing in the FT spectrum. In this work, using an FT spectrum and a computer program, the centers of gravity of numerous optical transitions are improved. Moreover, energies of 227 fine structure electronic levels of Pr II are re-determined.

6.1 FT spectrum

A Michelson interferometer can also be used as a Fourier transform spectrometer. Light from the source is divided into two beams by a beam splitter (different beam splitters for different wavelengths are used). One beam is reflected by a flat mirror which is fixed in position and the other beam is reflected by a second movable flat mirror introducing a time delay between the two beams. The two beams recombine at the beam splitter. Since the path travelled by the two beams is different the interference of two beams occurs. This interference pattern is recorded as a function of the path difference between the two beams – the interferogram, which is converted into a plot of intensity in inverse space (wave number) or inverse time (frequency) domain (spectrum) by using a mathematical function Fourier transform. The spectrum is known as the FT spectrum.

Advantages of the FT spectroscopy:

- It provides a high resolution of the spectrum as the path difference of the two beams is μm to 1m and thus the apparatus width is 0.01cm^{-1}.
- Within a single scan a large spectral range with a low scan time can be covered e.g. up to 300 Å.
- The FT spectra are available in electronic form and can be easily used for further analysis.

The FT spectrum used in this work was recorded by Gamper et al. [5] at the Institute of Quantum Optics at the Leibniz University in Hannover. This spectrum was recorded under the Doppler-limited conditions using a continuous scanning high resolution FT-IR spectrometer (IFS 120 HR, Brucker Corp.) A hollow cathode discharge lamp was used as light source and operated at a current of about 65 mA (dc). Argon was used at a pressure of about 0.6 mbar as a working gas of the discharge. The Ar ions of the discharge hit the Pr-cathode, causing sputtering of Pr atoms. Subsequently, a Pr-Ar plasma is produced which emits Ar I, Ar II, Pr I and Pr II spectral lines (for details see [110]). The emitted light was focused on the entrance aperture of the FT spectrometer and the FT spectrum was recorded over the large range from 2380 to 12500 Å [5]. Different beam splitters were used for different regions. CaF_2 coated with silicon for near-infrared region (12500 Å to 10000 Å), quartz with dielectric coating for the region from 10000 Å to 4000 Å and quartz with aluminum coating from 4000 Å to UV, were employed. For the detection of light, a silicon photo-diode was used for infra-red region and a photomultiplier tube (Hamamatsu R955 or R928) was used for the visible and UV regions. The diameter of the entrance aperture was varied from 0.5 to 1.3 mm. The signal to noise ratio (SNR) was improved by using different filters (optical dielectric low pass and high pass filters) and also by averaging multiple scans. The FT spectrum was wave number calibrated with argon spectral lines. Its resolution in different regions is: 0.001 Å or 0.025 cm^{-1} at 50000 cm^{-1}, 0.002 Å or 0.0125 cm^{-1} at 25000 cm^{-1} and 0.005 Å or 0.005 cm^{-1} at 10000 cm^{-1}. The observed line width, limited by the Doppler width and the apparatus profile, was between 1100 MHz and 1800 MHz. The spectra, recorded in different regions, were combined then to form one spectrum. Finally, the spectrum was converted to intensity versus wavelength in air. For the refractive index of air the following formula (Peck and Reeder dispersion relation [111]) was used, where n is the refractive index of air and σ is the wave number in vacuum.

$$(n-1)\times 10^{8} = 8060.51 + \frac{2480990}{132.274-(\sigma/\mu m^{-1})^{2}} + \frac{17455.7}{39.32957-(\sigma/\mu m^{-1})^{2}} \tag{6.1}$$

The wavelength in air is then calculated by $\lambda_{air} = {}^{2\pi}/_{n\sigma}$. (6.2)

A small part of the high resolution FT spectrum is shown in figure 6.1 illustrating well resolved many hyperfine structures within a range of 2 Å. Many spectral lines can be classified without laser excitation [41, 42] if a hyperfine structure is clear and well resolved in the FT spectrum. The high resolution of the FT spectrum permits to set the excitation wavelength more precisely when performing laser induced fluorescence spectroscopy.

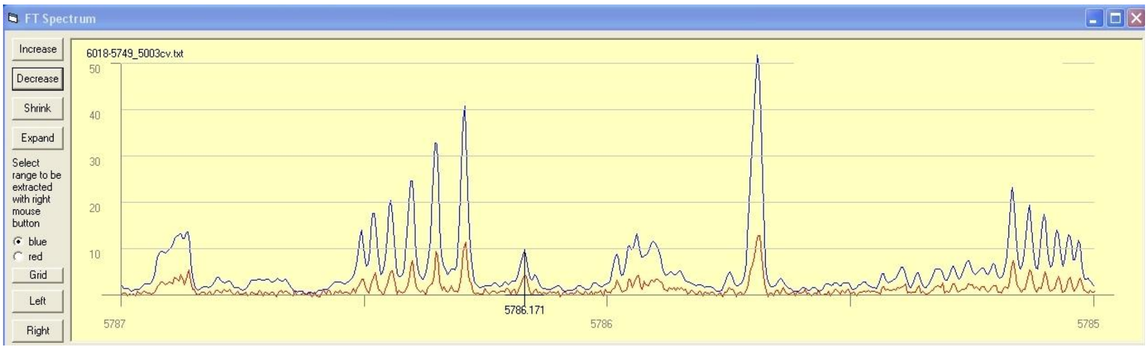

Figure 6.1. Part of FT spectrum of praseodymium.

6.2 Classification program

In order to investigate the hyperfine structures of spectral lines of praseodymium, a computer program called “Classification program” is used. This program was developed by Prof. L. Windholz [112] in 2003. The program can be used for any element e.g. tantalum, praseodymium, lanthanum, neodymium etc. For any specific element e.g. praseodymium (Pr), the program uses three data files:

I. The wavelength table: wpr.dat. This file contains information about all known classified or unclassified spectral lines whether ionic or atomic transitions and also lines of the discharge gas (here Ar I and Ar II). The data about a spectral line is entered following a specific format, one example of the entry is given below

*4044.092, 6, , , , 35978.302, 5, o, 817.6, -, *Gi89 ,11257.857, 4, e, 1015, -, *Gi89, (pr II) #Nd11.*

The first entry is the center of gravity wavelength in air of the spectral line, next is the intensity of the line appeared in FT spectrum, in next three entries the intensities from different sources can be entered. For a classified line the next entry is the energy (in cm^{-1}), angular momentum, parity, *A* and *B* values (in MHz) of the upper level. Then the entries are energy, angular momentum, parity *A* value, *B* values and comments about the lower level involved in the transition. Finally comments concerning the spectral line can be added. If any of the levels is investigated using laser excitation, the recorded files, the excitation wavelength, observed fluorescence wavelengths can also be entered to store information on the classified line.

II. The file Level_pr.dat contains all known atomic levels of praseodymium. The format of the entries is

*6.5, o, 26586.578, 950.5, 60, *LW061230 a5772.80, f4930 f5274 f5365 a5838.80 a5845.23.*

The order of the entries is: *J* values, parity, energy of the level, *A* value, *B* value and finally the comments about the level.

III. The data regarding ionic levels is stored in a file lev_prii.dat. The format of the entries is same as that of Level_pr.dat, an example is given below
5, e, 26146.060, 622.2(1), 7(7), *Gi89 Nd110529 CLIBS pr060610 a5874.74 pr077801 a 5662.19 pr077501 a5654.23 energie korr. Nd11(3889.343).

When the program is executed for a specific element, the main window of the program is displayed with a menu bar at the top as shown in figure 6.2. The main window comprises of three sections (left, middle and right). The icons/buttons of various commands are also provided e.g. “Go to Lambda”, “Select for Entry”, “Insert Line” etc., which allow easy to operate the program. When a wavelength is entered by selecting “Go To Lambda” button, program goes to the nearest entry next to the given value. When a line is selected using “Insert Line” a new line is introduced at the selected value. For any wavelength introduced to the program, it searches for all possible transitions (within a certain range i.e. ±0.5 cm^{-1}), so that the difference of levels energies matches with the wave number of the selected wavelength. Then in the right section of the main window all these possible transitions (also called suggestions) along with their expected hyperfine structures are displayed (hyperfine patterns only, if the hyperfine constants of upper and lower levels are known). The wave number differences of these lines from the selected line are also displayed on top left of each suggestion. In the middle section, the hyperfine structure of a selected suggestion is displayed. In the upper part of this section, energies, *J* values and hyperfine constants of the levels involved in the transitions are displayed. In the left section, the wavelength is displayed for the current line. If a line is already classified in the vicinity of the selected wavelength, the details about the levels involved in the transition (energy, angular momentum, *A* and *B* values and name of the person who discovered/classified the line) are displayed. In this section, the wavelengths of previous and next lines are also provided. The hyperfine structure of the classified line is displayed in the lower part of this section. Just for an example, the wavelength 4096.8 Å is selected by pressing “Go to Lambda”. The line next to “4096.8” is 4096.814 so the program jumps to this line. The program displays 3 suggestions in the right section within the wavenumber differences between ±0.5cm^{-1}. In the left section an ionic line classified by Ginibre [42] is displayed which is suggestion 3 displayed in the middle section.

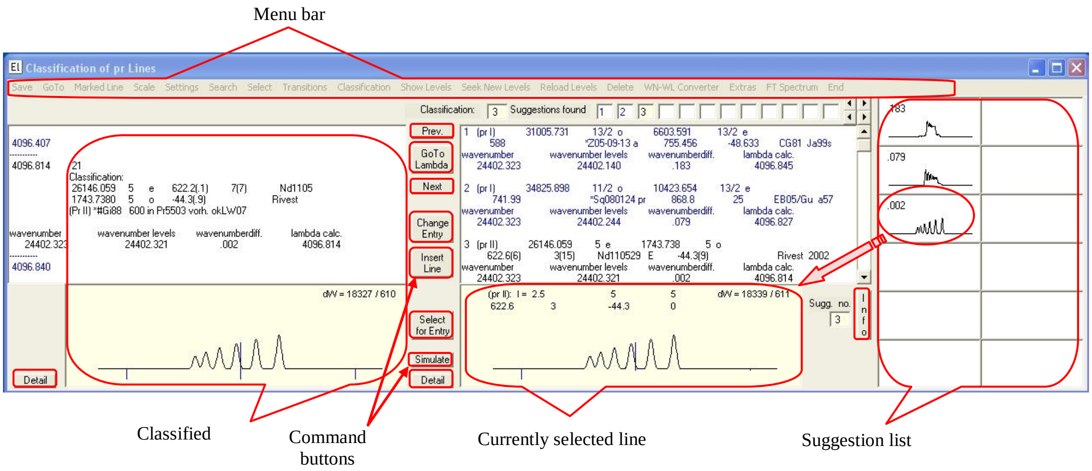

```
4096.407
----------
4096.814      21
              Classification:
               26146.059   5   e    622.2(.1)    7(7)       Nd1105
               1743.7380   5   o    -44.3(.9)              Rivest
              (Pr II) *#Gi88  600 in Pr5503 vorh. okLW07

wavenumber        wavenumber levels    wavenumberdiff.    lambda calc.
  24402.323          24402.321              .002            4096.814
----------
4096.840

                                                       dW = 18327 / 610
```

```
Classification:  3  Suggestions found  1  2  3

1  (pr I)     31005.731     13/2  o      6603.591     13/2  e
      588                 *Z05-09-13 a    755.456      -48.633     CG81  Ja99s
wavenumber        wavenumber levels    wavenumberdiff.     lambda calc.
  24402.323            24402.140             .183            4096.845

2  (pr I)     34825.898     11/2  o      10423.654    13/2  e
     741.99               *Sq080124 pr    868.8        25          EB05/Gu  a57
wavenumber        wavenumber levels    wavenumberdiff.     lambda calc.
  24402.323            24402.244             .079            4096.827

3  (pr II)     26146.059     5  e       1743.738       5  o
     622.6(6)       3(15)      Nd110529  E      -44.3(9)              Rivest  2002
wavenumber        wavenumber levels    wavenumberdiff.     lambda calc.
  24402.323            24402.321             .002            4096.814

(pr II):  I =  2.5              5            5           dW = 18339 / 611
 622.6          3             -44.3          0
```

```
.183
.079
.002
```

Figure 6.2. Left, middle and right sections in the main window of Classifcation program, illustrating the classified Pr II line 4096.814 Å.

Some important features of command buttons:

- A classified line can be selected, by entering its estimated cg wavelength using “***Go to Lambda***”.
- A new line in the wave length table can be added using “***Insert Line***”.

- “***Next***” and “***Prev.***” buttons can be used to navigate through different spectral lines in the wave length table.
- To classify a line, “***Select for Entry***” is used to select a particular transition from the suggestion list.
- The detailed information about the hyperfine structure of the selected/classified line can be displayed using “***Details***” button.
- The information about the selected line can be modified using “***Change Entry***”
- Information about a particular suggestion is provided by the “***Info***” button.
- The “***Simulate***” button recalls the program “***Simulation***” which can be used to compare the hyperfine structure of a particular suggestion with the hyperfine structure appearing in the FT spectrum. This program automatically takes the *J* values and hyperfine constants of the levels involved in the selected suggestion. A portion of the FT spectrum is copied and can be compared with the suggestion. The two hyperfine patterns (one from the suggestion list and second from the FT spectrum) can be shifted against each other and the correct center of gravity wavelength of the transition can be found as shown in figure 6.3. The *A* and *B* values of a selected line can also be determined (if needed) by matching the two hyperfine spectra.

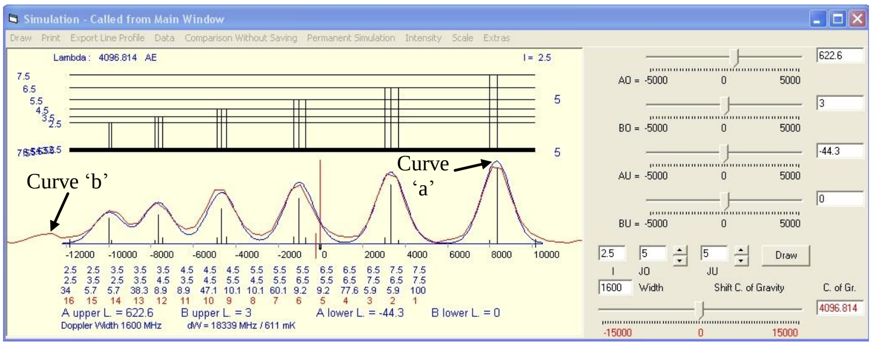

```
Lambda :  4096.814  AE                                              I = 2.5

2.5  2.5  3.5  3.5  3.5  4.5  4.5  4.5   5.5   5.5   5.5  6.5  6.5   6.5  7.5  7.5
2.5  3.5  2.5  3.5  4.5  3.5  4.5  5.5   4.5   5.5   6.5  5.5  6.5   7.5  6.5  7.5
34   5.7  5.7  38.3 8.9  8.9  47.1 10.1  10.1  60.1  9.2  9.2  77.6  5.9  5.9  100
16   15   14   13   12   11   10   9     8     7     6    5    4     3    2    1
A upper L. = 622.6     B upper L. = 3          A lower L. = -44.3      B lower L. = 0
Doppler Width 1600 MHz     dW = 18339 MHz / 611 mK
```

AO = 622.6
BO = 3
AU = -44.3
BU = 0
I 2.5
JO 5
JU 5
Width 1600
C. of Gr. 4096.814

Figure 6.3. Simulation of the line 4096.814 Å. The curve ‘a’ is the hyperfine pattern from the suggestion list and the curve ‘b’ is the hyperfine pattern from the FT spectrum.

In this program, many parameters are provided like *J* values, *A* and *B* values of the upper and lower levels, nuclear spin and the Doppler width. Therefore, for an unknown/unclassified line, this program can be used to estimate the *J* values, *A* and *B* constants of the levels involved in the transition.

Some important features of the Menu bar:

- Any changes made during the use of classification program can be saved in the wavelength table using the "***Save***" option.
- Different wavelengths can be selected using the "***GoTo***" option.
- Two wave lengths can be memorized using the option "***Marked Line***".
- The "***Scale***" option can be employed to view a hyperfine pattern in different frequency scales.
- The "***Settings***" option can be used to change different parameters of the Classification program for example, wave length difference limit, wave number difference limit, Doppler width, nuclear spin quantum number etc.
- The transitions between atomic levels, ionic levels or both can be selected using the "***Search***" option. The transitions with $\Delta J = 0, \pm 1$ or for arbitrary ΔJ (if J values of a level is not known) can also be selected.
- The "***Select***" option offers the user to either select all lines in the wavelength list or to select lines based on specific comments, energy level or intensity of lines.
- The transition list from the upper, from the lower level, to the upper level or to the levels of a selected line can be viewed using the "***Transitions***" option.
- The classification routine can be activated or suppressed using "***Classification***" option.
- The option "***Show Levels***" in the menu bar can be used to view the all ionic or atomic levels (along with their J, A and B values) stored in the data files.
- New levels can be search using "***Seek New Levels***" based on, current line, special levels, and fluorescence lines and on A and J values.
- The updated data files: Level_pr.dat and Lev_prii.dat are reloaded using "***Reload Levels***" command.
- Any wrong line entry or classification can be deleted using "***Delete***" option.
- The "***WN-WN Converter***" recalls a program that converts the wavelength in air to wavelength in vacuum and in wave number or vice-versa using the equation 6.1. The difference between two wave numbers in terms of wavelengths can also be calculated.
- To show or hide the window of FT spectrum (figure 6.1), the option "***FT Spectrum***" is used.

6.3 Fitter program

To analyze the experimentally recorded hyperfine structures or a profile from the FT spectrum, a fitter program is used. The fitter program was developed by T. Quiering [113] in 1984. This program fits the recorded profile to a function using the method of least squares and calculates the *A* and *B* constants and the center of gravity wavelength of the hyperfine structure. To start with the fitter, a recorded hyperfine structure must be converted to intensity versus linear frequency scale, this process is called linearization. The hyperfine structure is recorded as a function of equal time intervals (not in frequency scale). A linearization process is employed which converts the intensity distribution $I(\mathrm{t})$ into the intensity distribution $I(\nu)$ (intensity as a function of frequency ν) using the equal frequency marker etalon signal which is simultaneously recorded with the LIF signals. The process of linearization is performed by supplying start wavelength of laser scan and FSR of the marker etalon along with the measured data file to the fitting program. Additionally, the measured file is converted to a file having equidistant data points (on frequency scale). The data points are made equidistant because the method of least square fit has a faster convergence towards optimum (best fit situation) values of the required parameters (*A*, *B* values etc.).

The position of individual hyperfine components is determined using the following equation (section 3.4.1)

$$\nu \;=\; \nu_c \;+\; \alpha_o \cdot A_o \;+\; \beta_o \cdot B_o \;-\; \alpha_u \cdot A_u - \; \beta_u \cdot B_u$$

The intensity of each component is calculated using 6j symbols (section 3.4.2).

When some input parameters are fed in the input file (*.ein file) of the fitter program, the program gradually varies the values of these parameters and adjust the calculated curve according to the Gauss-Newton least square method to the experimentally recorded curve i.e. minimizing squared error sum *ESS* given by

$$ESS \;=\; \sum_{k=1}^{n} [I_V(k) - I_V(\nu_k, \vec{a})\,]^2$$

where $\vec{a}$ corresponds to a set of fit parameters, $I_V(k)$ is the measured intensity at a particular frequency point ν_k and $I_V(\nu_k, \vec{a})$ is the calculated intensity at the same point.

Many iterations are performed to get the minimum value of *ESS* and finally a new set of parameters is obtained, which presents the best fit of the calculated curve with the experimentally recorded curve.

The important parameters are *J* values and hyperfine constants of the upper and the lower levels, the half width of the hyperfine components, the frequency position of the highest intensity component etc. A suitable model function: Gaussian model, Lorentzian model or Voigt model can also be selected depending upon the shape of the recorded profile. When Voigt profile is selected, a parameter η is used to select different weights of the Gaussian and Lorentzian profiles. The contents of a typical input and output files of the fitter program are given below:

Input file of Fitter (*.ein)

```
91 0.001 10       // Fitverfahren (klassisch 1, Einzellinien 2)

1       // Anzahl der Isotope
4      // Jo
3      // Ju
2.5   // I
1     // Haeufigkeit
0.0   // Offsetfrequenz
1 7933.6 // lage der hoechsten Komponente

623.0 10 1168.2 -11.5 //Ao,Bo,Au,Bu
1090.2 1090.2   // Untergrund

3        // Modellfunktion (Voigt)
188.0      // HWB1.0
.8   //  weight of the Lorenzian profile (η)

1 1 1 1 1 1 1  // Steuerparameter: Ao, Bo, Au, Bu, nus, hwbG,
1 0            // Steuerparameter Untergrund
NE          // Cross-Over Resonanzen
JA          // Intensitaeten im th. Verh. koppeln ?


3 1    // deltaF = deltaJ = +1
6 1    // deltaF = deltaJ = +1
9 1    // deltaF = deltaJ = +1
12 1    // deltaF = deltaJ = +1
15 1    // deltaF = deltaJ = +1
```

Output file of Fitter (*.aus)

```
_______________________________________________
  Endergebnis  (  5.te Iteration)      Fitverfahren 1
______________________________________________
Startwellenlänge in A           :    5787.01
Startwellenzahl in 1/cm         :    17280.081
Fluoreszenzwellenlänge in A     :     3800.00
Fluoreszenzwellenzahl in 1/cm   :    26315.789
Anzahl der Datenpunkte          :     9032
Anzahl der Isotope/Einzellinien  :       1
Anzahl der Parameter            :       18
Eichfaktor                  :    1.701852000 MHz
Alle Isotope: Lagen und Häufigkeiten (errechnet aus den Intens.)
Iso |  Lage/MHz   | abs.Lage*cm | Intensitaet  |  Hfk.th. | Hfk.fit | Hfit/Hth.
----+-------------+-------------+--------------+----------+---------+----------
  1 |  10459.52   | 17280.430   |  1595.95    | 100.00   | 100.00  |  1.000
Isotope mit Kernspin :
Isotop   1 :       I = 5/2   Jo = 4   Ju = 3
 Nr | Fo  ->  Fu  |  Lage/MHz  |Intensitaet |rel. Int. |Ifit/Ith.| Flaeche
----+-------------+------------+------------+----------+---------+---------
  4 | 9/2 -> 11/2 |  443.80    |    2.22    | 0.004638 | 1.00    |0.000e+000
  2 |11/2 -> 11/2 | 3874.47    |   19.63    | 0.040962 | 0.42    |0.000e+000
  7 | 7/2 ->  9/2 | 4063.77    |    4.89    | 0.010204 | 1.00    |0.000e+000
  5 | 9/2 ->  9/2 | 6868.06    |   40.24    | 0.083941 | 0.57    |0.000e+000
 10 | 5/2 ->  7/2 | 7144.88    |    6.29    | 0.013120 | 1.00    |0.000e+000
  1 |13/2 -> 11/2 | 7933.44    |  479.35    | 1.000000 | 1.00    |0.000e+000
  8 | 7/2 ->  7/2 | 9324.36    |   47.82    | 0.099763 | 0.62    |0.000e+000
 13 | 3/2 ->  5/2 | 9683.28    |    4.89    | 0.010204 | 1.00    |0.000e+000
  3 |11/2 ->  9/2 |10298.73    |  336.76    | 0.702546 | 0.92    |0.000e+000
 11 | 5/2 ->  5/2 |11239.17    |   38.47    | 0.080255 | 0.57    |0.000e+000
  6 | 9/2 ->  7/2 |12128.65    |  233.84    | 0.487828 | 0.87    |0.000e+000
```

```
2 1    // deltaF = 0
5 1    // deltaF = 0
8 1    // deltaF = 0
11 1    // deltaF = 0
14 1    // deltaF = 0

4 1    // deltaF = -1
7 1    // deltaF = -1
10 1    // deltaF = -1
13 1    // deltaF = -1

NE          // Intensitaeten mit bel. Verh. koppeln ?
NE         // Hyperfeinkonstanten koppeln ?
NE         // Halbwertsbreite/Kurvenformparameter koppeln ?
NE          // Abs. Isotopieverschiebung vorgeben ?
NE         // Rel. Isotopieverschiebung vorgeben ?
NE         // Abs. Abstaende vorgeben
NE         // Rel. Abstaende vorgeben
NE         // Intensitaeten zusammenfassen ?
NE         // Intensitaeten vorgeben ?
ne         // Fitintervalle vorgeben ?
NE         // Guetenintervall vorgeben?
1.0        // Skalierungsfaktor
NE         // Flaechennormierung
NE         // Penalty-Funktionen
0 0 0 0   100 500  500 //
100  0       //
0.1        //
```

```
 14 | 3/2 ->  3/2 |12609.23    |   19.98    | 0.041688 | 0.45    |0.000e+000
  9 | 7/2 ->  5/2 |13418.65    |  167.79    | 0.350042 | 0.87    |0.000e+000
 12 | 5/2 ->  3/2 |14165.12    |  116.26    | 0.242535 | 0.88    |0.000e+000
 15 | 3/2 ->  1/2 |14365.38    |   77.51    | 0.161690 | 0.88    |0.000e+000
    Summe der Intens. =     1595.953
    rel. Schwerpunkt  =    10459.524 MHz
    abs. Schwerpunkt  =    17280.430 1/cm
    Vakuumwellenlänge =     5786.893 A
    Luftwellenlänge   =     5785.289 A
Profilfunktion:   Mischfunktion  (eta : Lorentzanteil)
Iso |   HWB/MHz   |  1-eta  |   eta
----+-------------+---------+--------
  1 |  214.76     |  0.450  |  0.550
Hyperfeinstrukturkonstanten :
  Isotop   1 :     I = 5/2   Jo = 4   Ju = 3
               Ao =   623.64 MHz      Au =  1169.02 MHz
               Bo =    10.89 MHz      Bu =    -9.72 MHz
Untergrund          =      1093.13
Fehlerquadratsumme  = 743039.279075
Intervall-Guete     =        7.88
Guete               =        7.88
Iterationsverlauf:
-------------------------------------------------------------------
Iteration    Guete           FQS        Marq-Steps       Pen-Summe
-------------------------------------------------------------------
   0        5.9137       1365918.1       0             0.0
   1        7.8232        758149.4       0             0.0
   2        7.8802        744022.0       0             0.0
   3        7.8794        743116.8       0             0.0
   4        7.8786        743045.0       0             0.0
   5        7.8783        743039.3       0             0.0
---------------------------------------------------
```

Sometimes the minimizing of *ESS* leads to some nonrealistic values of the fit parameters (e.g. negative intensities and negative frequencies). This problem can be avoided by reducing the number of input parameters. This is done by fixing the values of certain parameters, for example, if the hyperfine constants of any of the level are known (with acceptable tolerances) then *A* and *B* values of this level can be fixed, hence, the number of input parameters can be reduced by 2. The values of a parameter can be fixed by replacing 1 with 0, e.g. if 0 is written at second place in the 14 line (in above input file) the value of B_o is fixed which is 10 MHz (second value in the line number 9). The number of fitting parameters can also be reduced using intensity parameters coupling this is also called correlation between the fitting parameters. Coupling of hyperfine components can, for example, be done when relative intensities of the hyperfine components are changed due to the saturation effects.

The fitter program can also be used for multiline fitting i.e. hyperfine structures of more than one line can be fitted simultaneously. Multiline fitting is used in situations when the hyperfine structures of two or more lines are observed for a single isotope of the same element, when different isotopes are observed in the same line or hyperfine structures of the lines belonging to different isotopes of the same elements are observed. Some multiline fit results are discussed in section 10.3. For a single line, the best fit of the recorded curve is shown in figure 6.4

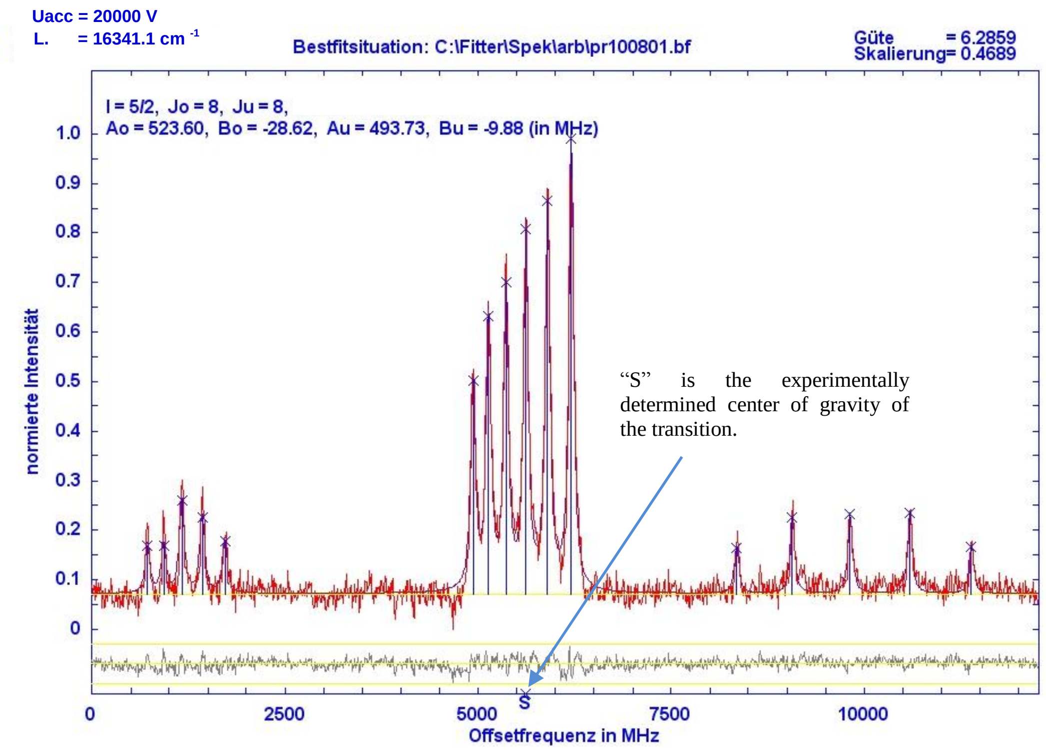

“S” is the experimentally determined center of gravity of the transition.

Figure 6.4: A single line best fit result of fitter program. The hyperfine structure of a Pr II transition is recorded at 6114.33 Å using the CLIBS method (chapter 10).

Some features of Fitter program:

- **Rechnen → Linearisieren** option is used to linearize the recorded hyperfine structure. In this regard the start wavelength (air) in Å of the laser scan and free spectral range of the marker etalon are required.
- **Rechnen → Fitten** option is used to start fitting process.

- Input file can be viewed using **Ansicht → Eingabedatei**, whereas **Ansicht → Ausgabedatei** can be used to view the output file. The output file contains calculated intensities, center of gravity of the line, best fit values of the hyperfine constants etc.
- The unlinearized recorded file can be viewed using **Grafik → unlinearistierte Messung**, the linearized recording can be displayed using **Grafik → linearistierte Messung**. To see the start situation of the fitting **Grafik → Startsituation** is used and the best situation can be graphically displayed using **Grafik→Bestsituation**.
- The values of best fit parameters can be selected as input parameters in input files using the option **Rechnen → Eingabedatei übernehmen**.

6.4 Classification of Pr II lines

The classification program discussed above is used for the investigation of the spectral lines of Pr II. A transition is said to be classified if the suggested hyperfine structure, calculated by means of the energies and hyperfine constants of the combining levels, matches with a structure in the FT spectrum with respect to shape and position.

In order to determine the center of gravity wavelength of a particular transition with high accuracy, the hyperfine constants of both combining levels must be known. First, a wavelength corresponding to the estimated center of gravity wavelength of the spectral line under investigation is introduced to the data base of the program. Then the program searches for transitions, so that the difference of levels energies matches with the wave number of the line within a preset range, e.g. ±0.3 cm^{-1}. A number of suggestions for the selected line are displayed along with the energy, *J* values and hyperfine constants of the involved levels. If the hyperfine constants are known a graphical representation of the hyperfine structures of the lines are also shown. With the help of these suggestions one can decide which transition appears in the FT spectrum. The hyperfine pattern of these suggestions can be compared with the hyperfine structure of the FT spectrum. Provided the hyperfine structure of the line in FT spectrum is visible and resolved, the two patterns are shifted against each other to have a better overlap, in this way the correct center of gravity wavelength of the transition is found with an accuracy of 0.001Å, because the human eye can easily recognize a mis-shift of two patterns against each other. From this corrected center of gravity wavelength, the center of gravity wave number of the transition is calculated which is then used to improve the energy values of the levels involved in the transition. The corrected energies of the levels and center of gravity wave lengths are stored in the data base of the classification program.

Sometimes it is observed that the hyperfine pattern in the suggestion list, calculated using literature values of hyperfine constants, does not match completely the FT pattern. In such cases the hyperfine structure visible in the FT spectrum is fitted (using Fitter program) in order to improve (or determine even not known) *A*-values of the combining levels.

As an example, Figure 6.5 [6] shows a part of the FT spectrum. The previously unclassified line shows a typical flag pattern and can be interpreted as transition from the upper even level $26570.208(5)_4$ to the lower odd level $1743.737(5)°_5$. The 6 main components (ΔF = -1) are completely resolved. Since A = -44.3(9) MHz for the lower level is precisely known (with CLIBS measurements) [48], the hyperfine constant A = 733(5) MHz for the upper level is found. By comparing the calculated hyperfine pattern with the FT pattern, the center of gravity wavelength of this line is determined precisely to be 4026.821 Å.

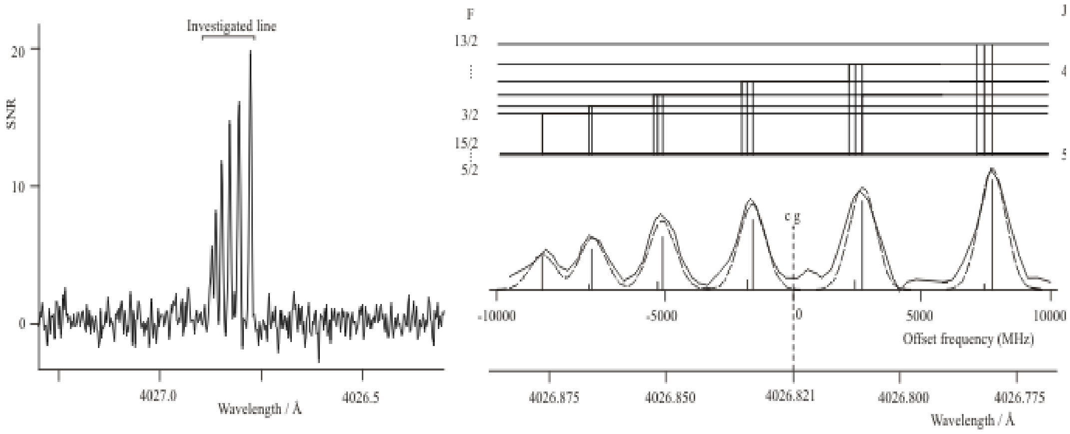

Figure 6.5: Left: Part of the FT spectrum showing an unclassified line at 4026.8 Å which could be classified as Pr II transition between the levels 26570.208_4 and $1743.737°_5$. Right: the comparison with the calculated hf pattern allowed to determine the cg wavelength to be 4026.821 Å. Full line: Pattern from FT spectrum, dotted: Calculated pattern assuming a Gaussian line profile with FWHM 1200 MHz.

6.5 Correction of energies of Pr II fine structure levels

In the first step of the energy corrections, hyperfine patterns of transitions between the odd ground level ($0°_4$ cm^{-1}) and high lying even levels are investigated and the energy values of these even levels are determined by converting the accurate center of gravity wavelengths of the lines to wave numbers. From these corrected energy levels, prominent transitions to the next odd lower level, $441.95°_5$, are searched. Then, the energy is optimized with the new value 442.060(5) cm^{-1}. From this odd level some more upper even levels are corrected with respect to their energy, and using the same approach, the lower level $1649.088(5)°_6$ is corrected, and so on. In this way, many upper even levels and many lower odd levels are corrected.

As can be learned from tables 6.1 and 6.2, the odd energy levels of Pr II can be divided into two groups, one in the energy range 0 to 14705 cm^{-1} and a second one with energies higher than 30844 cm^{-1}, while the even energy levels range from 5854 to 31654 cm^{-1}. Limited by our FT spectrum in the infrared region, in the way described before we could not correct even levels below 10000 cm^{-1}, and of course not the high lying odd levels.

The next step is the investigation of transitions of the high lying odd energy levels to even energy levels having energies higher than 10000 cm^{-1}. Amongst these already corrected even levels, $10801.853(5)_5$ is the only one combining with one of the upper odd levels, $35497.56°_5$, at 4048.131 Å. Using this center of gravity wavelength, a correction of 0.073 cm^{-1} has to be introduced, leading to the value 35497.663(5) cm^{-1}. A decay from this odd level ($35497.634(5)°_5$) to the lowest known even level 5854.54_6 is observed in the FT spectrum at 3372.505 Å. The predicted hyperfine structure is found in good agreement with the FT spectrum with improved A values of the involved levels: A_{up} = 1067(10) MHz and A_{lo} = 1050(10) MHz. Therefore, from the center of gravity transition wavelength 3372.505 Å, the energy value of the lowest even level is determined to be 5854.600(10) cm^{-1}.

Using now this energy and the newly determined A-factor; energy- and A-values for the combining high lying upper odd levels are determined. Transitions from these levels allow then the energy correction of the next higher even levels in the range up to 10000 cm^{-1}.

Finally, the energies of all levels, having transitions appearing with a good signal to noise ratio (SNR) in the FT spectrum, to any of the corrected lower/upper levels are corrected. The procedure is shown simplified in Figure 6.6 [6].

In order to avoid an increase of errors with increasing number of treated lines, finally a global fit has been performed, taking care to minimize the squared errors of the level energies. Due to the special level structure of Pr II (see figure 6.6) this fit was made of the two groups of levels separately. The groups were then combined by level 10801.853(5)$_5$, which participated in the transitions within both groups, compared to the first procedure, the energies changed only by few 0.001 cm^{-1}.

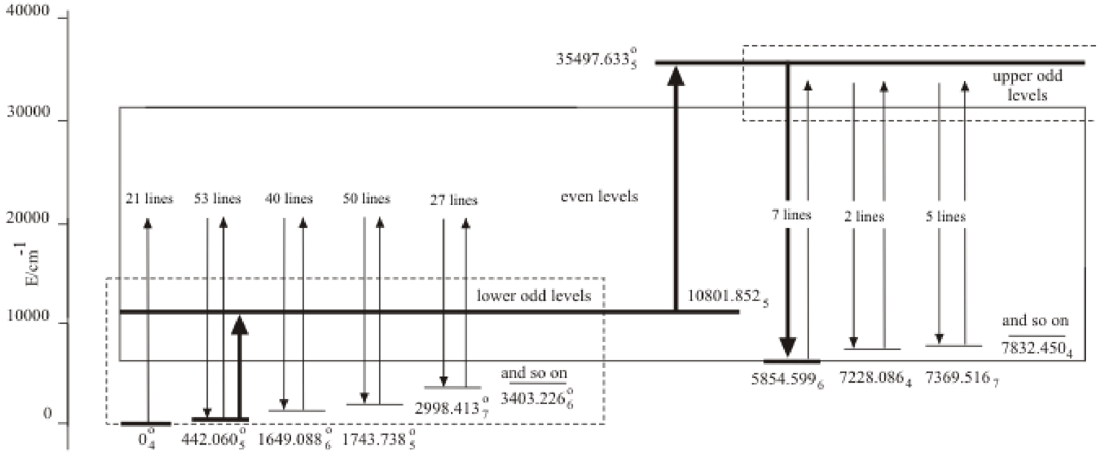

Figure 6.6: Energy correction of Pr II fine structure levels.

During this work, the large difference of 0.193 cm^{-1} of the energy value of the odd lower level 8965.57°$_2$ to the new value 8965.764 cm^{-1} is observed. This level is energy corrected at wavelength 5951.773 Å using the upper level 25762.825(5)$_3$, which is already corrected at wavelength 3880.462 Å (transition to the ground level, correction made for this level is 0.105 cm^{-1}). The hyperfine structure is very clear in the FT spectrum and the A values of the combining levels are determined to be A_{up} = 860 MHz and A_{lo} = 1710 MHz (instead of A_{up} = 1610(92) MHz [42]), which is in good agreement with the results of Furmann [51] (A_{up} = 854.7(30) MHz and A_{lo} = 1705.1(53) MHz). The energy and A values of this lower level are confirmed at wavelength 6017.809 Å (decay of the upper level 25578.507(5)$_3$, which is already corrected using its transition to the ground level at wavelength 3908.425 Å).

6.6 Results

Table 6.1 contains corrected energy values of odd Pr II levels and Table 6.2 contains corrected energies for even levels. In each table, *J* values of the energy levels are listed in column 1, corrected and previous energy values are listed in columns 2 and 3, respectively, in increasing order. The accuracy is given in [42] with 0.01 cm^{-1}. Reference to previous energies is given in Column 4. Column 5 shows the difference ΔE between previous and improved energy values, column 6 presents the best *A* values available in the literature. References to column 6 are given in column 7. *A* value, given by Ginibre [42] in wave number, are converted to MHz. For determination of *A* values within this work we have used the fitter program. The electric quadrupole moment Q = -0.066b [27] is very small and therefore *B* values are assumed to be zero in this work.

Table 6.3 lists spectral lines of Pr II appearing in the FT spectrum, classified before or in this work. Columns 1 and 2 present improved and previous center of gravity wavelengths; the references to column 2 are given in column 3. The SNR of these lines as appearing in the FT spectrum is listed in column 4. The classification is given in columns 5 to 8.

It should be mentioned that the given SNR is not representative for the intensity of a transition, since (i) the intensity is proportional to the area under an hyperfine pattern and not to its height and (ii) the spectra are not intensity calibrated, thus the spectral response of the optical elements and the detectors of the FT spectrometer are not taken into account. Furthermore, the intensity of ionic lines compared to atomic lines is strongly dependent on the energy range in which the upper levels are lying, and on the kind and parameters of the discharge used to take an emission spectrum. Thus we think that in the spectra evaluated by Ginibre [42] more ionic lines were present than in our spectrum. This could be an explanation why several levels given by Ginibre could not be confirmed in this work, since no transitions could be found. On the other hand, when performing laser spectroscopic investigations, it is possible to excite transitions which are so weak that they do not appear in our FT spectrum. This seems to be the case for a large number of levels discovered by Furmann [33, 52]. In order to give a complete picture of the known Pr II levels, we have listed these remaining levels in Tables 6.4 (odd) and 6.5 (even). Column 1 contains *J* values, column 2 the level energy in cm^{-1}, columns 3 and 4 the hyperfine constants *A* and *B*, and column 5 the reference.

Table 6.1. Corrected odd energy levels of Pr II [6].

J value	Corrected energy / cm^{-1}	Previous energy / cm^{-1}	Ref. to column 3	Δ*E* / cm^{-1}	*A* / MHz	Ref. to column 6
4	0	0	[41]	0	-238.7(4)	[48]
5	442.060(5)	442.079	[45]	-0.019	1910.3(21)	[48]
6	1649.088(5)	1649.092	[45]	-0.004	1633.8(27)	[48]
5	1743.737(5)	1743.776	[45]	-0.039	-44.3(9)	[48]
7	2998.412(5)	2998.417	[45]	-0.005	1435.2(16)	[48]
6	3403.226(5)	3403.237	[45]	-0.011	-146.5(4)	[48]
6	3893.508(5)	3893.505	[45]	0.003	902(5)	[41]
5	4097.653(5)	4097.636	[45]	0.017	966(10)	This work
8	4437.176(5)	4437.117	[45]	0.059	1297.9(14)	[48]
7	5079.375(5)	5079.362	[45]	0.013	-166.2(5)	[48]
7	5108.437(5)	5108.476	[45]	-0.039	660(5)	This work
6	5226.567(5)	5226.591	[45]	-0.024	710(5)	This work
7	6413.969(5)	6414.020	[45]	-0.051	564(4)	[41]
8	6417.859(5)	6417.865	[45]	-0.006	547(4)	[41]
5	7438.301(5)	7438.23	[41]	0.071	709.3(12)	[47]
4	7446.530(5)	7446.43	[41]	0.100	1069.3(30)	[50]
8	7659.762(5)	7659.759	[45]	0.003	440(5)	This work
3	7744.295(5)	7744.16	[41]	0.135	1210(10)	This work
9	7805.637(5)	7805.571	[45]	0.066	445(5)	This work
4	8099.697(5)	8099.62	[41]	0.077	770.8(9)	[47]
6	8465.102(5)	8465.04	[41]	0.062	573.9(7)	[47]
5	8489.934(5)	8489.87	[41]	0.064	793.5(25)	[50]
9	8958.477(5)	8958.438	[45]	0.039	390(5)	This work
2	8965.764(5)	8965.57	[41]	0.194	1705.1(53)	[50]
3	9045.051(5)	9044.94	[41]	0.111	940.0(55)	[50]
4	9128.741(5)	9128.66	[41]	0.081	840.5(35)	[50]
10	9255.224(5)	9255.19	[41]	0.034	380(5)	This work
5	9378.612(5)	9378.55	[41]	0.062	613.8(8)	[47]
6	9646.679(5)	9646.62	[41]	0.059	626.9(20)	[50]
7	10030.351(5)	10030.32	[41]	0.031	462.3(30)	[50]
4	10116.696(10)	10116.63	[41]	0.066	653.9(25)	[50]
6	10163.531(5)	10163.48	[41]	0.051	683(9)	[41]
5	10535.868(5)	10535.80	[41]	0.068	680(5)	This work
6	10729.778(5)	10729.72	[41]	0.058	529.1(35)	[50]

J value	Corrected energy / cm^{-1}	Previous energy / cm^{-1}	Ref. to column 3	ΔE / cm^{-1}	*A* / MHz	Ref. to column 6
7	11005.557(5)	11005.52	[41]	0.037	546.7(10)	[47]
7	11418.672(5)	11418.61	[41]	0.062	675(8)	[41]
5	11447.788(5)	11447.73	[41]	0.058	566.8(44)	[50]
8	11611.054(5)	11611.01	[41]	0.044	419.9(30)	[50]
6	11749.526(5)	11749.49	[41]	0.036	556.3(50)	[50]
7	11794.384(5)	11794.35	[41]	0.034	527(4)	[41]
7	12243.537(5)	12243.51	[41]	0.027	493.1(50)	[50]
6	12826.982(5)	12826.94	[41]	0.042	487.3(10)	[47]
8	13029.112(5)	13029.09	[41]	0.022	574.2(55)	[50]
8	13373.648(5)	13373.61	[41]	0.038	498.5(30)	[50]
9	14705.965(5)	14705.96	[41]	0.005	505(5)	This work
5	30844.727(10)	30844.66	[41]	0.067	1150	[41]
6	30860.315(10)	30860.28	[41]	0.035	865(10)	This work
6	31120.691(10)	31120.63	[41]	0.061	1090(10)	This work
4	31776.030(10)	31775.95	[41]	0.080	872(10)	This work
5	32590.772(10)	32590.70	[41]	0.072	1010	[41]
6	32950.136(10)	32950.10	[41]	0.036	895	[41]
5	33277.599(10)	33277.54	[41]	0.059	839	[41]
5	33387.685(10)	33387.64	[41]	0.045	763	[41]
7	33397.060(10)	33397.06	[41]	0.000	896(10)	This work
4	33440.566(10)	33440.51	[41]	0.056	720	[41]
6	33616.733(10)	33616.69	[41]	0.043	702	[41]
5	33674.569(10)	33674.55	[41]	0.019	660(5)	This work
4	33981.313(10)	33981.24	[41]	0.073	999	[41]
6	34031.361(10)	34031.32	[41]	0.041	814(10)	This work
4	34322.751(10)	34322.70	[41]	0.051	906	[41]
6	34483.858(10)	34483.86	[41]	-0.002	738	[41]
7	35041.681(10)	35041.68	[41]	0.001	665(5)	This work
6	35133.646(10)	35133.62	[41]	0.026	660	[41]
5	35220.984(10)	35220.93	[41]	0.054	780	[41]
5	35497.634(5)	35497.56	[41]	0.074	1067(10)	This work
7	35522.425(10)	35522.43	[41]	-0.005	700(5)	This work
8	35692.193(10)	35692.19	[41]	0.003	705	[41]
5	35978.302(10)	35978.22	[41]	0.082	818	[41]

J value	Corrected energy / cm^{-1}	Previous energy / cm^{-1}	Ref. to column 3	ΔE / cm^{-1}	*A* / MHz	Ref. to column 6
5	36090.677(10)	36090.62	[41]	0.057	785	[41]
7	36180.343(10)	36180.33	[41]	0.013	560	[41]
7	36245.522(10)	36245.50	[41]	0.022	600	[41]
5	36605.881(10)	36605.87	[41]	0.011	839	[41]
7	36790.038(10)	36790.03	[41]	0.008	580(5)	This work
8	36847.309(10)	36847.30	[41]	0.009	635	[41]
5	36853.907(10)	36853.87	[41]	0.037	763	[41]

Table 6.2. Corrected even energy levels of Pr II [6].

J value	Corrected energy / cm^{-1}	Previous energy / cm^{-1}	Ref. to column 3	Δ*E* / cm^{-1}	*A* / MHz	Ref. to column 6
6	5854.600(10)	5854.54	[41]	0.060	1050(10)	This work
4	7228.086(10)	7228.00	[41]	0.086	1160(10)	This work
7	7369.522(10)	7369.50	[41]	0.022	784(5)	This work
4	7832.450(10)	7832.45	[41]	0.000	-272(13)	[41]
5	7888.598(10)	7888.52	[41]	0.078	1360(10)	This work
6	8140.743(10)	8140.69	[41]	0.053	1279(5)	[41]
5	8197.904(10)	8197.82	[41]	0.084	1463(6)	[41]
5	8379.485(10)	8379.46	[41]	0.025	144(6)	[41]
5	8477.890(10)	8477.86	[41]	0.030	981(6)	[41]
8	8931.437(10)	8931.43	[41]	0.007	576(10)	This work
6	9211.976(10)	9211.95	[41]	0.026	1189(10)	This work
4	9335.763(10)	9335.74	[41]	0.023	119(7)	[41]
5	9516.068(10)	9515.97	[41]	0.098	1826(6)	[41]
6	9532.553(10)	9532.54	[41]	0.013	843(4)	[41]
6	9670.825(10)	9670.82	[41]	0.005	490(5)	This work
7	9694.735(10)	9694.75	[41]	-0.015	760(4)	[41]
5	9733.453(10)	9733.44	[41]	0.013	55(6)	[41]
4	9768.042(10)	9767.98	[41]	0.062	685(7)	[41]
6	10137.964(10)	10137.93	[41]	0.034	1495(10)	This work
5	10330.238(10)	10330.26	[41]	-0.022	-230(5)	This work
6	10454.325(10)	10454.26	[41]	0.065	1584(5)	[41]
4	10466.538(5)	10466.41	[41]	0.128	1611(10)	This work
5	10801.853(5)	10801.80	[41]	0.053	795(6)	[41]
3	10843.790(5)	10843.73	[41]	0.060	763(5)	This work
7	10987.251(10)	10987.24	[41]	0.011	680(4)	[41]
7	11253.466(10)	11253.46	[41]	0.006	444(4)	[41]
4	11257.857(5)	11257.80	[41]	0.057	1015(10)	This work
6	11283.178(5)	11283.14	[41]	0.038	611(5)	This work
5	11927.071(5)	11927.00	[41]	0.071	958(11)	[41]
8	12237.159(10)	12237.15	[41]	0.009	801(4)	[41]
5	12450.863(5)	12450.81	[41]	0.053	783(5)	This work
4	12784.009(5)	12783.95	[41]	0.059	580(7)	[41]
6	13084.274(5)	13084.22	[41]	0.054	632(5)	[41]
4	13248.256(5)	13248.22	[41]	0.036	293(14)	[41]

J value	Corrected energy / cm^{-1}	Previous energy / cm^{-1}	Ref. to column 3	ΔE / cm^{-1}	A / MHz	Ref. to column 6
3	13257.176(5)	13257.17	[41]	0.006	-77(9)	[41]
6	13365.087(5)	13365.02	[41]	0.067	1316(5)	[41]
4	13457.190(5)	13457.05	[41]	0.140	1533(10)	This work
6	13472.652(5)	13472.66	[41]	-0.008	673(9)	[41]
6	13776.859(5)	13776.80	[41]	0.059	829(5)	[41]
5	14095.072(5)	14095.02	[41]	0.052	409(11)	[41]
4	14102.284(5)	14102.24	[41]	0.044	365(5)	This work
4	14167.985(5)	14167.90	[41]	0.085	875(7)	[41]
7	14307.131(5)	14307.10	[41]	0.031	550(5)	This work
6	14416.824(5)	14416.78	[41]	0.044	687(9)	[41]
5	14493.281(5)	14493.22	[41]	0.061	580(5)	This work
5	14607.726(5)	14607.64	[41]	0.086	1352(6)	[41]
5	14745.863(5)	14745.81	[41]	0.053	603(5)	This work
8	14791.817(5)	14791.79	[41]	0.027	318(7)	[41]
5	14908.952(5)	14908.91	[41]	0.042	680(5)	This work
7	15087.176(5)	15087.14	[41]	0.036	600(4)	[41]
5	15166.091(5)	15166.04	[41]	0.051	330(5)	This work
7	15990.436(5)	15990.40	[41]	0.036	712	[41]
6	16022.502(5)	16022.45	[41]	0.052	609(46)	[41]
6	16243.010(5)	16242.97	[41]	0.040	396(5)	[41]
6	16967.741(5)	16967.72	[41]	0.021	396(5)	This work
7	17124.934(5)	17124.91	[41]	0.024	728(16)	[41]
7	17235.249(5)	17235.20	[41]	0.049	983(16)	[41]
7	17387.039(5)	17387.02	[41]	0.019	464(4)	[41]
8	17483.420(5)	17483.38	[41]	0.040	483(14)	[41]
5	17676.112(5)	17676.04	[41]	0.072	805(10)	This work
7	18077.281(5)	18077.23	[41]	0.051	907(10)	This work
6	18835.807(5)	18835.77	[41]	0.037	608(5)	This work
5	18910.166(5)	18910.11	[41]	0.056	709(11)	[41]
4	18919.277(5)	18919.25	[41]	0.027	333(27)	[41]
4	19567.503(5)	19567.48	[41]	0.023	48(7)	[41]
8	19721.768(5)	19721.75	[41]	0.018	841(4)	[41]
4	19845.408(5)	19845.33	[41]	0.078	744(7)	[41]
6	19882.192(5)	19882.14	[41]	0.052	688(19)	[41]
6	20115.016(5)	20114.95	[41]	0.066	707(19)	[41]

J value	Corrected energy / cm^{-1}	Previous energy / cm^{-1}	Ref. to column 3	ΔE / cm^{-1}	A / MHz	Ref. to column 6
7	20490.649(5)	20490.61	[41]	0.039	438(5)	This work
6	20554.360(5)	20554.30	[41]	0.060	887(19)	[41]
6	21061.047(5)	21060.99	[41]	0.057	590(9)	[41]
5	21131.306(5)	21131.26	[41]	0.046	676(5)	This work
4	21462.045(5)	21462.00	[41]	0.045	401(67)	[41]
5	21494.812(5)	21494.75	[41]	0.062	1003(11)	[41]
5	21676.163(5)	21676.12	[41]	0.043	266(5)	This work
6	21781.101(5)	21781.06	[41]	0.041	579(5)	This work
4	21971.534(5)	21971.46	[41]	0.074	688	[41]
5	22040.073(5)	22040.05	[41]	0.023	539.3(6)	[48]
7	22184.306(5)	22184.27	[41]	0.036	592(16)	[41]
5	22317.109(5)	22317.04	[41]	0.069	782(5)	This work
6	22472.061(5)	22472.02	[41]	0.041	707	[41]
5	22571.510(5)	22571.46	[41]	0.050	512.3(9)	[48]
7	22660.794(5)	22660.77	[41]	0.024	472	[41]
5	22675.492(5)	22675.489	[45]	0.003	765.7(8)	[48]
4	22686.710(5)	22686.69	[41]	0.020	400	[41]
6	22718.404(5)	22718.35	[41]	0.054	748	[41]
8	22808.753(5)	22808.72	[41]	0.033	430	[41]
5	22885.634(5)	22885.56	[41]	0.074	909.7(10)	[48]
6	23141.491(5)	23141.44	[41]	0.051	702	[41]
5	23261.402(5)	23261.399	[45]	0.003	584.3(6)	[48]
6	23505.499(5)	23505.46	[41]	0.039	672(5)	This work
4	23527.947(5)	23527.90	[41]	0.047	628(5)	This work
5	23616.903(5)	23616.86	[41]	0.043	698(5)	This work
5	23652.274(5)	23652.25	[41]	0.024	682(5)	This work
4	23660.171(5)	23660.177	[45]	-0.006	870.8(12)	[48]
6	23712.665(5)	23712.63	[41]	0.035	498	[41]
4	23892.445(5)	23892.38	[41]	0.065	576(5)	This work
7	23898.387(5)	23898.34	[41]	0.047	862(10)	This work
8	23970.489(5)	23970.45	[41]	0.039	724	[41]
6	23977.880(5)	23977.83	[41]	0.050	610.3(10)	[48]
6	24115.536(5)	24115.564	[45]	-0.028	821.4(9)	[48]
6	24393.769(5)	24393.75	[41]	0.019	549.9(7)	[48]
5	24716.093(5)	24716.087	[45]	-0.006	731.9(17)	[48]

J value	Corrected energy / cm^{-1}	Previous energy / cm^{-1}	Ref. to column 3	ΔE / cm^{-1}	*A* / MHz	Ref. to column 6
4	24755.017(5)	24754.95	[41]	0.067	604.1(20)	[50]
7	24818.564(5)	24818.54	[41]	0.024	630(5)	This work
6	24835.064(5)	24835.03	[41]	0.034	467.2(6)	[48]
7	25248.709(5)	25248.69	[41]	0.019	545.0(7)	[48]
5	25330.823(5)	25330.78	[41]	0.043	632	[41]
4	25467.549(5)	25467.565	[45]	-0.016	732.7(11)	[48]
5	25499.570(5)	25499.583	[45]	-0.013	633.3(7)	[48]
4	25545.086(5)	25545.04	[41]	0.046	590(5)	This work
7	25569.218(5)	25569.217	[45]	0.001	689.7(9)	[48]
3	25578.507(5)	25578.555	[45]	-0.048	1031.6(22)	[47]
6	25610.227(5)	25610.20	[41]	0.027	539.4(7)	[48]
6	25656.737(5)	25656.762	[45]	-0.025	656.1(7)	[48]
3	25762.825(5)	25762.72	[41]	0.105	854.7(30)	[50]
4	25814.499(5)	25814.44	[41]	0.059	608	[41]
5	25842.444(5)	25842.39	[41]	0.054	677	[41]
6	26062.412(5)	26062.38	[41]	0.032	480	[41]
8	26139.792(5)	26139.77	[41]	0.022	550	[41]
5	26146.060(5)	26146.01	[41]	0.050	621.9(9)	[48]
4	26226.628(10)	26226.646	[45]	-0.018	678.1(60)	[50]
6	26398.569(5)	26398.603	[45]	-0.034	658.3(7)	[48]
7	26445.138(5)	26445.09	[41]	0.048	514.1(16)	[48]
6	26524.040(5)	26524.00	[41]	0.040	653.0(65)	[48]
4	26570.208(5)	26570.14	[41]	0.068	733(5)	This work
5	26640.915(5)	26640.86	[41]	0.055	621.2(7)	[48]
5	26707.364(5)	26707.31	[41]	0.054	519.8(6)	[48]
7	26860.974(5)	26860.970	[45]	0.004	603.2(7)	[48]
6	26962.021(5)	26961.96	[41]	0.061	610.9(7)	[48]
5	26973.549(5)	26973.49	[41]	0.059	601.7(12)	[47]
8	27128.016(5)	27127.948	[45]	0.068	591.4(10)	[48]
5	27198.297(5)	27198.24	[41]	0.057	583.3(11)	[47]
5	27380.527(5)	27380.45	[41]	0.077	682	[41]
6	27604.990(5)	27604.94	[41]	0.050	581	[41]
4	27705.071(5)	27705.01	[41]	0.061	643.5(55)	[50]
8	27781.688(5)	27781.69	[41]	-0.002	560.3(8)	[48]
4	27841.105(5)	27841.06	[41]	0.045	542.7(35)	[50]

J value	Corrected energy / cm^{-1}	Previous energy / cm^{-1}	Ref. to column 3	Δ*E* / cm^{-1}	*A* / MHz	Ref. to column 6
7	28009.828(5)	28009.80	[41]	0.028	556.8(7)	[48]
6	28034.127(5)	28034.08	[41]	0.047	462.3(6)	[48]
4	28049.986(5)	28049.92	[41]	0.066	621.4(35)	[50]
7	28172.968(5)	28172.96	[41]	0.008	474.1(14)	[48]
8	28201.980(5)	28201.936	[45]	0.044	538.5(6)	[48]
6	28508.823(5)	28508.828	[45]	-0.005	619.5(35)	[50]
7	28577.821(5)	28577.757	[45]	0.064	530.8(6)	[48]
9	28816.267(5)	28816.253	[45]	0.014	504.1(50)	[50]
5	29351.015(5)	29350.98	[41]	0.035	487.2(35)	[50]
5	29601.104(5)	29601.05	[41]	0.054	510.9(35)	[50]
8	29723.998(5)	29723.983	[45]	0.015	529.4(40)	[50]
7	30018.138(5)	30018.124	[45]	0.014	525.9(11)	[47]
6	31261.745(5)	31261.68	[41]	0.065	730.2(30)	[50]
6	31654.388(5)	31654.31	[41]	0.078	531.6(35)	[50]

Table 6.3. List of previously and new classified lines of Pr II appearing in the FT spectrum [6].

Improved wavelength λ_{air} / Å	Previous wavelength λ_{air} / Å	Ref. to column 2	SNR	Even level		Odd level	
				J	Energy / cm^{-1}	*J*	Energy / cm^{-1}
3372.505	3372.510	[114]	6	6	5854.600	5	35497.634
3581.169		This work	5	8	8931.437	8	36847.309
3600.743	3600.745	[41]	5	7	7369.522	6	35133.646
3630.959	3630.960	[41]	7	6	5854.600	5	33387.685
3645.535	3645.534	[41]	8	6	5854.600	5	33277.599
3660.072	3660.074	[41]	6	8	8931.437	7	36245.522
3667.672	3667.672	[41]	5	6	9532.553	7	36790.038
3668.827	3668.827	[41]	27	8	8931.437	7	36180.343
3687.036	3687.033	[41]	18	7	7369.522	6	34483.858
3689.713	3689.707	[41]	5	4	7228.086	4	34322.751
3692.621	3692.624	[25]	4	6	9532.553	5	36605.881
3735.753	3735.755	[41]	10	8	8931.437	8	35692.193
3739.188	3739.181	[41]	15	6	5854.600	5	32590.772
3749.613	3749.617	[25]	7	7	7369.522	6	34031.361
3750.987	3750.981	[41]	6	6	10137.964	7	36790.038
3759.604	3759.604	[41]	4	8	8931.437	7	35522.425
3761.864	3761.870	[41]	10	6	31654.388	7	5079.375
3792.443[a]	3792.436	[41]	2	7	28009.828	6	1649.088
3800.299	3800.305	[41]	17	4	28049.986	5	1743.737
3811.837	3811.845	[41]	4	4	26226.628	4	0
3816.020	3816.023	[41]	18	5	29601.104	6	3403.226
3818.280	3818.285	[41]	12	6	31261.745	7	5079.375
3823.173	3823.184	[41]	2	4	7832.450	4	33981.313
3823.583	3823.589	[41]	2	5	26146.060	4	0
3826.204	3826.198	[41]	6	4	26570.208	5	442.060
3830.717	3830.721	[41]	22	4	27841.105	5	1743.737
3832.977	3832.966	[41]	3	6	26524.040	5	442.060
3840.995	3840.995	[41]	5	7	7369.522	7	33397.060
3850.790	3850.797	[41]	26	4	27705.071	5	1743.737
3851.506	3851.495	[41]	9	6	26398.569	5	442.060
3851.596[a]	3851.590	[41]	7	6	27604.990	6	1649.088
3852.800	3852.803	[41]	22	5	29351.015	6	3403.226
3865.693	3865.696	[25]	2	6	27604.990	5	1743.737
3870.414	3870.412	[41]	2	6	9211.976	7	35041.681

Improved wavelength λ_{air} / Å	Previous wavelength λ_{air} / Å	Ref. to column 2	SNR	Even level		Odd level	
				J	Energy / cm^{-1}	*J*	Energy / cm^{-1}
3870.716	3870.716	[41]	6	7	9694.735	7	35522.425
3872.694 [a]	3872.694	[41]	3	4	25814.499	4	0
3874.452	3874.452	[41]	4	7	10987.251	7	36790.038
3876.193	3876.187	[41]	7	6	10454.325	7	36245.522
3877.190	3877.1900	[45]	33	4	26226.628	5	442.060
3880.462	3880.467	[41]	26	3	25762.825	4	0
3885.195	3885.195	[41]	16	5	27380.527	6	1649.088
3889.343	3889.335	[41]	11	5	26146.060	5	442.060
3897.246	3897.249	[41]	4	5	8379.485	6	34031.361
3899.540	3899.546	[41]	2	5	27380.527	5	1743.737
3902.464	3902.453	[41]	3	5	9516.068	6	35133.646
3908.050	3908.050	[41]	16	7	30018.138	8	4437.176
3908.103 [a]		This work	5	7	7369.522	6	32950.136
3908.287 [a]	3908.284	[41]	10	7	28577.821	7	2998.412
3908.425	3908.4256	[45]	56	3	25578.507	4	0
3909.614	3909.614	[41]	8	6	11283.178	5	36853.907
3911.984	3911.991	[41]	2	4	7832.450	5	33387.685
3912.907	3912.904	[41]	26	5	27198.297	6	1649.088
3918.858	3918.8586	[45]	27	6	28508.823	7	2998.412
3920.524	3920.531	[41]	8	5	25499.570	4	0
3924.153	3924.147	[41]	3	6	8140.743	6	33616.733
3925.454	3925.466	[41]	22	4	25467.549	4	0
3927.457	3927.459	[41]	17	5	27198.297	5	1743.737
3928.910	3928.917	[41]	3	4	7832.450	5	33277.599
3932.978	3932.973	[41]	3	5	8197.904	6	33616.733
3935.834	3935.822	[41]	8	5	25842.444	5	442.060
3938.303	3938.297	[41]	4	6	10137.964	7	35522.425
3940.169	3940.161	[41]	9	4	25814.499	5	442.060
3944.132	3944.135	[41]	3	7	9694.735	7	35041.681
3947.634	3947.631	[41]	26	5	26973.549	6	1649.088
3949.432	3949.429	[41]	26	6	26962.021	6	1649.088
3953.197	3953.201	[114]	2	5	10801.853	5	36090.677
3953.510	3953.511	[41]	22	8	29723.998	8	4437.176
3956.754	3956.754	[41]	30	6	5854.600	6	31120.691
3962.444	3962.446	[41]	21	5	26973.549	5	1743.737

Improved wavelength λ_{air} / Å	Previous wavelength λ_{air} / Å	Ref. to column 2	SNR	Even level		Odd level	
				J	Energy / cm^{-1}	J	Energy / cm^{-1}
3964.255	3964.257	[41]	21	6	26962.021	5	1743.737
3964.822	3964.8230	[45]	53	6	25656.737	5	442.060
3965.261	3965.2611	[45]	36	7	26860.974	6	1649.088
3966.570	3966.5794	[45]	17	8	28201.980	7	2998.412
3971.135 [a]	3971.136	[41]	13	7	28577.821	6	3403.226
3972.149	3972.136	[41]	24	6	25610.227	5	442.060
3977.097	3977.095	[25]	3	6	8140.743	5	33277.599
3982.049	3982.0499	[45]	42	6	28508.823	6	3403.226
3982.457	3982.447	[41]	12	4	25545.086	5	442.060
3989.691	3989.6922	[45]	33	5	25499.570	5	442.060
3992.171 [a]	3992.170	[41]	3	7	10650.240	8	35692.193
3993.164	3993.162	[41]	3	6	28034.127	7	2998.412
3994.796	3994.7968	[45]	44	4	25467.549	5	442.060
3997.044	3997.042	[41]	12	7	28009.828	7	2998.412
3997.955 [a]	3997.953	[41]	5	6	5854.600	6	30860.315
4000.177	4000.173	[25]	18	5	26640.915	6	1649.088
4000.449	4000.452	[25]	7	6	5854.600	5	30844.727
4004.696	4004.702	[25]	29	5	26707.364	5	1743.737
4006.673		This work	4	6	9532.553	6	34483.858
4008.688	4008.6887	[45]	37	7	30018.138	7	5079.375
4010.600		This work	7	7	11253.466	7	36180.343
4014.330		This work	2	6	10137.964	7	35041.681
4015.384	4015.391	[25]	20	5	26640.915	5	1743.737
4016.742	4016.730	[25]	7	5	25330.823	5	442.060
4026.821		This work	10	4	26570.208	5	1743.737
4029.002		This work	4	6	9670.825	6	34483.858
4031.761	4031.753	[25]	25	7	26445.138	6	1649.088
4033.839 [a]	4033.827	[25]	22	8	27781.688	7	2998.412
4034.323	4034.325	[25]	10	6	26524.040	5	1743.737
4038.444	4038.455	[25]	35	4	24755.017	4	0
4039.347	4039.345	[25]	13	6	26398.569	6	1649.088
4044.092		This work	6	4	11257.857	5	35978.302
4044.804	4044.8050	[45]	25	5	24716.093	4	0
4046.630	4046.635	[114]	4	7	10987.251	8	35692.193
4047.083	4047.083	[25]	4	5	7888.598	5	32590.772

Improved wavelength λ_{air} / Å	Previous wavelength λ_{air} / Å	Ref. to column 2	SNR	Even level		Odd level	
				J	Energy / cm^{-1}	*J*	Energy / cm^{-1}
4048.131	4048.133	[25]	6	5	10801.853	5	35497.634
4054.855	4054.8554	[45]	46	6	26398.569	5	1743.737
4056.534	4056.5347	[45]	40	8	29723.998	7	5079.375
4058.794	4058.800	[25]	16	6	28034.127	6	3403.226
4062.217	4062.225	[114]	3	8	12237.159	8	36847.309
4062.802	4062.806	[25]	52	7	28009.828	6	3403.226
4062.806 [a]	4062.803	[25]	28	6	27604.990	7	2998.412
4072.511	4072.503	[25]	3	4	7228.086	4	31776.030
4080.985	4080.980	[25]	12	5	26146.060	6	1649.088
4083.332	4083.341	[25]	16	4	26226.628	5	1743.737
4085.108		This work	5	5	8477.890	6	32950.136
4094.968	4094.962	[25]	8	6	26062.412	6	1649.088
4096.814	4096.820	[25]	21	5	26146.060	5	1743.737
4098.402 [a]	4098.400	[25]	7	5	8197.904	5	32590.772
4100.718	4100.7185	[45]	52	9	28816.267	8	4437.176
4111.873	4111.875	[25]	6	4	24755.017	5	442.060
4118.466	4118.4668	[45]	54	5	24716.093	5	442.060
4129.140	4129.148	[25]	4	5	8379.485	5	32590.772
4130.765	4130.771	[25]	9	6	27604.990	6	3403.226
4132.201	4132.197	[25]	10	5	25842.444	6	1649.088
4133.614	4133.618	[114]	6	6	9211.976	7	33397.060
4141.223	4141.2242	[45]	28	7	28577.821	8	4437.176
4143.118	4143.1179	[45]	62	8	27128.016	7	2998.412
4148.430	4148.433	[25]	13	5	25842.444	5	1743.737
4156.500	4156.504	[25]	4	4	9335.763	5	33387.685
4164.165 [a]	4164.1638	[45]	37	6	25656.737	6	1649.088
4169.435	4169.447	[25]	16	5	27380.527	6	3403.226
4171.818	4171.818	[25]	15	6	26962.021	7	2998.412
4172.248	4172.246	[25]	23	6	25610.227	6	1649.088
4175.308	4175.316	[25]	4	4	7832.450	4	31776.030
4175.612	4175.622	[25]	7	4	9335.763	5	33277.599
4176.315		This work	4	6	11283.178	5	35220.984
4178.638	4178.633	[25]	7	5	9516.068	4	33440.566
4179.401	4179.4022	[45]	95	7	25569.218	6	1649.088
4180.647	4180.655	[25]	4	6	25656.737	5	1743.737

Improved wavelength λ_{air} / Å	Previous wavelength λ_{air} / Å	Ref. to column 2	SNR	Even level		Odd level	
				J	Energy / cm^{-1}	*J*	Energy / cm^{-1}
4184.244	4184.244	[25]	8	4	23892.445	4	0
4185.122	4185.123	[25]	5	5	7888.598	4	31776.030
4189.484	4189.4838	[45]	50	7	26860.974	7	2998.412
4191.606	4191.605	[25]	22	5	25499.570	6	1649.088
4206.718	4206.7160	[45]	53	8	28201.980	8	4437.176
4208.307	4208.315	[25]	16	5	25499.570	5	1743.737
4211.860 [a]	4211.862	[25]	10	7	28172.968	8	4437.176
4213.556		This work	4	6	9670.825	7	33397.060
4217.807	4217.81	[114]	5	7	9694.735	7	33397.060
4222.947	4222.9469	[45]	49	6	24115.536	5	442.060
4223.117	4223.113	[25]	8	4	9768.042	4	33440.566
4225.322	4225.3229	[45]	126	4	23660.171	4	0
4233.063 [a]	4233.071	[25]	6	5	23616.903	4	0
4236.163	4236.153	[25]	15	7	25248.709	6	1649.088
4240.025	4240.026	[25]	5	5	8197.904	4	31776.030
4241.010	4241.010	[25]	22	7	28009.828	8	4437.176
4243.504	4243.507	[25]	6	6	26962.021	6	3403.226
4247.505 [a]	4247.501	[25]	4	6	10137.964	5	33674.569
4247.647	4247.631	[25]	30	6	23977.880	5	442.060
4249.068	4249.067	[25]	5	4	23527.947	4	0
4249.487	4249.485	[25]	6	6	26524.040	7	2998.412
4254.403	4254.402	[25]	9	7	28577.821	7	5079.375
4262.277		This work	3	8	12237.159	8	35692.193
4263.787	4263.781	[25]	7	7	26445.138	7	2998.412
4269.094	4269.100	[114]	10	6	9532.553	6	32950.136
4272.273 [a]	4272.273	[25]	21	6	26398.569	7	2998.412
4275.727		This work	3	6	13472.652	5	36853.907
4282.457 [a]	4282.456	[25]	17	8	27781.688	8	4437.176
4289.876	4289.878	[25]	4	5	26707.364	6	3403.226
4297.758	4297.7585	[45]	47	5	23261.402	4	0
4298.867		This work	7	7	9694.735	6	32950.136
4302.143	4302.149	[25]	2	5	26640.915	6	3403.226
4305.771	4305.7716	[45]	33	4	23660.171	5	442.060
4306.036		This work	5	5	9733.453	6	32950.136
4307.237	4307.233	[25]	2	5	23652.274	5	442.060

Improved wavelength λ_{air} / Å	Previous wavelength λ_{air} / Å	Ref. to column 2	SNR	Even level		Odd level	
				J	Energy / cm^{-1}	*J*	Energy / cm^{-1}
4314.810	4314.796	[25]	2	7	24818.564	6	1649.088
4323.556	4323.5499	[45]	3	8	28201.980	7	5079.375
4323.891	4323.891	[25]	3	6	26524.040	6	3403.226
4328.988 [a]	4328.983	[25]	8	7	28172.968	7	5079.375
4329.413	4329.411	[25]	10	6	24835.064	5	1743.737
4330.433	4330.418	[25]	4	4	23527.947	5	442.060
4333.978 [a]	4333.9783	[45]	19	5	24716.093	6	1649.088
4334.648	4334.650	[25]	8	6	23505.499	5	442.060
4338.698	4338.702	[25]	8	7	26445.138	6	3403.226
4344.285	4344.300	[25]	11	4	7832.450	5	30844.727
4344.473	4344.483	[25]	4	4	24755.017	5	1743.737
4347.484	4347.491	[25]	6	6	26398.569	6	3403.226
4350.397	4350.399	[114]	4	6	8140.743	6	31120.691
4351.835	4351.8443	[45]	11	5	24716.093	5	1743.737
4354.911	4354.913	[25]	4	5	7888.598	5	30844.727
4355.172	4355.180	[25]	2	6	28034.127	7	5079.375
4359.787	4359.788	[25]	4	7	28009.828	7	5079.375
4368.326	4368.334	[25]	36	5	22885.634	4	0
4382.393		This work	2	6	10137.964	6	32950.136
4396.069	4396.074	[25]	6	5	8379.485	6	31120.691
4403.276	4403.277	[25]	2	6	8140.743	5	30844.727
4403.600 [a]	4403.597	[25]	6	8	27781.688	7	5079.375
4405.827	4405.8278	[45]	8	8	27128.016	8	4437.176
4408.809	4408.8102	[45]	62	5	22675.492	4	0
4412.150	4412.1445	[45]	2	6	25656.737	7	2998.412
4413.765	4413.769	[25]	20	6	24393.769	5	1743.737
4419.645	4419.653	[25]	3	5	10330.238	6	32950.136
4421.225	4421.222	[25]	4	6	25610.227	7	2998.412
4429.120	4429.128	[25]	29	5	22571.510	4	0
4429.258 [a]	4429.2777	[45]	12	7	25569.218	7	2998.412
4446.986 [a]	4446.986	[114]	3	5	8379.485	6	30860.315
4449.833	4449.8330	[45]	15	6	24115.536	6	1649.088
4454.368	4454.355	[25]	4	5	22885.634	5	442.060
4468.659	4468.6604	[45]	17	6	24115.536	5	1743.737
4477.266 [a]	4477.259	[25]	8	6	23977.880	6	1649.088

Improved wavelength λ_{air} / Å	Previous wavelength λ_{air} / Å	Ref. to column 2	SNR	Even level		Odd level	
				J	Energy / cm^{-1}	*J*	Energy / cm^{-1}
4479.610	4479.618	[25]	3	5	22317.109	4	0
4487.808	4487.791	[25]	4	6	22718.404	5	442.060
4494.202	4494.199	[25]	6	4	22686.710	5	442.060
4496.326 [a]	4496.329	[25]	8	6	23977.880	5	1743.737
4496.470	4496.4722	[45]	21	5	22675.492	5	442.060
4510.150	4510.1515	[45]	12	7	25569.218	6	3403.226
4517.598	4517.582	[25]	8	5	22571.510	5	442.060
4531.086	4531.077	[25]	4	6	23712.665	6	1649.088
4534.155 [a]	4534.155	[25]	6	8	27128.016	7	5079.375
4535.918	4535.923	[25]	22	5	22040.073	4	0
4550.838	4550.837	[25]	3	5	23616.903	6	1649.088
4563.151	4563.151	[25]	6	5	23652.274	5	1743.737
4570.137	4570.125	[25]	2	5	22317.109	5	442.060
4570.530	4570.533	[25]	6	5	23616.903	5	1743.737
4576.323	4576.326	[25]	3	7	25248.709	6	3403.226
4578.173	4578.170	[25]	3	6	24835.064	7	2998.412
4579.843	4579.845	[114]	2	6	14416.824	7	36245.522
4593.929	4593.934	[25]	3	6	23505.499	5	1743.737
4606.449	4606.448	[25]	3	8	26139.792	8	4437.176
4612.070	4612.078	[25]	9	5	21676.163	4	0
4628.759	4628.743	[25]	16	5	22040.073	5	442.060
4643.495	4643.485	[25]	8	4	21971.534	5	442.060
4646.043	4646.051	[25]	4	5	23261.402	5	1743.737
4651.504	4651.501	[25]	9	6	23141.491	6	1649.088
4664.649 [a]	4664.656	[25]	6	6	24835.064	6	3403.226
4668.243	4668.243	[25]	3	7	24818.564	6	3403.226
4672.080	4672.090	[25]	12	6	23141.491	5	1743.737
4684.935	4684.938	[25]	6	6	21781.101	5	442.060
4707.546	4707.543	[25]	3	5	22885.634	6	1649.088
4708.088	4708.073	[25]	13	5	21676.163	5	442.060
4728.621 [a]	4728.634	[25]	3	5	22885.634	5	1743.737
4744.911	4744.906	[25]	8	6	22718.404	6	1649.088
4746.916	4746.920	[25]	9	8	26139.792	7	5079.375
4756.047	4756.034	[25]	8	4	21462.045	5	442.060
4757.921	4757.911	[25]	7	7	22660.794	6	1649.088

Improved wavelength λ_{air} / Å	Previous wavelength λ_{air} / Å	Ref. to column 2	SNR	Even level		Odd level	
				J	Energy / cm^{-1}	*J*	Energy / cm^{-1}
4762.718[a]	4762.719	[25]	6	6	24393.769	6	3403.226
4765.232	4765.232	[25]	2	6	23977.880	7	2998.412
4783.357[a]	4783.359	[25]	10	7	23898.387	7	2998.412
4801.046	4801.038	[25]	6	6	22472.061	6	1649.088
4822.969	4822.977	[25]	9	6	22472.061	5	1743.737
4832.078[a]	4832.064	[25]	6	5	21131.306	5	442.060
4837.041	4837.040	[25]	6	5	22317.109	6	1649.088
4848.544	4848.527	[25]	6	6	21061.047	5	442.060
4877.838	4877.844	[25]	10	7	23898.387	6	3403.226
4890.256	4890.260	[25]	6	7	26860.974	8	6417.859
4901.471[a]	4901.474	[25]	3	8	28201.980	9	7805.637
4912.617	4912.625	[25]	4	7	28009.828	8	7659.762
4956.638	4956.640	[25]	4	7	25248.709	7	5079.375
4989.284	4989.292	[25]	8	6	21781.101	5	1743.737
4997.386		This work	2	7	23898.387	6	3893.508
5002.457[a]	5002.462	[25]	8	6	26398.569	7	6413.969
5015.552	5015.544	[25]	5	5	21676.163	5	1743.737
5034.403[a]	5034.406	[25]	9	9	28816.267	9	8958.477
5037.464[a]	5037.457	[25]	11	5	21494.812	6	1649.088
5064.889[a]	5064.896	[25]	6	6	23141.491	6	3403.226
5110.392	5110.394	[25]	25	4	23660.171	5	4097.653
5110.777[a]	5110.778	[25]	36	9	28816.267	10	9255.224
5118.033[a]	5118.031	[25]	6	8	23970.489	8	4437.176
5129.532	5129.536	[25]	41	5	24716.093	6	5226.567
5145.169[a]	5145.173	[25]	4	4	23527.947	5	4097.653
5152.314	5152.305	[25]	26	4	19845.408	5	442.060
5156.508[a]	5156.515	[25]	16	5	21131.306	5	1743.737
5161.746[a]	5161.746	[25]	19	5	23261.402	6	3893.508
5173.905	5173.9054	[45]	50	8	27128.016	9	7805.637
5175.263[a]	5175.271	[25]	16	6	21061.047	5	1743.737
5175.834[a]	5175.843	[25]	10	6	22718.404	6	3403.226
5183.844	5183.853	[25]	7	6	24393.769	7	5108.437
5191.318	5191.323	[25]	46	7	22660.794	6	3403.226
5195.112[a]	5195.1135	[45]	18	8	28201.980	9	8958.477
5195.310[a]	5195.3135	[45]	48	6	25656.737	7	6413.969

Improved wavelength λ_{air} / Å	Previous wavelength λ_{air} / Å	Ref. to column 2	SNR	Even level		Odd level	
				J	Energy / cm^{-1}	*J*	Energy / cm^{-1}
5206.554	5206.5551	[45]	22	7	26860.974	8	7659.762
5216.733 [a]	5216.719	[25]	7	5	23261.402	5	4097.653
5219.047 [a]	5219.0522	[45]	16	7	25569.218	7	6413.969
5220.108	5220.1098	[45]	71	7	25569.218	8	6417.859
5227.182 [a]	5227.155	[25]	14	4	19567.503	5	442.060
5251.698 [a]	5251.707	[25]	5	6	24115.536	7	5079.375
5259.728	5259.7315	[45]	101	6	24115.536	7	5108.437
5263.875	5263.882	[25]	45	5	22885.634	6	3893.508
5288.058 [a]	5288.06	[114]	5	6	20554.360	6	1649.088
5289.952 [a]	5289.959	[25]	4	6	23977.880	7	5079.375
5292.021 [a]	5292.024	[25]	50	8	23970.489	7	5079.375
5292.622	5292.6218	[45]	27	6	24115.536	6	5226.567
5298.099	5298.099	[25]	24	6	23977.880	7	5108.437
5307.861 [a]	5307.858	[25]	4	7	25248.709	7	6413.969
5312.297 [a]	5312.301	[25]	16	7	23898.387	7	5079.375
5314.666 [a]	5314.679	[25]	5	6	20554.360	5	1743.737
5321.071 [a]	5321.074	[25]	23	5	22885.634	5	4097.653
5321.809 [a]		This work	16	7	26445.138	8	7659.762
5322.770	5322.7705	[45]	50	5	22675.492	6	3893.508
5331.477	5331.478	[25]	12	6	23977.880	6	5226.567
5352.403	5352.404	[25]	21	5	22571.510	6	3893.508
5381.261 [a]	5381.2570	[45]	22	5	22675.492	5	4097.653
5404.803 [a]	5404.806	[25]	5	6	26962.021	6	8465.102
5410.566 [a]	5410.539	[25]	16	4	18919.277	5	442.060
5413.236 [a]	5413.220	[25]	32	5	18910.166	5	442.060
5432.048 [a]	5432.050	[25]	10	5	25842.444	5	7438.301
5487.421 [a]	5487.423	[25]	6	6	25656.737	5	7438.301
5502.188 [a]	5502.188	[25]	3	8	27128.016	9	8958.477
5507.105 [a]	5507.104	[25]	4	5	29601.104	5	11447.788
5509.154 [a]	5509.153	[25]	19	5	22040.073	6	3893.508
5522.818 [a]	5522.831	[25]	21	4	19845.408	5	1743.737
5525.896 [a]	5525.910	[25]	12	5	21494.812	6	3403.226
5534.912 [a]	5534.917	[25]	4	6	23141.491	7	5079.375
5535.172 [a]	5535.175	[25]	13	5	25499.570	5	7438.301
5566.906 [a]	5566.907	[25]	5	6	27604.990	6	9646.679

Improved wavelength λ_{air} / Å	Previous wavelength λ_{air} / Å	Ref. to column 2	SNR	Even level		Odd level	
				J	Energy / cm^{-1}	*J*	Energy / cm^{-1}
5571.837[a]	5571.828	[25]	10	5	22040.073	5	4097.653
5580.389[a]	5580.387	[25]	8	6	23141.491	6	5226.567
5605.644[a]	5605.654	[25]	7	3	25578.507	3	7744.295
5608.929[a]	5608.925	[25]	17	4	19567.503	5	1743.737
5610.214[a]	5610.216	[25]	12	5	27198.297	5	9378.612
5621.896[a]	5621.892	[25]	10	5	21676.163	6	3893.508
5624.444	5624.448	[25]	13	7	30018.138	7	12243.537
5638.790[a]	5638.787	[25]	16	8	22808.753	7	5079.375
5677.027	5677.033	[25]	14	6	22718.404	7	5108.437
5681.876[a]	5681.882	[25]	15	5	26973.549	5	9378.612
5687.186[a]	5687.173	[25]	6	5	21676.163	5	4097.653
5689.208[a]	5689.209	[25]	7	7	28577.821	7	11005.557
5704.500	5704.490	[25]	6	4	26570.208	3	9045.051
5711.634[a]	5711.637	[25]	6	6	28508.823	7	11005.557
5715.236[a]	5715.229	[25]	5	7	20490.649	7	2998.412
5715.366[a]	5715.369	[25]	9	6	22718.404	6	5226.567
5719.086	5719.087	[25]	10	8	29723.998	7	12243.537
5719.626[a]	5719.633	[25]	5	3	25578.507	4	8099.697
5747.948[a]	5747.955	[25]	20	6	22472.061	7	5079.375
5756.168[a]	5756.169	[25]	16	4	25467.549	4	8099.697
5773.165[a]	5773.165	[25]	4	4	24755.017	5	7438.301
5775.911[a]	5775.906	[25]	4	4	24755.017	4	7446.530
5777.291	5777.295	[25]	5	6	28034.127	6	10729.778
5786.172[a]	5786.173	[25]	9	5	24716.093	5	7438.301
5788.928[a]	5788.930	[25]	7	5	24716.093	4	7446.530
5791.363[a]	5791.365	[25]	15	5	26640.915	5	9378.612
5797.008[a]	5797.000	[25]	8	6	22472.061	6	5226.567
5800.857[a]	5800.841	[25]	10	5	17676.112	5	442.060
5810.581	5810.579	[25]	4	9	28816.267	8	11611.054
5813.550[a]	5813.546	[25]	14	8	28201.980	7	11005.557
5815.169[a]	5815.165	[25]	17	6	25656.737	6	8465.102
5815.332[a]	5815.331	[25]	7	7	30018.138	6	12826.982
5816.834[a]	5816.813	[25]	12	6	18835.807	6	1649.088
5818.574[a]	5818.573	[25]	11	4	26226.628	3	9045.051
5823.709	5823.722	[25]	25	5	18910.166	5	1743.737

Improved wavelength λ_{air} / Å	Previous wavelength λ_{air} / Å	Ref. to column 2	SNR	Even level		Odd level	
				J	Energy / cm^{-1}	*J*	Energy / cm^{-1}
5828.902[a]	5828.910	[25]	8	6	20554.360	6	3403.226
5830.945[a]	5830.944	[25]	11	6	25610.227	6	8465.102
5844.646[a]	5844.644	[25]	12	7	22184.306	7	5079.375
5850.635	5850.630	[25]	15	7	20490.649	6	3403.226
5852.630	5852.627	[25]	11	5	27198.297	4	10116.696
5856.908[a]	5856.909	[25]	12	6	27604.990	5	10535.868
5868.824[a]	5868.827	[25]	17	5	25499.570	6	8465.102
5879.246[a]	5879.246	[25]	20	7	28009.828	7	11005.557
5921.203[a]	5921.204	[25]	3	6	19882.192	7	2998.412
5930.662[a]	5930.663	[25]	11	5	26973.549	4	10116.696
5933.772[a]	5933.776	[25]	8	4	26226.628	5	9378.612
5939.904	5939.906	[25]	10	7	26860.974	7	10030.351
5940.726	5940.721	[25]	8	7	28577.821	6	11749.526
5951.268	5951.268	[25]	9	6	26962.021	6	10163.531
5951.773	5951.739	[25]	4	3	25762.825	2	8965.764
5956.604[a]	5956.604	[25]	16	7	28577.821	7	11794.384
5967.822	5967.821	[25]	19	6	26398.569	6	9646.679
5978.005[a]	5977.993	[25]	4	8	19721.768	7	2998.412
5981.194[a]	5981.195	[25]	19	6	28508.823	7	11794.384
5981.458[a]	5981.451	[25]	6	5	25842.444	4	9128.741
5985.747[a]	5985.757	[25]	4	6	21781.101	7	5079.375
5988.199[a]	5988.209	[25]	3	8	29723.998	8	13029.112
6016.486[a]	6016.478	[25]	8	5	24716.093	4	8099.697
6017.809	6017.799	[25]	13	3	25578.507	2	8965.764
6025.722[a]	6025.718	[25]	10	8	28201.980	8	11611.054
6025.816[a]	6025.812	[25]	4	5	26707.364	4	10116.696
6027.389[a]	6027.384	[25]	4	6	28034.127	5	11447.788
6049.513[a]	6049.479	[25]	8	6	16967.741	5	442.060
6050.049	6050.041	[25]	5	5	26640.915	4	10116.696
6086.168[a]	6086.166	[25]	5	6	26962.021	5	10535.868
6087.172[a]		This work	5	7	28172.968	6	11749.526
6087.522[a]	6087.515	[25]	11	4	25467.549	3	9045.051
6090.381	6090.381	[25]	5	7	26445.138	7	10030.351
6114.385	6114.383	[25]	8	8	29723.998	8	13373.648
6159.112	6159.098	[25]	7	6	25610.227	5	9378.612

Improved wavelength λ_{air} / Å	Previous wavelength λ_{air} / Å	Ref. to column 2	SNR	Even level		Odd level	
				J	Energy / cm^{-1}	*J*	Energy / cm^{-1}
6161.182	6161.185	[25]	16	5	24716.093	5	8489.934
6165.940 [a]	6165.940	[25]	13	4	23660.171	4	7446.530
6179.294 [a]	6179.291	[25]	2	5	23616.903	5	7438.301
6182.338	6182.340	[25]	4	8	27781.688	8	11611.054
6197.453	6197.445	[25]	2	7	26860.974	6	10729.778
6205.632 [a]	6205.633	[25]	4	4	26226.628	4	10116.696
6244.346	6244.345	[25]	6	6	25656.737	6	9646.679
6255.101 [a]	6255.098	[25]	3	5	26146.060	6	10163.531
6262.538	6262.539	[25]	6	6	25610.227	6	9646.679
6274.793 [a]	6274.807	[25]	6	5	17676.112	5	1743.737
6278.669	6278.684	[25]	4	7	25569.218	6	9646.679
6302.353	6302.355	[25]	5	6	26398.569	5	10535.868
6347.112	6347.109	[25]	6	7	28577.821	6	12826.982
6397.984	6397.986	[25]	3	6	24115.536	5	8489.934
6413.684 [a]	6413.677	[25]	6	5	24716.093	4	9128.741
6429.624	6429.629	[25]	5	7	28577.821	8	13029.112
6431.841	6431.842	[25]	4	6	26962.021	7	11418.672
6443.913	6443.906	[25]	2	6	26962.021	5	11447.788
6459.897 [a]	6459.875	[25]	2	7	17124.934	6	1649.088
6475.270	6475.260	[25]	4	5	22885.634	4	7446.530
6478.006 [a]	6478.011	[25]	7	6	18835.807	6	3403.226
6486.963 [a]	6486.962	[25]	6	7	20490.649	7	5079.375
6564.622	6564.611	[25]	4	5	22675.492	4	7446.530
6566.760	6566.767	[25]	11	6	16967.741	5	1743.737
6649.027 [a]	6649.046	[25]	2	6	20115.016	7	5079.375
6656.823	6656.827	[25]	25	8	29723.998	9	14705.965
6673.405	6673.409	[25]	10	7	28009.828	8	13029.112
6673.769	6673.774	[25]	15	6	26398.569	7	11418.672
6690.511 [a]	6690.473	[25]	2	4	22686.710	3	7744.295
6812.869 [a]	6812.870	[25]	6	7	18077.281	6	3403.226
6814.040 [a]	6814.055	[25]	2	6	24835.064	6	10163.531
6827.599 [a]	6827.595	[25]	8	8	19721.768	7	5079.375
6830.499 [a]	6830.502	[25]	7	7	28009.828	8	13373.648
6846.935 [a]		This work	3	5	25330.823	6	10729.778
6850.277	6850.253	[25]	6	6	16243.010	6	1649.088

Improved wavelength λ_{air} / Å	Previous wavelength λ_{air} / Å	Ref. to column 2	SNR	Even level		Odd level	
				J	Energy / cm^{-1}	*J*	Energy / cm^{-1}
6900.284[a]	6900.274	[25]	28	5	23616.903	4	9128.741
6910.428[a]		This work	10	5	14908.952	5	442.060
6948.016[a]		This work	11	7	17387.039	7	2998.412
6970.922[a]		This work	14	7	15990.436	6	1649.088
7114.857[a]	7114.859	[25]	15	5	14493.281	5	442.060
7153.784[a]	7153.735	[25]	5	6	14416.824	5	442.060
7167.752[a]	7167.758	[25]	3	6	23977.880	7	10030.351
7208.839	7208.845	[25]	4	7	23898.387	7	10030.351
7227.693[a]	7227.700	[25]	6	7	26860.974	8	13029.112
7285.714[a]	7285.721	[25]	5	7	17124.934	6	3403.226
7287.817[a]		This work	4	4	21462.045	3	7744.295
7318.506[a]	7318.468	[25]	20	4	14102.284	5	442.060
7396.052[a]	7396.032	[25]	6	5	15166.091	6	1649.088
7497.111[a]	7497.066	[25]	2	6	13776.859	5	442.060
7541.008	7541.011	[25]	6	3	13257.176	4	0
7548.169[a]	7548.163	[25]	4	6	16243.010	7	2998.412
7633.366	7633.351	[25]	4	5	14745.863	6	1649.088
7645.656[a]	7645.668	[25]	9	8	27781.688	9	14705.965
7675.966[a]	7675.964	[25]	3	6	16022.502	7	2998.412
7681.251	7681.261	[25]	4	4	13457.190	5	442.060
7691.428[a]	7691.442	[25]	3	7	18077.281	7	5079.375
7714.737[a]	7714.745	[25]	6	5	14607.726	6	1649.088
7806.572[a]	7806.527	[25]	5	4	13248.256	5	442.060
7811.527[a]	7811.542	[25]	3	7	17235.249	8	4437.176
7841.261[a]	7841.287	[25]	6	5	14493.281	5	1743.737
7888.567[a]	7888.583	[25]	4	6	14416.824	5	1743.737
7942.387[a]	7942.399	[25]	5	7	15990.436	6	3403.226
7970.219		This work	13	5	21131.306	5	33674.569
8046.564[a]	8046.607	[25]	3	4	14167.985	5	1743.737
8059.669[a]	8059.673	[25]	5	8	17483.420	7	5079.375
8088.760	8088.766	[25]	2	8	23970.489	8	11611.054
8089.343[a]	8089.359	[25]	2	4	14102.284	5	1743.737
8094.065[a]	8094.086	[25]	2	5	14095.072	5	1743.737
8122.785	8122.794	[25]	6	7	17387.039	7	5079.375
8269.533[a]	8269.547	[25]	2	6	20554.360	6	8465.102

Improved wavelength λ_{air} / Å	Previous wavelength λ_{air} / Å	Ref. to column 2	SNR	Even level		Odd level	
				J	Energy / cm^{-1}	*J*	Energy / cm^{-1}
8299.533 [a]	8299.554	[25]	2	7	17124.934	7	5079.375
8308.112	8308.137	[25]	3	6	13776.859	5	1743.737
8324.936 [a]	8324.901	[25]	3	5	12450.863	5	442.060
8476.985 [a]	8476.968	[25]	2	8	14791.817	7	2998.412
8528.028	8528.050	[25]	3	6	23141.491	7	11418.672
8602.489 [a]	8602.525	[25]	6	6	13365.087	5	1743.737
8653.189 [a]	8653.205	[25]	3	7	15990.436	8	4437.176
8714.584	8714.590	[25]	13	5	18910.166	5	7438.301
8943.090 [a]	8943.094	[25]	4	7	22184.306	7	11005.557
9044.518 [a]	9044.541	[25]	3	6	22472.061	7	11418.672
9055.262 [a]	9055.299	[25]	4	4	12784.009	5	1743.737
9115.118	9115.119	[25]	4	5	21131.306	6	10163.531
9168.509 [a]	9168.522	[25]	10	7	14307.131	6	3403.226
9219.338 [a]	9219.404	[25]	14	3	10843.790	4	0
9221.610	9221.546	[25]	8	6	11283.178	5	442.060
9243.199	9243.178	[25]	3	4	11257.857	5	442.060
9387.096 [a]	9387.106	[25]	2	7	15087.176	8	4437.176
9434.185 [a]	9434.192	[25]	6	8	23970.489	8	13373.648
9571.272	9571.291	[25]	7	5	18910.166	6	8465.102
9650.056	9650.007	[25]	6	5	10801.853	5	442.060
9817.275 [a]	9817.328	[25]	8	5	11927.071	5	1743.737
9912.150 [a]	9912.149	[25]	7	6	13084.274	7	2998.412
9972.847	9972.868	[25]	8	4	10466.538	5	442.060

[a] The hyperfine structure appeared in a blend with other Pr I or Pr II transitions, nevertheless, the hyperfine structure could easily be identified.

Table 6.4. Odd energy levels of Pr II not corrected in this work [6].

J values	Energy / cm^{-1}	*A* / MHz	*B* / MHz	Ref.
1	9164.17	-1880.8(30)	9(4)	[51]
2	9450.75	2842.1(20)	-21(10)	[51]
4	10043.06	-341.2(20)	90(30)	[51]
3	10082.54	2203.4(15)	-24(10)	[51]
5	10088.45	1922.0(30)	-290(70)	[51]
2	10431.09	-225.0(30)	-5(3)	[51]
4	10749.38	1849.7(25)	21(10)	[51]
3	10769.48	1161.7(25)	-72(30)	[52]
3	11252.69	-551.4(30)	8(5)	[51]
5	11613.02	1718.7(20)	64(25)	[51]
4	12160.30	-593.4(30)	12(6)	[51]
4	12431.39	855.2(15)	-49(30)	[52]
6	12444.93	1568.3(15)	61(15)	[51]
5	12651.51	-399.8(20)	-37(15)	[51]
5	14157.81	688.0(30)	-66(35)	[52]
3	14287.73	1647.3(30)	-62(20)	[51]
3	14339.95	1485.4(30)	-29(12)	[51]
2	14548.71	957.1(30)	28(15)	[51]
4	15042.10	592.0(30)	-21(12)	[51]
3	15215.98	648.7(30)	-176(50)	[51]
5	15243.94	758.3(30)	-80(30)	[51]
6	15433.26	652.5(30)	-135(50)	[51]
6	15631.29	-118.6(20)	6(4)	[51]
7	15839.97	1569.3(15)	-122(40)	[51]
5	15971.14	474.8(30)	57(20)	[51]
6	16496.00	616.5(20)	57(20)	[51]
6	16684.71	391.3(20)	-8(5)	[51]
7	16946.80	462.4(30)	170(60)	[51]
7	17747.07	316.4(30)	-24(15)	[51]
6	17955.82	539.2(30)	20(10)	[51]
8	21039.46	729.5(30)	5(4)	[51]
7	30977.671	440	-	[41]
5	34124.85	709	-	[41]
5	34600.34	632	-	[41]
6	35519.89	664	-	[41]

J values	Energy / cm^{-1}	A / MHz	B / MHz	Ref.
6	36142.62	646	-	[41]
6	36404.14	738	-	[41]
6	36742.09	830	-	[41]
4	37110.44	959	-	[41]
6	37128.87	646	-	[41]
7	37388.50	879	-	[41]
5	37612.64	491	-	[41]
7	37747.30	640	-	[41]
8	37873.15	480	-	[41]
8	37926.40	705	-	[41]
9	37987.89	568	-	[41]
7	38199.90	512	-	[41]
8	38248.70	473	-	[41]
6	38358.86	692	-	[41]
7	38670.17	608	-	[41]
9	38790.18	480	-	[41]
8	39676.86	529	-	[41]
9	39723.28	442	-	[41]
7	39788.91	560	-	[41]
8	40249.97	617	-	[41]
7	40348.30	720	-	[41]
10	40420.52	497	-	[41]
8	40799.59	494	-	[41]
7	41015.57	560	-	[41]
7	41512.62	640	-	[41]
9	42194.03	473	-	[41]

Table 6.5. Even energy levels of Pr II not corrected in this work [6].

J values	Energy / cm^{-1}	*A* / MHz	*B* / MHz	Ref.
3	9333.93	1329(190)	-	[41]
3	10289.48	2114(9)	-	[41]
9	10570.64	442(32)	-	[41]
7	10650.24	1147(40)	-	[41]
4	11054.70	1249(7)	-	[41]
6	11088.78	412(5)	-	[41]
8	11310.17	451(7)	-	[41]
7	11694.14	1375(8)	-	[41]
4	11943.32	240(7)	-	[41]
6	12076.31	185(5)	-	[41]
10	12301.21	337(11)	-	[41]
8	12545.20	946(7)	-	[41]
7	12916.25	403(4)	-	[41]
8	13021.33	623(4)	-	[41]
5	13094.30	491(11)	-	[41]
7	13122.55	197(4)	-	[41]
6	13216.22	942(5)	-	[41]
5	13238.44	-104(22)	-	[41]
8	13448.40	959(4)	-	[41]
9	13639.13	385(3)	-	[41]
4	13700.50	1093(7)	-	[41]
3	13766.34	747(9)	-	[41]
4	13858.47	573(67)	-	[41]
7	14035.46	682(4)	-	[41]
7	14198.60	749(4)	-	[41]
9	14330.52	1177(6)	-	[41]
4	14398.60	710(13)	-	[41]
7	14810.95	384(8)	-	[41]
5	15500.00	218(11)	-	[41]
8	15503.15	308	-	[41]
6	15937.73	1015(46)	-	[41]
8	16464.33	441(14)	-	[41]
6	16638.96	480(18)	-	[41]
4	18470.25	680(7)	-	[41]
2	21521.535	1373	-	[41]

J values	Energy / cm^{-1}	*A* / MHz	*B* / MHz	Ref.
6	30011.9	891	-	[41]
2	31906.76	1362.5(20)	6(4)	[52]
3	32705.54	843.5(20)	71(20)	[51]
5	32911.53	1057.4(20)	-73(15)	[51]
4	33445.97	669.7(20)	-98(30)	[51]
4	33603.18	637.8(20)	13(8)	[51]
4	34139.31	366.0(20)	5(8)	[51]
5	34545.57	565.3(20)	-1(2)	[51]
6	34579.99	661.6(20)	10(5)	[51]
5	35087.04	667.2(40)	17(10)	[51]
6	35722.94	559.4(25)	5(5)	[51]
6	36103.62	471.5(20)	10(7)	[51]
6	36290.53	579.9(25)	10(5)	[51]
7	38434.63	843.8(30)	15(10)	[51]
6	38861.07	690.8(30)	-5(5)	[51]

7 INTER-MODULATED LASER INDUCED FLUORESCENCE SPECTROSCOPY

An elaborated discussion on one of the Doppler reduced spectroscopic techniques, i.e. the saturation spectroscopy, was given in chapter 5. This chapter is devoted to the experimental investigations of the hyperfine spectrum of singly ionized praseodymium using saturation spectroscopy. The method is commonly called as the inter-modulated laser induced fluorescence saturation spectroscopy or Lamb dip spectroscopy. Two counter-propagating laser beams are derived from a single laser source, which interact simultaneously with zero velocity group of atoms/molecules. The pump laser beam burns a hole in the Maxwell distribution curve of the lower level and when the probe laser beam come across this hole, a Lamb dip is observed in the absorption spectrum. The laser beam is split into pump and probe beams of almost equal intensities in order to get better signal to noise ratio. The pump laser beam and probe laser beam are chopped at different frequencies f_1 and f_2, respectively. The fluorescence signal is detected by a lock-in amplifier at a modulation frequency f_1+f_2. Using this technique a spectral line width up to 200 MHz is achieved, much smaller than the Doppler width of ca. 800 MHz.

7.1 Experimental setup

To employ this method, the excitation source used is a CW-ring dye laser pumped by a solid state diode-pumped, frequency doubled Nd:Vanadate Nd:YVO_4 Verdi V-18 or by an Argon ion laser. To work in the desired wavelength region, the dye Rhodamine 6G is used as a lasing medium.

A hollow cathode discharge lamp is used as a light source. A hollow cylinder made up of praseodymium (inner diameter 3 mm and length 19 mm) is fitted inside a hollow copper cathode. The anodes made of aluminum are mounted on both sides of the cathode (figure 7.1). Ceramic holders are used to avoid any contact between the cathode and the anodes. The distance between anode and cathode is ~ 0.75 mm. This coaxial assembly of anodes, cathode and ceramic parts is mounted inside a glass tube (for details see ref. [115, 116]). The hollow cathode lamp is filled with argon as a working gas of the discharge. To perform saturation spectroscopy of Pr II, it is observed that the signal is sufficiently improved if the pressure of the gas is maintained between 0.015 to 0.2 mbar. The discharge current is about 60 mA. Argon gas is ionized, accelerated and hit the cathode, thus causing sputtering of the cathode material, i.e. Pr atoms. Due to the collisions between sputtered Pr atoms and argon gas, a Pr-Ar plasma is produced. In such kind of a light source, the atoms and the ions are produced not only in the ground state but also in their higher excited states. Therefore, numerous Ar I, Ar II, Pr I and Pr II spectral lines are observed. The typical Doppler broadening in the hollow cathode discharge lamp is of the order of 1000 MHz. In order to reduce the Doppler broadening, the hollow cathode lamp is cooled by the liquid nitrogen and a typical width of 600 MHz is observed.

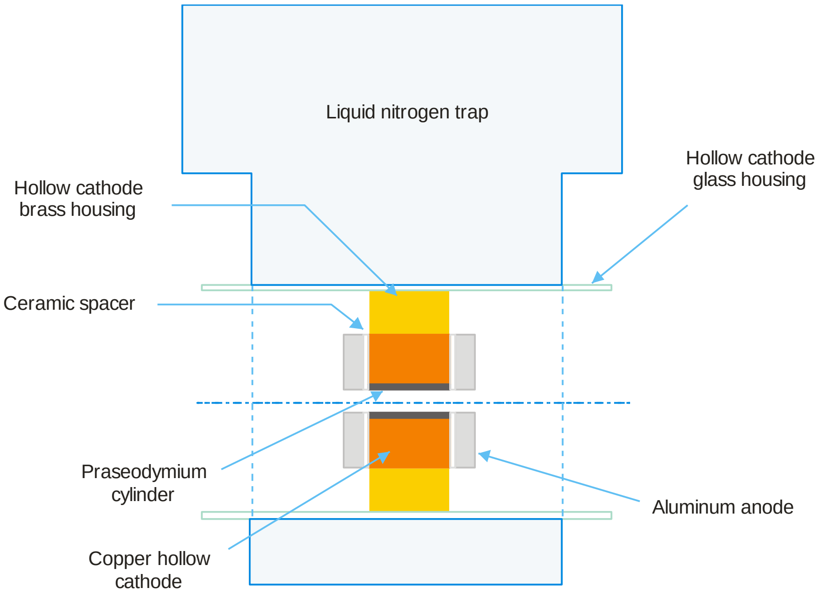

Figure 7.1. A Schematic diagram of a hollow cathode discharge lamp.

The experimental setup used for saturation spectroscopy is shown in figure 7.2. A single mode CW laser beam is produced using a ring dye laser (Coherent 899-21) pumped by an Argon ion laser. The laser beam falls on a beam splitter BS1which splits the beam into two parts. One beam (relatively weaker one) is further split into three parts using beam splitters BS2 and BS3. One part is reflected by mirror M2 into a wave meter. The second part goes to a spectrum analyzer and the third part is reflected by mirror M3 into a marker etalon. A temperature stabilized Fabry-Perot interferometer is used to produce equidistant frequency markers.

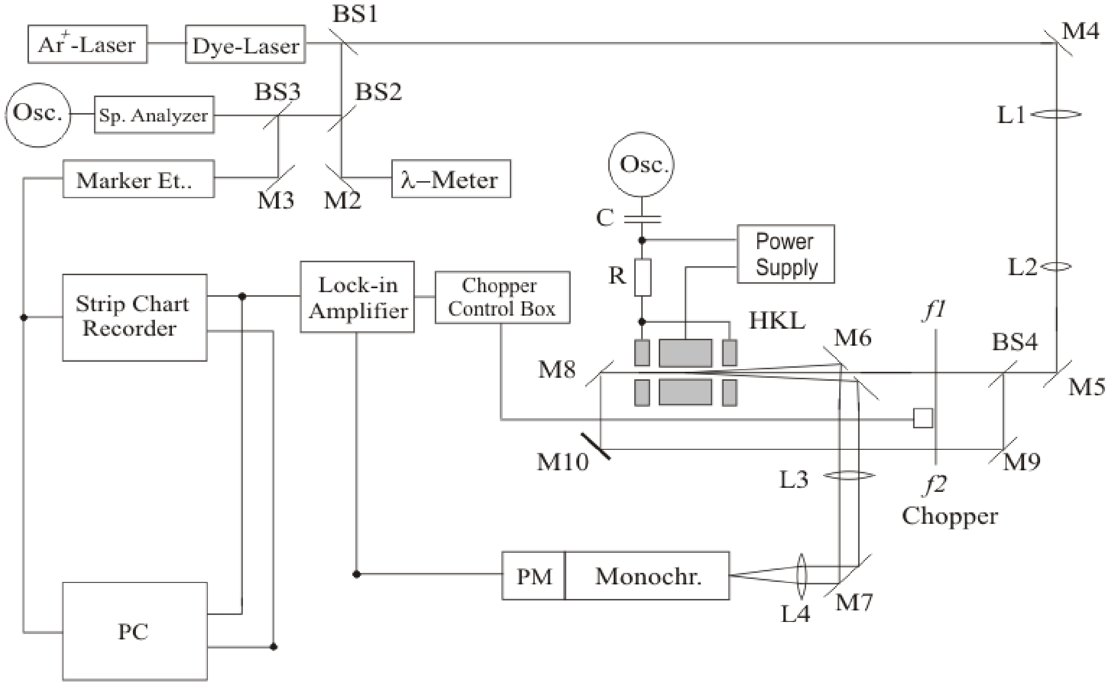

Figure 7.2: Experimental setup used for inter-modulated laser induced fluorescence spectroscopy. HKL: hollow cathode lamp, M1…… M10: mirrors, BS1… BS4: beam splitters, L1…L4: lenses, Osc.: oscilloscope, C:capacitor, R: resistance, PM: photomultiplier tube, PC: computer.

The main laser beam from the BS1 falls on mirror M4 and is then passed through a telescope arrangement of lenses L1 and L2 which collimates the laser beam. The telescope is used to: 1) reduce the divergence of the laser beam and 2) make sure that the Ar-Pr cloud inside the hollow cathode is irradiated uniformly. After passing through the telescope, the laser beam falls on mirror M5. The beam splitter BS4 is used to split the laser beam into two equal intensity pump and probe beams. The pump beam is chopped with a frequency f_1 and the probe beam chopped with a frequency f_2 using a mechanical chopper. The pump beam passes directly into the hollow cathode lamp whereas the probe beam is guided into the hollow cathode from opposite directions using a configuration of mirrors M9, M10 and M8.

The two laser beams (pump and probe) interact with the plasma and excite the atoms/ions from a lower energy level to a higher energy level if the laser frequency exactly matches the difference of the levels energies, i.e. $\Delta E = h\nu$. The laser induced fluorescence (LIF) is emitted when the excited level decays to a lower level. This LIF signal is reflected by mirror M6 and with the combination of lens L3, mirror M7 and lens L4 led to a grating monochromator of 0.5 m focal length and 1200 lines/mm (JOBIN YVON HRS2). A monochromator plays an important role in the LIF spectroscopy because the fluorescence lines corresponding to different upper levels can easily be identified. For the detection of fluorescence light a photomultiplier tube (Hamamatsu R955) is used at the exit slit of the monochromator. The signal from the photomultiplier tube is fed into a phase sensitive lock-in amplifier. The sum of the chopping frequencies is used as a reference frequency of the lock-in amplifier. The signals from the lock-in amplifier and from the marker etalon are simultaneously recorded on a strip chart recorder as well as on a computer for further analysis.

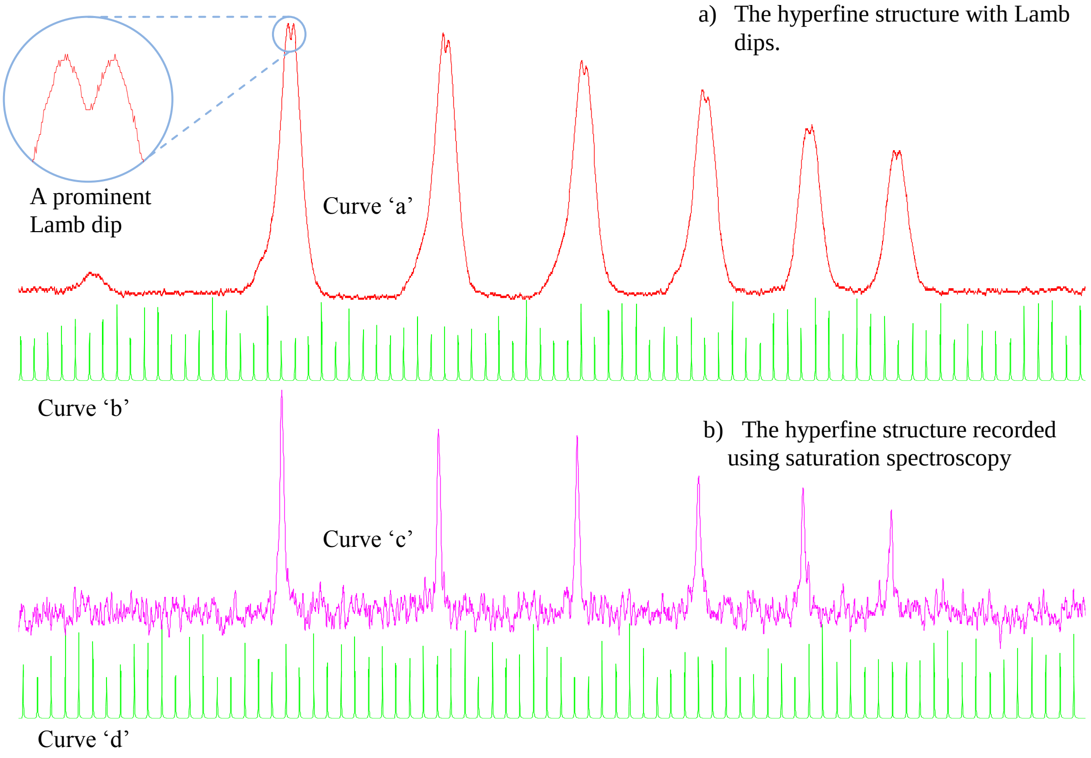

Figure 7.3. The hyperfine structre of the Pr I transition at 5841.025 Å. The levels involved in the transition are $10168.95^{\circ}_{15/2} \rightarrow 27784.489_{17/2}$.

a) Lamb dips are observed at the center of each diagonal component when pump and probe laser beams are chopped with same frequency. b) The Doppler broadend background is eliminated when pump and probe laser beams are chopped with different frequencies and only the Lamb dips are recorded.

In order to investigate the hyperfine structure using saturation spectroscopy a high laser power is required. In this work, laser power between 300 - 700 mW (measured at the output coupler (OPC) of the ring dye laser), is used to saturate the zero velocity group (ions moving perpendicular to the laser beams). Then the Ar-Pr plasma is irradiated by pump and probe laser beams from opposite directions. The pump laser beam saturates the zero velocity group and the probe laser beam is used to detect the Lamb dips. If both beams are chopped with the same frequency, Lamb dips are observed at the centers of the Doppler broadened hyperfine components as shown in figure 7.3a.

If both laser beams are chopped with different frequencies and the fluorescence signal is monitored through the lock-in amplifier tuned at sum frequency $f_1 + f_2$ (or $f_1 - f_2$) the Doppler broadened background is suppressed and saturation signals (Lamb dips) are recorded (figure 7.3b). A rotating disc with two rows of a different number of holes is used to chop the two laser beams, which interrupted the laser beams at $f_1 = 92$ Hz and $f_2 = 138$ Hz.

To find suitable fluorescence line, the laser frequency is tuned to the strongest hyperfine component and then the fluorescence signals are searched by scanning the transmission wavelengths of the monochromator. Then a fluorescence line with a strong LIF signal is selected and the laser frequency is scanned over the entire width of the hyperfine structure to record the Lamb dips.

The Doppler limited hyperfine structures of some transitions are also investigated, which are recorded by chopping the intensity of both laser beams with the same frequency (or by just removing the beam splitter BS4). The Doppler limited measurements of hyperfine constants are compared with the CLIBS measurements in chapter 10.

In case of saturation spectroscopy, the Doppler width is reduced to almost 1/3 to that of Doppler limited spectroscopy: Therefore, the laser frequency is scanned with a slower speed. Usually the entire hyperfine structure (~ 15 GHz) is recorded in 25 × 25 sec. It is observed that the quality of the signal is improved if the time constant of the lock-in amplifier is increased to 100 msec.

For precise measurements of the hyperfine constants, the frequency distances between different hyperfine components must be accurately known. This is done by the marker etalon having a spectral range (FSR) of 367.33 MHz. The equidistance markers are also plotted parallel to the hyperfine structure (b and d curves figure 7.2).

For further analysis the programs “data viewer” and “fitter” (discussed in section 6.3) are used. The “data viewer” is used to view the recorded hyperfine structures. This program also creates the input “mess” file for the fitter program. The hyperfine structure is recorded as a function of equal time intervals. Since the frequency is not varying linearly with the time, the intensity distribution of the spectrum cannot be recorded as function of equidistant frequency spacing. To overcome this problem a linearization process is employed which converts the intensity distribution $I(\mathrm{t})$ into the intensity distribution $I(\nu)$ (intensity as a function of frequency ν) using the equal frequency marker etalon signal which is simultaneously recorded with the LIF signals. The process of linearization is performed by supplying the start wavelength of laser scan and the FSR of the marker etalon along with the measured data file to the fitting program. Finally, the hyperfine constants and the center of gravity of the hyperfine structure are determined using a least square curve fitting (section 6.3).

7.2 The hyperfine structures of Pr II lines recorded using saturation spectroscopy

Few examples of hyperfine structures of Pr lines are discussed here and some more results are compared with the CLIBS measurements in chapter 10. In the following examples, the red curve (curve ‘a’) presents the Doppler broadened hyperfine structure and the violet curve (curve ‘b’) presents the Doppler reduced hyperfine structure of the same line, recorded using saturation spectroscopy *⁾.

*⁾ This work is done by the author and N. Anjum and is partially published [117].

7.2.1 The hyperfine structure of the line 5785.28 Å

The hyperfine structure of the transition at 5785.28 Å is shown in figure 7.4. The transition is taking place from the upper levels 28049.987_4 to the lower level 10769.537°_3. The transmission wavelength of the monochromator is set at 3800 Å (the strongest LIF signal). The line width is reduced from 675 MHz to 210 MHz using saturation spectroscopy. Laser power used to observe the saturation effects for this transition was 550 mW and the pressure of the Ar gas was maintained at 0.2 mbar.

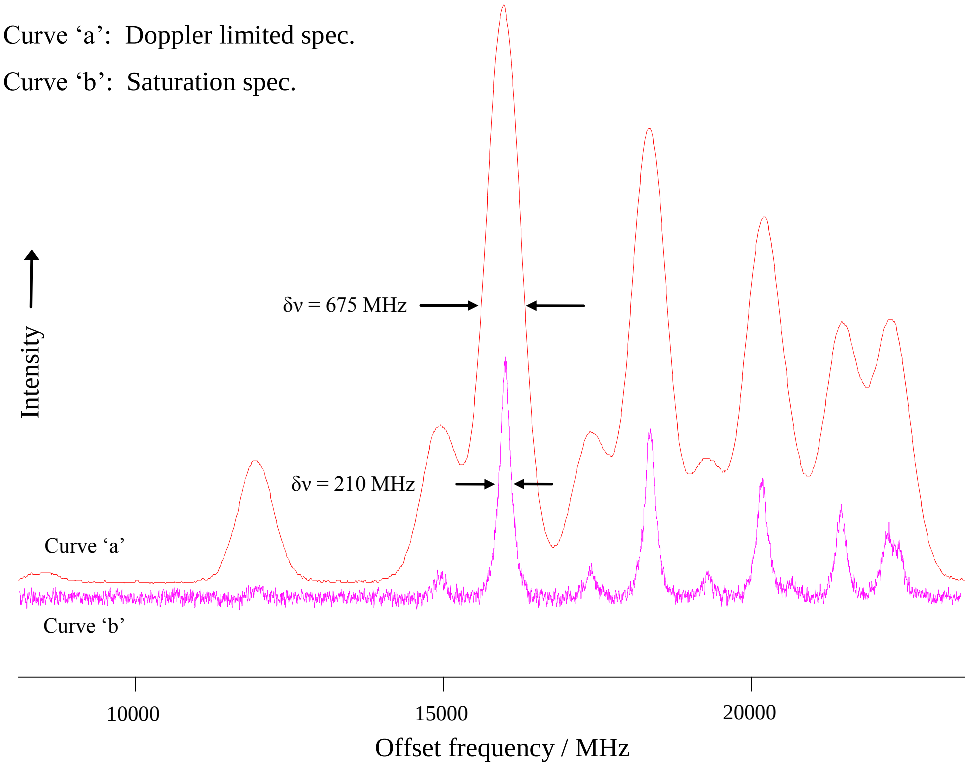

Figure 7.4: The hyperfine structure of the Pr II line 5785.28 Å.

7.2.2 The hyperfine structure of the line 5823.73 Å

The hyperfine structure of the transition at 5823.73 Å is shown in figure 7.5. The transition is taking place from the upper levels 18910.166_5 to the lower level $1743.737°_5$. The hyperfine structure is recorded at the strongest LIF signal 5412 Å. Laser power used to record the Doppler reduced hyperfine structure was 550 mW and the pressure of the Ar gas was 0.2 mbar. A relatively large Doppler width i.e. 350 MHz is obtained for this transition.

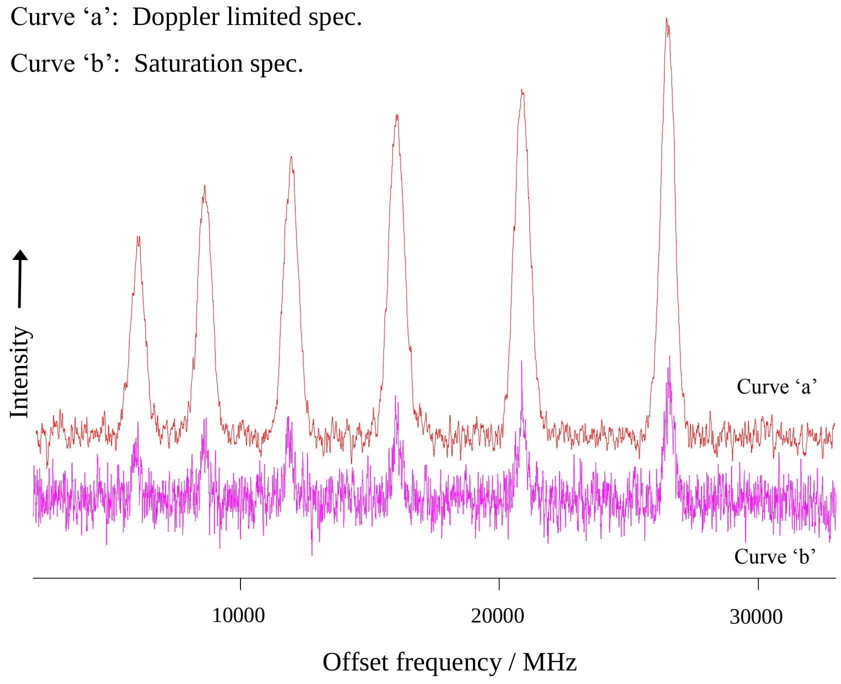

Figure 7.5: The hyperfine structure of the Pr II line 5823.73 Å.

7.2.3 The hyperfine structure of the line 5786.17 Å

In figure 7.6 the hyperfine structure of the transition at 5786.17 Å is shown. The transition is taking place from the upper level 24716.093_5 to the lower level 7348.301°_5. The hyperfine structure is recorded at the strongest LIF signal 4118 Å. Laser power used to record the hyperfine structure of this line was 680 mW and the pressure of the Ar gas was 0.2 mbar. Using Doppler limited spectroscopy, most of the hyperfine components are not resolved for this transition. In case of saturation spectroscopic measurement, the diagonal (or strong) hyperfine components are still unresolved. The off diagonal (or weak) components are resolved and their intensities are about 60% less than the theoretical intensities, even some of the off diagonal components disappear in the noise. In such cases, the hyperfine constants cannot be determined accurately.

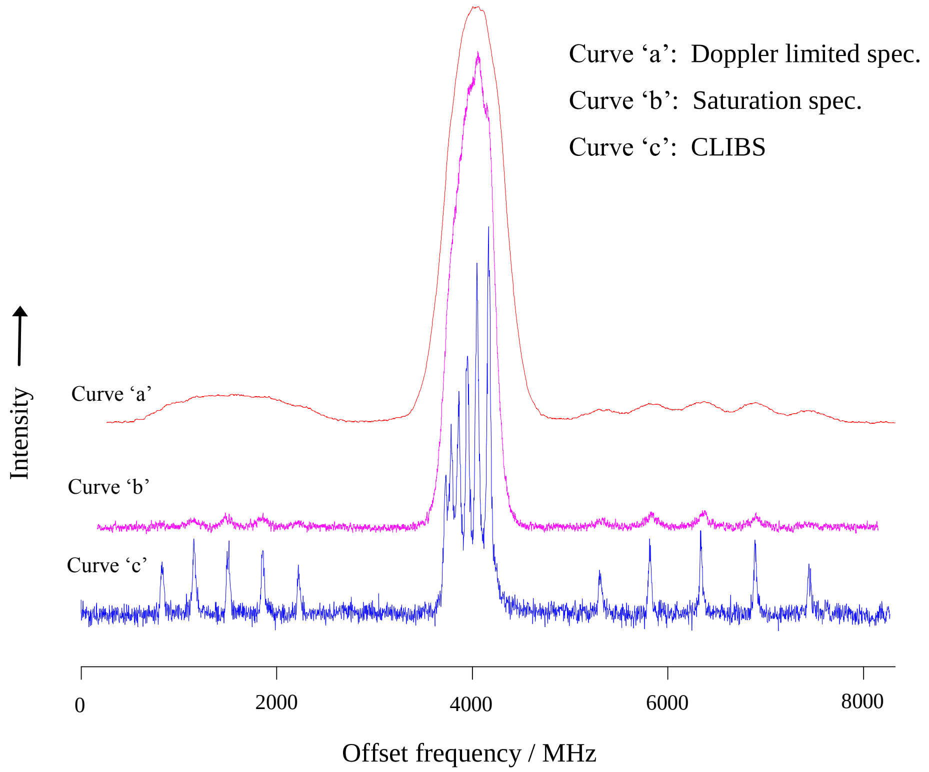

Figure 7.6: The hyperfine structure of the line 5786.17 Å [117].

The blue curve (curve ‘c’) in figure 7.6 shows a well resolved hyperfine structure of the same line. This structure is recorded using a high resolution method of spectroscopy known as Collinear Laser Ion Beam Spectroscopy (CLIBS). Using this method a line width of ca. 40-80 MHz can be obtained and the hyperfine constants can be determined with accuracy of 1 MHz or even better, much better than other commonly used spectroscopic methods. For this particular hyperfine structure, the observed line width is 60 MHz and all of the 16 hyperfine components are completely resolved. The hyperfine constants determined using different techniques are compared in table 7.1.

Table 7.1: Hyperfine constants measured using different methods.

Excitation wavelength (air) / Å	Energy of the levels / cm^{-1}	Method used					
		Doppler limited spectroscopy		Saturation spectroscopy		CLIBS	
		A / MHz	*B* / MHz	*A* / MHz	*B* / MHz	*A* / MHz	*B* / MHz
5823.73	1743.737°_{5}	-47(3)		-46 (5)		-44.3(9) [48]	
	18910.166_{5}	704(3)		704 (5)			
5785.28	10769.537°_{3}	1171(3)	-8(5)	1169(3)	-20(18)		
	28049.987_{4}	626(3)	10(5)	623(3)	10(8)		
5786.17	7348.301°_{5}	710(6)		706(2)	50(30)	704.2(2)	26(4)
	24716.093_{5}	740(6)		730(2)	40(30)	730.1(3)	18(6)

Discussion:

It is clear from figures 7.4 – 7.6 that the line width is significantly reduced i.e. from 650 MHz to 200 MHz, using the inter-modulated laser induced fluorescence spectroscopy. Using saturation spectroscopy, the diagonal components could be recorded but the weak components are not so prominent in the recordings. Most of the times, intensity of the weaker components is recorded about 60% less than the theoretical values and sometimes they are even not observed. For example, in figure 7.4 four weak components of ΔF = -1 group are not visible and in figure 7.5, only the diagonal components are observed (the weak components coincide with the diagonal components, therefore are not prominent in the curve ‘á’ also). In figure 7.6, the weak components are observed but with the intensity only 14-26 % of the theoretical values.

For the above three examples, the hyperfine constants are determined using different methods and are compared in Table 7.1. The results obtained by saturation spectroscopy still have large deviation in the hyperfine constants due to the diminishing of weak components which play an important role in the accurate determination of the *A* and *B* values. This is due to the nonlinear saturation effects, saturation effect is larger for diagonal components and lesser for off diagonal components. This effect is most commonly observed if a high laser power is used in the laser induced florescence spectroscopy, then the weak components have relatively larger intensity than the theoretical values (as can be seen clearly in figures 7.4 and 7.6. The weak components have almost doubled intensity than the calculated one). Actually the diagonal components have less signals due to the strong optical pumping and weak components exhibit the theoretical values of intensities. In the case of saturation spectroscopy the line width is limited by the saturation broadening (section 4.3).

Some experimental difficulties are also associated with saturation spectroscopy. A constant high output laser power is required, which is not feasible to run the dye lasers for longer period of time. When a dye laser is operated at a high lasing power, the optical components become warm, which can cause mode hoping, hence it is difficult to record the spectrum. Moreover, not all the laser dyes have high efficiency nor they have a long lasing lifetime.

The major application of this method is the stabilization of laser frequency. The steep zero crossing of the third derivation of the lamb dip gives a good reference for the stabilization of the laser frequency onto an atomic/ionic transition and drift in laser frequency can be avoided. The laser frequency can be locked within 1/3 of the natural line width. As for an example, using intra-cavity saturation spectroscopy (in this method the absorbing sample is placed inside the resonator of a tunable laser), Lamb dips of a vibration-rotation transition of CH_4 at 3.39 μm or of CO_2 around 10 μm are used for the frequency stabilization of the He-Ne laser at 3.39 μm or CO_2 laser. Using Lamb dips, stability in laser frequency of better than 1 Hz is reported [118, 119].

CLIBS is most commonly used for accurate measurements of hyperfine constants of ionic levels. Using this method the hyperfine constants (especially *A*-factors) can be measured with accuracy of 1 MHz or even better. In next chapters, the experiment set up and measurements of CLIBS are discussed.

8 COLLINEAR LASER ION BEAM SPECTROSCOPY (CLIBS)

Collinear Laser ion Beam Spectroscopy (CLIBS) is known as a high resolution spectroscopic method in atomic physics. CLIBS provides a resolution improved by a factor of 10-20 compared to Doppler broadened emission lines from a hollow cathode lamp. Using this technique well resolved hyperfine structures (FWHM ~ 60 MHz) are obtained which enable to determine the hyperfine constants and isotopic shifts of spectral lines of different isotopes very precisely which lead to the information on the nuclear spin, magnetic moments and electric quadrupole moments and nuclear deformation. Another important application of CLIBS is high resolution spectroscopy of short living radioactive isotopes. Isotopes having a half life time in the millisecond range can be investigated. High resolution spectroscopic measurements of fast atoms can be performed by neutralizing the ions using an alkali-vapor cell in the CLIBS setup.

8.1 Principle of CLIBS

The main idea of CLIBS is to reduce the velocity spread of the ions in order to get rid of a large Doppler broadening. This can be done by increasing the velocity of the ions, to a velocity much larger compared with the thermal velocity, by applying an accelerating potential. After being accelerated, the ions are mass separated and interact collinearly with the excitation light. The working of CLIBS can be divided into three stages. First, the ions are produced in an ion source and due to thermal collisions low lying metastable states are populated. The velocity spread in ions velocity is reduced by applying a high acceleration voltage. In the second stage, a pure ion beam of a single isotope is selected using a mass separator e.g. an 80˚ or 90˚ sector magnet. Finally, the ion beam is superposed collinearly with the laser beam and the hyperfine structure is studied by detecting the fluorescence light.

8.1.1 Acceleration cooling

In 1976, Kaufman [62] and Wing et al. [63] independently proposed an arrangement to narrowing the longitudinal velocity distribution of fast ions using an acceleration potential. This phenomenon is known as acceleration cooling or velocity bunching effect.

Let us consider two ions each of mass *M* and charge *e*, starting from an ion source with initial velocities (thermal velocities) u_{th1} and u_{th2}. After being accelerated by the acceleration potential *U*, their kinetic energies become

$$\frac{1}{2}M{u_1}^2 = \frac{1}{2}Mu_{th1}^2 + eU$$

$$\frac{1}{2}M{u_2}^2 = \frac{1}{2}Mu_{th2}^2 + eU \quad .$$

Comparing these two equations, we get

$$\Delta u_D = \frac{u_{th}}{u}\Delta u_{th}$$

where

$$\Delta u_D = u_2 - u_1 \quad , \quad \Delta u_{th} = u_{th2} - u_{th1}$$

$$u = \frac{1}{2}(u_2 + u_1)$$

and

$$u_{th} = \frac{1}{2}[u_{th2} + u_{th1}] \quad .$$

The kinetic energy gained by the ions in the electric field is given by

$$\frac{1}{2}Mu^2 = eU$$

therefore

$$u = \sqrt{2eU/M} \quad . \tag{8.1}$$

The initial thermal velocity can be calculated from the initial thermal energy

$$E_{th} = \frac{1}{2} M u_{th}^2 \quad \Rightarrow \quad u_{th} = \sqrt{2E_{th}/M}$$

so, the spread in final velocity becomes

$$\Delta u_D = \Delta u_{th} \sqrt{E_{th}/eU} \quad . \tag{8.2}$$

In terms of frequency the above equation can be written as

$$\Delta\nu_D = \Delta\nu_{th} \sqrt{E_{th}/eU} \quad .$$

Equation 8.2 gives $\Delta u_D = R \Delta u_{th}$ or $\Delta\nu_D = R \Delta\nu_{th}$

where $R = \sqrt{E_{th}/eU}$ is known as Doppler width reduction factor.
Since $E_{th} = k_B T$ (k_B is the Boltzmann constant);

To calculate Δu_{th}, minimum value of u_{th} i.e. $u_{th2} = -u_{th}$ and $u_{th2} = u_{th}$ therefore

$$\Delta u_{th} = 2 \sqrt{k_B T / M \, ({}^{kg}/_{J})}$$

A calculation for praseodymium (M = 141) gives:

at U = 20 keV, T = 3000 ˚C and λ = 6000 Å

E_{th} = 0.1 eV

$R = 2\times10^{-3}$

Δu_{th} = 1212 m/s

$\Delta\nu_{th}$ = 1740 MHz (using equation 4.2)

Δu_D = 2.4 m/s

$\Delta\nu_D$ = 3.5 MHz

The Doppler width of the ions in the ion source has been reduced by a factor of 500 using acceleration cooling (demonstrated in figure 8.1).

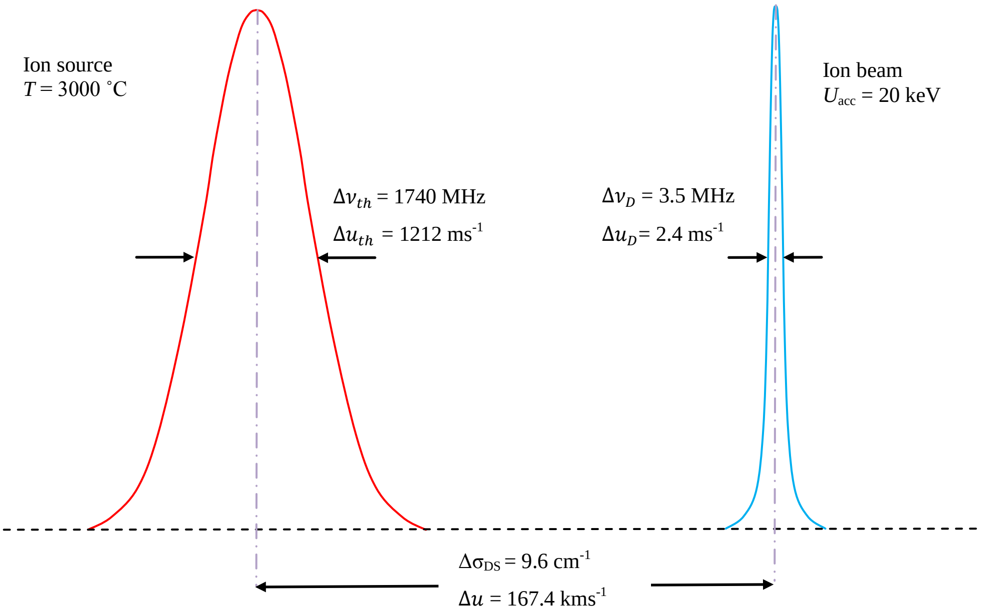

Figure 8.1: Compression of the Doppler broadening and velocity spread in the collinear laser ion beam spectroscopy in the spectral line 6000 Å of Pr II (the figure is not to scale).

A graph showing the dependency of the ion velocity and the acceleration potential (equation 8.1) is plotted in figure 8.2. It can be seen that at a high kinetic energy the velocity spread is significantly reduced and all ions have almost uniform velocity, giving rise to the reduction of the Doppler width of the spectral lines. This reduction of the velocity spread results from the fact that the energies and not the velocities are added. For higher acceleration potential, the velocity change is mainly determined by the acceleration voltage and hardly affected by the fluctuations of the initial thermal velocity.

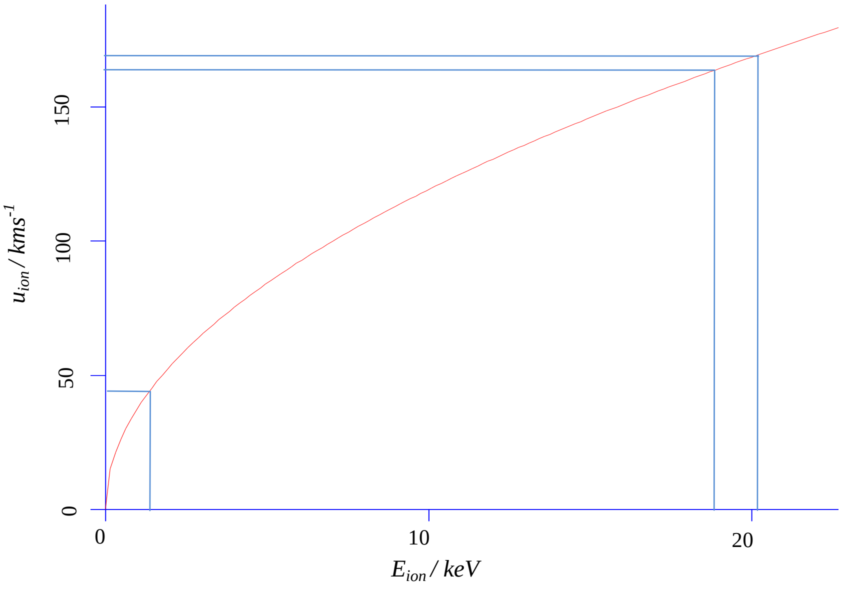

Figure 8.2: Acceleration cooling: The spread in the velocity of the ions reduces for the same energy spans with increasing the velocity.

8.1.2 Mass separator

An electric field or a magnetic field can be used to deflect an ion beam and to separate different isotopes. Electromagnetic separators are most commonly used in CLIBS setups because of their simple designs and high mass resolution. A mass separator is considered as an important part in collinear ion beam spectroscopy due to the following reasons:

- A specific isotope can be selected, so there is no mixing of hyperfine components of other isotopes in the hyperfine spectrum under investigation.
- Using a multichannel CLIBS arrangement, a mass separator provides an opportunity to have simultaneously a reference beam along with the investigated one. Thus, the isotopic shifts in spectral lines of different isotopes can be measured precisely.

8.1.2.1 Principle of an electromagnetic mass separator

In a mass separator, different ions are deflected and separated according to their mass and charge. The force acting on an ion in a magnetic field is given by

$$\vec{F} = e\left(\vec{u} \times \vec{B}\right) \tag{8.3}$$

where e is the charge of the ion, B is the magnetic flux density. The velocity u can be determined from equation 8.1.

In the mass separator considered here, the trajectories are always perpendicular to the direction of the magnetic field. The radius of curvature of the trajectories is given by

$$euB = \frac{Mu^2}{R} \ .$$

Thus for R we get,

$$R = \frac{1}{B}\sqrt{\frac{2UM}{e}} \ . \tag{8.4}$$

From equation 8.4 it is clear that for a given accelerating voltage and magnetic field the different isotopes travel on different circular trajectories according to their masses. In this way the isotopes can be separated using a magnetic field.

8.1.2.2 Dispersion and resolving power

If a is the displacement between the focused ion beams with mass M and $M + \Delta M$ in the image plane, the dispersion (D) is given by the relation

$$D = a\frac{M}{\Delta M} \tag{8.5}$$

If δM is the line width of a mass at mass M of the image, the resolving power (R_p) of a mass separator is given by

$$R_p = \frac{D}{\delta M} = a\frac{M}{\Delta M \delta M} \tag{8.6}$$

So in order to have a high resolution: The dispersion of the magnet should be high. This can be done by increasing the radius of the magnet. Secondly, the width of the line must be small; this can be done by reducing the diameter of the orifice of the ion source (but it will reduce the number of ions in the ion beam).

8.1.3 LIF detection

Finally, the mass separated ion beam is superposed with the laser beam in an interaction chamber as shown in figure 8.3. A transition takes place from a lower metastable state to a higher excited state if the laser frequency matches (in the ion frame of reference) with the energy difference of two energy states i.e. $h\nu = E_2\text{-}E_1$. The excited states have a short life time, usually in the order of nano-seconds, and decay to low energy levels by emitting fluorescence light. The optical spectrum of the hyperfine structure of the ions is investigated by observing the fluorescence light emitted by these excited ions.

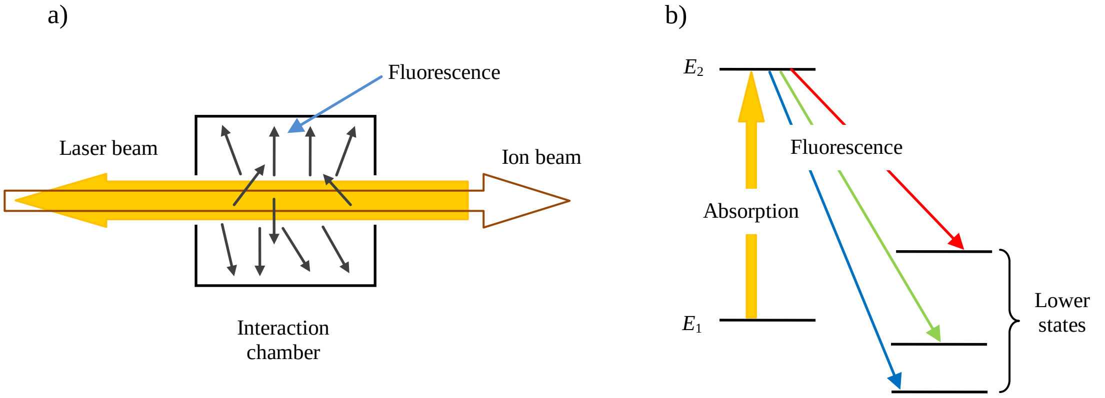

Figure 8.3: a) Superposition of laser beam and ion beam in the interaction chamber. b) Level scheme of an excitation from a lower metastable state E_1 to an excited state E_2 which decays to some lower states emitting fluorescence light.

8.1.3.1 Doppler tuning

An interaction chamber is designed in such a way that the interaction between superposed ion and laser beams takes place in front of the fluorescence light collector (chapter 9). There are two ways to record the hyperfine structure of a transition:

1) The acceleration voltage is kept fixed and the laser frequency is scanned over the entire hyperfine structure.

2) The laser frequency and the acceleration voltage both are fixed while the fluorescence signal is observed by applying a post accelerating (or decelerating) voltage to the interaction chamber. This method is called Doppler tuning (the acceleration voltage U is kept constant as its change influences the beam path and collimation).

In this work the Doppler tuning is employed because in this technique a comparatively simpler electronics is involved. Moreover, it is also convenient to fix the laser frequency; problems like mode hoping can be avoided.

In CLIBS the laser frequency in the rest frame of the moving ions is Doppler shifted relative to the frequency in the laboratory frame of reference. The Doppler shift is given by

$$\Delta\nu_{DS} = \nu_0 \frac{k}{c}\sqrt{\frac{2eU}{M}} \tag{8.7}$$

where k indicates the direction of motion of the laser beam and the ion beam. k is -1 if both beams are superposed parallel to each other otherwise k is +1.

A precise measurement of the hyperfine structure needs the stabilization of the laser frequency and the acceleration voltage. In a ring dye laser system, the laser frequency can be internal locked using a reference cavity, and can be stabilized having a line width jitter within 1 MHz. Nevertheless, there is always a drift in the laser frequency during the operation time. The drift in laser frequency and fluctuations in the acceleration voltage influence the hyperfine measurements. The drift in laser frequency can be overcome by locking the laser frequency externally. For example, the transmission curve of a thermally stabilized Fabry Perot interferometer can used for this purpose, but still fluctuations in the acceleration voltage are unaddressed. In 1987 Hühnermann [120] proposed a very effective laser frequency stabilization technique for CLIBS measurements. In this method, one of the hyperfine components is used for the stabilization of the laser frequency. Using this technique drifts in the laser frequency and fluctuations in the acceleration voltage both can be addressed simultaneously. One more advantage is that a number of recordings of the hyperfine structure can be averaged to improve the signal to noise ratio. This method for the stabilization laser frequency is adopted in this work, and will be discussed in more details in chapter 9.

The LIF signals can be resolved using a monochromator, which is useful for the identification of an unknown level (as discussed in chapter 7). A photomultiplier is used for the detection of LIF signal. The output signal of the photomultiplier is fed either to an amplifier or to a photon counter. If a monochromator is used, a high intensity of the ion beam is required in order to get a strong LIF signal. Usually, 10 – 1000 μA of the ion beam current is required for the investigation of weak lines [47].

In this work, no monochromator is used and altogether all fluorescence lines are detected using a photomultiplier. In order to get rid of the background laser stray light, appropriate filters are mounted before the photomultiplier. In this method of detection of fluorescence light, weak lines, which cannot be observed using a monochromator, can also be investigated. An ion beam current of 1 - 20 nA is sufficient for strong lines and ~100 nA for weak lines.

8.1.3.2 Photon counting

In this work the photomultiplier is used in photon counting mode. Using a head-on photomultiplier with a gain of 10^8, a single photoelectron a produces current pulse with a rise time of about 1 ns, at the anode of the photomultiplier. These pulses trigger a fast discriminator, which delivers a TTL-norm pulse of 5 V to a digital analog converter (DAC) or to a counter driving a rate meter with variable time constant.

The photon counting method has many advantages over conventional analogue measurement of the anode current. Some of them are

- By selecting a suitable discriminator level, the dark current generated by thermal electrons from various dynodes can be suppressed.
- Each photoelectron induces the same normalized pulses from the discriminator (as long as the anode pulse exceeds the discriminator level): Therefore, the fluctuations due to the gain of photomultiplier are not significant.
- Contribution of leakage current between the leads in the photomultiplier socket can be eliminated if the discriminator is correctly biased.
- The pulses from the discriminator are in the digital from and can directly be fed into a computer for further analyses and may control the experiment (will be discussed in chapter 9).

Finally, the data of the optical spectra of the hyperfine structures are recorded and analyzed with the aid of some computer programs.

8.2 Line broadening in CLIBS

In the previous section, it is shown that the Doppler broadening of a spectral line can be reduced about a factor of 500 using the CLIBS spectroscopy. On the other hand, there are a number of factors, which enlarge the line width and prevent the ultimate theoretical resolution of CLIBS. In this section some broadening effects are discussed and the magnitude of these effects is estimated. The total line profile is then obtained as a convolution of all the individual profiles.

8.2.1 Fluctuations in the acceleration voltage

At high acceleration potential there is no effect of fluctuations in the initial thermal velocities, but the ion velocity is now determined by the acceleration voltage. This needs an extreme stabilization of the acceleration voltage. A change in absorption frequency due to change in acceleration voltage (ΔU) can be calculated with the help of equation 8.2 and $\nu = \nu_0(1 + u/c)$

$$\Delta\nu = \frac{\nu_0}{c}\Delta u = \nu_0\sqrt{\frac{eU}{2Mc^2}}\frac{\Delta U}{U} \tag{8.8}$$

In case of praseodymium, a ripple of 1 V at an acceleration voltage 20000 Volts, for absorption line at 6000 Å (= 5×10^{14} MHz), broadens the line profile about 7.5 MHz. Therefore, the acceleration voltage must be extremely stabilized in order to keep the high resolution of the optical spectra under investigations. The fluctuating plasma potentials also cause broadening of spectral lines because they change the acceleration.

8.2.2 Deviation from linearity

When ion beam and laser beam make a small angler ($\Delta\theta$) with each other, the velocity component in the direction (z-direction) of the laser beam leads to a line broadening given by the following equation [62]

$$\Delta\nu_{z\Delta\theta} \cong \frac{\nu_0 u_{th}}{4cR}(\Delta\theta)^2 \tag{8.9}$$

and in the direction perpendicular to the laser beam the width is given by [62]

$$\Delta\nu_{y\Delta\theta} \cong \frac{\nu_0 u_{th}}{c}(\Delta\theta) \qquad (8.10)$$

($\Delta\theta$ includes all angles subtended either due to laser beam divergence, ion beam divergence or due to misalignment in the laser and ion beams. In practice, the laser beam divergence is much smaller than the typical ion beam divergence).

For example, $\Delta\theta = 0.005$ rad, $\nu = 5 \times 10^{14}$ Hz ($\lambda = 6000$ Å):

The line broadening in a ^{141}Pr spectral line due to beam divergence becomes

$\Delta\nu_{z\Delta\theta}$ = 3.0 MHz and $\Delta\nu_{y\Delta\theta}$ = 5.5 MHz.

8.2.3 Time of flight broadening

Heisenberg's uncertainty relation for energy and time is given by

$$\Delta E \Delta t \geq \hbar$$

If Δt is the time spent by an ion in the interaction chamber, then the line broadening associated with the time of flight can be calculated by

$$\Delta E \Delta t = \Delta\nu h \Delta t \Rightarrow \Delta\nu = \frac{1}{2\pi\Delta t} \qquad (8.11)$$

In the experimental setup used in this work, the interaction length available is about 3 cm. If the ion velocity is 170 kms^{-1}, then the time of flight broadening can be calculated using equation 8.11 i.e. $\Delta\nu$ ~ 1 MHz.

Apart from these broadening mechanisms, there are also some other phenomena that broadens the line profile. For examples

- Instability of the laser frequency may broaden the line up to 10 MHz.
- At a pressure of 10^{-6} mbar, the collisional broadening can be estimated to 2 MHz [121].
- Working at a high lasing power, saturation broadening is always there, which depends on the laser power used to investigate the hyperfine spectra.

- Instability in ion beam current and fluctuations in the laser intensity results in variations of the LIF signal.
- If the ion beam is hitting inside the mass separator, there may be a velocity spread in the final velocity of the ions giving rise an additional broadening of the line profile. Therefore, while performing CLIBS experiments, the path of the ion beam must be clear and should pass through the centers of the apertures that define the beam path.
- If ion beam measuring instruments like Faraday cup, plates used to align the ion beam etc are not properly grounded, there could be an undesirable potential penetration which influences the ion beam quality (and broadens the velocity spread) and hence broadens the line profile.

8.2.4 The total line width

The total line width is determined by adding up all these line broadenings:

$$\Delta\nu_{tot} = \sum_{i=1}^{n} \Delta\nu_i = \Delta\nu_{nat} + \Delta\nu_{\Delta\theta} + \Delta\nu_{\Delta U} \dots\dots\dots \qquad (8.12)$$

If the life time of a state is taken as 10^{-8} sec, the natural line width is approximately equal to 15 MHz. Different broadenings can be summed up now

Natural line width	15 MHz
Instability in acceleration voltage	7 MHz
Ion beam divergence	6 MHz
Doppler broadening	4 MHz
Laser frequency instability	15 MHz
Collisional broadening	2 MHz
Time of flight broadening	1 MHz
Total line width	50 MHz

The typical line width observed in this work is ca. 40 - 60 MHz, whereas the minimum observed line width is 35 MHz. The experimental value of line width is in good agreement with this assessment. Sometimes a line width > 80 MHz is observed which is perhaps due to the saturation effect (laser power used during the study of hyperfine structures was ca. 50 to 100 W at the output coupler of the ring dye laser). Moreover, the diameter used for the extracting hole of the ion source is ~ 2 mm which is much larger as compared to used previously in Marburg (ø ~ 0.7 mm). The bigger hole of the ion extracting tube can produce a large divergence of the ion beam and a large final velocity spread. This could also be a reason that line width observed in this work is larger than in the previous measurements (ca. 30 MHz [121]).

9 THE EXPERIMENTAL SETUP OF CLIBS (MARS-II)

The Marburg mass separator MARS-II, originally installed at the University of Marburg a.d. Lahn (Germany), was moved to Graz in 2002. The system MARS-II had been extensively used in Marburg to investigate hyperfine structures and isotopic shifts of different elements such as cesium, xenon, samarium, promethium, lanthanum, barium, europium etc. and has produced about 15 PhDs and more than 60 journal publications. The system is now fully working at the Institute of Experimental Physics (IEP) at the Graz University of Technology. The results obtained at IEP have been presented in many conferences and one journal publication is awaited [54] and some more papers are expected based on the recent hyperfine measurements. A schematic diagram of MARS-II is shown in figure 9.1. Few pictures of the system are given in section 9.5. Some of the important components of the MARS-II are discussed in the upcoming sections.

9.1 Description of the mass separator MARS-II

The MARS-II isotope separator was designed and developed by W. Kornal and G. Krömer in the 1970s. This system can be operated with a mass resolving power 4000 at an ion current of 1 μA [122]. The ions are produced in an ion source where due to thermal collisions lower metastable ionic states are also populated. The ions are accelerated up to ~170 km/s by applying a high acceleration potential of approximately 20 kV. Different isotopes are mass separated by an 80° magnet and their mass spectrum is observed in a focusing chamber. Using deflection potentials, the ion beam of a particular isotope is selected and guided into the interaction chambers where a laser beam is superposed with the ion beam. When the laser frequency is in resonance with an optical transition, the hyperfine pattern of the transition is studied by observing the fluorescence light emitted by the ions.

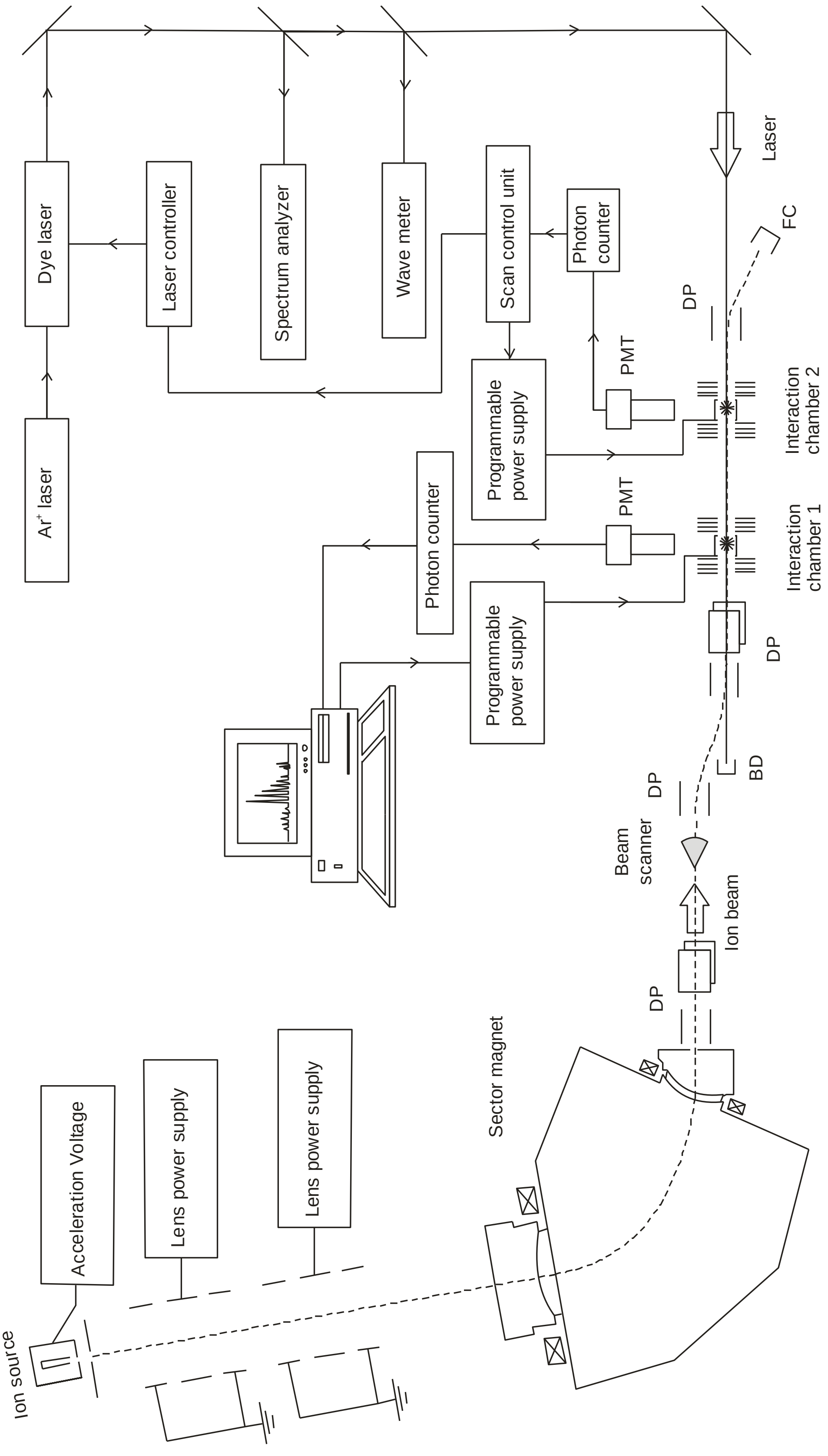

Figure 9.1. Schematic diagram of CLIBS setup (MARS-II). DP: Deflection plates, BD: Laser beam dump, PMT: Photomultiplier tube, FC: Faraday cup.

Originally the system had two interaction tubes (channels/vessels) and two ion beams could be studied simultaneously (one of them was chosen as a reference beam, see e.g. [73]). Each beam was deflected into the interaction tube by an angle of 42˚. The left channel is removed as it was not operational since the system arrived in Graz. The system is modified in order to avoid a large angle of deflection and is working now with one channel. Now the ion beam is deflected by an angle ~ 9˚ into the interaction tube. It is observed that the number of ions reaching at the end of the interaction tube is increased 4 times as compared to the previous configuration; hence, the LIF signal could be improved. Some parts of the MARS-II are discussed below.

9.1.1 Ion source

A Johnson type surface ion source [123] is used for the production of positive ions. The schematic diagram of the ion source is shown in figure 9.2. The oven and the ionizer are heated using Ohmic heating. The temperature of the ionizer should be sufficiently high to dissociate the sample molecules into neutral atoms and to ionize the atoms. The vapors of the sample are produced in the oven (Ta-cup), adsorbed on the heated surface of the ionizer and are ionized. The material of the ionizer is selected so that it has higher electron negativity than that of the sample. As soon as the ions are produced they are extracted from the ion source due to the presence of a strong acceleration potential (the oven works on a high acceleration potential).

For best yield of the ions, the ionizer should exhibit the following properties:

- It should have higher electron negativity than that of the sample material.
- It must not be reactive with the sample material and with air.
- It must be stable against high temperatures.
- It must be refractory.
- It should be free of impurities (about 99% purity is enough, which is normally available at nominal rates).

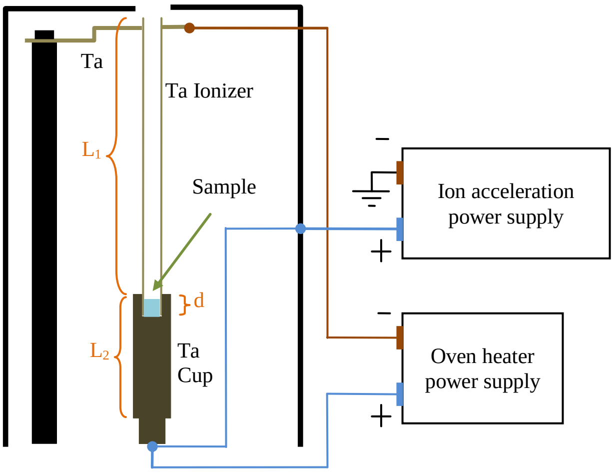

Figure 9.2: The positive surface ion source.

In this work, Pr metal powder is used for the production of the Pr^+ beam. The Pr powder is prepared indigenously by rubbing the pure Pr metal with a fine mechanical file. An oven cup made of tantalum (Ta) is used and a Ta foil is used as an ionizer. The ionizer is made by rolling a thin foil of Ta. Different dimensions of heating cups and ionizers were tried in the search of producing a stable and high ion beam of praseodymium. Best results are obtained for, Ionizer: thickness 0.025 mm, L_1 = 40 mm and inner diameter less than 2 mm. Ta cup: L_2 = 20 mm, outer diameter 5 mm, cavity of inner diameter (w) $1.5 \leq w \leq 2$ mm and depth (d) = 3 mm. The aperture of the extraction electrode is 5 mm.

For better results, it is observed that whenever the oven is loaded with a fresh sample, it must be heated for about half an hour at about 100 - 150 Watt under a vacuum ~ 1×10^{-6} mbar and be cooled down to room temperature under a pressure less than 10^{-4} mbar. Perhaps in this way, all impurities/oxides are vaporized and the heating cup is left with pure praseodymium. After re-heating, usually an ion current of 20 to 30 nA (measured at the far end of the interaction chamber) is produced with a heating power of 300 to 350 Watt for about 3 to 4 hours of continuous operation. After that, the number of ions decreases with time and therefore heating power has to be increased to increase the ion beam intensity. At about 400 – 430 W, the Ta heating tube breaks up (perhaps temperature is quite high and localized melting takes place in the Ta tube) and oven stops working. A new heating tube is installed and fresh praseodymium powder is filled in the oven to conduct another experiment. Wolfram (W) can also be used instead of Ta, but it is very hard to machine, therefore special machining tools e.g. diamond tools are required to fabricate a heating cup. One more problem is its brittleness; rolling a 0.03 mm thin foil to make an ionizer of 2 mm in diameter is really a difficult task. The ion beam current is measured using Faraday cups which are installed at different positions in the mass separator.

9.1.2 Electrostatic lens system

Before the ion beam enters into the magnetic field it comes across the two electrostatic lenses. In 1942, G. N. Plass [124], suggested a design of an electrostatic electron lens with a minimum spherical aberration. Figure 9.3 shows the plot of equipotential lines in space for this kind of an electrostatic lens. The same Einzel lens design is used in MARS-II for focusing the ion beam in z-direction.

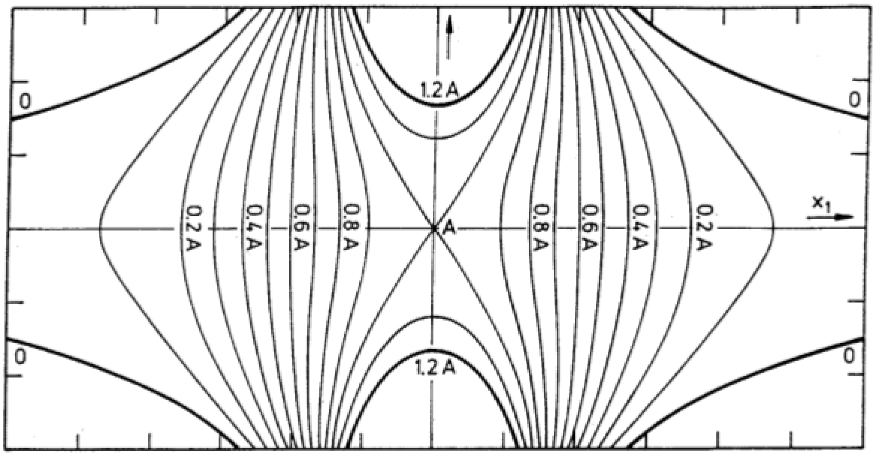

Figure 9.3: Plot of equipotential lines of an electrostatic lens with minimum spherical aberration. A is the potential at the center of the lens [122].

Fine focusing of the ion beam in the y-direction is obtained by using another electrostatic lens (y-lens).

When ions hit the surface of the electrostatic lens system, microdischarges occur if the surfaces of the lenses are contaminated (e.g. by oil vapors from pumps, oxides layers of different impurities). In order to avoid this problem and to increase the breakdown rigidity of the lens system:

- Lens electrodes are made of aluminum because it is resistive to oxidation, stable against corrosion and most importantly it produces fewer secondary electrons.

- Ceramic insulators are used.
- Lens surfaces are well polished and the edges are rounded.
- The system is operated under a low pressure i.e. ~ 10^{-6} mbar.

The voltage required to focus the ion beam depends upon the acceleration potential. Normally, 12 kV for the z-lens and 2 kV for the y-lens are required for optimal focusing of ^{141}Pr ion beam at an acceleration of 20 kV.

9.1.3 The magnet

In MARS-II, the sector magnet developed by W. Kornal and G. Krömer is used to separate different masses present in the ion beam. This is a large electromagnet of weight about 4000 kg. The mean radius of curvature is 80 cm and the angle of deflection of the central beam is 80˚. The nominal resolving power and the dispersion of the isotope separator are ~ 3000 and 1200 respectively [122]. Some parameters of the sector magnet are given in table 9.1 [122]. The ion optical system of the mass separator is described in figure 9.5.

Table 9.1: Some important parameters of the sector magnet.

Description	**Notation**	**Value**
Radius of curvature	R	80 cm
Angle of deflection	ϕ	80˚
Entrance angle	ϵ_1	0˚
Exit angle	ϵ_2	34.8˚
Radius of curvature of the field boundary at the entrance	r_1	50 cm
Radius of curvature of the field boundary at the exit	r_2	- 41 cm
Gap between the pole pieces (width × height)	g	16 cm × 6 cm
Distance between the ion source and the field entrance boundary	l_1	120 cm (1.5 R)
Distance between the image and the exit field boundary	l_2	143 cm (1.79 R)

The magnet coil is composed of four packets of coils. Each packet consists of ten coils and each coil is made of 56 windings. For the winding of the coils, a wire with a diameter 3 mm is used. The circuit of the coils is given in figure 9.4. In this work, a stabilized power supply (Transistor-Netzgerät TN 60 - 24000) of 100 V, 80 A is used and a magnetic field up to 6600 Gauss can be produced. For cooling the magnet coil, copper plates of 5 mm thickness are inserted between each of the magnetic coil packets. The copper plates are cooled by water which flows through copper pipes.

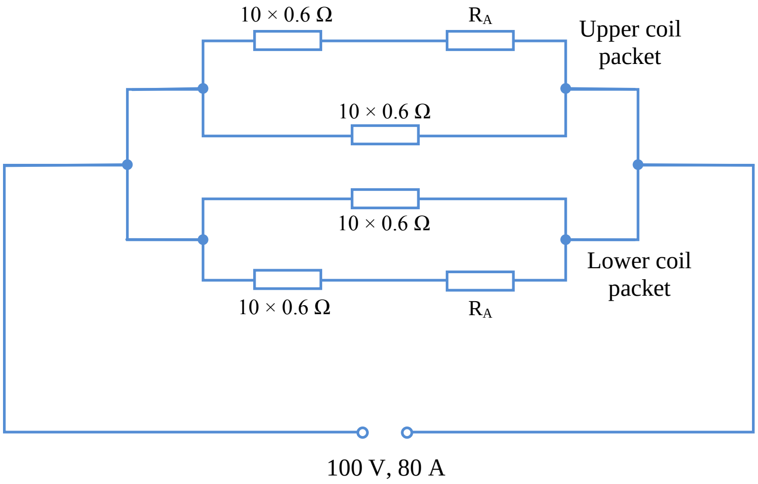

Figure 9.4: The circuit diagram of the magnetic winding. R_A (= 0.5 Ω, 200 Watt) is the compensating resistance of the upper and the lower packets of coils [122].

In order to obtain a small width of the image (a high resolving power), it is necessary to have a fringing free and homogenous magnetic field. To minimize the effect of fringing field, the entrance and exit of the magnet are made circular with radii which fulfill the Hintenberger condition [125]. At the entrance of the pole pieces a convex profile with a radius of curvature of 47.8 cm, and at the exit a concave profile with a radius of curvature 42.5 cm are fitted. The pole pieces (37 cm wide, 6.7 cm thick, having segment angle 67° and radius of curvature 78.5 cm) are bracketed between the vacuum chamber and the magnetic yoke extends over the full length of the magnet. Moreover, magnetic shields are mounted at the entrance and exit edges of the pole pieces for the attenuation of the fringing field.

The pole pieces are independent and separated from the magnetic yokes by two gaps of 2 mm wide. In order to have a better homogeneity of the magnetic field, this air gap must be changed slightly. A wax sheet with carefully calculated different thickness of iron powder can be placed between the pole pieces and magnetic yokes to vary the thickness of the air gap.

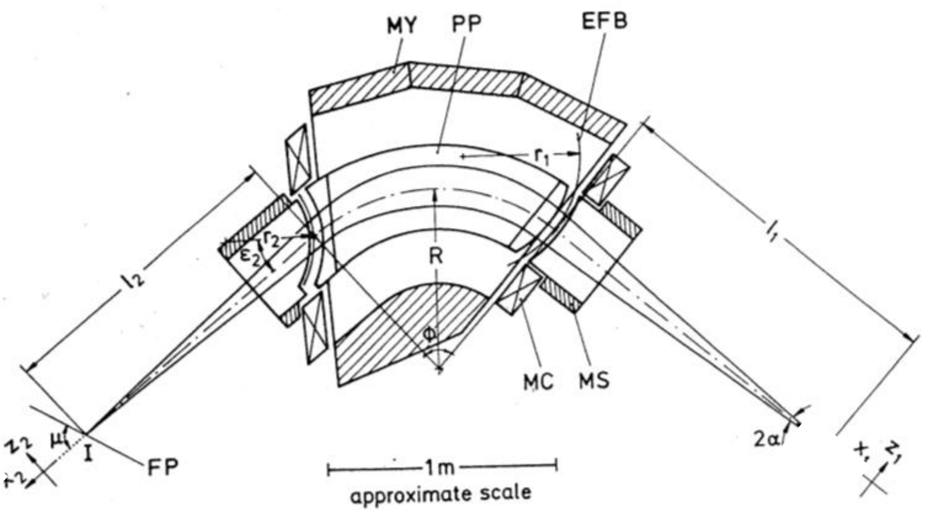

Figure 9.5: Schematic diagram of the ion optics of the separator in the horizontal plane. S: Ion source, MS: Magnetic shield, MC: Magnetic coil, EFB: Effective field boundary, PP: Pole piece, MY: Magnetic yoke, FP: Focal plane and I is the image (other notations are explained in table 9.1) [122].

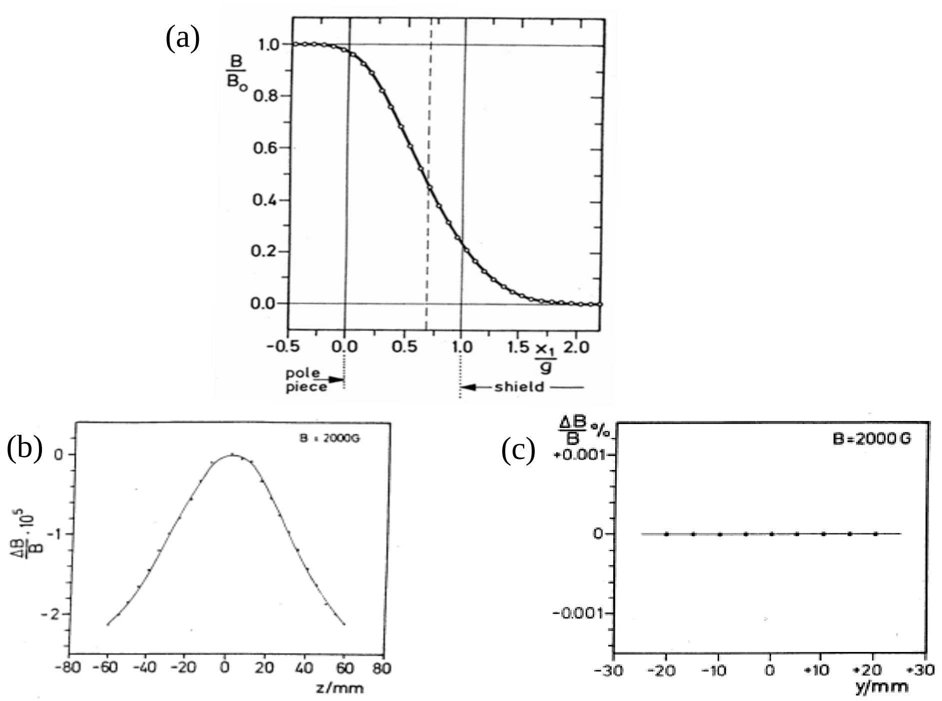

Figure 9.6: (a) The observed distribution of the fringing field B (x_1, $y_1 = 0$, $z_1 = 0$) of the sector magnet in the middle plane of deflection at the boundary along the normal direction of the magnetic pole boundary. B_0 is the magnetic field inside the magnet (B_0 = 2000 Gauss), g is the gap between the pole pieces. (b) ΔB/B (y_1 = 0, z_1) in the horizontal direction on the median plane. The magnetic field at the entrance of the magnet is 2000 Gauss. (c) ΔB/B (y_1, z_1 = 0) in the vertical direction. The magnetic field at the entrance of the magnet is 2000 Gauss [122].

More details about the investigations of fringing field and homogeneity of the magnet can be found in ref. [122]. The distribution of the fringing field and homogeneity of the magnetic field observed in the work of Th. Win are shown in figure 9.6. The variations observed in the magnetic field are: 0.001% in the range of $-3 \geq z \geq +3$ cm in the median plane and 0.002% in the range of $-5.5 \geq y \geq +5.5$ cm.

9.1.4 Interaction chamber

In MARS-II, there are two identical interaction chambers where laser and ion beams are superposed collinearly. The first interaction chamber (with respect to the ion beam) is used for recording the hyperfine structures and the second interaction chamber is used for the laser frequency stabilization on one of the hyperfine components.

In figure 9.7, the top and the side views of a four stage interaction chamber are shown. By applying a post acceleration scanning voltage (Doppler tuning) between 0 to 3000 V to the interaction chamber, the ion velocity and thus the Doppler shift of the absorption frequency in the lab-system can be scanned up to 25 GHz. The potential lines near to the incoming and outgoing holes may not be as uniform as inside the chamber, which can lead to an asymmetric line profile of the recorded hyperfine structures. The interaction chamber is especially designed (with additional electrodes) to minimize these disturbing effects. The resonance between ions and the laser photons, and following laser-induced fluorescence, takes place only in front of the light collecting plexiglass. This minimizes the depletion of the metastable states of the ions by the laser light before they enter the interaction region.

The interaction region has a length of about 30 mm, therefore a much better LIF signal is observed as compared to transverse laser atomic beam spectroscopy in which the interaction region is limited to the diameter of the atomic beam. The entrance and exit of the chamber are 8 mm in diameter. In order to detect most of the fluorescence light, the inner walls of the interaction chamber are covered with an aluminum reflector. The fluorescence light is collected by a plexiglass rod which serves as a light pipe. A Schott BG-12 glass filter is used to suppress the background light from the ion beam as well as stray laser light. The LIF signal is then detected by a head-on photomultiplier tube (Photonis XP2020).

As the velocity of the ions before entering and after leaving the interaction chamber is the same, the second interaction chamber can also be used to observe the LIF signal. Observing an LIF signal in the second interaction chamber means that there are still many ions in the lower meta-stable levels. This LIF signal is utilized for the stabilization of the laser frequency (section 9.2.4).

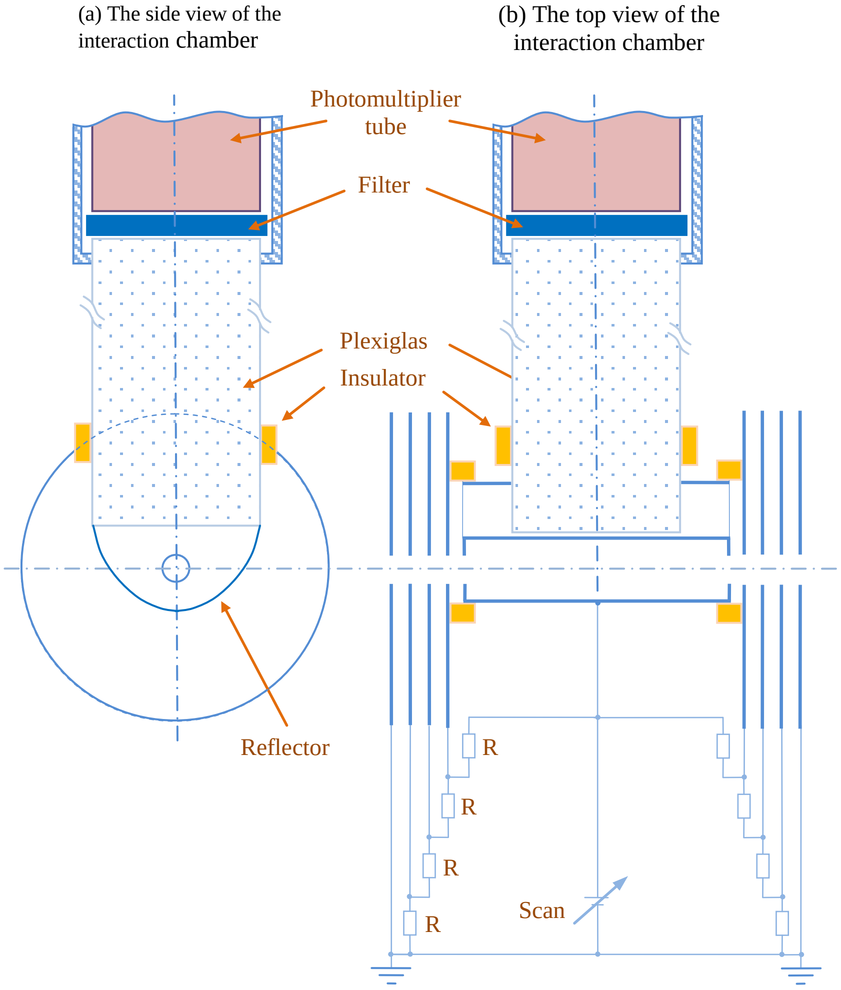

Figure 9.7: (a) The side and (b) top view of the MARS-II interaction chamber. R = 1MΩ.

It is better to employ acceleration Doppler tuning rather than deceleration Doppler tuning, because background light stays almost constant in the first case. It is observed that, if the ions are decelerated, the background counts increases enormously (especially after 1.5 kV) with increasing scanning voltage. The reason is; the positive scanning potential increases the divergency of the ion beam and the ions hit the walls of the interaction chamber, producing more background light. Using an accelerating scanning voltage, this phenomenon can be minimized and smooth recordings up to 3 kV post acceleration voltage are observed.

9.1.5 Vacuum system of MARS-II

Figure 9.8 shows a schematic diagram of the vacuum system of MARS-II. In this figure the different symbols mean: R1…: Rotary pumps, V1…: Vacuum valves, S1…: Pneumatically controlled vacuum valves, LNT….: Liquid nitrogen traps, TK-FR: Turbo Klein (small turbo molecular pump for fore vacuum), TG: Turbo Groß (big turbo molecular pump), SI: Ion pump, Cyl…: Cylinders, mm1…, 1A…etc.: used for different pressure heads.

In the MARS-II mass separator the ion beam travels about 5.5 meters from the ion source to the interaction chamber. In order to avoid neutralization and scattering of the ions by residual neutral atoms, it is necessary to keep the entire system under a high vacuum.

The vacuum system of MARS-II fulfills the criterion of high vacuum technology. The vacuum chambers are made from stainless steel because of its low degassing. Viton O-rings are used between the vacuum flanges, valves etc. to integrate different parts and accessories of the system. The system was examined for the presence of any leak using a helium leak detector, and observed leaks were removed.

The vacuum system has 5 main sections: Ion source, electrostatic lenses chamber, magnet chamber, ion collector chamber, and a vacuum tube where the interaction chambers are located. These sections can be isolated from each other using pneumatically controlled vacuum valves, which closes when any of the chambers is ventilated. The vacuum valve S4 can be operated in manual as well as in automatic mode. In the automatic mode, if the pressure in the interaction region increases for some reason to ~ 10^{-1} mbar, it is automatically closed; therefore the rest of the vacuum system is isolated and is protected from ventilation. This valve is also controlled by the flow signal of cooling water of some turbo molecular pumps (TK and TG) and closes if the flow of cooling water stops during operation. Similarly, the vacuum valve S1 is synchronized with the flow of cooling water of the big turbo-molecular pump (TG-IS) in the ion source section. The vacuum valve S5 is installed between the lenses chamber and the ion source. The ion source chamber is opened more often in order to fill the oven with a fresh material to be investigated:

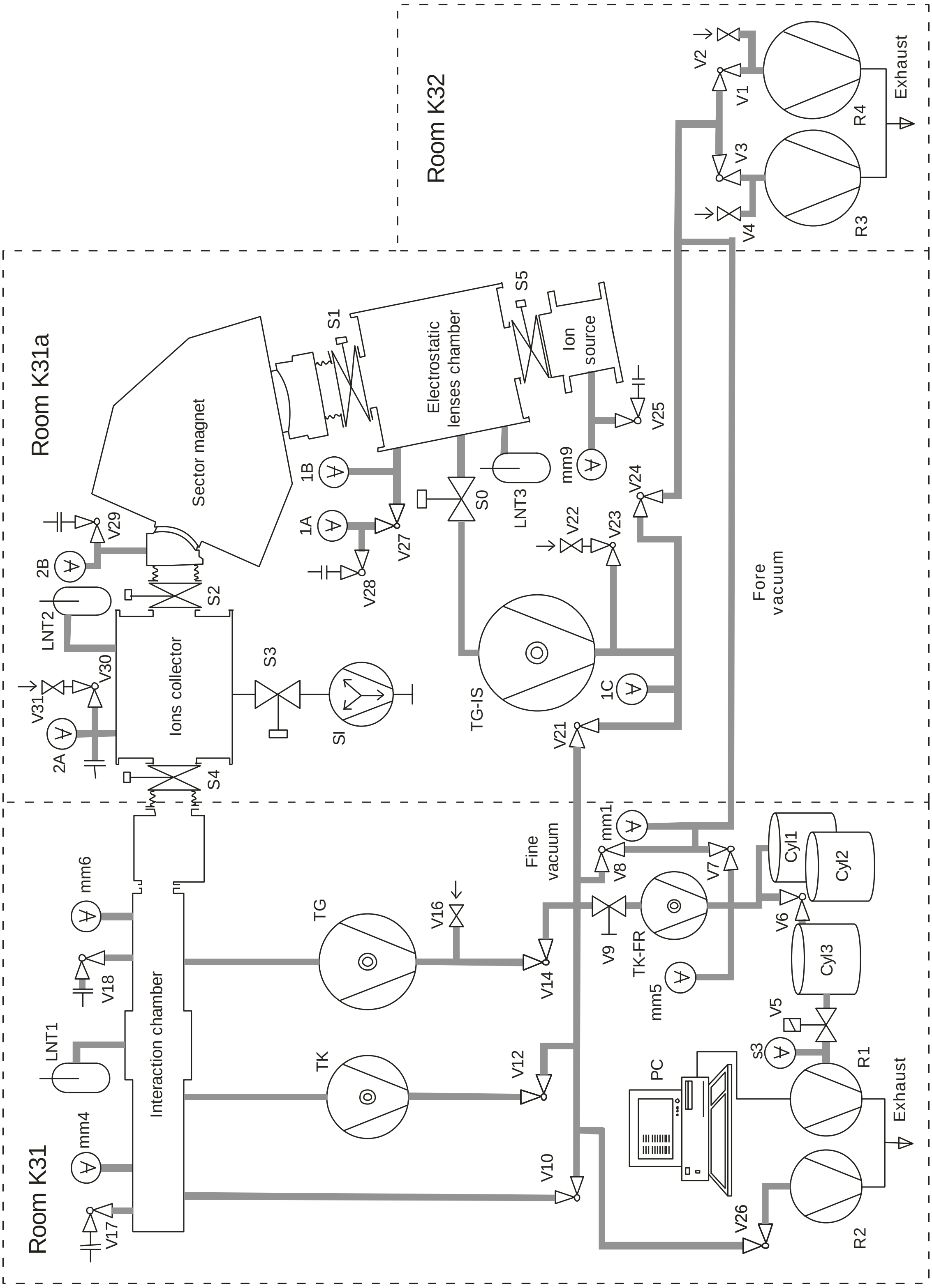

Figure 9.8: Schematic diagram of the vacuum system of the MARS-II. (See section 9.1.5 for the description of labels used in this figure).

Therefore, this chamber can be ventilated separately without exposing the rest of the mass separator to air. A portable assembly of a turbo molecular pump backed by a rotary pumped is available in the laboratory which is used to create a fore-vacuum in an isolated vacuum chamber.

In order to attain a high vacuum inside the mass separator, the system is equipped with three turbo molecular pumps: TK (Turbovac 150 Leybold-Heraeus) with a power of 115 l/s, TG (Turbovac 450 Leybold-Heraeus) with a power of 450 l/s and TGIS (Turbovac 1500 Leybold-Heraeus) with a pumping power of 1500 l/s. These pumps are backed by a sophisticated fore-vacuum system (the region pumped by turbo pumps can be named as fine vacuum region). The fore-vacuum system consists of a small air cooled turbo molecular pump TK-FR (Adixen ACT 100) and a rotary pump R1 (Pfeiffer Balzers Model: DUO 008 B, pumping speed 8 m^3/h). Another rotary pump R2 (Pfeiffer Vacuum Model: DUO 2.5, pumping speed 2.5 m^3/h) is also provided which can be operated in case of malfunctioning of R1. Two big rotary pumps R3 (Balzers Model: D12) and R4 (Balzers Model: DUO 25, pumping speed 28 m^3/h) are attached with the fore-vacuum line. These are operated when the whole system have to be ventilated from atmospheric pressure. The data about the vacuum pumps used in the vacuum system of MARS-II is listed in table 9.2.

Table 9.2: specifications of pumps used in the MARS-II vacuum system.

Pump name/model	**Pumping power**	**Power supply used**	**Used in**
R1: Pfeiffer Balzers Model: DUO 008 B	8 m^3/h	AC 220 V, 50 Hz	Fore-vacuum
R2: Pfeiffer Vacuum Model: DUO 2.5	2.5 m^3/h	AC 220 V, 50 Hz	Fore-vacuum
R3: Balzers Model: D12	12 m^3/h	AC 220 V, 50 Hz	Fore-vacuum
R4: Balzers Model: DUO 25	28 m^3/h	AC 220 V, 50 Hz	Fore-vacuum
TK-FR: Turbo molecular drag high vacuum pump ATW 398043 MDP 5011	7.5 l/s	Adixen ACT 100	Fore-vacuum
TK: Leybold-Heraeus: Turbovac 150	115 l/s	Leybold-Heraeus Turbotronik NT 120	Fine-vacuum
TG: Leybold-Heraeus: Turbovac 450	450 l/s	Leybold-Heraeus NT 450	Fine-vacuum
TGIS: Leybold-Heraeus: Turbovac 1500	1500 l/s	Leybold-Heraeus NT 1500	Fine-vacuum

Fore Vacuum:

To start evacuating the MARS-II from atmospheric pressure, all vacuum components must be properly installed and all valves must be properly closed. Pneumatic vacuum valves S1, S2, S4 and S5 and vacuum valves V10, V21, V3 and V1 are opened. The big rotary pumps R3 and R4 are switched on. When the pressure inside the system is reduced to 10^{-1} mbar, the small turbo pump TK-FR is started. The valves V1, V3, V7 and V8 are closed and the rotary pumps R3 and R4 are switched off. V2 and V4 are opened to increase the pressure inside the rotary pumps (to avoid rising of oil in the fore-vacuum line). When TK-FR attains its normal speed, V6, V9 and V10 are opened. Now the air inside the mass separator is evacuated into the cylinders Cyl1, Cyl2 and Cyl3. A pressure gauge mm5 (Leybold-Heraeus, Model: Thermovac TM201 S2) is installed to measure the pressure in the cylinders. A pressure limit with P1 > P2 (e.g. P1 = 4 mbar and P2 = 2. 10^{-1} mbar is used in this work) is fed into mm5, the voltage signals corresponding to P1 and P2 are sent to the electromagnetic valve V5 and the rotary pump R1. The start/stop of the rotary pump R1 is controlled by pressure readings P1 and P2. When the pressure in the cylinders reaches P1, V5 is opened and the rotary pump R1 is turned on and starts evacuating the three cylinders. When the pressure reading at mm5 reaches P2, the rotary R1 is stopped and V5 is closed automatically. The electromagnetic valve V5 is interfaced with a computer which stores the OPEN/CLOSE timings of V5. This data reflects the leak tightness (quality of the vacuum) of the vacuum system.

Fine vacuum:

When the pressure inside the mass separator is reaching ~ 10^{-2} mbar, the turbo pumps can be started by following their standard operating procedure (SOP). First the cooling water of TK and TG and then the pumps are turned on. The valve V10 is closed and V12 and V14 are opened. When the vacuum inside the system reaches to ~ 10^{-5} mbar, further rapid evacuation can be done by operating TG-IS. When TG-IS attains its normal speed, the pneumatic valve S0 is opened. Note: the ion pump SI is not working, therefore the valve S3 should never be opened during the operation of the mass separator or even when system is operating under fore-vacuum. By filling three liquid nitrogen traps (LNT) with liquid nitrogen, the pressure inside the mass separator can be reduced down to ~ 10^{-6}. During this work, a pressure down to 2×10^{-7} mbar in the interaction tube, and ~ 8×10^{-7} mbar in the ion source chamber was observed.

After performing an experiment, the turbo molecular pumps are turned off. Vacuum valves V12, V14 and S0 are closed. Vacuum valve V10 is opened and the system is left on fore-vacuum and is pumped by TK-FR and R1.

In order to check the vacuum system, many pressure heads have been mounted at different places of the mass separator. A pressure head mm6 (Balzers TPG 251) is used for the pressure measurements in the interaction tube and mm9 in the ion source chamber. To monitor the pressure in the ion collector chamber, pressure heads 2A and 2B are installed, whereas 1A and 2B measure the pressure in the electrostatic lenses chamber. In the fore-vacuum line, mm1, s3, mm5 and 1C are installed for pressure measurements.

9.1.6 Electronic system of MARS-II

The layout of the electronic system of MARS-II is shown in figure 9.9. For the guiding and alignment of the ion beam, different deflection plates are installed inside the mass separator. In addition to the z-lens, the vertical direction of the ion beam is adjusted using the deflection potentials 1V and 2VR. For the deflection of ion beam in the horizontal direction, the y-lens, the deflection potentials 1T, YK, 2UR and 3UR are used (of course, the acceleration voltage and the magnetic field can also be used for the adjustment of the ion beam in the horizontal plane). Moreover, the ion source and the focusing chamber are mounted on moveable ports for the fine adjustment of the trajectory of the ion beam.

For the diagnostics of the ion beam, different plates and Faraday cups are placed inside the mass separator at different positions. The Faraday cups (1FR 2FR, 3FR and 4FR) and the plates 1B and AK are mounted on vacuum feedthroughs and can be inserted into the path of the ion beam. To select a narrow ion beam, two orifices 1ZB (in front of the ion source and mounted on a 3-axis movable stage) and 2ZB (in front of the first interaction chamber) are provided. A beam scanner is mounted in the ion collector chamber to observe the mass spectrum of the ions. Two 4 quadrant detectors 14QR and 24QR are installed in the interaction tube to monitor the direction of the ion beam.

Alignment of the ion beam:

When the ion source is filled and the pressure inside the mass separator is below the limit ~ 10^{-6} mbar, the alignment of the ion beam is made as follows:

All power supplies and modules are switched on. First the magnetic field and acceleration voltage is adjusted; for a particular mass number, the value of the current required through the magnet coils can be selected (as a function of the acceleration voltage) from the graph available in the laboratory (e.g. figure 9.10) and the acceleration voltage, z-lens voltage and y-lens voltages are adjusted accordingly. The heating of the oven is turned on and increased gradually. Ions are produced and the current of the ion beam is measured at 1ZB. The 1B is inserted vertically into the lenses chamber and the current on this plate is maximized by adjusting the position of the orifice 1ZB. 1B is taken away from the path of the ion beam and the ion beam passes through the electrostatic lenses, electromagnet and is extracted at the exit of the magnet. Now a mass spectrum can be observed with help of the beam scanner. The plate AK is inserted into the ion collector chamber and the height of the ion beam is adjusted using the z-lens and by fine adjustment of the stage of electrostatic lenses chamber. The AK plate is exactly in front of 1VO/1VU plates (O and U stand for the upper and lower plates, respectively) and the height of the ion beam should be adjusted so that it passes exactly through 1V. The plate AK is taken out of the way of the ion beam. Now the position and the shape of the ion beam are observed at the beam scanner and can be optimized using acceleration, z-lens, magnetic field etc. The deflection potentials 1V, 1T YK, 2VR and 2UR are adjusted to pass the ion beam through the center (a hole of 8 mm in diameter) of 14QR. The Faraday cups are inserted in the path of the ion beam and the current of the ion beam at location of 1FR, 2FR or 3FR is measured. Then the ion beam passes through the interaction chambers and falls on 24QR. To avoid the deposition of ions on the Brewster window, the ion beam is deflected into the Faraday cup 4FR by applying proper voltages to the deflection plates 3URR / 3URL. The orifice 2ZB and apertures of 14QR/24QR are adjusted collinearly with each other; therefore these apertures define the path of the laser beam and the ion beam in the interaction tube. Finally, the intensity of the ion beam is optimized at 4FR.

In order to avoid an undesirable potential penetration (which can distort the ion beam), the modules which are not being used are properly grounded. To deflect the ion beam it is better to use a particular potential on each plate to have a uniform electric field between the deflection plates and to differentiate from the grounded walls.

In table 9.3, the specifications of some of the important modules used in this work are listed.

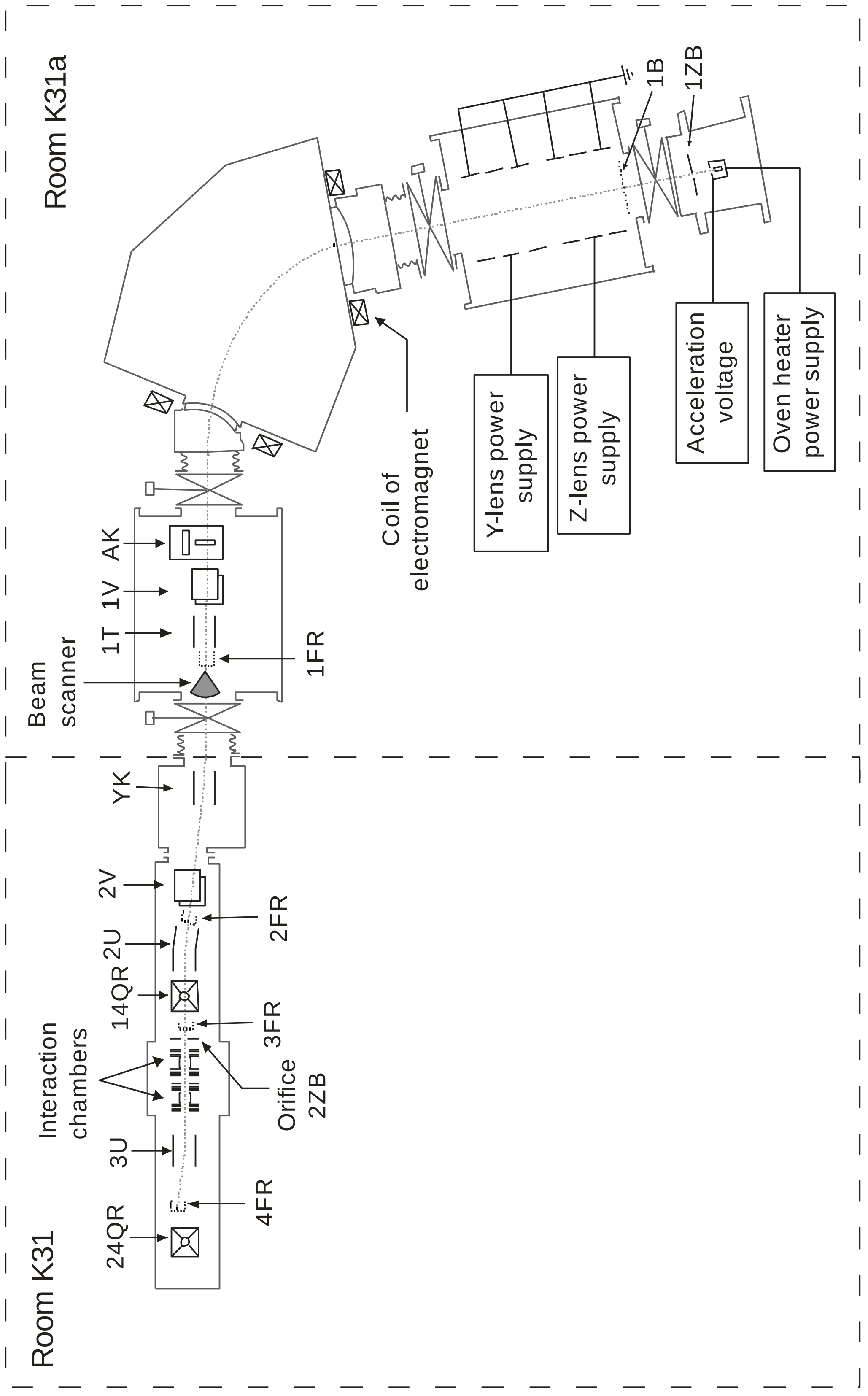

Figure 9.9: Schematic diagram of electronic system of MARS-II.

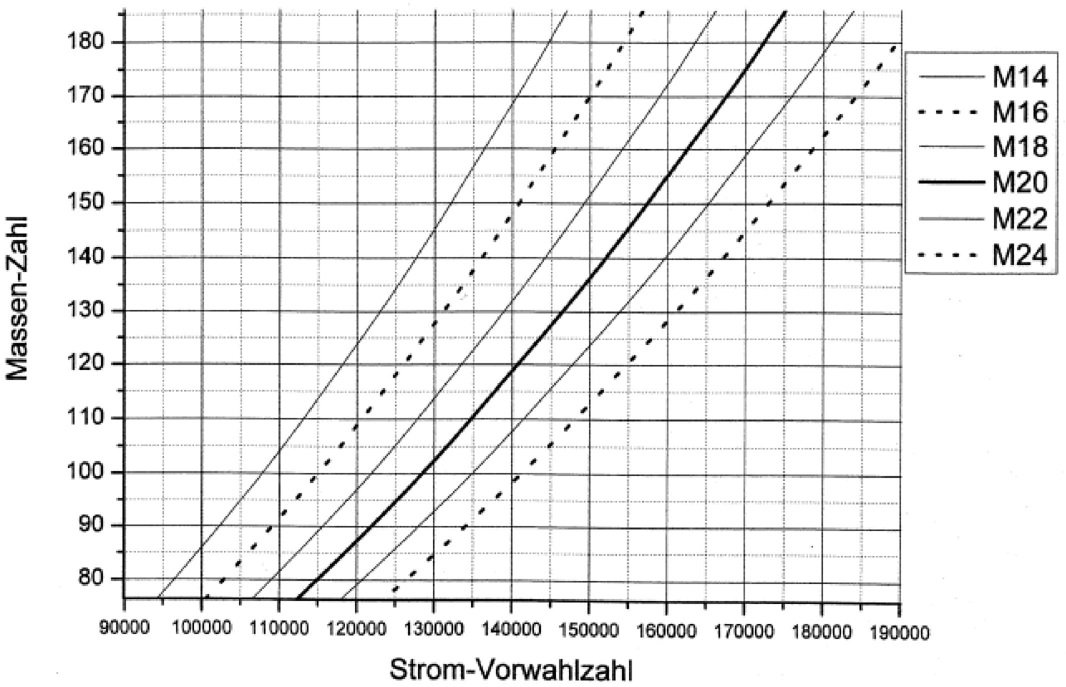

Figure 9.10. The mass number versus current code number of electromagnet. The oblique lines correspond to the acceleration voltage (in kV). For Pr Vorwahlzahl 150000 (equal to ~ 40 A) is used.

Table 9.3: Specifications of some important electronic units used in MARS-II for aligning the ion beam.

Used for	**Specification**
Power supply for electromagnet	Heinzinger: Transistor-Netzgerät TN 60-24000 (100 V, 80 A)
Power supply for acceleration	Fug: HCN 140M - 35000
Power supply for z-lens	Fug: HCN 140M - 20000
Power supply for y-lens	Fug: HCN 140M - 20000
Power supply oven heating	Manson SPS 9400
Power supplies for 8 channel potential dividers	Wenzel-Elektronik: HV power supply N1130
8 channel potential dividers (for deflection plates)	Hochspannungsgerät: HSG-09 (manufactured at Marburg University)
Beam scanner	Sinusgenerator: SIG-02 (manufactured at Marburg University)
Monitor to observe mass spectrum	Hewlett Packard: 143A Oscilloscope
Measurements of ion current	417 High speed PICOAMPEREMETER
4 Quadrant detectors	Monitor: MON-03 (manufactured at Marburg University)

9.1.7 Cooling system of the turbo molecular pumps and the electromagnet

There are three water cooling loops in the MARS-II setup. Their layout is shown in figure 9.11.

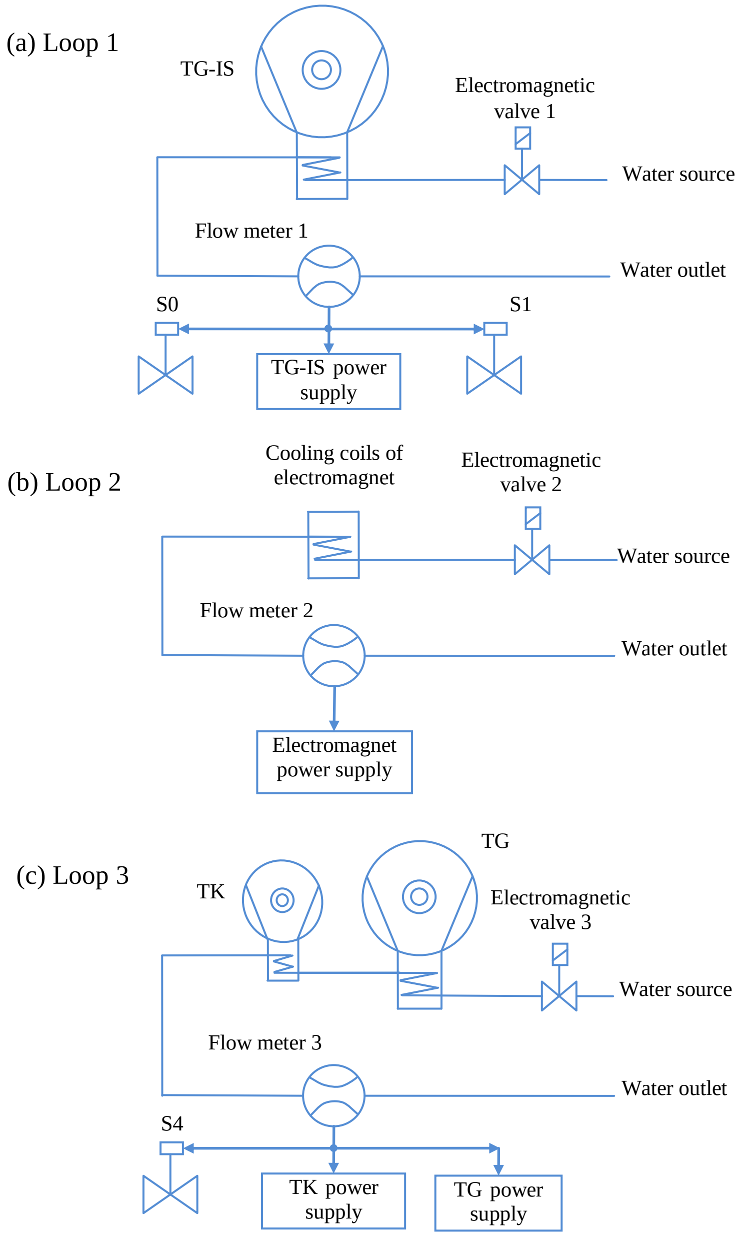

Figure 9.11: Cooling system of MARS-II. (a) Water flow circuit of loop1 that cools the Turbo pump TG-IS. (b) Cooling circuit for electromagnet coils. (c) Water flow through turbo pumps TK and TG.

Loop 1 cools the big turbo molecular pump TG-IS. For monitoring the flow of cooling water, flow meter 1 (Kurt Egner, 6082 Mörfelden) is installed in this loop. The signal from the flow meter is fed into the power supply of TG-IS and to the pneumatic valves S0 and S1. In case the cooling water through the loop is stopped (or flow rate is not sufficient to the requirements), the valves S0 and S1 are closed automatically for safety purpose and isolate the focusing chamber from rest of the mass separator. The loop 2 runs through the cooling copper coils of the electromagnet. Cooling of turbo molecular pumps TK and TG is done by the loop 3.

9.2 Optical instruments

9.2.1 Lasers

In order to perform high resolution spectroscopy using CLIBS, a single mode laser is required. For this purpose, a CW Coherent 699-21 ring dye laser (as discussed in chapter 5) is used to provide excitation laser light with a bandwidth less than 1 MHz. The ring dye laser is pumped by a CW Ar ion laser (model: Coherent INNOVA 200) operating with multi line visible spectrum (MLVS) mode at approximately 7 W output power. A Coherent power meter (model: Fieldmate) is used for the measurement of the output power of the lasers. The dyes Rhodamine 6G and Sulforhodamine B (Kiton red) are used to cover the desired wavelength range. A Coherent pump (model: 591 utility model) is used to circulate the dyes through the jet of the ring dye laser. The dyes are cooled with cooling water to avoid instabilities in the laser frequencies due to heated dye solvents.

The dye laser frequency is locked to a certain ionic optical transition (section 9.2.4) in order to stabilize the laser frequency within approximately 10 MHz.

9.2.2 Optical system

The optical part of the experimental setup of MARS-II is shown in figure 9.12. The dye laser beam falls on a beam splitter BS1 which divides the laser beam into a weak and a strong laser beam, in almost 1:9 ratios. The weak laser beam is further divided into two parts. One part goes to the spectrum analyzer (Spectra Physics, Model 470, free spectral range of 2 GHz) and second falls on mirror M2 which sends the laser beam into the wavemeter (will be discussed in next section) to measure the wavelength of the dye laser.

The strong laser beam, after reflected by a mirror M1, falls on a beam shifter. With the help of another beam shifter and mirrors M3 and M4 (as shown in the figure) the height of the laser beam is increased equal to the height of the ion beam. Beam splitter 1 is a kind of spectral aperture and allows only the yellow laser to pass. The green light of the Ar^+ pump laser is directed to a side, which if allowed to enter the mass separator can illuminate the pin holes giving rise an increase in the stray light. Thus, the beam shifter cleans the yellow laser and suppresses the background light.

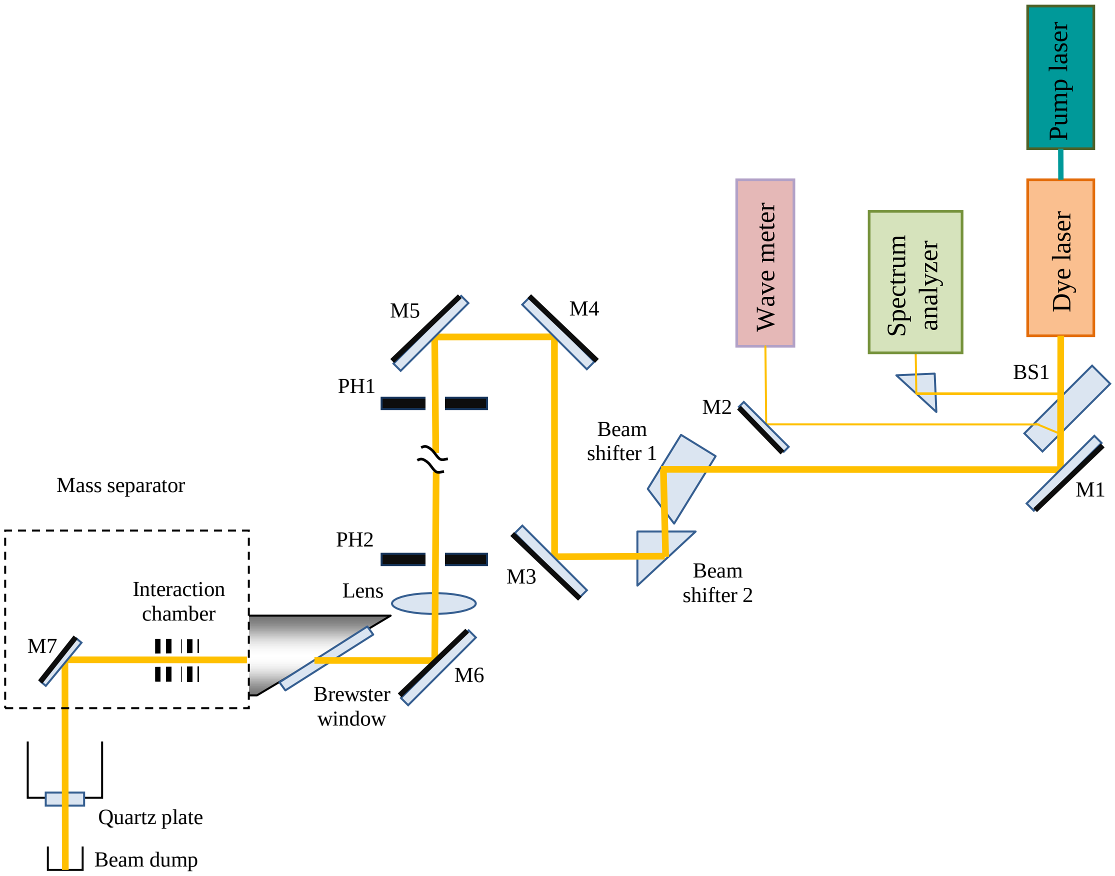

Figure 9.12: Schematic diagram of the optical system of MARS-II. BS: Beam splitter M: Mirror, PH: Pin hole.

Now the laser beam propagates in almost similar plane of motion of the ion beam. Then, from mirror M5 the laser beam passes through two pin holes that determine the proper direction of the laser beam. The laser beam is then reflected by the mirror M6 into the mass separator through a Brewster window. Before entering into the mass separator, the laser beam is passing through a focusing lens (focal length 1.5 m) to reduce the divergency of the laser beam and to focus the laser beam in front of the light collectors. The laser beam, after passing through the interaction chambers, is reflected out of the interaction tube by a mirror M7, which is installed inside the mass separator. The mechanical mount of the mirror M7 is properly grounded in order to avoid any deformation of the electric field lines.

All optical components must be cleaned and free of scratches as they can produce a lot of laser stray light.

9.2.3 Wave meter

A wave meter is used for a rough estimate of the frequency of the dye laser. The optical layout of the wavemeter is shown in figure 9.13. It is basically a double Michelson interferometer and allows calibration of an unknown wave number by a known one. Two beams, one from the He-Ne laser (the reference beam) and another from the dye laser (frequency to be measured) follow the same path in the wavemeter, when the wave meter is perfectly aligned. The working of the wavemeter can be understood as follows:

The He-Ne laser beam is divided into two parts by beam splitter 1. One part passes through the beam splitter 1, falls on the beam splitter 2 and is then reflected onto a photodiode. The other part is reflected by the beam splitter 1 towards a moveable triple prism. The backward reflected beam from this prism (has now a path difference as compared with the first part of the He-Ne laser beam and passes through the beam splitter 1) combines with the first part of the He-Ne laser beam on the BS2. These laser beams interfere with each other. The triple prism is moved with an electromagnetic coil over a range of 12 cm. When the prism is moved, the interference pattern changes on the photodiode therefore the current of the photodiode rises and drops. The same consideration is valid for the dye laser beam as well.

The signals from the photodiodes are amplified, converted to TTL pulses and then counted. The movement of the triple prism is monitored by another photodiode which generates a signal to start a count cycle when the prism crosses a certain position. The count cycle is stopped when the photodiode 1 gives 158023 pulses [73]. Since the wave number for the He-Ne light is 15802.3 cm^{-1}, the wave number in cm^{-1} of the dye laser can be determined by:

$$\sigma_{\text{dye laser}} = [(\text{number of pulses counted by photodiode 2}) \times 0.1] \pm 0.1$$

The electronic unit used is “Wavemeter Controller WMC-01”. In this unit, a required value of the wave number of laser frequency can be selected using push buttons available on the front panel. The difference between actual wave number of the dye laser and the selected one is displayed which gives an idea of how far or near is the laser frequency to the selected value.

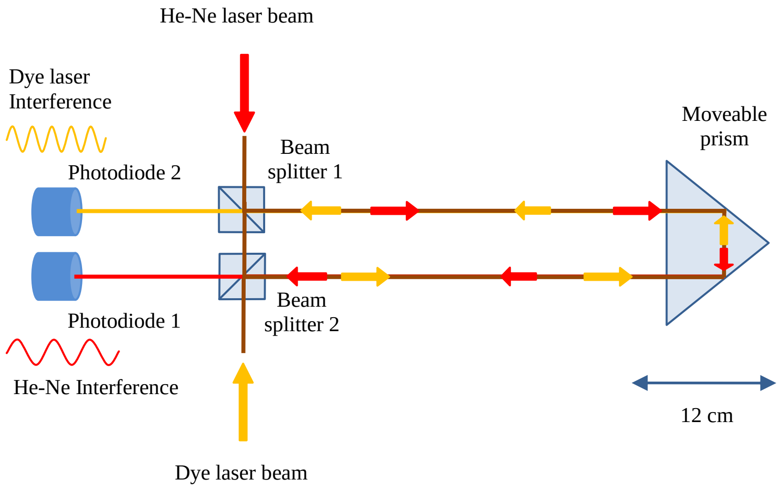

Figure 9.13: Optics of the wavemeter used for wavelength measurements.

9.2.4 Laser frequency stabilization

The laser frequency is stabilized to one of the hyperfine components in order to compensate fluctuations in the acceleration voltage and drift of the laser frequency. The fluorescence light detected in the interaction chamber 2 is used for locking the laser frequency. When the laser frequency is in resonance with the transition frequency at a post-acceleration voltage $U_{pa} = U_0$, then the PMT produces the maximum pulse rate. The post-acceleration voltage is now modulated by a square voltage with peak to peak amplitude equal to the line width of the hyperfine component (e.g. 6 V corresponding to ~ 50 MHz). As clear from figure 9.14, in the first one-half modulation period and in the next one-half modulation period the count rate (N_1, N_2) is same i.e. $\Delta N = N_2 - N_1 = 0$. This reference signal is provided to a “forward-backward counter” and a proper phase is adjusted for $\Delta N = 0$. If voltage is changed from U_0 (for example due to the fluctuations/drift or due to the drift in laser frequency), $\Delta N \neq 0$ (dashed curve in figure 9.14). This difference is converted into a DC voltage by a digital analog converter and is sent to the laser control unit. The laser control unit makes a correction according to the DC voltage and brings back the laser frequency into resonance. For the modulation of the post acceleration voltage, for forward-backward counting and to convert the difference in photon counts into DC voltage signal, a scan control unit (Scan u. Regeleinheit SRE-01 Gerät Nr. 01/03) is used. The modulation frequency used in this work is 2 kHz.

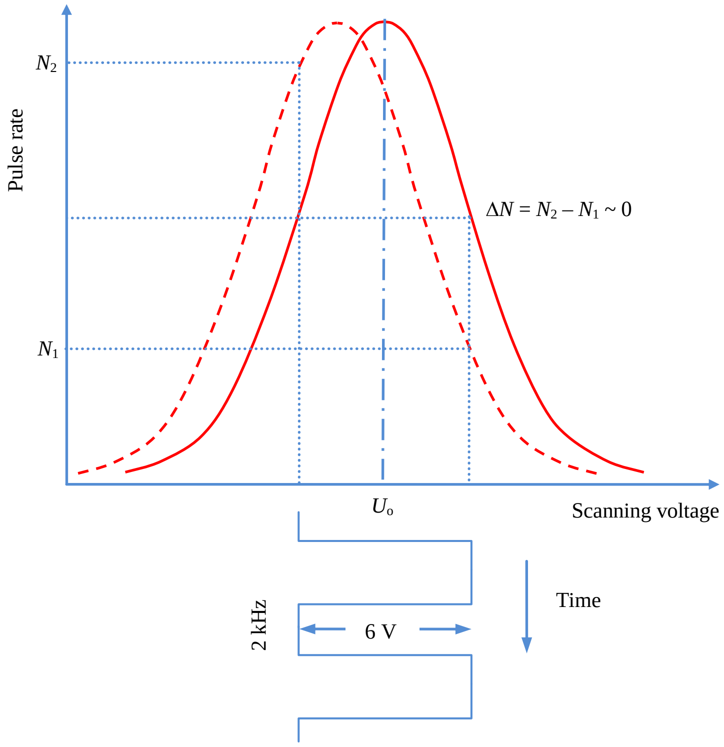

Figure 9.14: The stabilization of laser frequency at a hyperfine component: The laser frequency is at resonance with the hyperfine component (solid curve) at a post-acceleration voltage U_0 and $\Delta N=0$. A little change in voltage results in different count rate (dashed curve) and $\Delta N \neq 0$.

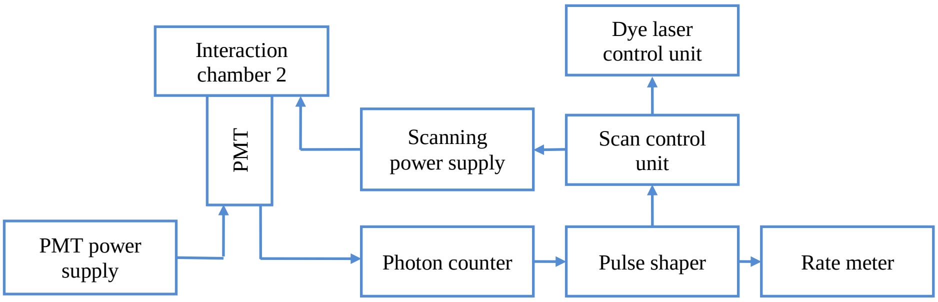

Figure 9.15: Electronics for the stabilization of the laser frequency.

The block diagram of the electronics used for the detection of the fluorescence light in the interaction chamber 2 and for the stabilization of the laser frequency is shown in figure 9.15.

The specifications of different electronic modules used for the laser frequency stabilization are given in table 9.4.

Table 9.4. Specifications of electronic units used in the MARS-II experimental setup for the stabilization of the laser frequency.

Electronic unit	**Specification**
Photomultiplier tube	Photonis: Head on type: XP2020
Power supply for PMT (operated at 2500 V)	Fug: HCN 35 M-3500: ±3500 V, ±10 mA
Photon counter	SSR Instruments Co. Photon Counter, Model: 1120 Amplifier-Discriminator
Pulse distributor	Signalverteiler: SV-04 Gerät Nr. 02 (manufactured at Marburg University)
Rate meter	Wenzel-Elektronik: Rate meter N-R-107
Scan control unit	Scan u. Regeleinheit: SRE-01 Gerät Nr. 01/03 (manufactured at Marburg University)
Scanning power supply	Fug: HCN 35 M-3500: ±3500 V, ±10 mA Programmable 0-10 V = 0-3.5 kV

9.3 Computer programs used for recordings and analysis

Different programs have been employed in order to record the hyperfine structures and to measure their physical quantities (magnetic dipole interaction constant, quadrupole interaction constant constants, line width etc.). A computer software is developed in lab-view to interface a photon counter (Stanford Research Systems Inc. SR400) and a programmable power supply (TTi QPX1200) with a computer. Using this software the hyperfine structures are scanned and recorded in a digital computer. To view the recorded hyperfine structures, a program “data viewer” developed by Prof. L. Windholz is used. For voltage to frequency conversion and to linearize the recorded data points, a computer program is developed in the language “visual basic”. In this work, the influences of the fluctuations in the acceleration voltage and the drift in the laser frequency are minimized by locking the laser frequency (section 9.4.1) to one of the hyperfine components. Therefore, many recordings of same hyperfine structure can be averaged and the signal to noise ratio can be improved. The commercially available software for data analysis “Origin” is used to average multiple recordings. Finally, the hyperfine constants are determined using the “Fitter” program (already discussed in section 6.3).

9.3.1 Interfacing of photon counter and programmable power supply with a computer

A photon counter (Stanford Research Systems Inc. SR400) is used to count the current pulses from a photomultiplier tube (XP2020). For scanning the hyperfine structures using Doppler tuning a programmable high voltage power supply (FUG Elektronik GmBH, programmable 0-10 V = 0 - 3.5 kV) is used. This power supply is controlled by another computer controlled programmable power supply (TTi QPX1200). In this way, a scanning of voltage from 0 – 10 V at QPX1200 corresponds to 0 – 3500 V (about 30 GHz) across the interaction chamber. The photon counter and the QPX1200 are interfaced with a digital computer through separate RS232 serial ports, using a software “Scan(SR400-QPX1200)”. The Doppler tuning is controlled by the software and the data of the hyperfine structures are recorded digitally in a computer. The data can be used for further analysis.

The front panel, block diagram and flow chart of the software are shown in figures 9.16, 9.17 and 9.18 respectively. Different parameters e.g. start and stop voltage value of the scan, voltage step size, count period (time to count photons at a particular voltage) etc. are fed from the front panel. A sequence (name) and a destination folder to record the files are also provided. The files are named as “**element**sequence.dat” e.g. in figure 9.16, name of the first recorded file is **pr**063007. During a scan, the photon counts are plotted against scanning voltage. The program executes as follow:

1. First of all the communication ports are assigned to each unit: COM1 is assigned to the power supply and COM2 is assigned to the photon counter.

2. The software reads the entries from the front panel. For example scan start voltage “V1”, step size “DELTAV1”, destination folder to save the recorded files, scan stop voltage etc.
3. The photon counter is reset and some parameters are fixed e.g. dwell time “dt = 0”, period counts “NP”.
4. Then a loop starts in which the scanning is performed. The photons are counted for a counting period (this value is manually fed in the photon counter therefore, before starting the scanning these values must be confirmed). In the scanning loop, a delay corresponding to the counting time is introduced.

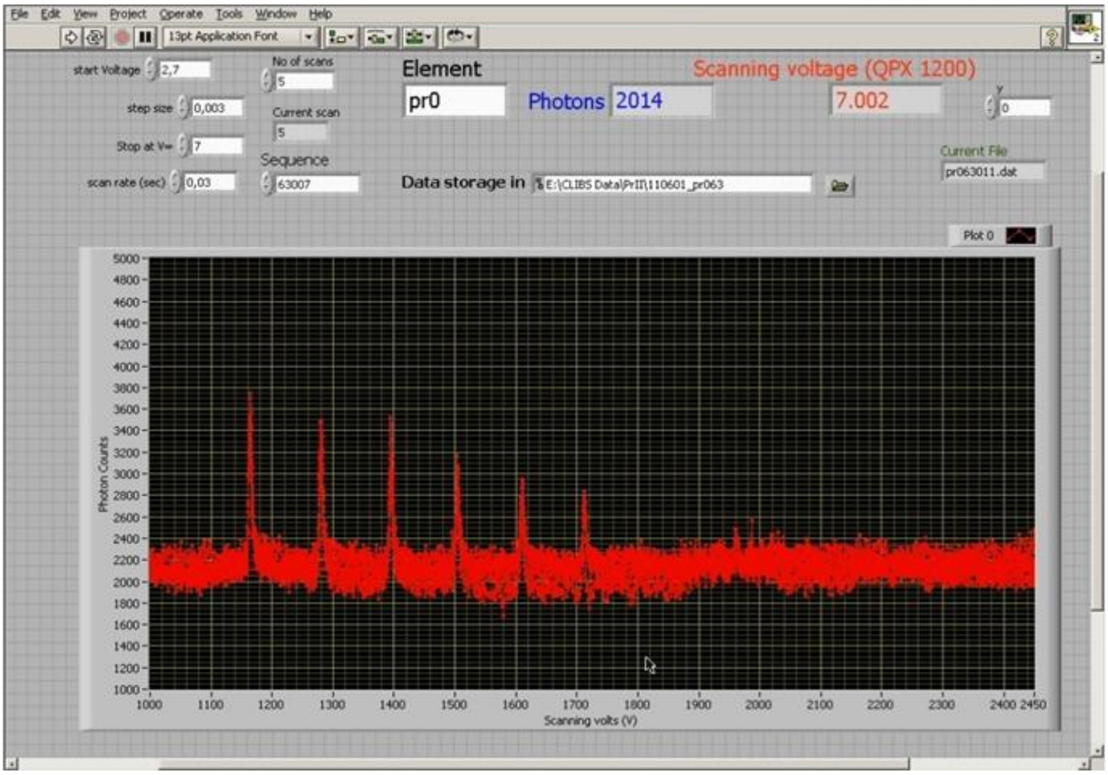
start Voltage 2,7
step size 0,003
Stop at V= 7
scan rate (sec) 0,03
No of scans 5
Current scan 5
Sequence 63007
Element pr0
Photons 2014
Scanning voltage (QPX 1200) 7.002
y 0
Current File pr063011.dat
Data storage in E:\CLIBS Data\PrII\110601_pr063

Figure 9.16: The front panel of the software “Scan(SR400QPX1200)” developed to record the hyperfine structures digitally in a computer. The graphs of five recordings of an optical transition of Pr II are shown with a complete overlap with each other.

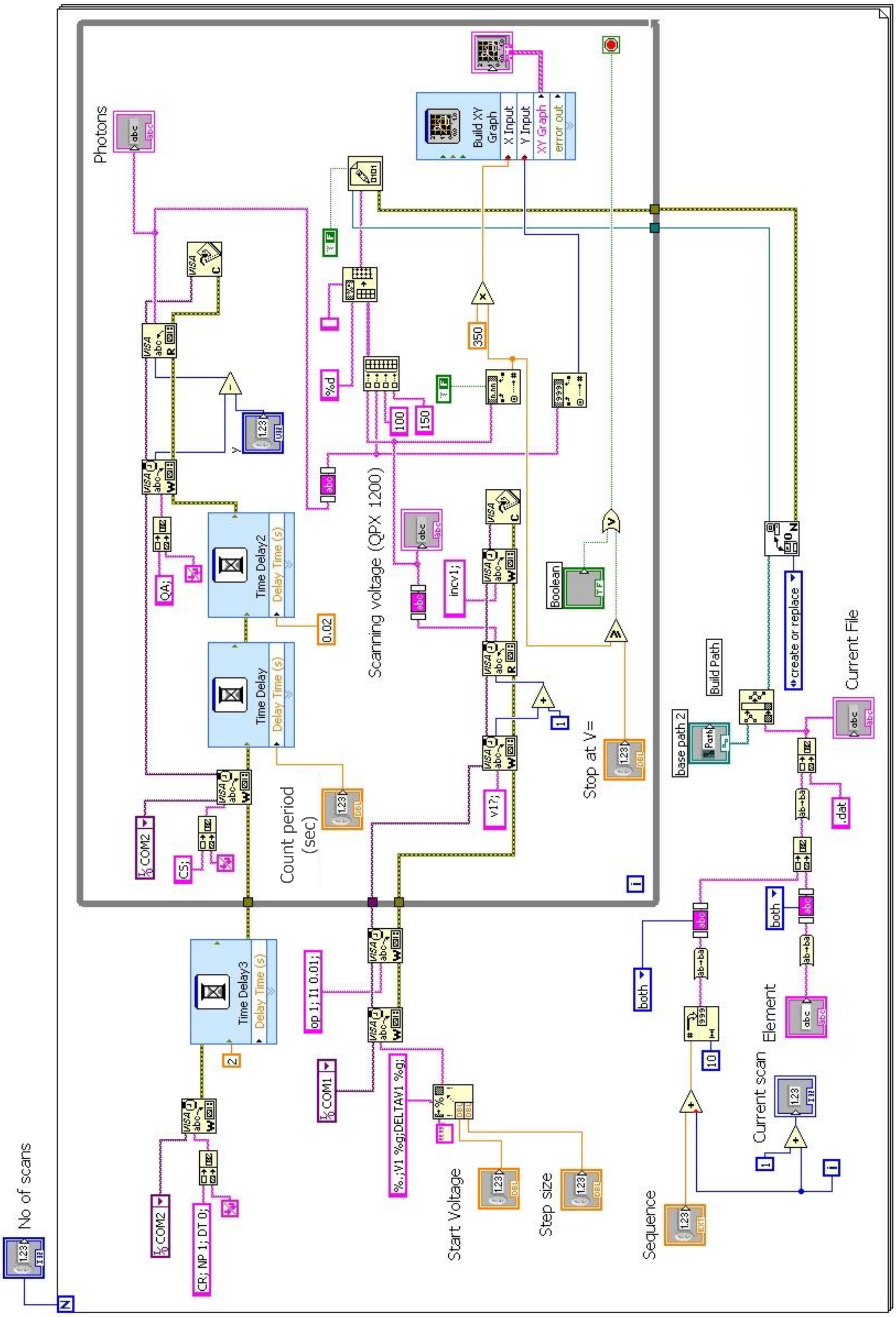

Figure 9.17: The block diagram of the software "Scan(SR400QPX1200)".

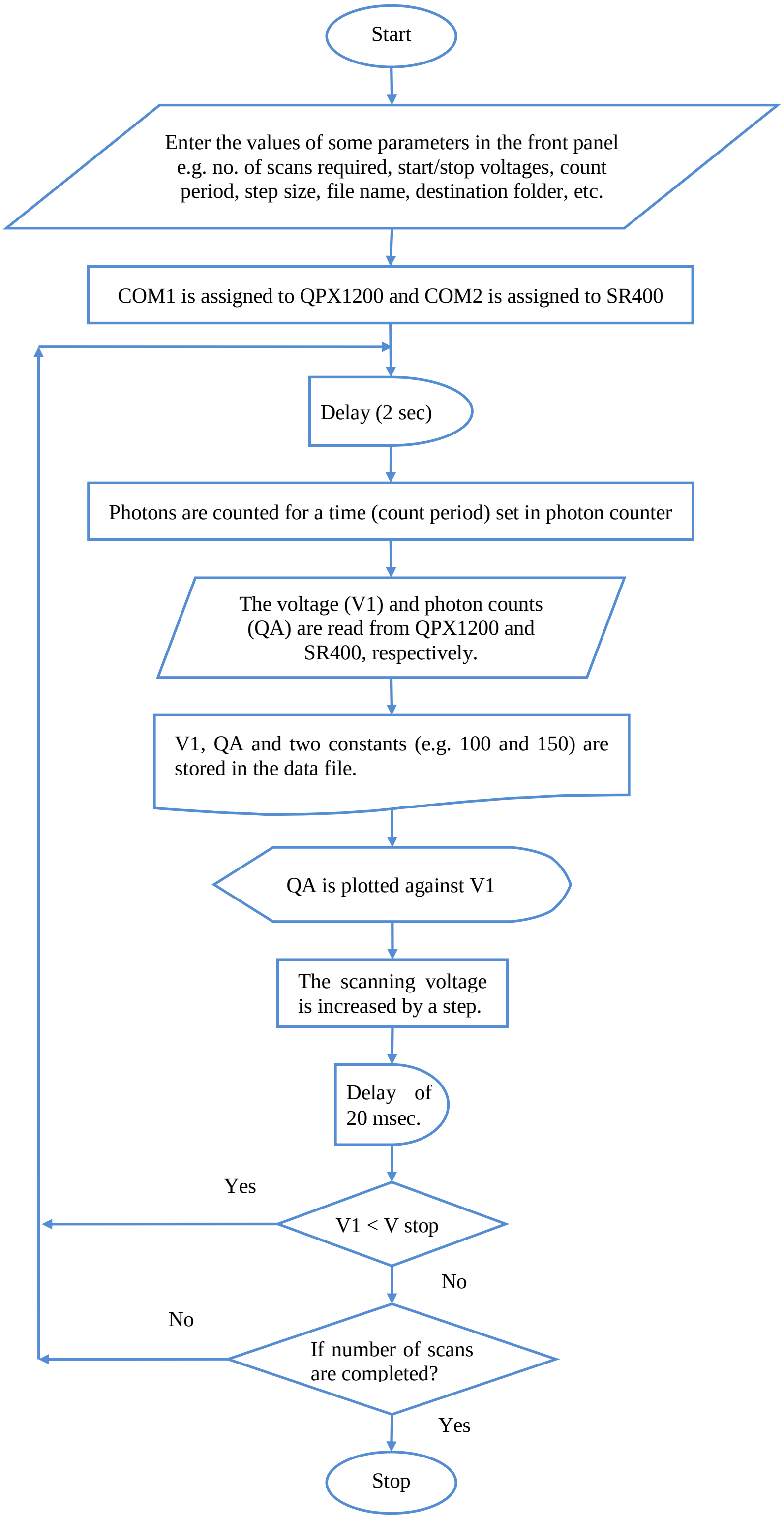

Figure 9.18: The flow chart of the software "Scan(SR400QPX1200)".

5. The displays of the power supply (voltage value: x-axis) and photon counter (photon counts: y-axis) are read.
6. A data file is created in the destination folder: The photon counts are saved in column 1, the scanning voltage is saved in column 2, and in columns 3 and 4 constant values for example 100 and 150 are stored, respectively. The entries in a row are separated by a double space. This format of data entries is the requirement of the data viewer. The file is created for the first measurement. For next measurements, the data points are stored in next rows of this file. A new file is created for a new scan.
7. The recorded data point is displayed in the digital form as well as in the graphical form on the front panel.
8. The scanning voltage is increased by a step size. The rise time of the high voltage scanning power supply is about 15 msec therefore, a delay of 0.02 sec is also introduced so that the counting starts when the voltage is stable at its new value.
9. Steps from 4-8 are repeated until the stop voltage is reached or the program is forcibly stopped.
10. If more than one scan is required, the QPX1200 is set to the start voltage again. A delay of 2 seconds is provided before the start of each additional scan so that the high voltage power supply becomes stable at start voltage. Steps from 2 to 9 are repeated.

9.3.2 The data viewer

The "data viewer" is used for the graphical presentation of the recorded hyperfine structures. To view a recorded file using this program, a special format of data entries is required. In this format; each row of a data file must have 4 entries, separated by a double space i.e.

X(space)(space)Y(space)(space)C(space)(space)B

.

.

Basically, the data viewer can be used for the graphical display of 4 measureable quantities. In this case, only X (the independent variable e.g. scanning voltage) and Y (the recorded intensity) are the variables so C and D are treated as constant numbers here.

In the latest version of the data viewer, the background noise can be subtracted using either a linear or a spline function. A curve using up to 50 supporting points is generated which is then subtract from the recorded intensities to remove the variable background. An example is shown figure 9.19.

(a) A recorded file with a variable background

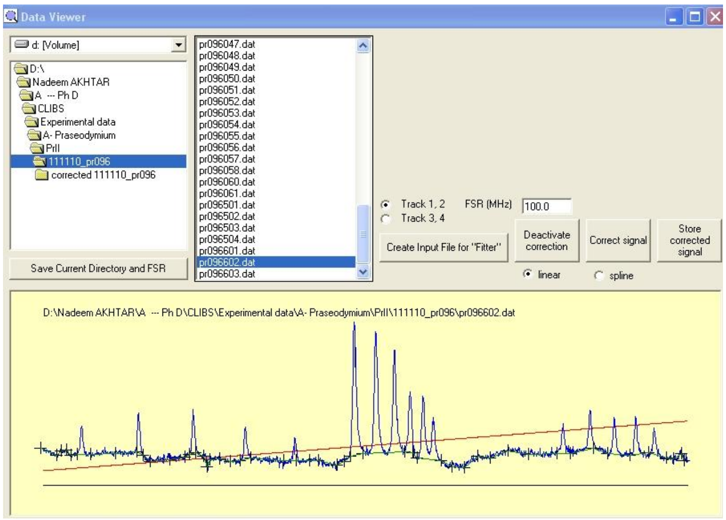

D:\
Nadeem AKHTAR
A --- Ph D
CLIBS
Experimental data
A- Praseodymium
PrII
111110_pr096
corrected 111110_pr096

pr096047.dat
pr096048.dat
pr096049.dat
pr096050.dat
pr096051.dat
pr096052.dat
pr096053.dat
pr096054.dat
pr096055.dat
pr096056.dat
pr096057.dat
pr096058.dat
pr096060.dat
pr096061.dat
pr096501.dat
pr096502.dat
pr096503.dat
pr096504.dat
pr096601.dat
pr096602.dat
pr096603.dat

● Track 1, 2
○ Track 3, 4
FSR (MHz) 100.0
● linear ○ spline

D:\Nadeem AKHTAR\A --- Ph D\CLIBS\Experimental data\A- Praseodymium\PrII\111110_pr096\pr096602.dat

(b) Background is removed

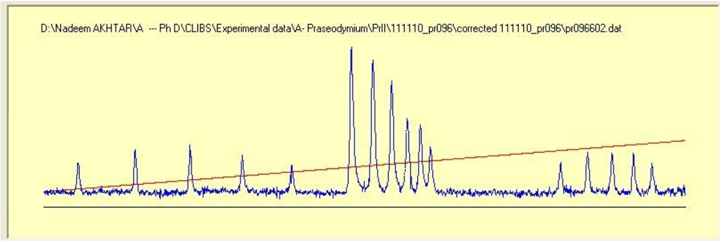

D:\Nadeem AKHTAR\A --- Ph D\CLIBS\Experimental data\A- Praseodymium\PrII\111110_pr096\corrected 111110_pr096\pr096602.dat

Figure 9.19: (a) A recording with a variable background. Background to remove is selected (with black crosses). (b) Shows the same corrected file after the removal of background.

9.3.3 Linearization program "PrLinRel"

The scanning is carried out with equal steps of voltage. Equation 8.7 shows that the relationship between frequency and the acceleration voltage is not linear. But for fitting, (section 6.3) a faster convergence to the best values of the hyperfine constants is obtained when the data points are linear in frequency scale. A software is developed in visual basic for linearization of the recorded data. The frequency points are calculated from the voltage. To take into account the relativistic effects, the following relation [126] is used:

$$\nu = \nu_L(1+\beta)/\sqrt{(1-\beta^2)} \qquad (9.1)$$

$$\text{where } \beta = \frac{v}{c} = \sqrt{1-(1+b)^{-2}} \text{ and } b = \frac{eU}{mc^2} .$$

(e is the elementary charge, m is the rest mass of the ions and c is the velocity of light in vacuum, U is the acceleration voltage).

In the linearization procedure new values of the independent variable (x-values), let say X, are calculated with an equal difference (sz) between them. At a particular point X_L, a new value of Y_L is calculated from the recorded x and y values by adding the weighted y-values which lie within ± sz. The weights are larger for the points which are nearer to X_L and vice versa. If weights are denoted by ds, the value of Y_L at X_L can be calculated using the following relation.

$$Y_L = \frac{\sum(y_i)(ds_i)}{\sum(ds_i)} \qquad \forall\, ds < sz \tag{9.2}$$

where

$$ds_i = \frac{sz - |X_L - x_i|}{sz} .$$

This type of linearization can be performed only if

$$sz \geq \max_{i=1\ to\ n} |x_i - x_{i-1}| \tag{9.3}$$

where n is total number of data points.

The flow chart of the software is shown if figure 9.20.

Algorithm for PrLinRel:

1. A data file is selected and input parameters, like wave number, acceleration voltage and step size are provided.
2. The data points X1 (voltages) and T (intensities) are extracted from the data file and frequency points (X5) are calculated using equation 9.1.
3. For a = 1 to bb (total no. of points), a linear frequency scale is generated by linx(a) = a * sz.

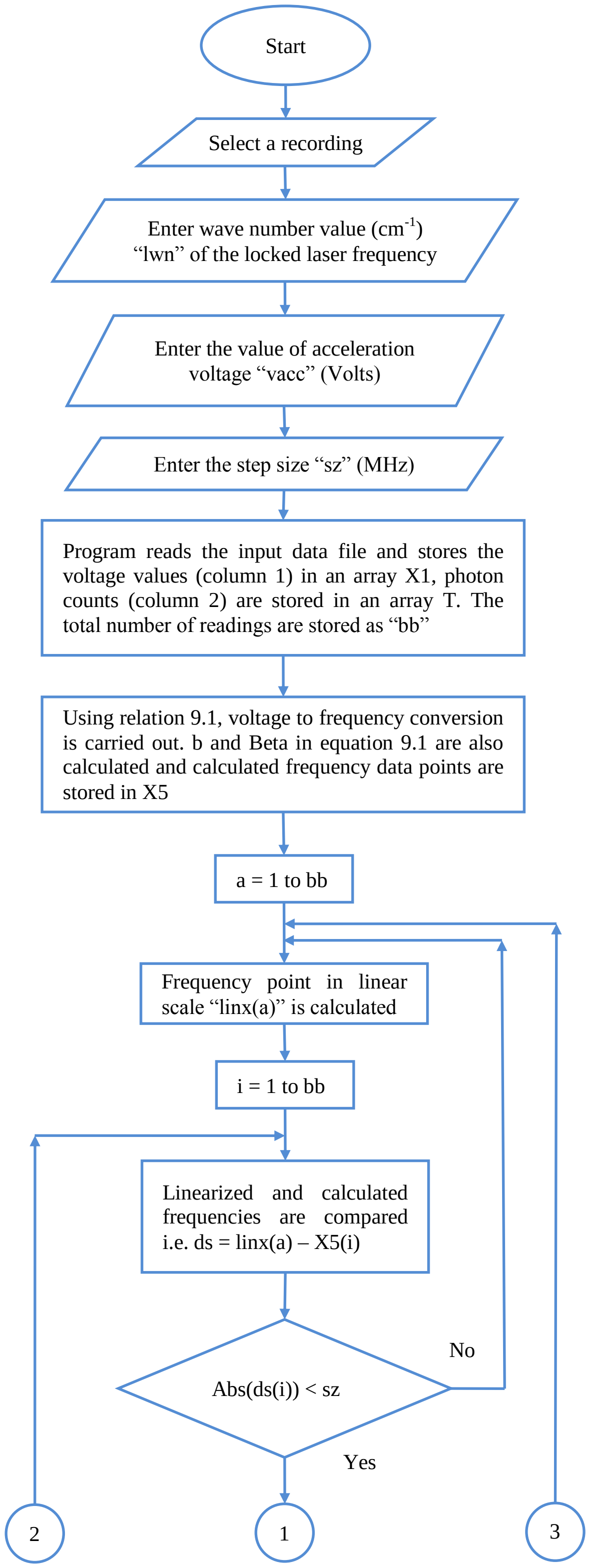
Start
Select a recording
Enter wave number value (cm^{-1}) "lwn" of the locked laser frequency
Enter the value of acceleration voltage "vacc" (Volts)
Enter the step size "sz" (MHz)
Program reads the input data file and stores the voltage values (column 1) in an array X1, photon counts (column 2) are stored in an array T. The total number of readings are stored as "bb"
Using relation 9.1, voltage to frequency conversion is carried out. b and Beta in equation 9.1 are also calculated and calculated frequency data points are stored in X5
a = 1 to bb
Frequency point in linear scale "linx(a)" is calculated
i = 1 to bb
Linearized and calculated frequencies are compared i.e. ds = linx(a) – X5(i)
Abs(ds(i)) < sz
No
Yes
2
1
3

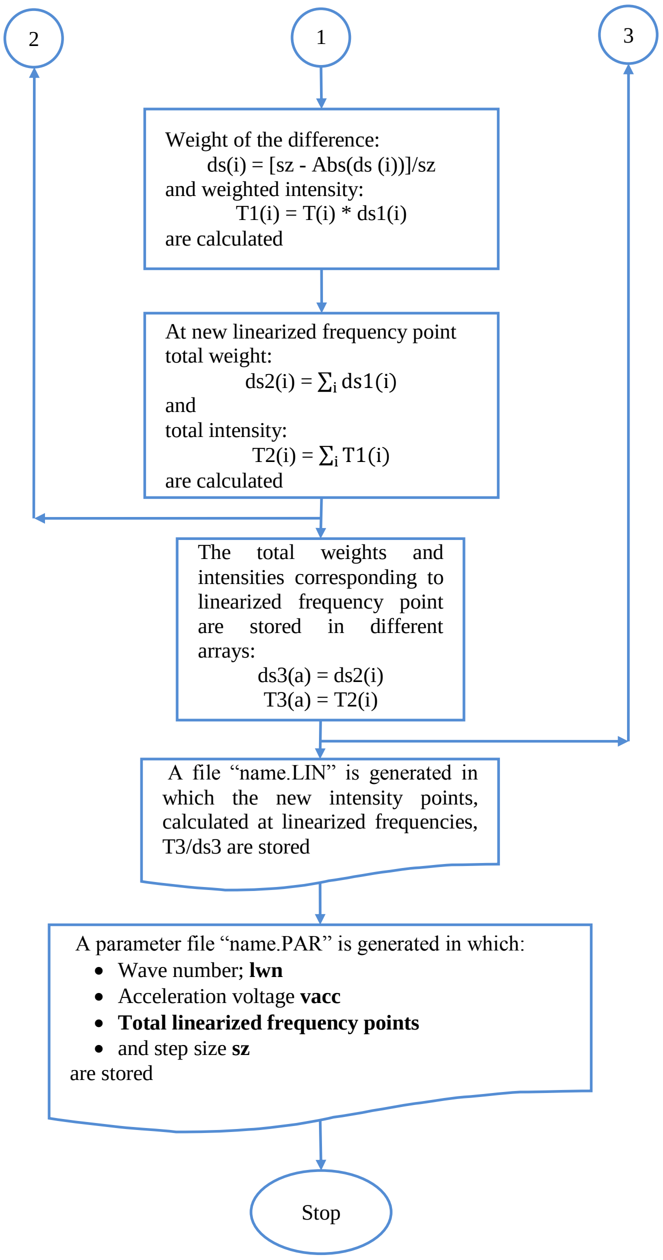

Figure 9.20: The flow chart of the linearization program "PrLinRel".

4. For i = 1 to bb, the linear frequency point is compared with the recorded data points i.e. ds(i) = linx(a) - X5(i).
5. The weights for all points which lie within the ± sz of the linear frequency point are calculated using ds1(i) = [sz-|ds(i)|]/sz.
6. Weighted intensity of ith point is calculated as T1(i) = T(i)*ds1(i)
7. Total weights ds2(i) = $\sum_i$ ds1(i) and total intensities T2(i) = $\sum_i$ T1(i) are calculated.

8. New intensity at linear frequency point is calculated by T2/ds2.
9. Steps 5 to 10 are repeated for next data point.
10. The calculated intensities are stored in a “LIN” file.
11. Some parameters are stored in a “PAR” file.

9.4 Measurements of hyperfine structures

For systematic investigations of the hyperfine structures of transitions of singly ionized praseodymium, the experimental setup MARS-II is used. The ion source is filled with praseodymium powder. Pressure of the system is reduced to ~ 10^{-6} mbar. The ions are produced in the ion source, accelerated to 20 kV and focused by the electrostatic lenses. The 80° magnet separates the ionized oxides and other impurities from the Pr^+ beam. Then the pure Pr^+ beam enters the interaction chambers. The ion beam current is measured at the Faraday cup 4FR at the far end of the vacuum vessel. From the other direction, the laser beam enters into the mass separator through a quartz Brewster window. The ion and the laser beams are superposed collinearly in the interaction chambers.

9.4.1 Scanning and recording of the hyperfine structure

The center of gravity wave number (in air) of a particular transition is calculated using the dispersion relation (equation 6.1 and 6.2) of Peck and Reeder. Then the laser frequency is tuned to the Doppler shifted (~ -9.5 cm^{-1} for Pr) center of gravity of the transition. A voltage scan up to 2.5 kV is performed in the interaction chamber 1 and fast ions are excited and emit fluorescence light if the Doppler shifted transition frequency and the laser frequency are in resonance. Normally, within a range of ±0.4 cm^{-1}, the fluorescence signal is observed. When a fluorescence signal is found, it is optimized by aligning the laser and the ion beams. For weak signals the oven heating is increased a little bit to increase the number of ions. In this work, 10-20 nA ion current measured at 4FR was found to be sufficient for strong transitions (even some lines were recorded at 1-2 nA as well), whereas weak transitions were recorded at 50-100 nA.

In the interaction chamber 2, the fluorescence signal is searched and scanning voltage is tuned to a hyperfine component. The modulation voltage is turned on, phase is matched and the signal from the digital to analog convertor is sent to the laser controller for locking the laser frequency.

After locking the laser frequency at one of the hyperfine components, the fluorescence light in the interaction camber 1 is recorded by applying a post acceleration voltage to chamber 1. The software "Scan(SR400-QPX1200)" (section 9.3.1) is used for the scanning and recording of the hyperfine structures. A step size 0.003 V which corresponds to (0.003×3.5 =) 1.05 V (~ 7.5 MHz) across the interaction chamber is selected for the recording of Pr II optical transitions. The count period is set to 0.030 sec. Many files are recorded for a particular transition. Most of the times 3-5 recordings are averaged to make one file for the measurements of the hyperfine constants and at least three averaged files are treated in order to estimate statistical deviations of the hyperfine constants.

The block diagram of the electronics used for scanning the hyperfine structures is shown in figure 9.21. The specifications of electronic units used in this work are listed in table 9.5.

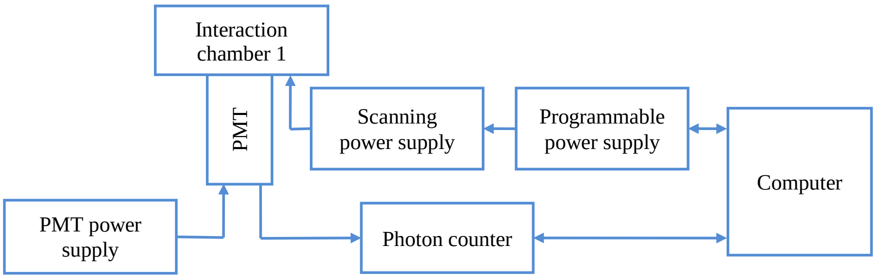

Figure 9.21: Electronics for the scanning of the hyperfine structure.

Table 9.5: Electronic units used for the scanning and recording of the hyperfine structures in the MARS-II experimental setup.

Electronic unit	**Specification/Part number**
Photomultiplier tube	Photonis: Head on type: XP2020 (operating voltage 2000V)
Power supply for PMT (operated at 2000 V)	Heinzinger: Transistor-Netzgerät HN 2000-10
Photon counter	Stanford Research Systems Inc. SR400, Two channel gated photon counter
Computer controlled power supply	PSU Power Flex: TTi QPX1200: 60 V, 50 A;
High voltage programmable power supply	Fug: HCN 35 M-3500: ±3500 V, ±10 mA Programmable 0-10 V ≅ 0-3.5 kV

9.4.2 Data analysis

The recorded data files are viewed using the data viewer program. Good recordings are selected and their background variations are removed (if necessary). The locking of the laser frequency employed in this work minimizes the effects of fluctuations in acceleration voltage as well as the drift in laser frequency: Therefore, multiple recordings can be averaged and the signal to noise ratio can be improved for the averaged files (figure 9.22). The corrected recordings are averaged using the commercially available software “Origin”.

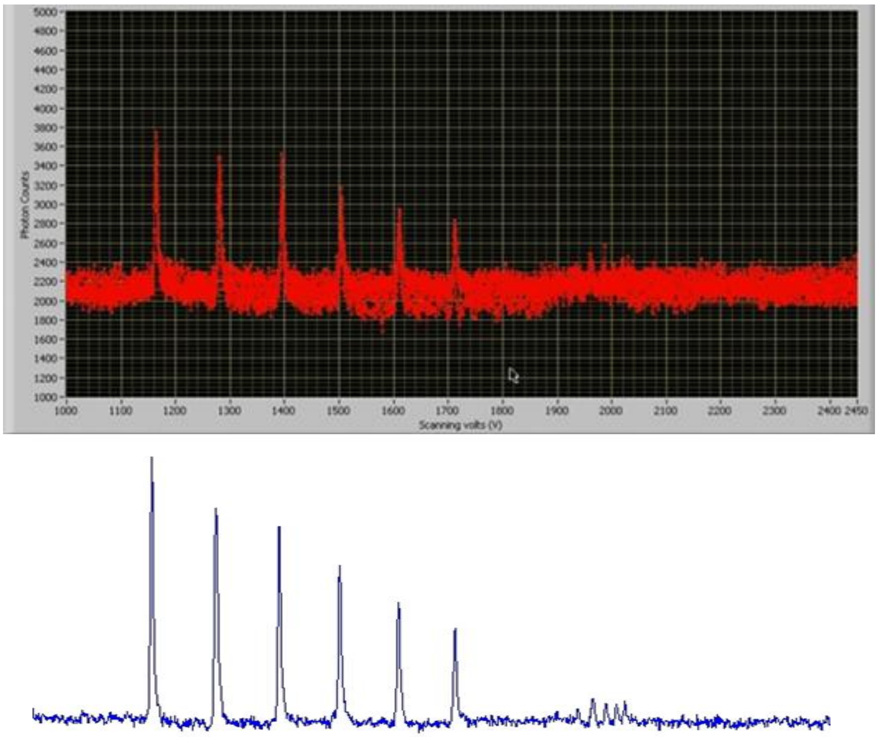

Figure 9.22: The signal to noise ratio can be improved by averaging different recordings. In the upper part of this figure, 5 recordings are shown which are completely overlapping. In the lower part of this figure, the average of these recordings is shown. Now the off diagonal components are much more prominent than in the individual recordings.

If the files are recorded at the same acceleration voltage and laser frequency, the data files can be averaged first and then the resultant file is linearized. If either the acceleration voltage or the laser frequency is different for different recordings, the linearization is performed first and then the LIN files are averaged.

The linearization is performed using the program “PrLinRel”. According to equation 9.3 sz = 9 MHz is chosen for a step size of the scanning voltages 0.003×3.5 V. After linearization, the magnetic dipole interaction constant *A* and quadrupole interaction constant *B* of the levels involved in the transition are determined using “Fitter program”.

9.5 Some pictures of MARS-II

For better understanding of the MARS-II experimental setup, some snap shots of the system are given below.

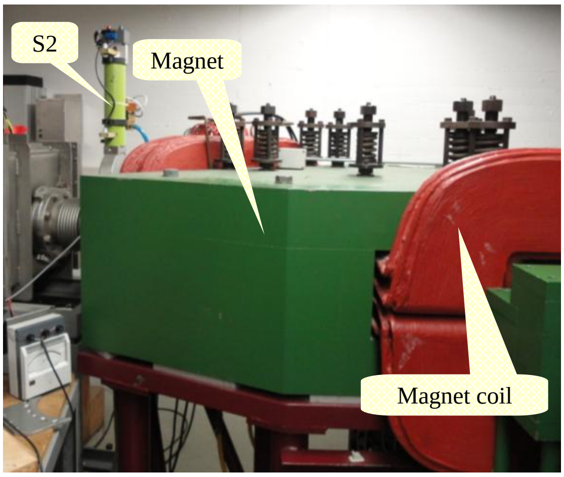

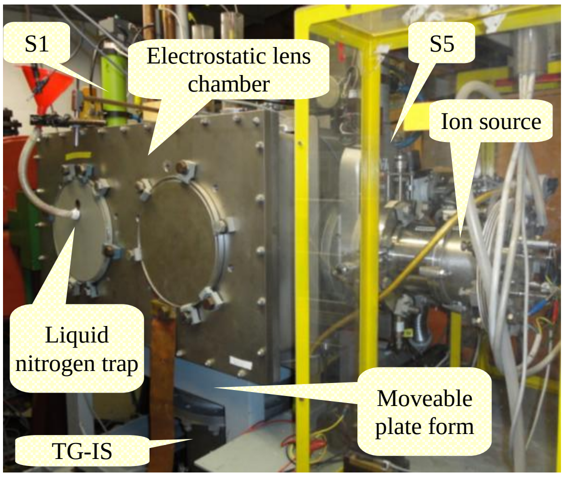

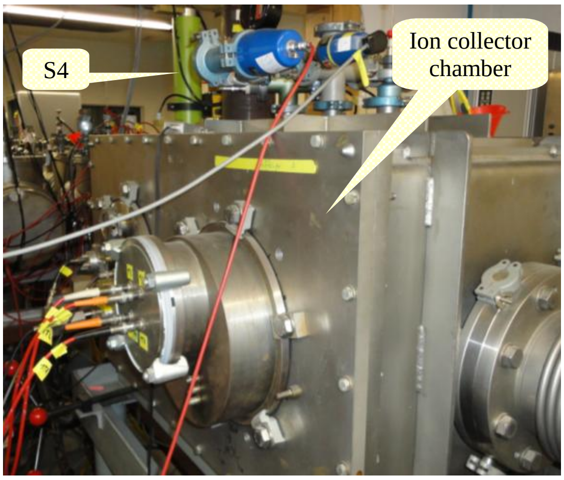

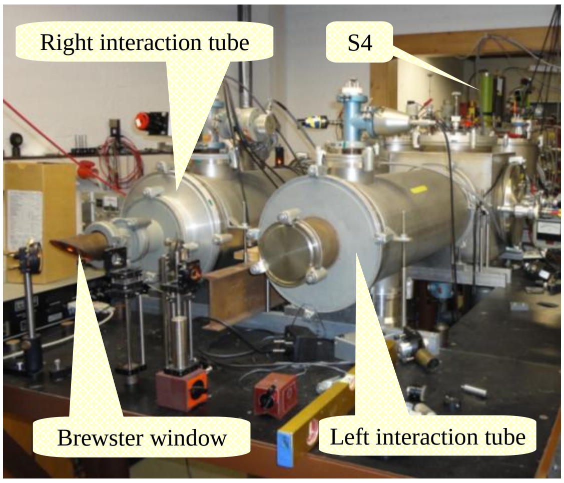

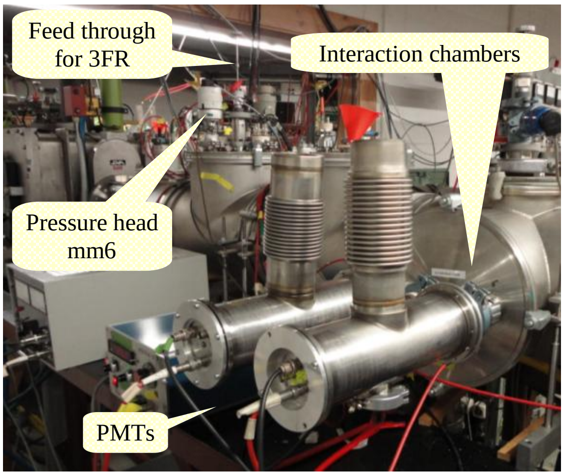
Feed through for 3FR
Interaction chambers
Pressure head mm6
PMTs

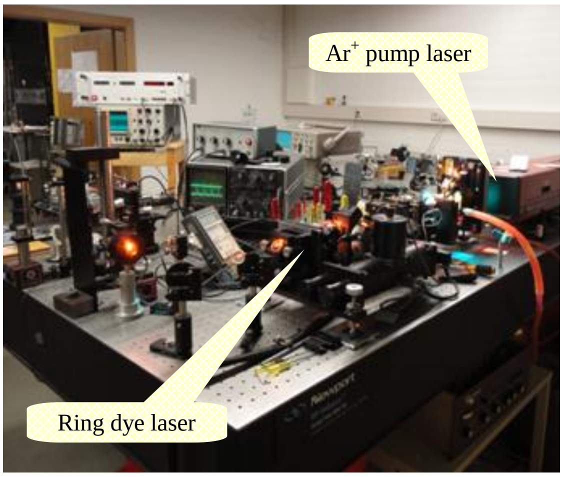
Ar$^+$ pump laser
Ring dye laser

10 RESULTS AND DISCUSSION

In this chapter the results obtained using the MARS-II experimental setup are discussed. As the system was re-installed at the technical university Graz, the system has been first calibrated. For calibration, the ^{137}Ba II line 5853.723 Å was used. Later the hyperfine structures of Pr II transitions were investigated. Using the experimental arrangement of MARS-II, 99 optical transitions of singly ionized praseodymium were recorded and the hyperfine constants of 70 (29 odd and 41 even) ionic levels involved in the transitions were improved.

10.1 Calibration of MARS-II using the barium line 5853.7 Å

Barium is the chemical element with atomic number Z = 56 and with 2 valence electrons. The electronic configuration of singly ionized barium is $1s^22s^2p^63s^2p^6d^{10}4s^2p^6\text{-}d^{10}5s^2p^66s$ [^{2}S]. Barium has 37 isotopes but most of them are highly radioactive and have half-lives in the several milliseconds to several days range. Naturally occurring barium has six isotopes; the most abundant is ^{138}Ba (71.7 %) with nuclear spin I = 0, then ^{137}Ba (11.2 %) with nuclear spin I = 3/2 etc.

Barium is a soft silvery metallic alkaline earth metal. It is never found in pure form because it quickly oxidizes in air. Naturally, it occurs in the form of barium sulfate and barium carbonate. The melting point of pure barium, barium sulfate and barium carbonate are 727 ˚C, 1200 ˚C and 811 ˚C, respectively.

For the calibration of MARS-II, the optical transition of singly ionized barium-137 (^{137}Ba) at 5853.7 Å is investigated. For the investigation of the hyperfine structure of this line, barium nitrate, $Ba(NO_3)_2$, is used for the production of barium ions. Due to the low melting point of ($Ba(NO_3)_2$) (592 ˚C), it is possible to operate the ion source for a long period of time. At a heating power of ~ 180 Watt, about 1 nA of ion current of ^{137}Ba (measured at 4FR) is produced which is sufficient to observe the LIF signal of the line 5853.7 Å. The ions are accelerated to 20 keV, focused with the help of the electrostatic lens system and are mass separated by the magnet. The mass spectrum of barium isotopes is observed at the beam scanner in the ion collector chamber (figure 10.1). Using the deflection potentials 1V, 1T, YK etc. the ion beam of ^{137}Ba is selected and guided into the interaction chambers, where it is superposed with the laser beam.

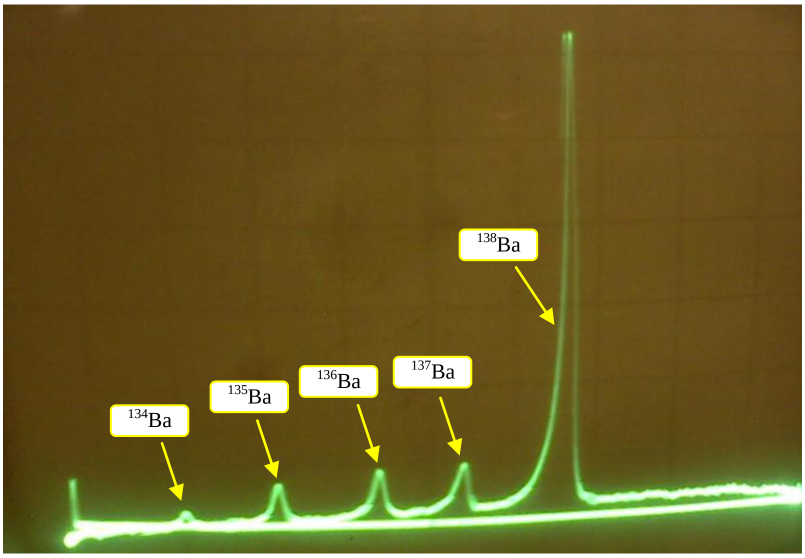

Figure 10.1: The mass spectrum of barium isotopes observed at the beam scanner. This spectrum reflects the natural abundance of these barium isotopes (the natural abundance of ^{138}Ba is about 71.7%, ^{137}Ba is 11.2%, ^{136}Ba is 7.9%, ^{135}Ba is 6.6% and ^{134}Ba is about 2%).

Two low lying metastable d-levels are populated in the ion source. By means of the laser excitation, level 5*d* $^2D_{3/2}$ $\sigma = 4873.852$ cm^{-1} [127] is excited to 6*p* $^2P°_{3/2}$ $\sigma = 21952.404$ cm^{-1} [127] with $\lambda = 5853.7$ Å. The upper level decays to the ground state by emitting blue resonance light with $\lambda = 4554$ Å (figure 10.2), which serves as monitor line. To observe the resonance, the laser frequency is tuned to 17068.81 cm^{-1} (the Doppler shift amounts to 9.6 cm^{-1} at $U = 20$ kV). To record the hyperfine structure of the line, a voltage scan of about 200 Volts is carried out with a step size 0.7 V ≅ 5.3 MHz. The recorded hyperfine structure is shown in figure 10.3a.

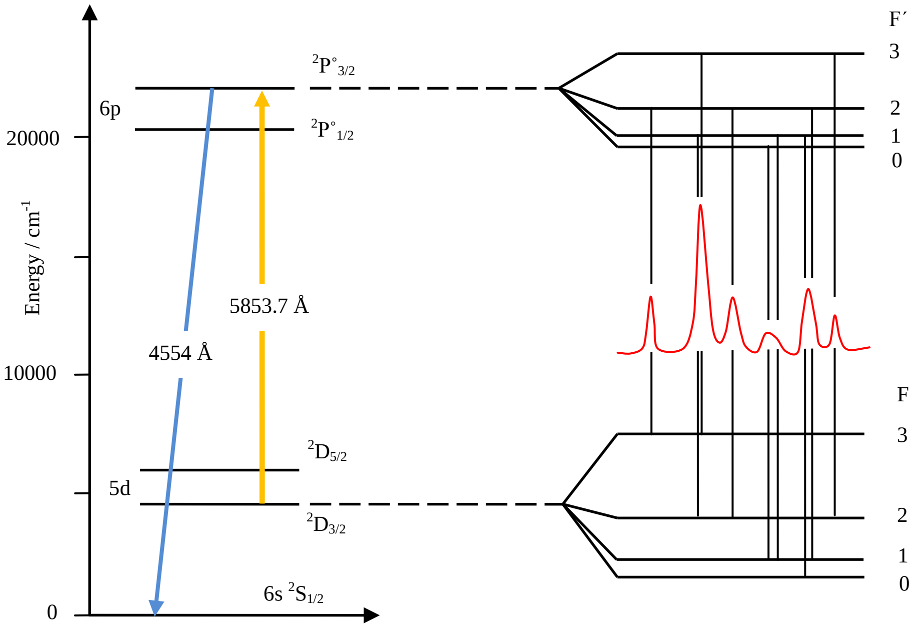

Figure 10.2: The level scheme of ^{137}Ba II and the hyperfine structure splitting of the transition 5d $^2D_{3/2}$ to 6p $^2P°_{3/2}$ with λ = 5853.7 Å.

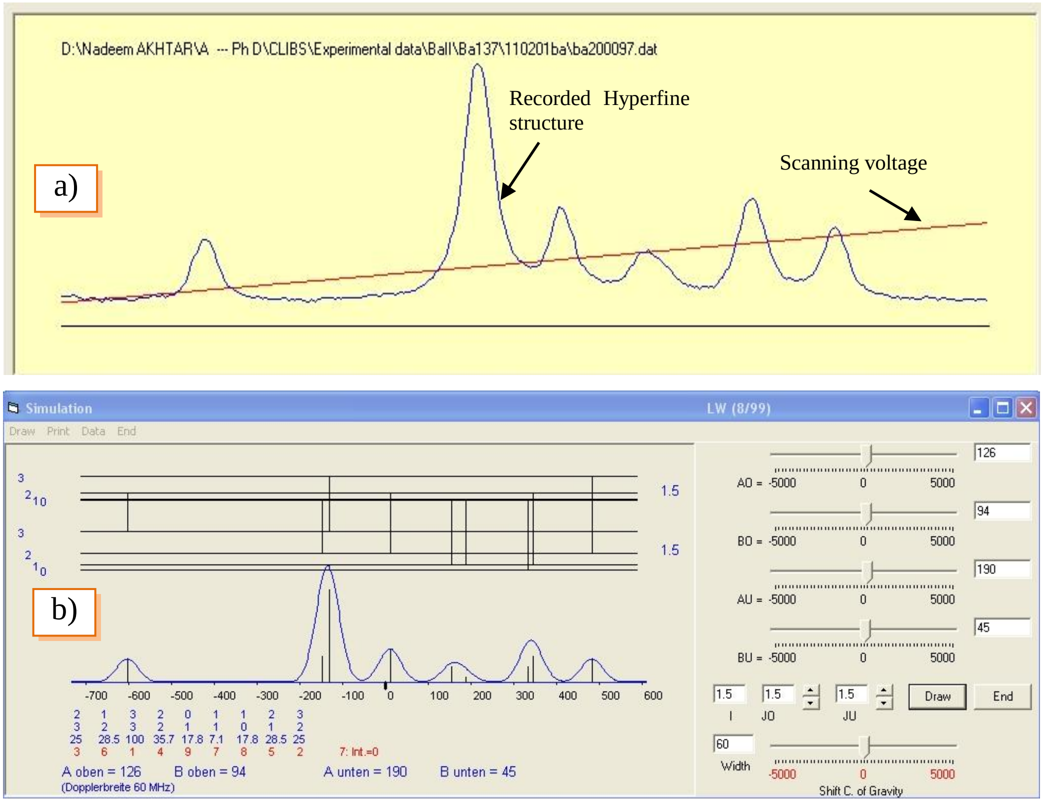

D:\Nadeem AKHTAR\A --- Ph D\CLIBS\Experimental data\BaII\Ba137\110201ba\ba200097.dat

LW (8/99)

```
2     1     3     2     0     1     1     2     3
3     2     3     2     1     1     0     1     2
25    28.5  100   35.7  17.8  7.1   17.8  28.5  25
3     6     1     4     9     7     8     5     2          7: Int.=0
A oben = 126       B oben = 94          A unten = 190       B unten = 45
(Dopplerbreite 60 MHz)
```

AO = -5000 0 5000: 126

BO = -5000 0 5000: 94

AU = -5000 0 5000: 190

BU = -5000 0 5000: 45

I: 1.5

JO: 1.5

JU: 1.5

Width: 60

Shift C. of Gravity: -5000 0 5000

Figure 10.3: (a) The recorded and (b) the simulated hyperfine structure of the ^{137}Ba II line λ = 5853.7 Å.

The nuclear spin quantum number of ^{137}Ba is I = 3/2. For $J = 3/2 = I$, both combining levels split into four hyperfine levels (F = 3, 2, 1, 0). The hyperfine structure contains 3 diagonal hyperfine components with $\Delta F = \Delta J = 0$ (F'-F: 3-3, 2-2, 1-1: 0-0 is not allowed), a first group of 3 off-diagonal components with $\Delta F = -1$ (F'-F: 2-3, 1-2, 0-1) and a second group of 3 off-diagonal components with $\Delta F = +1$ (F'-F: 3-2, 2-1, 1-0). The hyperfine constants of the levels involved in the transition are determined by fitting the recorded hyperfine structure using the fitter program. The best fit situation of the recorded hyperfine structure is shown in figure 10.4.

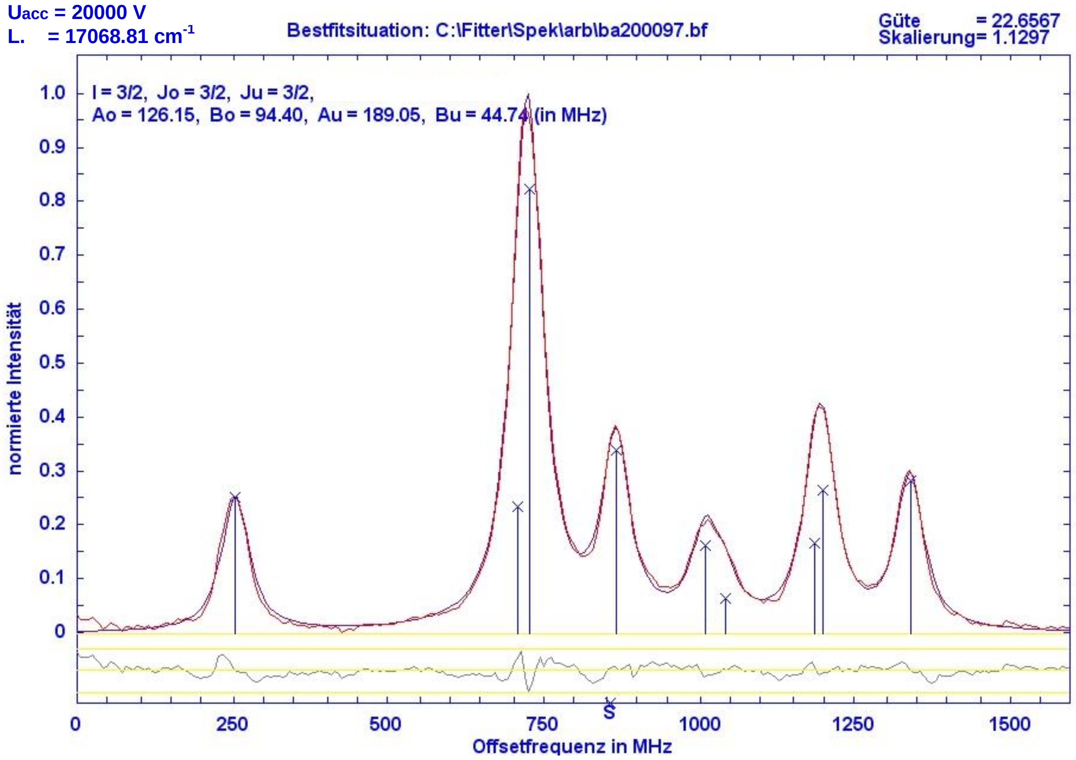

Figure 10.4: The best fit situation of the recorded hyperfine structure of the ^{137}Ba II line λ = 5853.7 Å.

The measured line width is about 55 MHz. The curve fitting is performed using a mixed line profile. The best results are obtained for 10% Gaussian and 90% Lorentzian profiles. The results obtained in this work are compared with the previously measured values using the same setup in Marburg and with literature values in table 10.1. The results are found in good agreement with the literature values. Thus we concluded that the setup is suitable to investigate the hyperfine patterns of ionic transitions of other elements.

Table 10.1: Comparison of hyperfine constants A and B of the Ba II line λ = 5853.7 Å determined in this work with literature values. The upper and the lower levels involved in the transition are: σ = 21952.404 cm^{-1} [127] *(6s $^2P^\circ_{3/2}$) and σ = 4873.852 cm^{-1}* [127] *(5d $^2D_{3/2}$).*

Method of measurements	A_{up}	B_{up}	A_{lo}	B_{lo}	Reference
CLIBS	**126.3(4)**	**94.3(20)**	**189.5(5)**	**44.6(20)**	**This work**
Theoretical	128.27	92.87	189.92	46.23	B. K. Sahoo [128]
CLIBS	126.2(8)	95.8(15)	191.1(6)	46.8(20)	C. Höhle [66]
CLIBS (laser-rf spectroscopy)	127.1(6)	89.7(15)	189.7288(7)	44.5408(17)	M. V. Hove [129]

10.2 Investigation of hyperfine structures of Pr II optical transitions

After checking the setup by an investigation of a ^{137}Ba II transition, a study of the hyperfine structures of Pr ionic transitions is carried out in order to determine accurate values of the hyperfine constants of Pr II levels. Using collinear laser ion beam spectroscopy with the MARS-II experimental setup, 99 Pr II ionic transitions are investigated resulting in an improvement of the hyperfine constants of 70 ionic levels. The energy level diagram of the investigated lines is shown in figure 10.5.

The investigated transitions are listed in Table 10.5. The hyperfine constants of the odd levels and the even levels determined in this work are given in Table 10.6 and table 10.7, respectively. The results are compared with available literature values.

This section is divided into three sub-sections: In the first section 10.2.1, some specific examples of the investigation of hyperfine structures using CLIBS are discussed in increasing order of *J* values of the lower levels. In the second section 10.2.2, the results obtained using CLIBS and saturation spectroscopy (chapter 7) are compared.

The optical spectrum of Pr II is rich on lines and there are many chances that the centers of gravity of two or more ionic transitions overlap or lie close to each other and the hyperfine components of different hyperfine structures overlap. During this research work, some hyperfine structures are recorded with their centers of gravity lying very close to each other. These measurements are discussed in the third section 10.2.3.

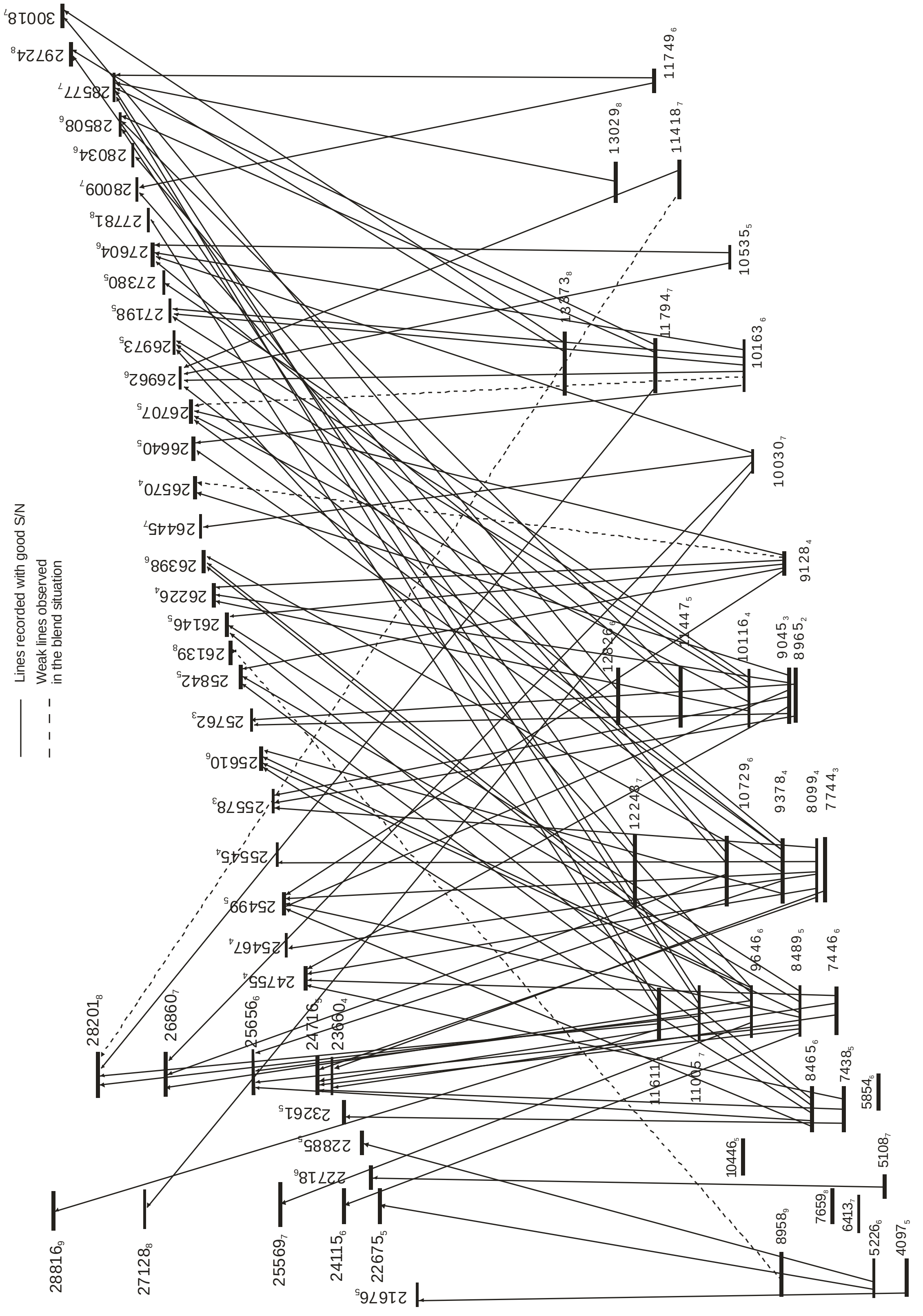

Figure 10.5: Energy level diagram of transitions investigated using CLIBS.

10.2.1 Investigation of hyperfine structures using CLIBS

A typical hyperfine pattern of a Pr II spectral line consists of 6 diagonal (strong) components (for $J \geq I$) with $\Delta F = \Delta J$ and two groups of off-diagonal components (containing 4 or 5 components, depending upon the transition rules). These hyperfine components are well resolved if a hyperfine structure is widely spread. Sometimes, this is not the case and some hyperfine components overlap with each other. Nevertheless, the hyperfine constants can still be determined if some of the off-diagonal components are prominent and well resolved. In the following examples some hyperfine patterns of Pr II transitions are discussed with different A and J values of the combining levels.

Experimentally recorded hyperfine structures of Pr II spectral lines:

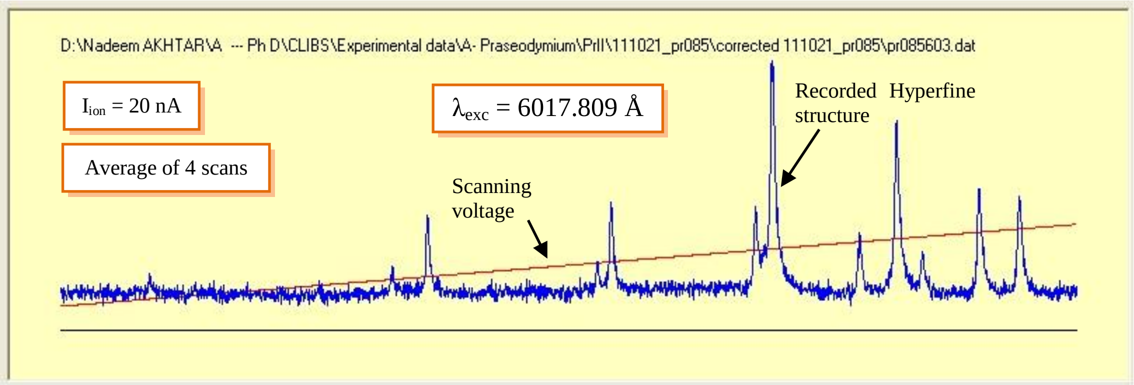

Figure 10.6: See section 10.2.1.1.

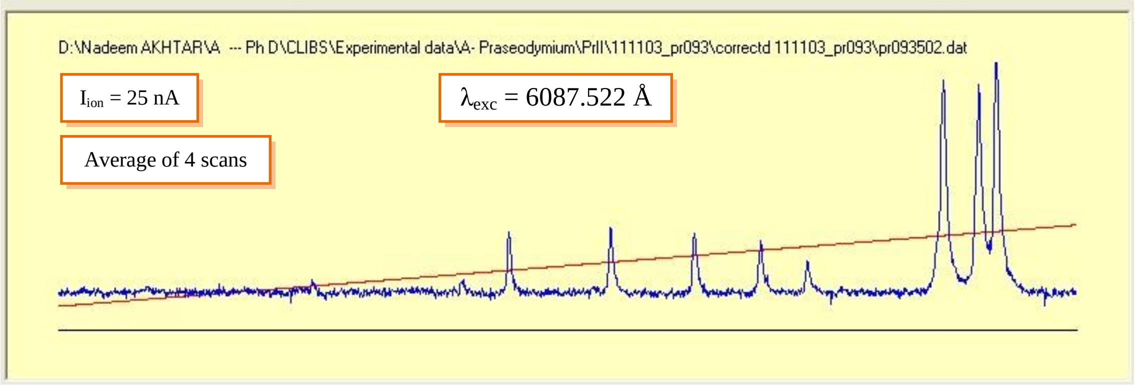

Figure 10.7: See section 10.2.1.2.

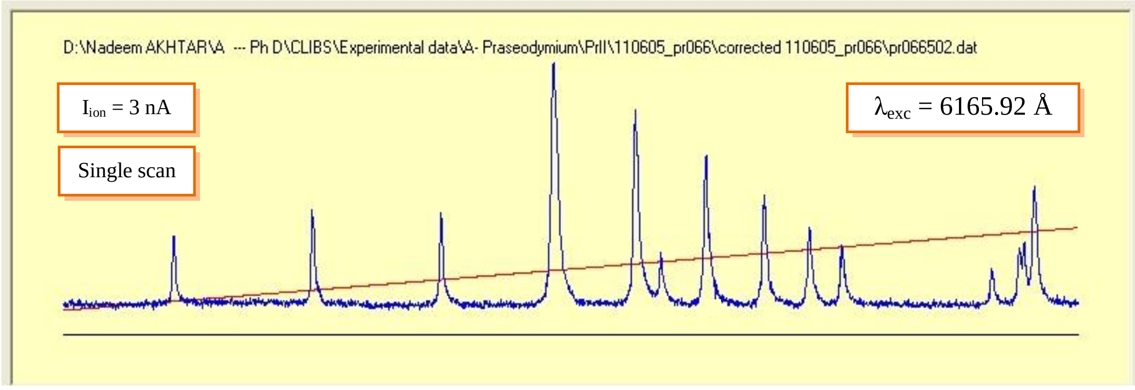

Figure 10.8: See section 10.2.1.3.

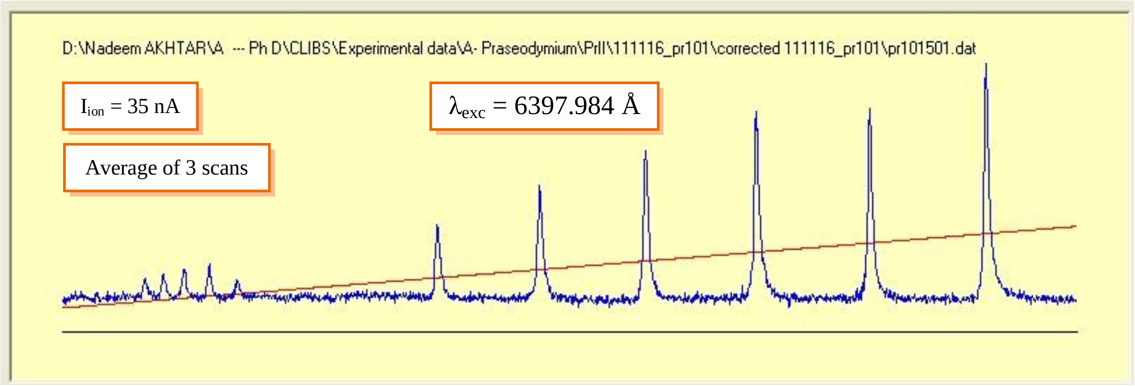

Figure 10.9: See section 10.2.1.4.

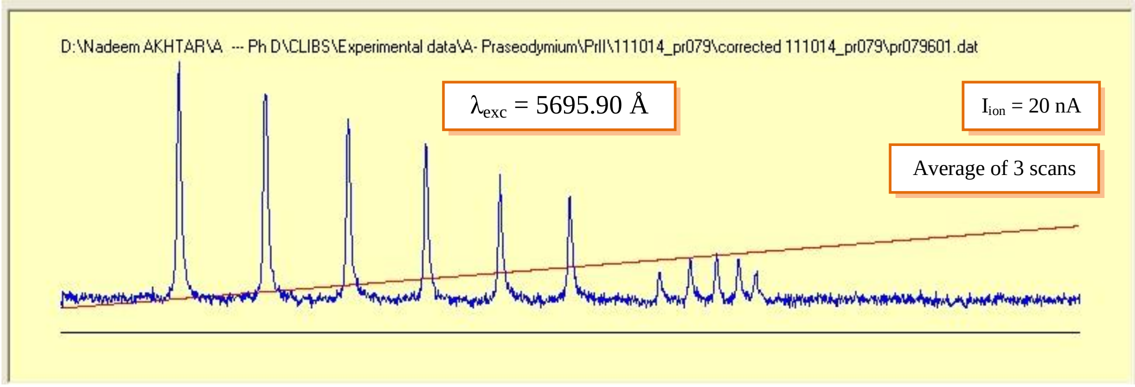

Figure 10.10: See section 10.2.1.5.

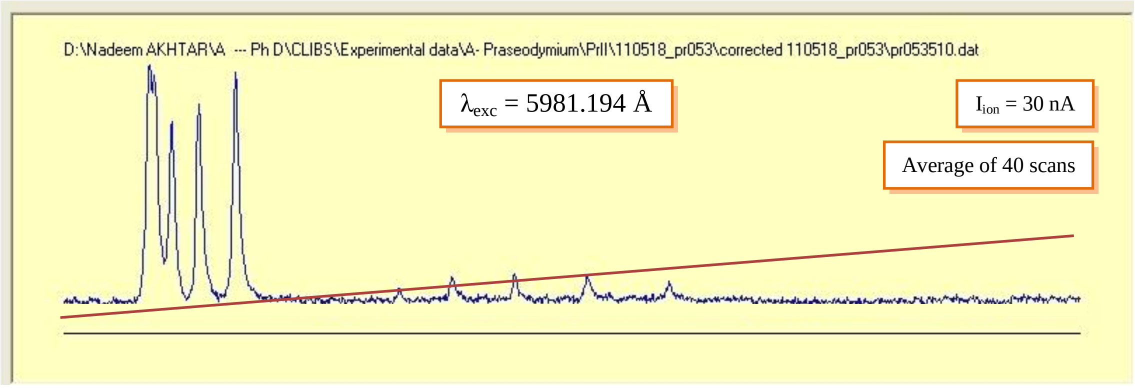

Figure 10.11: See section 10.2.1.6.

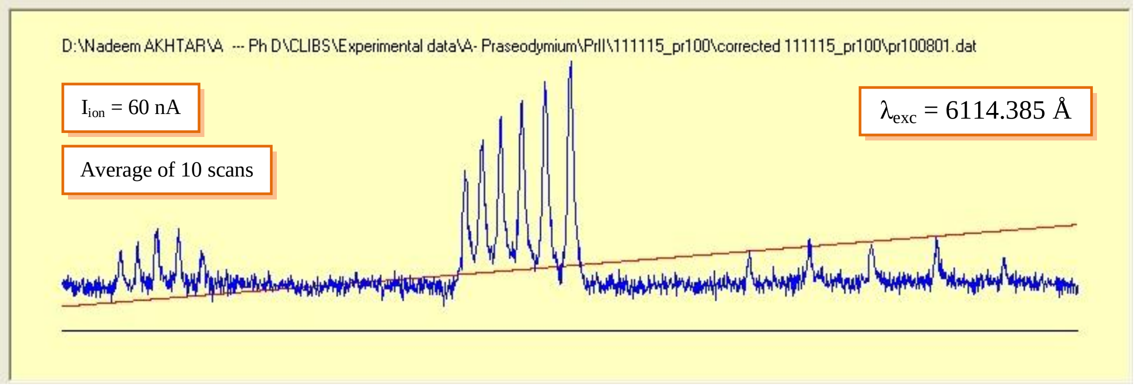

Figure 10.12: See section 10.2.1.7.

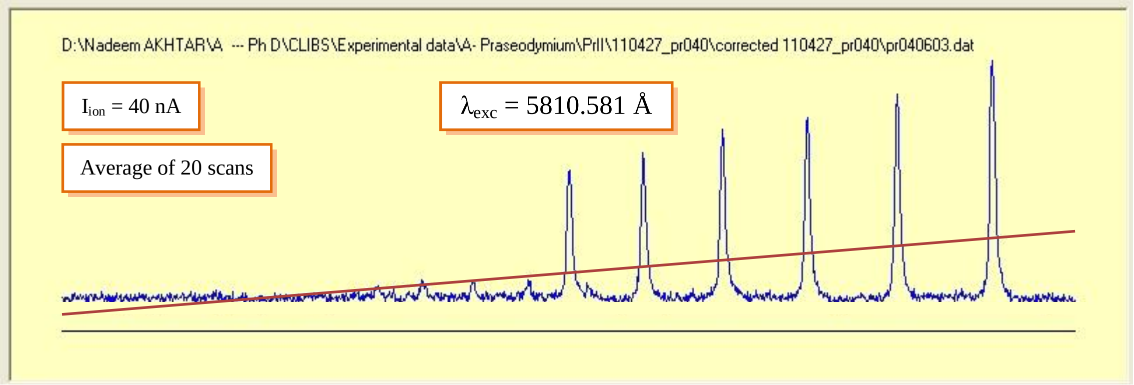

Figure 10.13: See section 10.2.1.8.

10.2.1.1 Hyperfine structure of the Pr II line 6017.809 Å

The recorded hyperfine structure of the Pr II line 6017.809 Å is shown in figure 10.6. Here ions being in the lower odd energy level $\sigma = 8965.764°_2$ cm^{-1} are excited to the upper even energy level $\sigma = 25578.507_3$ cm^{-1}. The upper level splits into 6 hyperfine levels with total quantum numbers $F = 11/2$, ….. 1/2 as $J = 3 > I$ for this level. The J value of the lower level is $2 < I$, so it splits into 5 hyperfine levels with the total quantum numbers $F = 9/2$, ….. 1/2 ($J = 2$ is the lowest J value observed, of the levels investigated during this work). Therefore, instead of 6, there are 5 diagonal hyperfine components for $\Delta F = \Delta J = +1$ in this hyperfine pattern. The 4 strong peaks represent the 5 diagonal components with an overlap of the 4th and 5th components (the last peak in figure 10.6 or figure 10.14). There are five off-diagonal components with $\Delta F = 0$ and four off-diagonal components with $\Delta F = -1$. The strongest diagonal component lies towards the lower frequency side that means the splitting of the lower level is larger than that of the upper level i.e. $A_{\mathrm{lo}} > A_{\mathrm{up}}$. Figure 10.14 shows the best fit results obtained from fitter program.

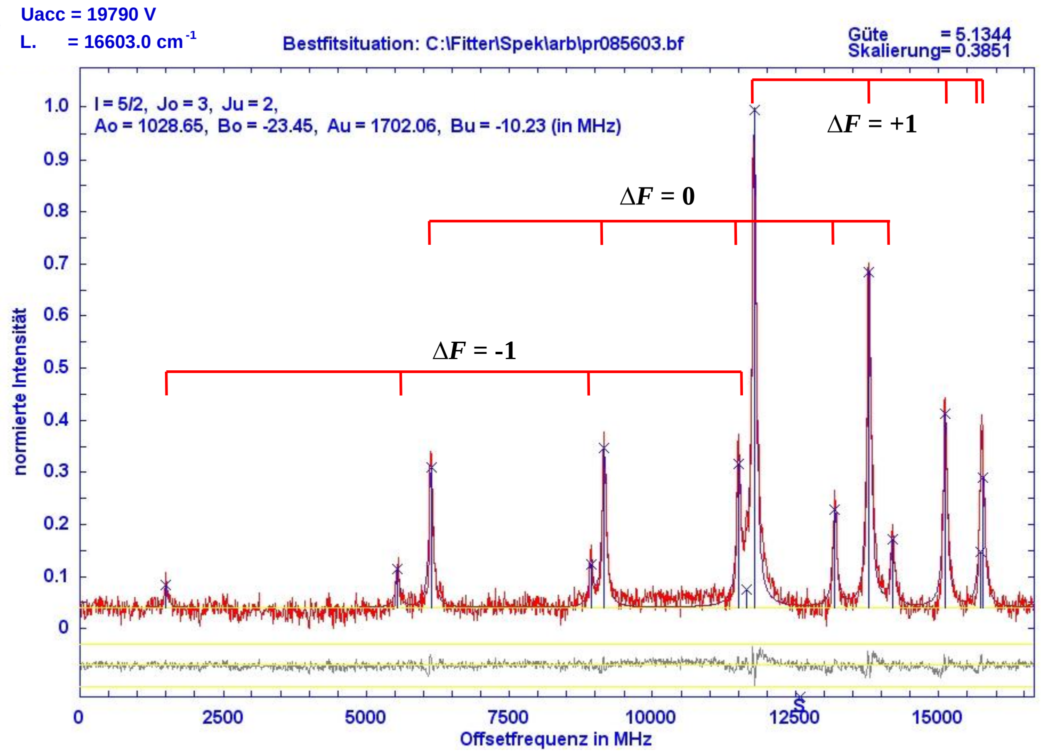

Figure 10.14: The best fit situation of the hyperfine structure of the line 6017.809 Å.

10.2.1.2 Hyperfine structure of the Pr II line 6087.522 Å

In figure 10.15, the hyperfine pattern of the transition 6087.522 Å is shown. The lower and the upper levels involved in the transition are $\sigma = 9045.051^{\circ}{}_{3}$ cm^{-1} and $\sigma = 25467.549_{4}$ cm^{-1}, respectively. The upper level splits into 6 hyperfine levels with total quantum numbers F = 13/2, ….. 3/2 and the lower level splits into 6 hyperfine levels with total quantum numbers F = 11/2, ….. 1/2. Three strong peaks represent the 6 diagonal hyperfine components with $\Delta F = \Delta J = +1$. The strongest diagonal component ($F' - F$: 13/2 – 11/2) is overlapping with the 6th diagonal component (3/2 – 1/2), the 2nd diagonal component (11/2 – 3/2) overlaps with 5th diagonal component and the 3rd diagonal component is combining with the 4th diagonal component (as can be seen in the best fit situation in figure 10.15), therefore instead of 6 diagonal components, 3 strong peaks are prominent in the recorded hyperfine structure. There are five off-diagonal components with $\Delta F = 0$ and four off-diagonal components with $\Delta F = -1$.

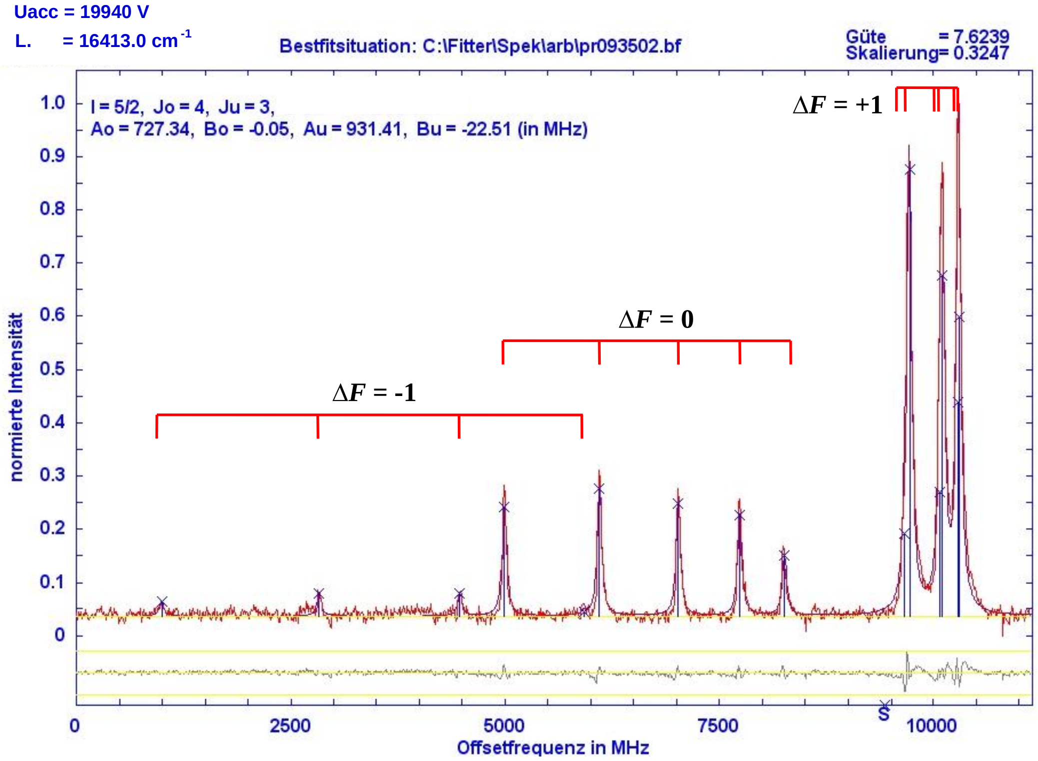

Figure 10.15: The best fit situation of the hyperfine structure of the line 6087.522 Å.

10.2.1.3 Hyperfine structure of the Pr II line 6165.92 Å

In figure 10.16, the best curve of the recorded hyperfine pattern of the transition 6165.92 Å is shown. The lower and the upper levels involved in the transition are $\sigma = 7446.530^{\circ}_{4}$ cm^{-1} and $\sigma = 23660.171_{4}$ cm^{-1} respectively. The 6 diagonal hyperfine components with $\Delta F = \Delta J = 0$ are the most prominent ones. To the right as well as to the left side of the diagonal components there are two groups with 5 components, they belong to the off-diagonal $\Delta F = \pm 1$ hyperfine transitions. One component of the $\Delta F = -1$ group coincides with the strong component $\Delta F = 0$, $F = 13/2 - 13/2$.

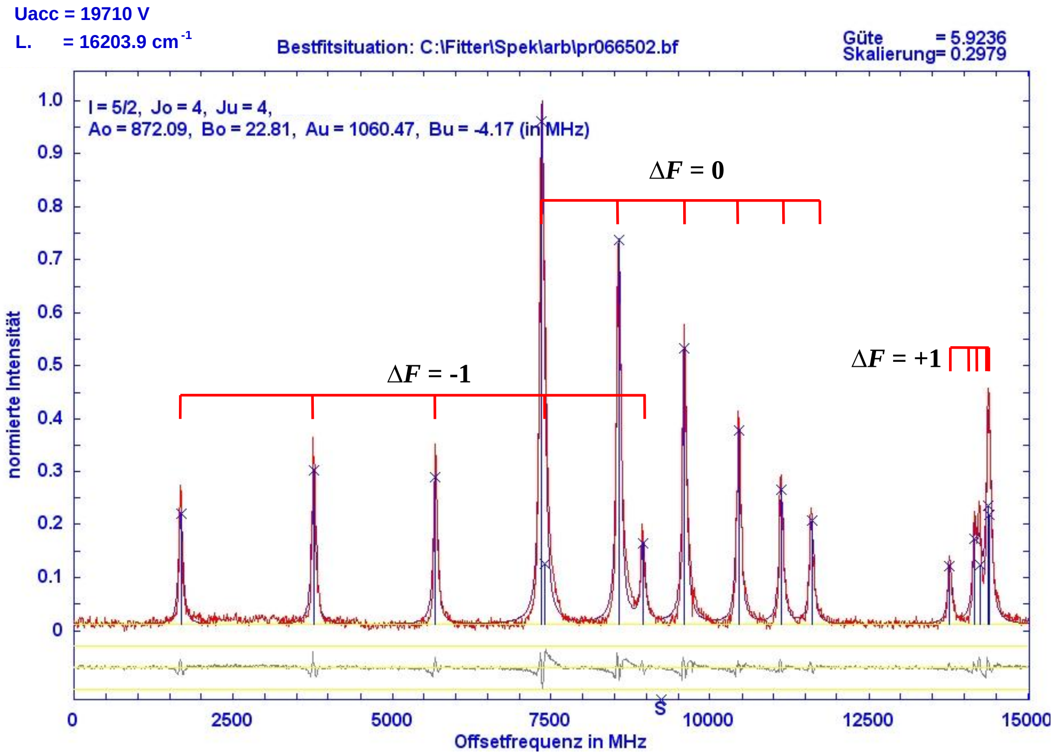

Figure 10.16: The best fit situation of the hyperfine structure of the line 6165.92 Å.

10.2.1.4 Hyperfine structure of the Pr II line 6397.984 Å

Figure 10.17 shows a typical flag pattern of the hyperfine structure of the Pr II transition at 6397.984 Å. The lower and the upper levels involved in the transition are $\sigma = 8489.934^{\circ}{}_{5}$ cm^{-1} and $\sigma = 24115.536_{6}$ cm^{-1} respectively. The 6 diagonal hyperfine components with $\Delta F = \Delta J = +1$ are well resolved and the strongest diagonal component is placed towards the higher frequency side, that means the hyperfine splitting of the upper level is larger than the splitting of the lower level. To the left side of the 6 strong components there is a group with 5 components and belongs to the off-diagonal $\Delta F = 0$ hyperfine transitions. The third group of off-diagonal components with $\Delta F = -1$ has very low intensity and disappears in the noise.

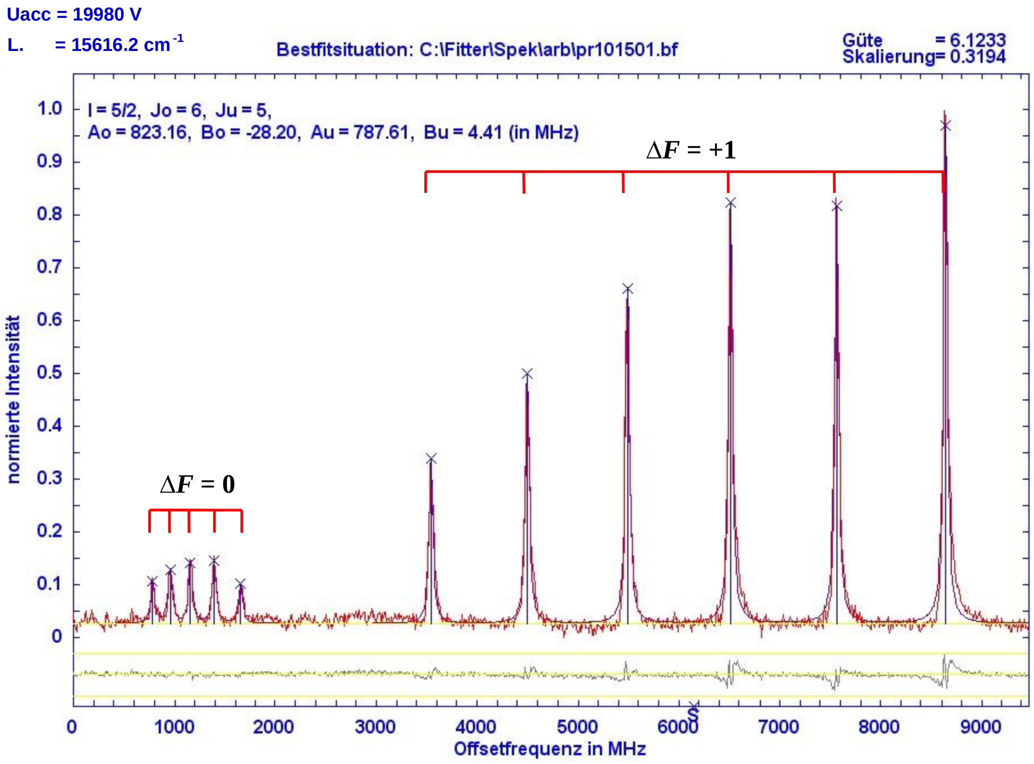

Figure 10.17: The best fit situation of the hyperfine structure of the line 6397.984 Å.

10.2.1.5 Hyperfine structure of the Pr II line 5695.90 Å

The hyperfine structure of the Pr II line 5695.90 Å is shown in figure 10.18 which is approximately a mirror image of the hyperfine structure of the transition 6397.984 Å. The ions are excited from the lower metastable level $\sigma = 9646.679^{\circ}{}_{6}\ \mathrm{cm}^{-1}$ to the upper level $\sigma = 27198.297_{5}\ \mathrm{cm}^{-1}$. The 6 diagonal hyperfine components with $\Delta F = \Delta J = -1$ are well resolved and the strongest diagonal component is placed at the lower frequency side, therefore $A_{\mathrm{lo}} > A_{\mathrm{up}}$. To the right side of the diagonal components there is a group with 5 components belonging to the off-diagonal with $\Delta F = 0$. The third group of off-diagonal components with $\Delta F = +1$ has very low intensity and disappears in the noise.

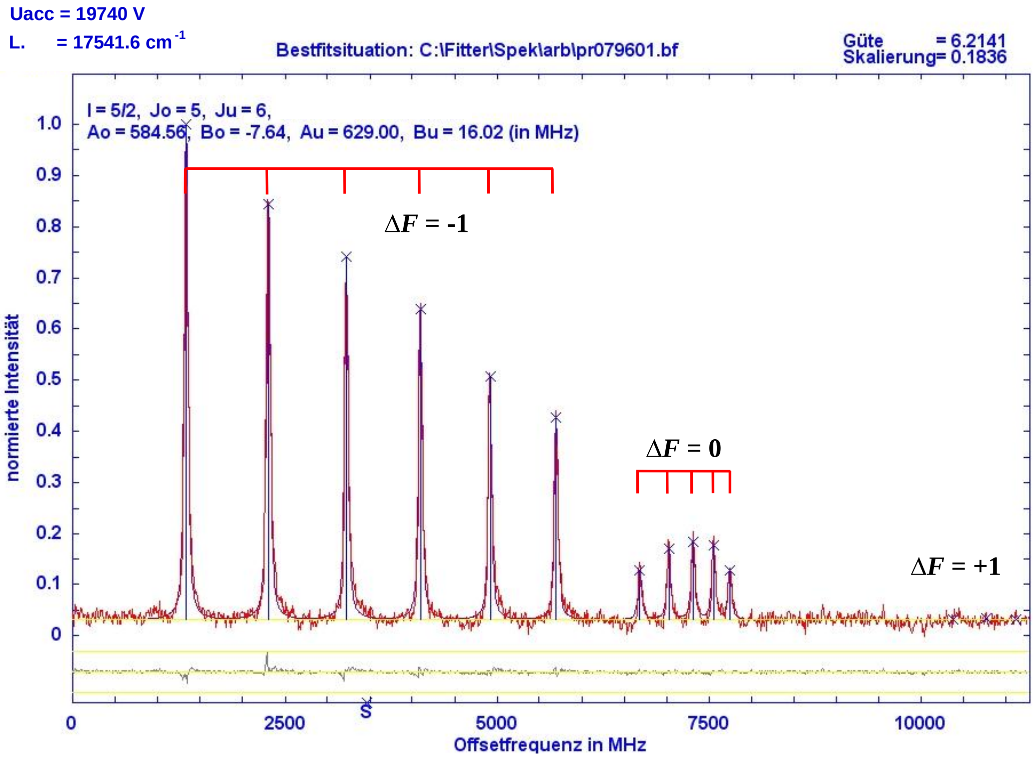

Figure 10.18: The best fit situation of the hyperfine structure of the line 5695.90 Å.

10.2.1.6 Hyperfine structure of the Pr II line 5981.194 Å

In figure 10.19 an optical spectrum of a Pr II transition with $\Delta J = -1$ and $A_{\mathrm{up}} > A_{\mathrm{lo}}$ is shown. The transition wavelength is 5981.194 Å and the levels involved in the transition are: The lower level $\sigma = 11794.384^{\circ}_{7}$ cm^{-1} and the upper level $\sigma = 28508.823_{6}$ cm^{-1}. The three diagonal components (4th, 5th and 6th) are overlapping with each other and form a large broad peak. The off-diagonal components with $\Delta F = 0$ can be found on the right side of the diagonal components. In this transition, large J values of the combining levels are involved, therefore the intensity of the off-diagonal components is small as compared to the previous examples.

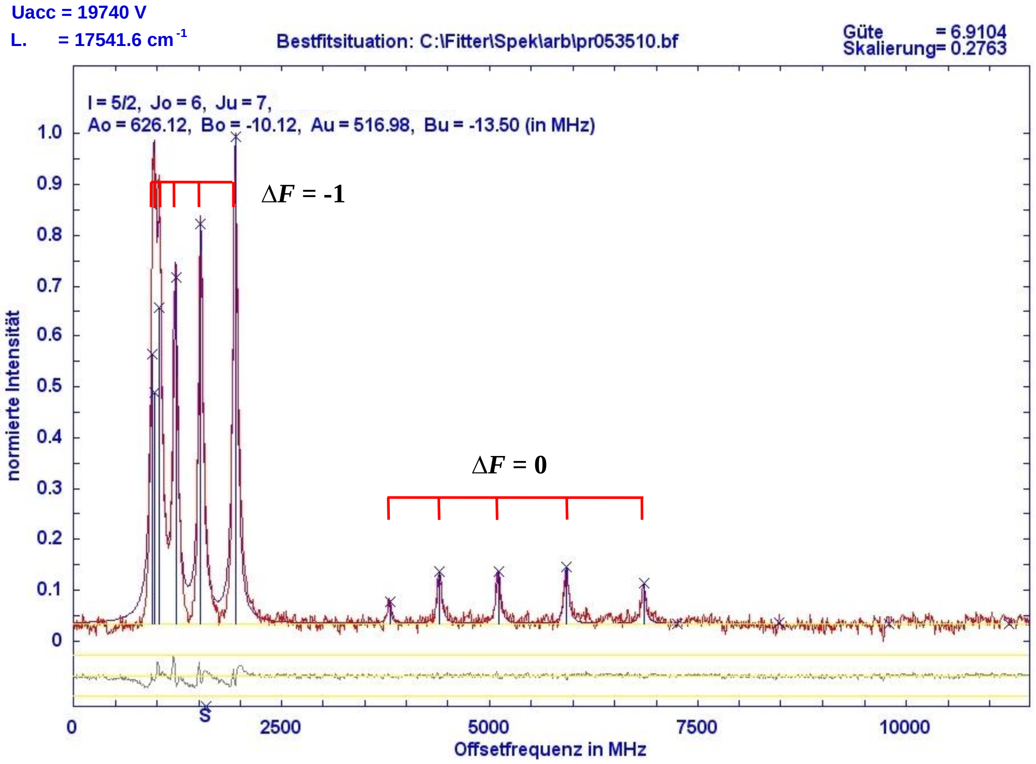

Figure 10.19: The best fit situation of the hyperfine structure of the line 5981.194 Å.

10.2.1.7 Hyperfine structure of the Pr II line 6114.385 Å

In this example, the hyperfine structure of the line 6144.385 Å is discussed. The lower level involved in the transition is $\sigma = 13373.648^{\circ}{}_{8}$ cm^{-1}. This is the highest lower level that is excited during this work. The combining upper level in this transition is $\sigma = 29723.998_{8}$ cm^{-1}. A Pr II hyperfine structure can have maximum 16 components, in this example all of 16 hyperfine components are completely resolved as can be seen clearly in figure 10.20. In this transition $\Delta J = 0$ and A_{up} is slightly greater than A_{lo}. The 6 diagonal components with $\Delta F = 0$ are at the centre of the hyperfine pattern. Two groups of off-diagonal components with $\Delta F = \pm 1$ on both sides of the diagonal components can be noticed. The intensities of the off-diagonal components seem to be higher than the theoretical ones. In fact, this is due to saturation of the central $\Delta J = 0$ components, which are not high as they should be following theoretical intensity ratios.

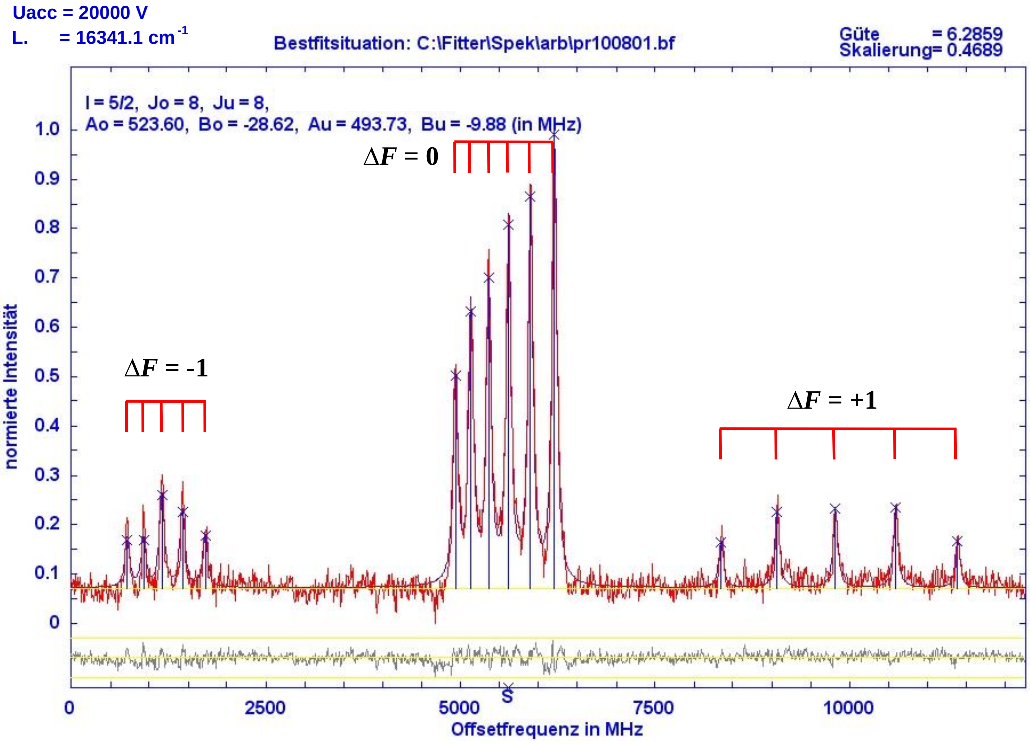

Figure 10.20: The best fit situation of the hyperfine structure of the line 6114.385 Å.

10.2.1.8 Hyperfine structure of the Pr II line 5810.581 Å

The hyperfine structure of the Pr II line 5810.581 Å is shown in figure 10.21 which is similar to the hyperfine structure of the transition 6397.984 Å (figures 10.9 and 10.17). The ions are excited from the lower metastable level $\sigma = 11611.054^{\circ}{}_{8}$ cm^{-1} to the upper level $\sigma = 28816.267_{9}$ cm^{-1} ($J = 9$ is the largest J value among the levels investigated during this work). For this transition $\Delta J = +1$ and $A_{\mathrm{lo}} < A_{\mathrm{up}}$. The most prominent components belong to the diagonal components with $\Delta F = +1$ and the weak components lying towards the lower frequency side belong to the off diagonal components with $\Delta F = 0$. Their intensities are very small because of the large J values of the levels involved in the transition. The third group of the off-diagonal components with $\Delta F = -1$ has very low intensity and disappears in the noise.

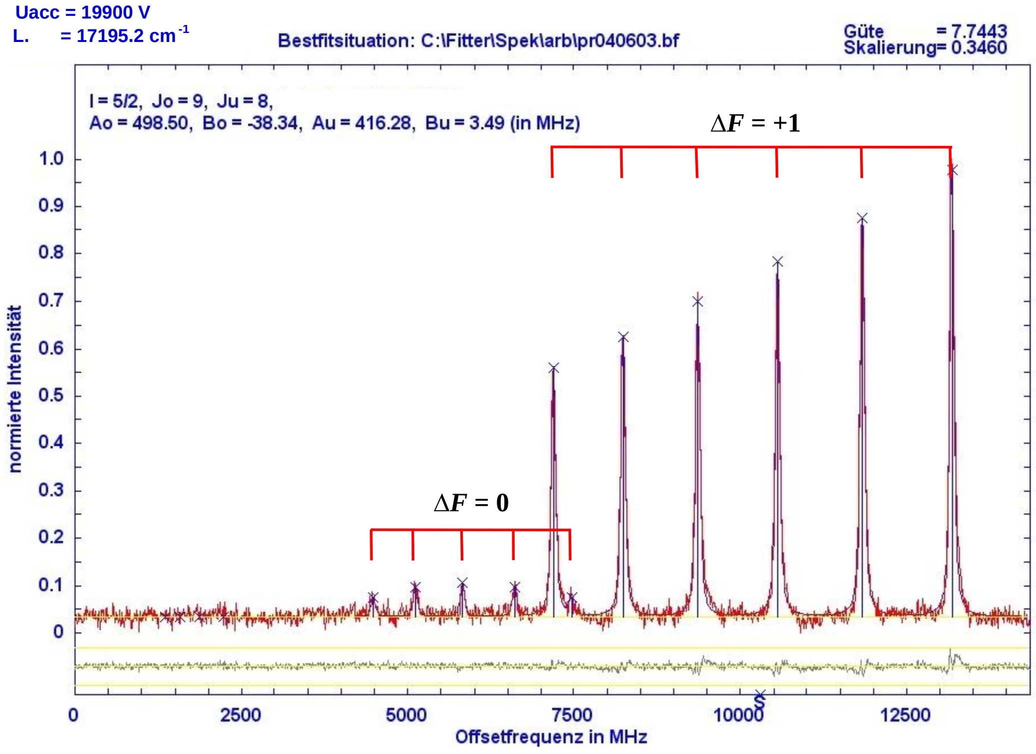

Figure 10.21: The best fit situation of the hyperfine structure of the line 5810.581 Å.

10.2.2 Comparison between CLIBS and saturation spectroscopic measurements

During the study of the hyperfine structures of the Pr II optical transitions, some of the transitions are also investigated using Doppler limited spectroscopy and saturation spectroscopy (chapter 7), using a hollow cathode discharge lamp. In this section some hyperfine structures, recorded using these three kinds of spectroscopic techniques, are discussed. The hyperfine constants are compared in table 10.2.

10.2.2.1 Hyperfine structure of the Pr II line 5719.626 Å

In figure 10.22 the hyperfine structure of the transition at 5719.626 Å is shown. The transition is taking place from the upper level $\sigma = 25578.507_3$ cm^{-1} to the lower level $\sigma =$ 8099.697°$_4$ cm^{-1}. The red (curve (a), Doppler limited) and the purple (curve (b), saturation spectroscopy) curves are recorded at the strongest LIF signal 3907 Å. The laser power used to record the hyperfine structure of this line was 350 mW and the pressure of the operating gas of the discharge, Ar, gas was 0.2 mbar.

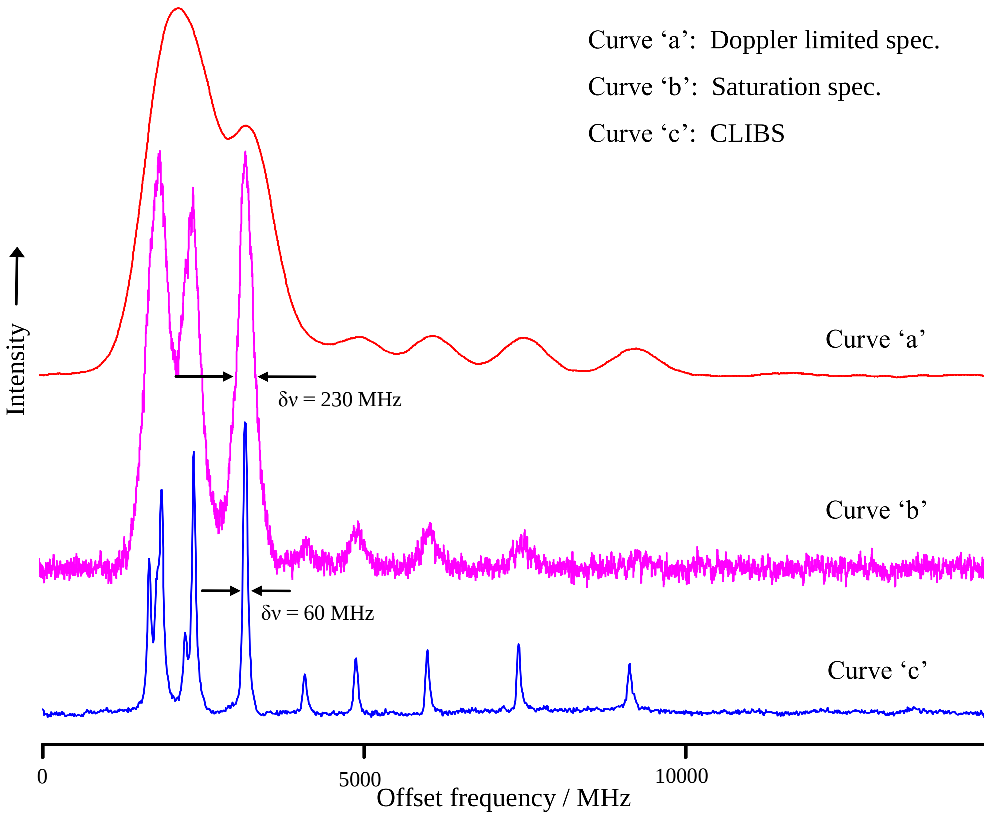

Figure 10.22: The hyperfine structure of the line 5719.626 *Å.*

Using Doppler limited spectroscopy, the diagonal hyperfine components are not resolved for this transition and remain still unresolved in the saturation spectroscopic measurement. The off diagonal (or weak) components are resolved and their intensities are about 50% less than the theoretical intensities. The blue curve (curve c) presents the hyperfine structure recorded using CLIBS method. In this case a line width of 60 MHz is obtained and the magnetic dipole interaction constants are determined with an accuracy < 0.5 MHz (table 10.2).

10.2.2.2 Hyperfine structure of the Pr II line 5788.911 Å

In figure 10.23 the hyperfine structure of the transition at 5788.911 Å is shown. The levels involved in the transition are: upper level $\sigma = 24716.093_5$ cm^{-1} and lower level $\sigma = 7446.530^{\circ}{}_4$ cm^{-1}. The red and the purple curves are recorded at the strongest LIF signal 4118 Å. The laser power used to record the hyperfine structure of this line was 650 mW and the Ar pressure was 0.2 mbar.

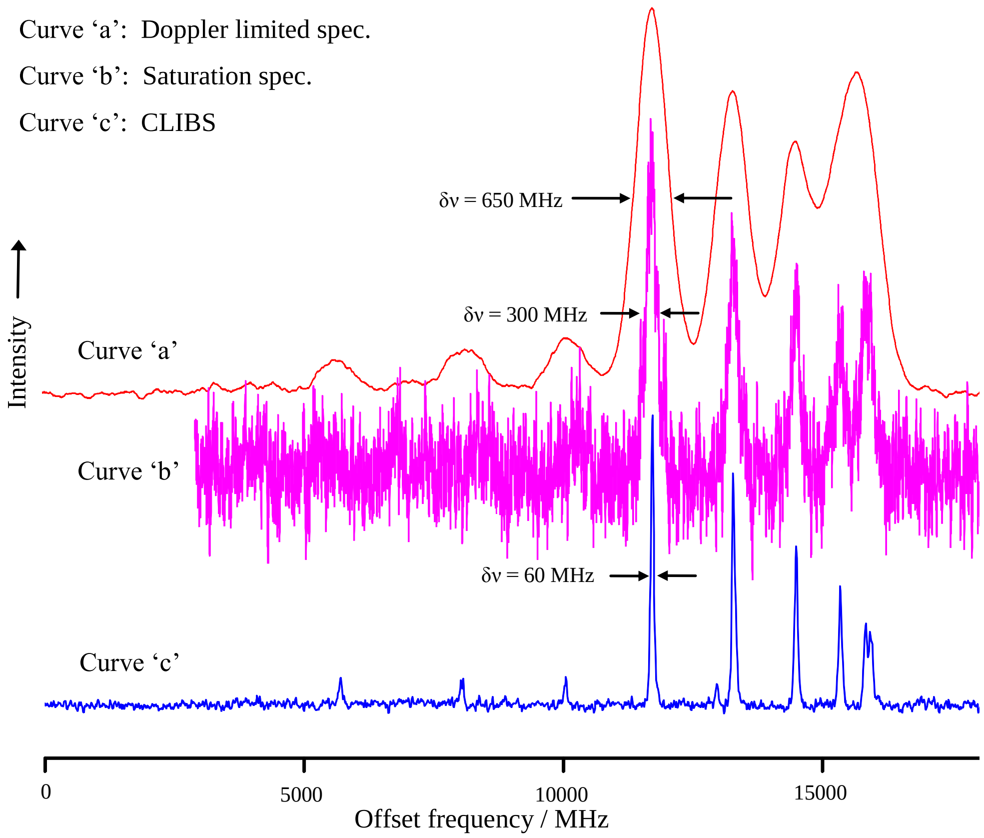

Figure 10.23: The hyperfine structure of the line 5788.911 Å.

In this example, the hyperfine structure recorded using saturation spectroscopy has a poor signal to noise ratio. The reason might be, the lower level σ = 7446.530°$_4$ cm^{-1} is highly populated because it can decay to only one even lower level σ = 7228.086$_4$ cm^{-1}. Therefore it is hard to saturate the transition. The line width of 60 MHz is obtained using CLIBS method which is much better as compared to the other measurements of the same line.

10.2.2.3 Hyperfine structure of the Pr II line 5791.362 Å

Different recordings of the hyperfine structure of the transition at 5791.362 Å are shown in figure 10.24. The transition is taking place from the upper level σ = 26640.915$_5$ cm^{-1} to the lower level σ = 9378.612°$_5$ cm^{-1}. Both levels have approximately the same hyperfine splitting (A_{up} = 619.8 MHz and A_{lo} = 614.7 MHz determined from CLIBS measurements), therefore all diagonal components lie very close together and form one large peak at the center of the hyperfine pattern. The diagonal components could not be resolved by any of the spectroscopic methods. The Doppler limited and the saturation LIF signals are recorded at the strongest LIF signal 3998 Å. The laser power used to record the hyperfine structure of this line was 650 mW and the Ar pressure was 0.15 mbar.

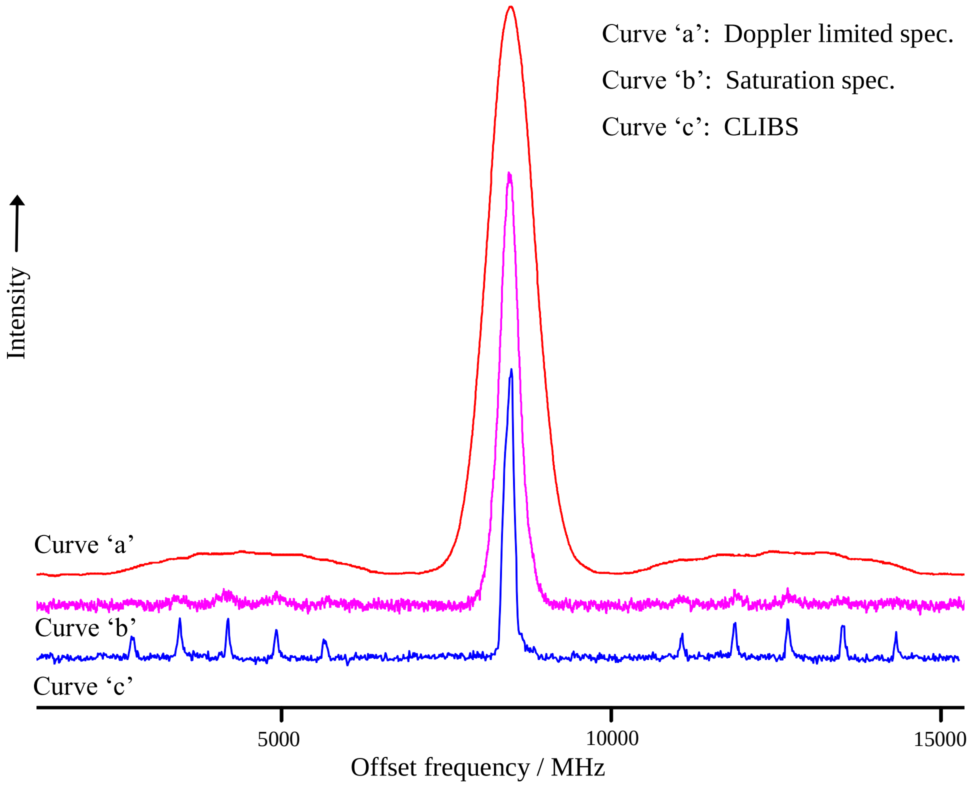

Figure 10.24: The hyperfine structure of the line 5791.362 Å.

Table 10.2: The hyperfine constants measured using different spectroscopic techniques (since the quadrupole moment for Pr is very small, therefore B values are neglected).

Excitation wavelength (air) / Å	Energy of the levels / cm^{-1}	Method used			
		Doppler limited spectroscopy	Saturation spectroscopy	CLIBS (this work)	
		A / MHz	A / MHz	A / MHz	B / MHz
5719.626	8099.697°_{4}	772(3)	764(3)	766.0(2)	-1 (2)
	25578.507_{3}	1040(3)	1027(4)	1029.1(3)	-22(5)
5791.362	9378.612°_{5}	612(5)	616(2)	615.1(3)	-8(1)
	26640.915_{5}	630(5)	622(2)	619.8(2)	-16(3)
5823.73[b]	1743.737°_{5}	-47(3)	-46 (5)	-	-
	18910.166_{5}	704(3)	704 (5)	-	-
5785.42	10729.778°_{6}	537(3)	530(5)	533.4(2)	17(22)
	28009.828_{7}	546(12)	552(5)	556.9(1)	32(23)
5786.17	7348.301°_{5}	710(6)	706(2)	704.2(2)	26(4)
	24716.093_{5}	740(6)	730(2)	730.1(3)	18(6)
5788.911	7446.530°_{4}	1062(2)	1055(5)	1059.6(4)	26(11)
	24716.093_{5}	732(2)	726(5)	729.9(4)	0(8)

[b] LIF is not observed in CLIBS because the the fluorescence light from the decay of 18910.166 is blocked by the blue filter (BG 12).

Doppler limited spectroscopy (results):

During the investigation of hyperfine structures using a hollow cathode discharge lamp, Doppler limited spectroscopic studies of some other Pr II lines are also performed. The results are given in table 10.3.

Table 10.3: The hyperfine interaction constants determined using Doppler limited spectroscopy (other than in table 10.2). The B values are neglected due to large variations during the fitting process.

Excitation wavelength (air) / Å	Upper level			Lower level		
	Energy / cm^{-1}	J, parity	A / MHz	Energy / cm^{-1}	J, parity	A / MHz
5715.39 [c]	22718.404	6, e	749(9)	5226.567	6, o	720(9)
5726.03 [d]	33397.060	7, o	893(10)	15937.73	6, e	996(4)
5745.58 [e]	25499.570	5, e	635(2)	8099.697	4, o	766(2)
5797.03 [d]	22472.061	6, e	740(20)	5226.567	6, o	745(20)
5801.86 [d]	25330.823	5, e	663(6)	8099.697	4, o	788(10)
5807.53 [e]	26860.974	7, e	604(1)	9646.679	6, o	629(1)

Excitation wavelength (air) / Å	Upper level			Lower level		
	Energy / cm^{-1}	*J*, parity	*A* / MHz	Energy / cm^{-1}	*J*, parity	*A* / MHz
5813.55 [e]	28201.980	8, e	539(2)	11005.557	7, o	549(2)
5815.20 [d]	26570.208	4, e	706(14)	9378.612	5, o	598(10)
5823.39 [c]	28172.968	7, e	474(8)	11005.557	7, o	547(4)
5844.65 [c]	22184.306	7, e	598(15)	5097.375	7, o	-160(18)
5852.63 [e]	27198.297	5, e	587(2)	10116.696	4, o	660(2)

[c] A weak signal is observed using CLIBS.
[d] No signal is observed using CLIBS.
[e] A good signal is observed and recorded using CLIBS.

10.2.3 CLIBS measurements of blend situations of optical transitions of Pr II

While performing CLIBS measurements, few structures are recorded in which the hyperfine components of neighboring Pr II transitions overlap, giving rise to a blend situation. Such recordings are helpful for the precise measurements of the difference of the centers of gravity (Δcg) of closely lying transitions. Using CLIBS measurements, Δcg can be determined up to 0.1 mK (1 cm^{-1} = 1000 mK). In table 10.4, experimentally determined values of Δcg are compared with the calculated values (from the improved energies, see chapter 6). In order to determine the hyperfine interaction constants of the levels involved in the transitions, a two line fitting is performed using the fitter program (chapter 6). Some examples of two structures blend recorded during this work are discussed below.

Experimentally recorded blend structures of Pr II spectral lines:

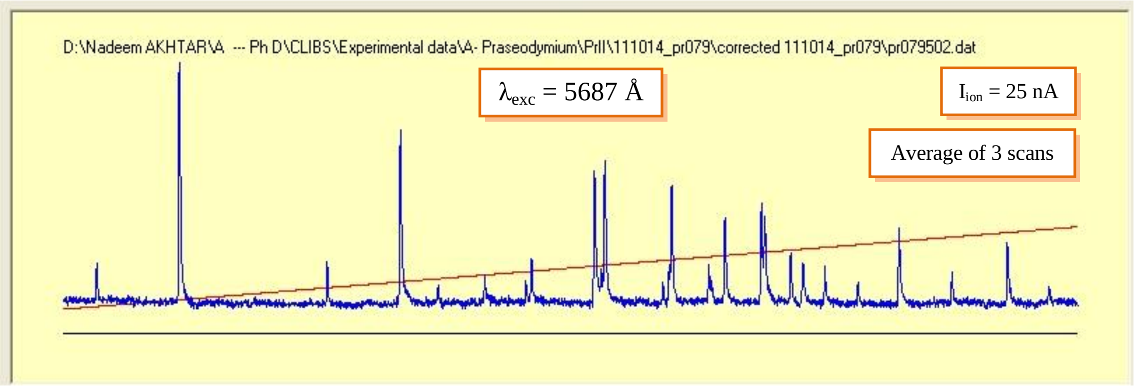

Figure 10.25: See section 10.2.3.1.

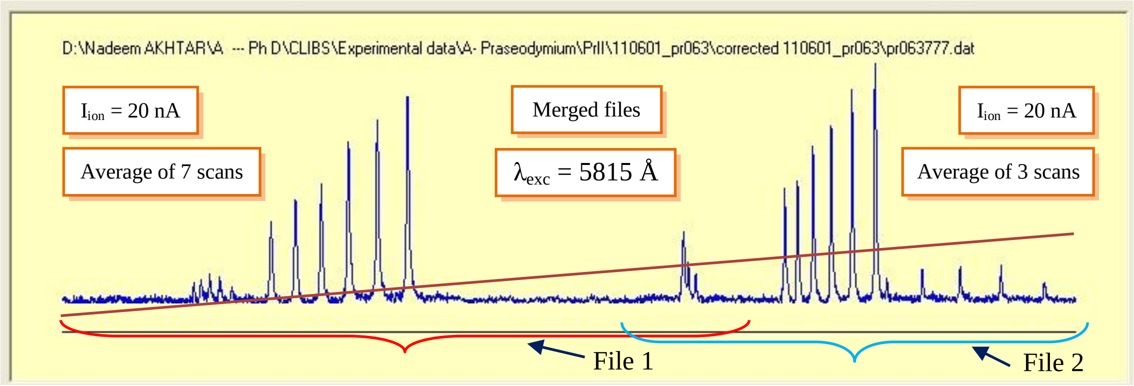

Figure 10.26: See section 10.2.3.2.

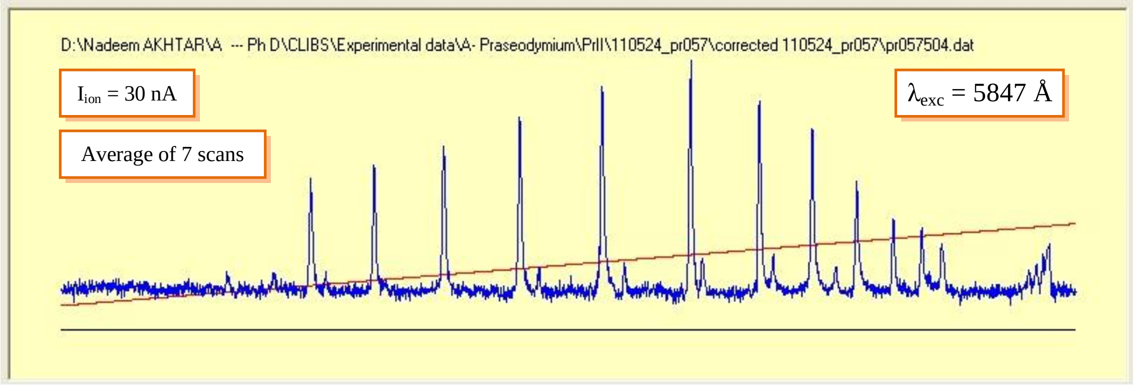

Figure 10.27: See section 10.2.3.3.

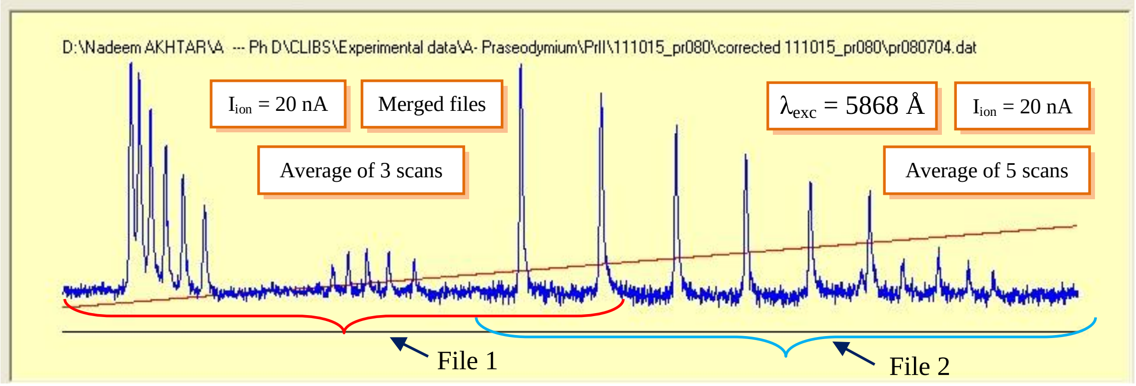

Figure 10.28: See section 10.2.3.4.

10.2.3.1 A blend of two structures in the region 5687 Å

An untypical hyperfine pattern is shown in figure 10.25 and 10.29. The large number of hyperfine components can only be understood if one assumes that two transitions of almost similar wavelength overlap. The widely spread hyperfine structure (components marked with ×) belongs to the transition from the lower odd level $\sigma = 4097.653^{\circ}_{5}$ cm^{-1} to the upper level $\sigma = 21676.163_5$ cm^{-1}. For this transition $A_{lo} > A_{up}$ and $\Delta J = 0$. For both levels $J = 5$, therefore there are 6 prominent hyperfine components with $\Delta F = \Delta J = 0$, 5 weak hyperfine components with $\Delta F = +1$ and 5 weak hyperfine components with $\Delta F = -1$. The second hyperfine pattern (components marked with △), appearing in this blend situation with lower intensity, can be recognized as the transition from the lower odd level $\sigma = 9128.741^{\circ}_{4}$ cm^{-1} to the upper even level $\sigma = 26707.364_5$ cm^{-1} and lies completely inside the hyperfine structure of other line.

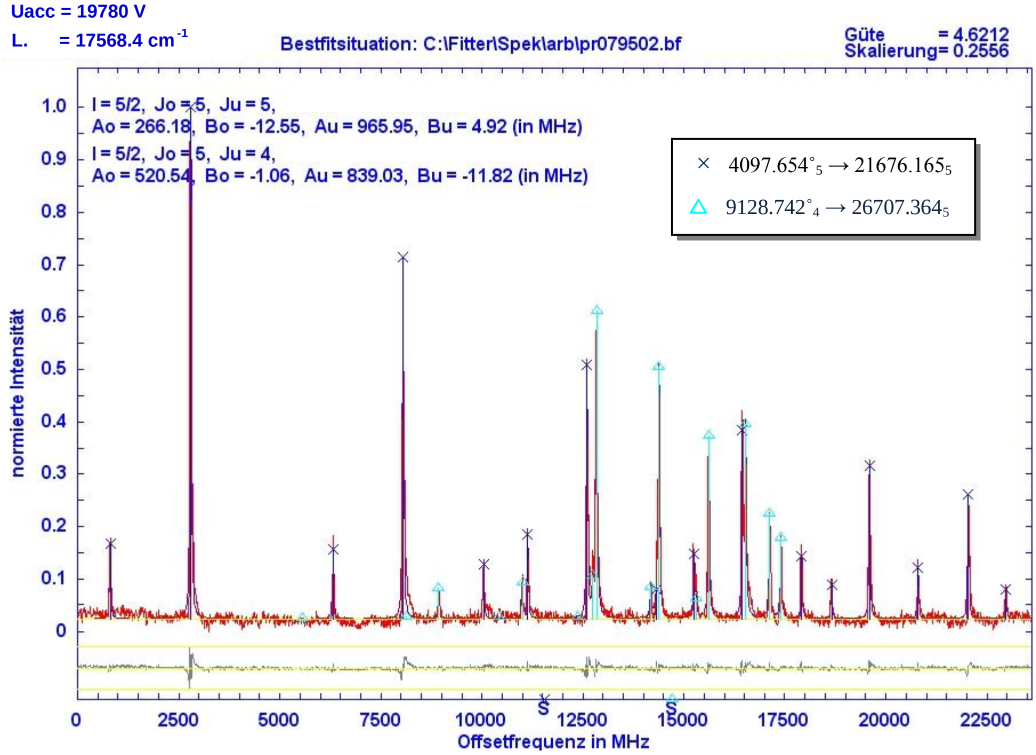

Figure 10.29: Best fit situation for two line fit of Pr II lines in the region 5687 Å.

For this transition $A_{lo} > A_{up}$ and $\Delta J = +1$. There are 6 prominent hyperfine components with $\Delta F = \Delta J = +1$. The 5 hyperfine components (first off-diagonal group) with $\Delta F = 0$ are weaker and the 4 hyperfine components (second off-diagonal group) with $\Delta F = -1$ are so weak that they disappear in the noise. A two line fitting is performed and the best fit situation of the recorded hyperfine patterns is shown in figure 10.29. For both hyperfine patterns, a line width of 48 MHz is observed. The center of gravity wave numbers of both transitions are separated by only 0.1058 cm^{-1}. The value calculated from the improved level energies is 0.113 cm^{-1} (table 10.4), which is in good agreement with the experimental value.

10.2.3.2 Two structures recorded in the region 5815 Å

In figure 10.30, two clear and well resolved hyperfine structures are shown. As the transitions are very closely lying, two separate recordings are merged together (file 1 and file 2 as shown in figure) in order to find the accurate difference in the centers of gravity of these transitions. The calculated value of $\Delta cg = 0.479$ cm^{-1} from the improved energy values is in good agreement with the experimentally observed value i.e. $\Delta cg = 0.4753$ cm^{-1}. The left hyperfine pattern belongs to the transition between the lower level $\sigma = 12826.982^{\circ}{}_6$ cm^{-1} to the upper level $\sigma = 30018.138_7$ cm^{-1}, with $\Delta J = +1$ and $A_{\mathrm{lo}} < A_{\mathrm{up}}$. The second hyperfine structure in figure 10.30, with $\Delta J = 0$ and $A_{\mathrm{lo}} < A_{\mathrm{up}}$, belongs to the transition between the lower level $\sigma = 8465.102^{\circ}{}_6$ cm^{-1} and the upper level $\sigma = 25656.737_6$ cm^{-1}.

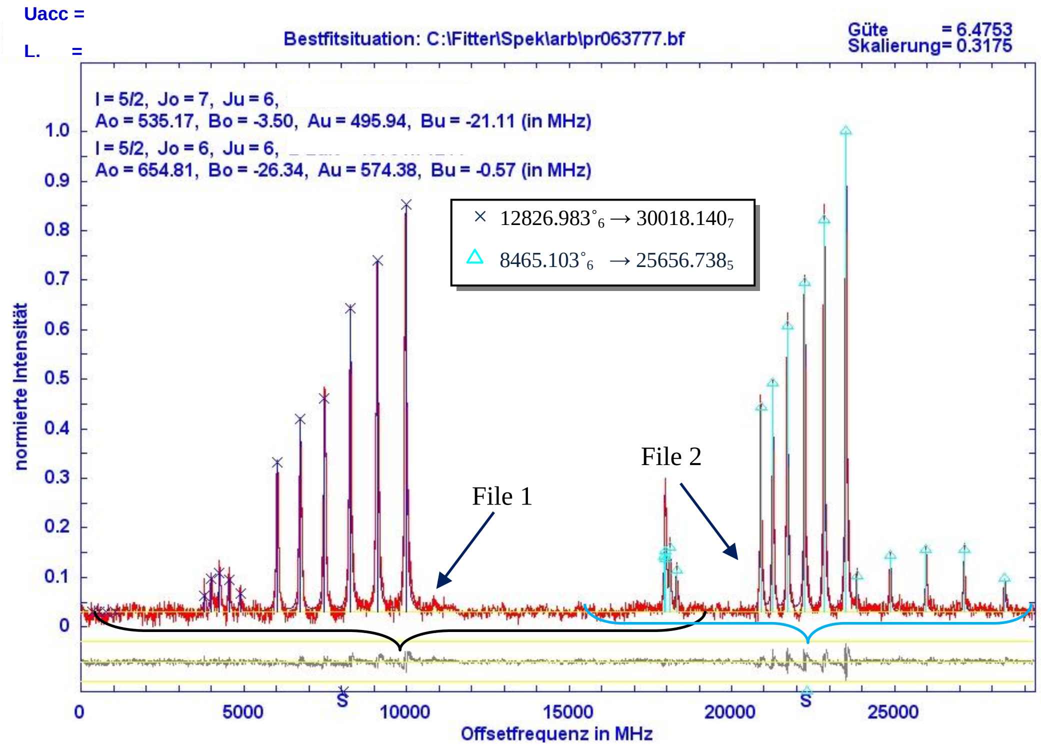

Figure 10.30: Best fit situation for two line fit of Pr II lines in the region 5815 Å.

10.2.3.3 A blend of two structures in the region 5847 Å

In figure 10.31, two hyperfine structures involving four Pr II levels are shown. The difference in centers of gravity of these two transitions is 0.2213 cm^{-1}. The value calculated from the improved level energies is $\Delta cg = 0.222\ \mathrm{cm}^{-1}$ (table 10.4). The first (left) hyperfine pattern is the transition between the lower level $\sigma = 10030.351^{\circ}{}_{7}\ \mathrm{cm}^{-1}$ to the upper level $\sigma = 27128.016_{8}\ \mathrm{cm}^{-1}$. The strongest diagonal component lies towards the higher frequency side which suggests that $A_{\mathrm{up}} > A_{\mathrm{lo}}$. The second (right) structure appearing in the spectrum belongs to the transition between the lower level $\sigma = 9128.741^{\circ}{}_{4}\ \mathrm{cm}^{-1}$ to the upper level $\sigma = 26226.628_{4}\ \mathrm{cm}^{-1}$. Six diagonal components belong to $\Delta F = \Delta J = 0$ transitions are visible. The strongest component lies towards lower frequency because $A_{\mathrm{up}} < A_{\mathrm{lo}}$. The group $\Delta F = +1$ of the hyperfine transitions lies on the left side of the diagonal components and five components of group $\Delta F = -1$ lie towards lower frequency.

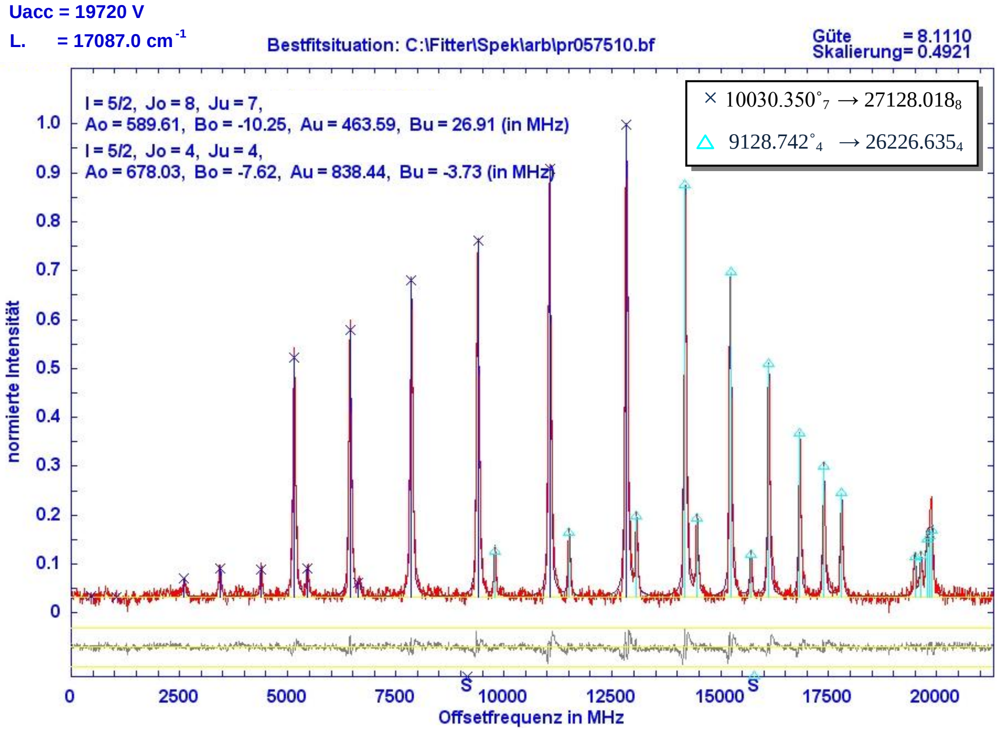

Figure 10.31: A two line fit in the region 5847 Å.

10.2.3.4 Two structures recording in the region 5868 Å

In figure 10.32, two similar hyperfine patterns are shown. File 1 and file 2 (as shown in figure) are merged together. Both transitions have ΔJ = -1 and $A_{lo} > A_{up}$. In the first transition, ions are being excited from the lower metastable level $\sigma = 8465.102°_6$ cm^{-1} to the upper level $\sigma = 25499.570_5$ cm^{-1} whereas in the second transition the laser excitation is taking place from the odd level $\sigma = 10163.531°_6$ cm^{-1} to the upper even level $\sigma = 27198.297_5$ cm^{-1}. The experimentally observed difference Δcg = 0.2943 cm^{-1}. From corrected energy levels: Δcg = 0.298 cm^{-1}.

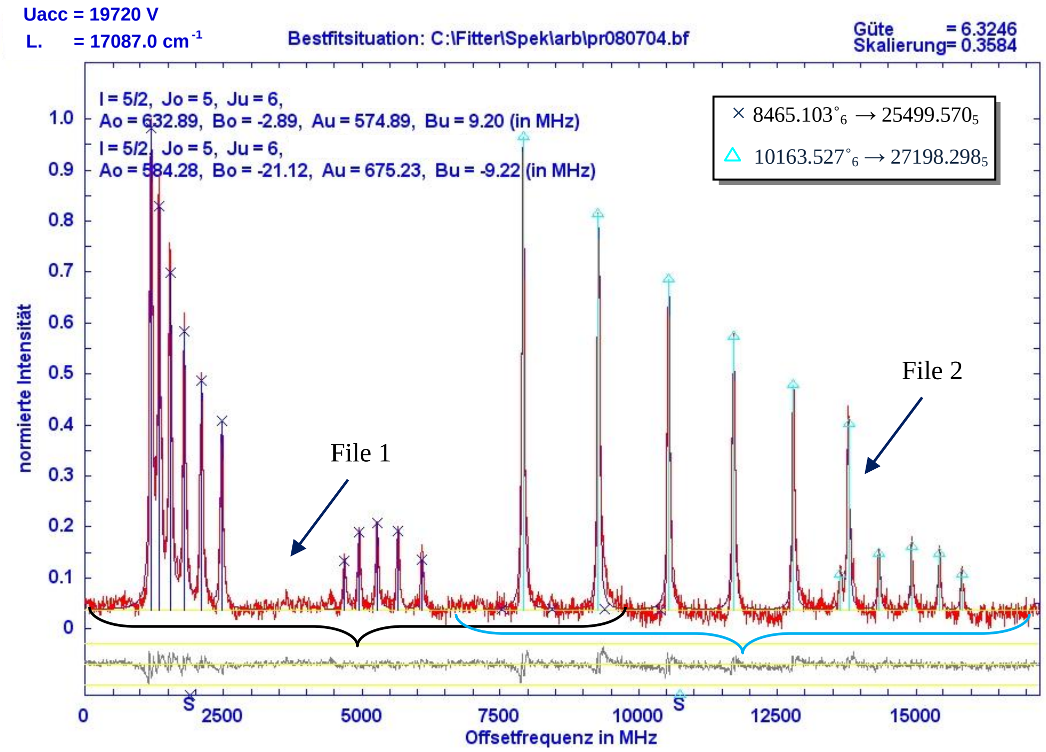

Figure 10.32: Best fit situation for two line fit of Pr II lines in the region 5868 Å.

Table 10.4: Comparison of experimental values and calculated values of Δcg.

Excitation wavelength (air) / Å	Levels involved in the transitions 1st structure - 2nd structure	Δcg / cm^{-1}		
		Exp. (CLIBS)	Calculated from	
			Improved energies [6]	Uncorrected energies [42]
5687	$4097.653^{\circ}_{5} - 21676.163_{5}$ $9128.741^{\circ}_{4} - 26707.364_{5}$	0.1058	0.113	0.11
5731	$10163.531^{\circ}_{6} - 27604.990_{6}$ $9128.741^{\circ}_{4} - 26570.208^{\circ}_{4}$	0.121	0.008	0.04
5815	$12826.982^{\circ}_{6} - 30018.138_{7}$ $8465.102^{\circ}_{6} - 25656.737_{5}$	0.4753	0.479	0.49
5818	$8958.477^{\circ}_{9} - 26139.793_{8}$ $9045.051^{\circ}_{3} - 26226.628_{4}$	0.2595	0.261	0.29
5847	$10030.351^{\circ}_{7} - 27128.016_{8}$ $9128.741^{\circ}_{4} - 26226.628_{4}$	0.2213	0.222	0.22
5868	$8465.102^{\circ}_{6} - 25499.570_{5}$ $10163.531^{\circ}_{6} - 27198.297_{5}$	0.2945	0.298	0.31
5956	$11418.672^{\circ}_{7} - 28201.980_{8}$ $11794.384^{\circ}_{7} - 28577.821_{7}$	0.1348	0.129	0.1
6025	$10116.696^{\circ}_{4} - 26707.364_{5}$ $11611.054^{\circ}_{8} - 28201.980_{8}$	0.2606	0.258	0.26

Table 10.5: Transitions investigated in Pr II using CLIBS.

Wavelength (air) λ / Å	Even level		Odd level	
	J value	Energy / cm^{-1} [6]	*J* value	Energy / cm^{-1} [6]
5654.23	5	26146.060	6	8465.102
5661.24	5	22885.634	6	5226.567
5662.19	5	26146.060	5	8489.934
5677.027	6	22718.404	7	5108.437
5681.876	5	26973.549	5	9378.608
5685.60	6	26962.021	5	9378.608
5687.150	5	26707.364	4	9128.741
5687.19	5	21676.163	5	4097.653
5688.44	6	27604.990	7	10030.351
5689.208	7	28577.821	7	11005.560
5695.90	5	27198.297	6	9646.682
5704.500	4	26570.208	3	9045.051
5711.634	6	28508.823	7	11005.560
5719.09	8	29723.998	7	12243.537
5719.626	3	25578.507	4	8099.697
5729.42	5	22675.492	6	5226.567
5730.58	4	25545.086	4	8099.697
5731.87	4	26570.208	4	9128.741
5731.87	6	27604.990	6	10163.531
5745.60	5	25499.570	4	8099.697
5753.02	5	25842.444	6	8465.102
5756.169	4	25467.549	4	8099.697
5761.26^{f}	5	25842.444	5	8489.934
5769.15	5	26707.364	5	9378.608
5769.784	5	26973.549	6	9646.682
5773.165	4	24755.017	5	7438.301
5775.900	4	24755.017	4	7446.477
5777.291	6	28034.127	6	10729.778
5785.42	7	28009.828	6	10729.778
5786.140	5	24716.093	5	7438.301
5788.911	5	24716.093	4	7446.477
5790.85	5	27380.527	4	10116.696
5791.362	5	26640.915	5	9378.608
5807.52	7	26860.974	6	9646.682
5810.581	9	28816.267	8	11611.037
5813.55	8	28201.980	7	11005.560
5815.17^{f}	6	25656.737	6	8465.102

Wavelength (air) λ / Å	Even level		Odd level	
	J value	Energy / cm^{-1} [6]	*J* value	Energy / cm^{-1} [6]
5815.330	7	30018.138	6	12826.982
5818.57	4	26226.628	3	9045.051
5818.663 [g]	8	26139.793	9	8958.477
5823.58	6	25656.737	5	8489.934
5830.945 [f]	6	25610.227	6	8465.102
5839.40 [f]	6	25610.227	5	8489.934
5847.05	4	26226.628	4	9128.741
5847.13	8	27128.016	7	10030.351
5852.630	5	27198.297	4	10116.696
5856.908	6	27604.990	5	10535.868
5859.68	6	28508.823	5	11447.788
5868.72	5	27198.297	6	10163.531
5868.824	5	25499.570	6	8465.102
5873.83	6	26398.569	5	9378.608
5874.74	5	26146.060	4	9128.741
5877.39	5	25499.570	5	8489.934
5892.24	7	28577.821	8	11611.037
5930.662	5	26973.549	4	10116.696
5939.90	7	26860.974	7	10030.351
5940.727	7	28577.821	6	11749.526
5947.19	5	26973.549	6	10163.531
5951.266	6	26962.021	6	10163.531
5951.773	3	25672.825	2	8965.764
5956.605	7	28577.821	7	11794.384
5956.610 [g]	8	28201.980	7	11418.672
5967.82	6	26398.569	6	9646.682
5980.00	3	25672.825	3	9045.051
5981.194	6	28508.823	7	11794.384
5981.458	5	25842.444	4	9128.741
6002.426	4	24755.017	4	8099.697
6006.33	7	30018.138	8	13373.648
6016.49	5	24716.093	4	8099.697
6017.809	3	25578.507	2	8965.764
6025.722	8	28201.980	8	11611.037
6025.817	5	26707.364	4	10116.696
6042.873	5	26707.364	6	10163.531
6046.67	3	25578.507	3	9045.051
6067.24	5	26640.915	6	10163.531

Wavelength (air) λ / Å	Even level		Odd level	
	J value	Energy / cm^{-1} [6]	J value	Energy / cm^{-1} [6]
6086.168	6	26962.021	7	10535.868
6087.522	4	25467.549	3	9045.051
6090.381	7	26445.138	7	10030.351
6093.05	8	28201.980	7	11794.384
6106.74	5	25499.570	4	9128.741
6114.385	8	29723.998	8	13373.648
6141.51	6	25656.737	5	9378.608
6148.25	7	28009.828	6	11749.526
6159.112	6	25610.227	5	9378.608
6161.18	5	24716.093	5	8489.934
6165.92	4	23660.171	4	7446.477
6182.340	8	27781.667	8	11611.037
6187.48	6	27604.990	5	11447.788
6197.453	7	26860.974	6	10729.778
6205.632	4	26226.628	4	10116.696
6244.347	6	25656.737	6	9646.682
6262.537	6	25610.227	6	9646.682
6278.671	7	25569.217	6	9646.682
6281.30	4	23660.171	3	7744.295
6318.12	5	23261.402	5	7438.301
6363.60	4	24755.017	3	9045.051
6397.984	6	24115.536	5	8489.934
6429.624	7	28577.821	8	13029.112
6431.842	6	26962.021	7	11418.672

[f] Reference [130].

[g] Weak signal is observed in a blend situation with neighboring transition.

Table 10.6. Measured hyperfine constants of odd parity fine energy levels of Pr II. The results are compared with the values obtained by M. Hongliang et al. [47] *(column 5, 6), A. Ginibre* [41] *(column 7) and B. Furmann et al.* [51] *(column 8, 9).*

Level Energy / cm^{-1}	Excitation wavelength / Å	*A* / MHz	*B* / MHz	A_H /MHz [47]	B_H / MH [47]	A_G / MHz [41]	A_F / MHz [51]	B_F / MHz [51]
4097.653	5687.19	966.0(4)	6(4)			974(6)		
5108.437	5677.027	661.4(4)	0(20)			666(4)		
5226.567	5661.24	715.1(3)	-20(4)					
	5729.42	715.0(3)	-21(6)					
Average		715.1(3)	-21(6)			720(5)		
7438.301	5773.165	704.4(3)	19(10)					
	5786.172	704.2(2)	26(4)					
	6318.12	704.7(2)	17(5)					
Average		704.4(5)	21(12)	709.3(12)	19.5(60)	714(6)	709.5(15)	8(5)
7446.530	5775.911	1059.6(2)	-8(4)					
	5788.93	1059.6(3)	-26(11)					
	6165.94	1060.4(2)	-9(6)					
Average		1059.9(7)	-14(22)			1062(7)	1069.3(30)	-7(4)
7744.295	6281.30	1227.4(4)	2(6)			1209(9)		
8099.697	5719.626	766.0(2)	-2(2)					
	5730.58	765.7(4)	2(5)					
	5745.58	765.9(3)	7(3)					
	5756.169	765.8(2)	3(2)					
	6002.43	765.3(2)	7(5)					
	6016.49	765.4(3)	-1(6)					

Level Energy / cm^{-1}	Excitation wavelength / Å	A / MHz	B / MHz	A_H /MHz [47]	B_H / MH [47]	A_G / MHz [41]	A_F / MHz [51]	B_F / MHz [51]
Average		765.7(6)	3(10)	770.8(9)	34.7(46)	768(13)	769.7(25)	44(12)
8465.102	5654.23	574.9(3)	7(4)					
	5753.02	574.9(4)	7(6)					
	5815.17	574.3(1)	1(3)					
	5830.945	574.7(3)	0(1)					
	5868.824	574.9(2)	10(2)					
Average		574.9(4)	5(5)	573.9(7)	-5.1(35)	576(5)	573.7(15)	-6(5)
8489.934	5662.19	787.5(2)	-2(6)					
	5761.26	787.5(1)	-1(3)					
	5823.58	787.1(3)	31(13)					
	5839.40	787.6(2)	34(8)					
	5877.39	787.7(2)	5(3)					
	6161.182	787.4(2)	3(4)					
	6397.984	787.5(3)	5(6)					
Average		787.4(6)	11(33)			795(6)	793.5(25)	43(20)
8958.477	5818.663	354						
8965.764	5951.773	1701.4(1)	-3(4)					
	6017.809	1702.0(1)	-10(1)					
Average		1701.7(4)	-7(6)			1614(120)	1705.1(53)	23(9)
9045.051	5704.500	931.5(2)	-20(5)					
	5818.57	931.9(2)	-17(2)					
	5980.00	931.3(2)	-9(1)					

Level Energy / cm^{-1}	Excitation wavelength / Å	A / MHz	B / MHz	A_{H} /MHz [47]	B_{H} / MH [47]	A_{G} / MHz [41]	A_{F} / MHz [51]	B_{F} / MHz [51]
	6046.67	931.4(2)	-17(3)					
	6087.522	931.5(3)	-23(2)					
	6363.60	931.1(3)	-20(1)					
Average		931.5(7)	-18(10)			943(17)	940.0(55)	7(10)
9128.741	5687.150	839.1(4)	-9(5)					
	5847.05	838.8(2)	-3(5)					
	5874.74	838.4(2)	-3(12)					
	5981.458	839.3(6)	-12(4)					
	6106.74	839.0(4)	-4(4)					
Average		839.0(9)	-7(10)			834(7)	840.5(35)	-37(20)
9378.612	5681.876	615.0(2)	-5(5)					
	5685.60	615.1(4)	13(5)					
	5769.154	614.3(2)	4(9)					
	5791.363	615.1(2)	-8(1)					
	5873.83	614.4(3)	14(10)					
	6141.51	614.6(2)	-8(7)					
	6159.112	614.4(4)	23(10)					
Average		614.7(4)	5(28)	613.8(8)	9.1(54)	612(11)	613.9(20)	-1(1)
9646.679	5695.90	628.9(2)	16(5)					
	5769.784	628.5(3)	-1(16)					
	5807.52	628.3(2)	52(7)					
	5967.822	628.5(2)	4(4)					

Level Energy / cm^{-1}	Excitation wavelength / Å	*A* / MHz	*B* / MHz	A_H /MHz [47]	B_H / MH [47]	A_G / MHz [41]	A_F / MHz [51]	B_F / MHz [51]
	6244.346	628.2(2)	-2(4)					
	6262.538	628.7(2)	8(2)					
	6278.669	628.5(2)	2(2)					
Average		628.5(6)	11(48)			618(9)	626.9(20)	20(5)
10030.351	5688.44	463.7(2)	2(7)					
	5847.13	463.7(3)	27(4)					
	5939.90	464.1(2)	7(8)					
	6090.381	463.6(2)	-1(5)					
Average		463.8(4)	9(22)			471(8)	462.3(30)	29(10)
10116.696	5790.85	656.1(6)	-5(9)					
	5852.630	656.6(3)	-5(3)					
	5930.662	656.8(4)	-9(2)					
	6025.817	656.5	-21					
	6205.632	656.8(2)	-16(5)					
Average		656.6(9)	-9(7)			666(27)	653.9(25)	0(10)
10163.531	5731.870	675.0(2)	-20(7)					
	5868.72	675.1(2)	-13(6)					
	5947.19	675.3(2)	-1(4)					
	5951.266	675.4(1)	-14(6)					
	6042.873	675.1(2)	-18(11)					
	6067.24	675.1(3)	-12(7)					
Average		675.2(4)	-15(18)			684(9)		

Level Energy / cm^{-1}	Excitation wavelength / Å	*A* / MHz	*B* / MHz	A_H /MHz [47]	B_H / MH [47]	A_G / MHz [41]	A_F / MHz [51]	B_F / MHz [51]
10535.868	5856.908	678.4(2)	-8(12)					
	6086.168	678.7(2)	-5(5)					
Average		678.6(4)	-7(13)			672(54)		
10729.778	5777.291	533.5(3)	-4(9)					
	5785.42	533.4(2)	-16(22)					
	6197.453	533.6(3)	-15(4)					
Average		533.5(4)	-12(26)			516(46)	529(4)	4(3)
11005.557	5689.208	546.0(3)	4(6)					
	5711.634	546.4(3)	-27(2)					
	5813.55	545.4(2)	14(10)					
Average		545.9(7)	-3(28)	546.7(10)	9.7(70)	558(40)	546.6(20)	8(7)
11418.672	6431.842	668.5(3)	-4(24)			676(10)		
11447.788	5859.68	576.2(3)	-1(2)					
	6187.48	576.4(5)	-13(7)					
Average		576.3(5)	-7(8)			600(110)	566.8(45)	-21(10)
11611.054	5810.581	416.2(3)	8(13)					
	5892.24	416.5(2)	-3(9)					
	6025.722	416.5(2)	4(6)					
	6182.338	416.5(2)	2(2)					
Average		416.4(5)	3(18)			432(14)	420(3)	33(15)
11749.526	5940.727	556.6(3)	-19(6)					
	6148.25	557.7(2)	8(5)					

Level Energy / cm^{-1}	Excitation wavelength / Å	A / MHz	B / MHz	A_H /MHz [47]	B_H / MH [47]	A_G / MHz [41]	A_F / MHz [51]	B_F / MHz [51]
Average		557.2(9)	-6(19)			546(92)	556.3(50)	27(10)
	5956.605	516.8(2)	-15(3)					
11794.384	5981.194	517.1(3)	-19(7)					
	6093.05	516.4(1)	-26(10)					
Average		516.8(6)	-20(16)			528(5)		
12243.537	5719.086	486.2(4)	10(5)			480(16)	493.1(50)	-16(10)
12826.982	5815.330	495.9(1)	-16(8)	487.3(10)	-17.4(56)	489(46)	487.5(25)	-23(10)
13029.112	6429.624	578.6(2)	-8(5)			588(14)	574.2(55)	-17(12)
13373.648	6006.33	493.5(2)	-1(8)					
	6114.385	493.6(1)	-12(5)					
Average		493.6(3)	-7(14)			507(46)	498.5(30)	-30(15)

Table 10.7. Measured hyperfine constants of even parity fine energy levels of Pr II. The results are compared with the values obtained by R. C. Rivest et al. [48] *(column 5), M. Hongliang et al.* [47] *(column 6, 7), A. Ginibre.* [41] *(column 8) and B. Furmann et al.* [51] *(column 9, 10).*

Level energy / cm^{-1}	Excitation wavelength / Å	A / MHz	B / MHz	A_{Ri} / MHz [48]	A_H / MHz [47]	B_H / MHz [47]	A_G / MHz [41]	A_F / MHz [51]	B_F / MHz [51]
21676.163	5687.19	266.3(4)	-8(5)				285(11)		
22675.492	5729.42	765.8(4)	-26(8)				774		
22718.404	5677.027	743.4(3)	0(20)				750		
22885.634	5661.24	908.0(3)	-1(5)	909.7(10)			912		
23261.402	6318.12	581.9(3)	-19(5)	584.3(6)			591		
23660.171	6165.94	872.1(3)	17(5)						
	6281.30	871.9(2)	18(9)						
Average		872.0(4)	18(9)	870.8(12)			876(27)		
24115.536	6397.984	823.2(3)	-23(6)	821.4(9)			828		
24716.093	5786.172	730.1(3)	18(6)						
	5788.99	729.9(3)	0(8)						
	6016.49	730.7(2)	3(6)						
	6161.182	730.5(2)	6(5)						
Average		730.3(6)	7(10)	731.9(17)	735.0(11)	15.9(35)	732(22)	734.9(20)	18(10)
24755.017	5773.165	591.8(4)	0(9)						
	5775.911	592.0(2)	2(6)						
	6002.43	592.8(2)	4(6)						
	6363.60	592.4(4)	-8(2)						
Average		592.2(8)	2(10)				561	604.1(20)	5(5)
25467.549	5756.169	727.5(3)	-2(5)						

Level energy / cm^{-1}	Excitation wavelength / Å	A / MHz	B / MHz	A_{Ri} / MHz [48]	A_{H} / MHz [47]	B_{H} / MHz [47]	A_{G} / MHz [41]	A_{F} / MHz [51]	B_{F} / MHz [51]
	6087.522	727.5(3)	-2(1)						
Average		727.5(3)	-2(5)	732.7(11)	736.2(15)	16.2(66)	732	735.4(25)	23(10)
25499.570	5745.58	632.8(3)	-23(3)						
	5868.824	632.8(2)	-3(3)						
	5877.39	632.5(3)	-7(4)						
	6106.74	632.7(3)	-6(7)						
Average		632.7(4)	-10(15)	633.3(7)	632.1(13)	-14.5(60)	639		
25545.086	5730.58	603.4(4)	0(5)				582(27)		
25569.218	6278.669	688.9(3)	-24(5)	689.7(9)			696(16)		
	5719.626	1029.1(3)	-22(3)						
25578.507	6017.809	1028.6(1)	-22(2)						
	6046.67	1029.0(3)	-15(2)						
Average		1029.9(6)	-20(5)		1031.6(22)	12.2(66)	891(17)	1030.9(18)	14(10)
25610.227	5830.945	540.4(1)	-52(9)						
	5839.40	540.1(1)	-15(10)						
	6159.112	540.3(3)	-25(13)						
	6262.538	540.5(2)	-33(2)						
Average		540.3(4)	-31(30)	539.4(7)	543.2(7)	-7.2(31)	546		
25656.737	5815.17	654.8(1)	-25(3)						
	5823.58	654.8(2)	29(14)						
	6141.51	655.1(3)	-20(5)						
	6244.346	655.0(3)	-20(3)						

Level energy / cm^{-1}	Excitation wavelength / Å	A / MHz	B / MHz	A_{Ri} / MHz [48]	A_{H} / MHz [47]	B_{H} / MHz [47]	A_{G} / MHz [41]	A_{F} / MHz [51]	B_{F} / MHz [51]
Average		654.9(5)	-9(51)	656.1(7)	656.4(10)	-10.0(21)	655(5)	654.3(15)	-3(5)
25672.825	5951.773	850.7(3)	-12(2)						
	5980.00	850.8(2)	-10(6)						
Average		850.8(4)	-11(7)				857(27)	854.7(30)	-42(15)
25842.444	5753.02	668.1(4)	-12(5)						
	5761.26	667.3(2)	-7(3)						
	5981.458	667.8(4)	-31(3)						
Average		668.0(5)	-22(15)				678		
26146.060	5654.23	623.0(4)	9(9)						
	5662.19	622.3(2)	-5(3)						
	5874.74	622.4(2)	5(9)						
Average		622.6(6)	3(15)	621.9(9)			618	632.7(30)	-28(15)
26226.628	5818.57	678.7(3)	-15(2)						
	5847.05	678.3(2)	-7(4)						
	6205.632	678.2(2)	-7(6)						
Average		678.4(6)	-10(9)				620(15)	678.1(60)	-2(8)
26398.569	5873.83	657.3(3)	-8(7)						
	5967.822	657.5(2)	-19(3)						
Average		657.4(4)	-14(13)	658.8(7)			660(10)	659.7(20)	-9(3)
26445.138	6090.381	513.3(4)	-28(3)	514.1(16)			512		
26570.208	5704.500	736.6(3)	-16(17)						
	5731.87 [h]	736.4(4)	-10(20)						

Level energy / cm^{-1}	Excitation wavelength / Å	A / MHz	B / MHz	A_{Ri} / MHz [48]	A_{H} / MHz [47]	B_{H} / MHz [47]	A_{G} / MHz [41]	A_{F} / MHz [51]	B_{F} / MHz [51]
Average		736.5(5)	-13(20)				733(27)		
26640.915	5791.363	619.8(3)	-16(5)						
	6067.24	619.3(3)	-16(7)						
Average		619.6(6)	-16(7)	621.2(7)	619.1(10)	5.4(40)	588		
26707.364	5687.150	520.5(3)	-2(2)						
	5769.154	519.6(3)	9(2)						
	6025.817	519.8	-8						
	6042.873	520.1(3)	4(13)						
Average		520.0(8)	1(16)	519.8(6)			459		
26860.974	5807.52	604.2(3)	-4(18)						
	5939.90	604.3(3)	5(2)						
	6197.453	604.0(3)	-11(6)						
Average		604.1(4)	-8(14)	603.2(7)			588	595.1(30)	3(5)
26962.021	5685.60	610.7(4)	-22(2)	610.9(7)					
	5951.266	610.4(1)	-19(6)						
	6086.168	610.9(1)	-9(5)						
	6431.842	610.3(3)	9(28)						
Average		610.6(6)	-10(30)				609(18)		
26973.549	5681.876	604.0(2)	-8(3)						
	5769.784	603.8(3)	39(7)						
	5930.662	603.9(3)	-11(2)						
	5947.19	604.0(2)	-10(4)						

Level energy / cm^{-1}	Excitation wavelength / Å	A / MHz	B / MHz	A_{Ri} / MHz [48]	A_{H} / MHz [47]	B_{H} / MHz [47]	A_{G} / MHz [41]	A_{F} / MHz [51]	B_{F} / MHz [51]
Average		603.9(4)	3(40)		601.7(12)	-1.6(37)	612(22)	601.3(10)	-3(3)
27128.016	5847.13	589.8(4)	-9(15)	591.4(10)			600(14)	598.6(30)	
27198.297	5695.90	584.5(3)	-8(5)						
	5852.630	584.0(2)	-15(10)						
	5868.72	584.1(3)	-25(6)						
Average		584.2(6)	-16(15)		583.3(11)	-4.6(43)	600	582.9(20)	-10(10)
27380.527	5790.85	687.0(5)	-18(7)						
27604.990	5688.44	596.7(2)	-5(11)						
	5731.870	597.1(3)	26(7)						
	5856.908	597.2(2)	-6(11)						
	6187.48	596.9(3)	-12(4)						
Average		597.0(5)	1(32)						
27781.688	6182.338	559.9(3)	-36(5)	560.3(8)			573		
28009.828	5785.42	556.9(3)	-32(23)						
	6148.25	556.0(3)	-35(8)						
Average		556.5(7)	-34(25)	556.8(7)	558.2(10)	5.4(40)	576		
28034.127	5777.291	459.8(3)	-15(9)	462.3(6)			468		
28201.980	5813.55	537.6(3)	-1(5)						
	6025.722	538.1(2)	-4(4)						
	6093.05	537.9(1)	-25(12)						
Average		537.9(6)	-10(27)	538.5(6)			543	538.8(20)	4(5)
28508.823	5711.634	626.5(4)	-24(5)						

Level energy / cm^{-1}	Excitation wavelength / Å	A / MHz	B / MHz	A_{Ri} / MHz [48]	A_{H} / MHz [47]	B_{H} / MHz [47]	A_{G} / MHz [41]	A_{F} / MHz [51]	B_{F} / MHz [51]
	5859.68	626.0(2)	5(1)						
	5981.194	626.3(4)	-1(10)						
Average		626.3(6)	-7(22)				636(18)	619.5(35)	-29(10)
28577.821	5689.208	530.1(3)	-14(6)						
	5892.24	530.4(3)	-31(8)						
	5940.727	530.3(2)	-1(5)						
	5956.605	530.1(2)	-19(4)						
	6429.624	530.6(2)	7(6)						
Average		530.3(5)	-12(27)	530.8(6)	530.8(11)	-4.9(54)	537(16)	531.1(30)	-12(10)
28816.267	5810.581	498.3(4)	-35(10)				507(13)	504.1(50)	-3(5)
29723.998	5719.086	523.4(4)	-10(4)						
	6114.385	523.6(2)	-25(2)						
Average		523.5(5)	-18(12)				531(14)	529.4(40)	-12(10)
30018.138	5815.330	535.2(1)	-1(8)						
	6006.33	535.0(3)	11(7)						
Average		535.1(4)	5(13)		525.9(11)	4.0(37)	495	528.6(30)	5(3)

[h] The recorded hyperfine structure of this line appeared in a blend with a weak signal. The hyperfine constants of the upper levels are determined by fixing the hyperfine constants of the lower level (9128.741°_{4}) involved in the transition.

10.3 Discussion

Using the experimental setup of MARS-II, the high resolution spectroscopic method of collinear laser ion beam spectroscopy is used to investigate the hyperfine structures of singly ionized praseodymium lines. The magnetic dipole interaction constants A and the electric quadrupole interaction constant B of the levels involved in the transitions are listed in tables 10.6 and 10.7. For each recorded line, the statistical deviations are relatively small. The hyperfine constants are found in good agreement when a level is investigated at different transitions. The statistical errors in averaged A and B values (averaged over different transitions) are determined so that they cover the total span of A and B values determined from different transitions. The results are compared with values obtained by different techniques: Fourier transform spectroscopy (Ginibre, ref. [25,41,42]), Doppler-limited laser spectroscopy using a hollow cathode discharge lamp as a source of Pr ions (Furmann, ref. [51]) and CLIBS measurements (results from Hongliang [47] and Rivest [48]). Most of the A values are in agreement with Ginibre's results within the uncertainties given in her work, whereas the accuracy is improved significantly. The electric quadrupole moment is quite small for praseodymium; therefore small B values with large errors are obtained, sometimes different compared with published values.

For the determination of the hyperfine constants of the levels involved in a particular transition at least three data files are used. In most cases, 3 - 15 recordings are averaged to make one data file in order to improve the signal to noise ratio. The best fit of the recorded curve is obtained with a Voigt profile composed of ca. 60 % Lorentzian and 40% Gaussian profile. The observed line width of ca. 60 MHz is much smaller than the Doppler width but still larger than the natural line width. Reasons could be (as discussed in section 8.2) fluctuations in the acceleration voltage, velocity-changing collisions during the flight of the ions and mainly fluctuations in the intensity of the ion source. These fluctuations limit the ion beam quality; it still has a certain velocity spread which also gives rise to statistical errors. Another reason could be self absorption or power broadening because the laser power used is ca. 20 - 80 mW, measured at the Brewster window of the mass separator (about 1 meter in front of the interaction chamber). Some experimental uncertainties such as uncertainty in the acceleration voltage, uncertainty in the scanning voltage and calibration of the laser frequency can lead to some systematic errors.

The *A* values are found consistent with the literature values determined using CLIBS within an error less than 1 MHz. *B* values could be determined only with large errors, due to the very small quadrupole moment of ^{141}Pr.

In table 10.4, the experimental value of difference in centers of gravity of two closely lying transitions = Δcg is compared with the calculated from the improved energy values (column 4) and from the previous energies (column 5). The column 4 values of Δcg are found in good agreement with the experimental values (column 3). This provides a counter check that the improvement of the energy values of the ionic fine structure levels energies is reliable.

In this work, the lower level $\sigma = 13373.648^{\circ}_{8}$ cm^{-1} was the highest lower meta-stable level which is populated in the ion source sufficiently enough to perform laser excitation and $\sigma = 30018.138_{7}$ was the highest upper level which could be probed using laser excitation. One of the limitations of collinear ion beam spectroscopy is the fact that only few levels can be investigated. Since the lowest upper even level which could be investigated during this work is $\sigma = 21676.163_{5}$ cm^{-1}, excited from the lower meta-stable odd level $\sigma = 4097.653^{\circ}_{5}$ cm^{-1}. Therefore, in order to investigate levels with energies less than e.g. 20000 cm^{-1}, a different filter (red, orange or yellow) should be used. To probe high lying energy levels (with $\sigma > 30000$ cm^{-1}), a green or blue laser can be used with appropriate sets of filters to suppress stray laser light.

11 CONCLUSION

This work is focused on the investigation of hyperfine structures of Pr II spectral lines. With the help of a highly resolved Fourier transform spectrum of praseodymium, the hyperfine structures of 477 Pr II transitions were analyzed and their center of gravity (cg) transition wavelengths (and hence their cg wave numbers) were improved. Then energy values of 227 Pr II levels (74 having odd and 153 even parity) were re-determined. The observed accuracy is between 0.005 and 0.01 cm^{-1}. Magnetic hyperfine interaction constants A for some energy levels were also improved. 25 Pr II spectral lines were classified and for more than 400 already classified lines the cg wavelengths were corrected. Differences between -0.066 to 0.064 Å were observed between corrected and previous wavelengths of the classified lines. In addition, 11 lines, listed in “wavelength tables” (ref. [114]), were classified as Pr II lines and their wavelengths were also corrected.

For the experimental investigation of Pr II hyperfine structures, two methods were used: Inter-modulated laser induced fluorescence saturation spectroscopy and collinear laser ion beam spectroscopy (CLIBS). Using saturation spectroscopy the line width of spectral line could be reduced to ca. 200 MHz and a nominal accuracy of ca. 2-5 MHz of the magnetic dipole interaction constants A of the fine structure energy levels could be obtained. Using CLIBS, the spectral lines of Pr II could be resolved up to ca. 60 MHz with an accuracy better than 1 MHz in the A values of Pr II fine structure energy levels. It could be concluded that, for the determination of hyperfine constants of Pr II energy levels, the CLIBS is the superior method compared to saturation spectroscopy.

The major part of this thesis is dedicated to the investigation of hyperfine structures of Pr II optical transitions using CLIBS. Using this method, 99 optical transitions were investigated and the hyperfine constants A and B of 70 Pr II fine structure energy levels were determined. The results were compared with the published data: For some levels the accuracy is significantly improved. The A values were found consistent with previous measurements within an error less than 1 MHz. The B values could be determined only with large errors, due to the very small quadrupole moment (Q) of Pr.

One of the limitations of the CLIBS method is the fact that only few lower metastable levels are populated (e.g. up to $\sigma = 13373.652^{\circ}_{8}$ in this work), consequently very few upper and lower levels can be investigated.

We hope that this work will provide useful information for, further accurate optical measurements regarding praseodymium ions, astrophysical studies of stellar spectra to determine Pr abundance values and for gaining a better understanding of the electronic configurations of the Pr atom.

Despite of this work, there are still many known Pr II fine energy levels for which accurate values of hyperfine constants are not known. For future experiments, different dyes e.g. blue (Stilbene 3), green (coumarin 540) or red (DCM) can be used to investigate Pr II optical transitions involving these energy levels. Different filters can also be incorporated to observe the fluorescence light. Once having accurate measurements of hyperfine constants of Pr II energy levels, it would be helpful to discover/classify Pr II fine energy levels in the missing configurations, especially low lying metastable energy levels.

12 WORK SITED

12.1 Literature consulted

- Halliday David, Robert Resnick and Kenneth S. Krane, Physics, fifth edition, Wiley 2002.
- H. E. White, Introduction to Atomic Spectra, McGraw-Hill Kogakusha, Ltd. 1934.
- W.Demtröder, Laser Spectroscopy, Springer 1982.
- I. I. Sobel'mann, "Atomic Spectra and Radiative Transitions", Springer-Verlag Berlin Heidelberg New York 1979.
- A. P. Thorne, Spectrophysics, 2nd edition, Chapman & Hall, London 1974.
- S. Svanberg, Atomic and Molecular Spectroscopy, Springer-Verlag Berlin Heidelberg New York 1991.
- H. G. Kuhn, Atomic Spectra, Academic Press, New york 1962.
- H. London, Separation of isotopes, George Newnes limited 1961.
- Radiant Dyes, CW-Ring Dye Laser Operation and Maintenance Manual Wermelskirchen, Germany

12.2 References

1. W. Pauli, Naturwissenschaften, **12,** 741 (1924)
2. H. Hühnermann, Phys. Scr., **T47,** 70 (1993)
3. L. Dolk, G. M. Wahlgren, H. Lundberg, Z. S. Li, U. Litzén, S. Ivarsson, I. Ilyin, and S. Hubrig, Astr. and Astrophys., **385,** 111 (2002)
4. G. M. Wahlgren, Phys. Scr., **T100,** 22 (2002)
5. B. Gamper, Z. Uddin, M. Jahangir, O. Allard, H. Knöckel, E. Tiemann and L. Windholz, J. Phys. B: At. Mol. Opt. Phys., **44,** 045003 (2011)
6. N. Akhtar and L. Windholz, J. Phys. B, accepted, (2012)
7. www.webelements.com/praseodymium/chemistry.html
8. D. R. Stephens, J. Phys. Chem., **26,** 943 (1965)
9. L. L. Rokhlin, CRC Press, ISBN 0-415-28414-7 (2003)

10. S. Nair and M. C. Mittal, Mat. Sci. Forum, **30,** 89 (1988)
11. C. R. Hammond, The elements, in Handbook of Chemistry and Physics 81st edition, ISBN 0-8493-0481-4, (2000)
12. Http://info.anu.edu.au/ovc/media/media_releases/2005/august/290805_stop_light.
13. A. Jha et al., J. Eur. Opt. Soc. Part A **4(4),** 417 (1995)
14. Y. Borchert et al., J. Phys. Chem. C, **112(8),** 3054 (2008)
15. A. S. King, Astrophys. J., **68,** 194 (1928)
16. H. E. White, Phys. Rev., **34,** 1397 (1929)
17. N. Rosen, G. R. Harrison and J. R. Mcnally, J. of Phys. Rev., **60,** 722 (1941)
18. H. Lew, Phys. Rev. **89,** 530 (1953)
19. P. Brix, Phys. Rev. **89,** 1245 (1953)
20. J. M. Baker and B. Bleaney, Proc. Phys. Soc. London, Sect. A, **68,** 936 (1955)
21. Y. C. Amado, Phys. Rev. **126,** 1004 (1962)
22. R. Zalubas and M. J. Wilson, Res. Nat. Bur. Stand. (U.S.), **69 A,** 59 (1965)
23. R. Zalubas and B. R. Borchardt, J. Opt. Soc. Am**.**, **63,** 102 (1973)
24. A. Ginibre, Phys. Scr., **23,** 260, (1981)
25. A. Ginibre, PhD Thesis Université de Paris-sud, unpublished (1988)
26. R. M. Macfarlane, D. P. Burum and R. M. Shelby., Phys. Rev. Lett., **49,** 636 (1982)
27. K. T. Cheng and W. J Childs, Phys. Rev. A, **31,** 2775 (1985)
28. M. N. Reddy and G. N. Rao, Physica C, **150,** 457 (1988)
29. T. Kuwamoto et al., J. Phys. Soc. Japan, **65(10),** 3180 (1996)
30. M. Song et al., Eur. Phys. J. D, **2(2),** 115 (1998)
31. A. Krzykowski, B. Furmann, D. Stefanska, A. Jarosz, A. Kajoch, Opt. Comm. **140,** 216 (1997)
32. J. Ruczkowski, E. Stachowska, M. Elantkowska, G. H. Guthöhrlein and J. Dembczynski, Phys. Scr., **68,** 133-140, 2003.
33. B. Furmann, A. Krzykowski, D. Stefanska and J. Dembczynski, Phys. Scr. **74,** 658 (2006)
34. S. G. Oppel, App. Phys. B: Lasers and Optics, **101,** 33 (2010)
35. K. Shamim, I. Siddiqui and L. Windholz, Eur. Phys. J. D, **64,** 209 (2011)
36. T. I. Syed, I. Siddiqui, K. Shamim, Z. Uddin, G. H. Guthöhrlein and L. Windholz, Phys. Scr., **84,** 065303 (2011)
37. K. Murakawa, J. Phys. Soc. Japan, **15,** 2306 (1960)

38. J. Blaise, J. Verges, J. F. Wyart, P. Camus and R. Zalubas, J. Opt. Soc. Am. **63,** 1315 (1973)
39. J. F. Wyart, J. Blaise and P. Camus, Phys. Scri., **9,** 325 (1974)
40. G. Racah, Phys. Rev., **76,** 1352 (1949)
41. A. Ginibre, Phys. Scr., **39,** 694 (1989)
42. A. Ginibre, Phys. Scr., **39,** 710 (1989)
43. H. Iimura, Y. Nakahara, S. Ichikawa, K. Kotani, M. Wakasugi and T. Horiguchi, J. of Phys. Soc. of Japan, **59,** 4208 (1990)
44. H. Iimura, Y. Nakahara, S. Ichikawa, M. Kubota and T. Horiguchi, Phys. Rev. C, **50,** 661 (1994)
45. S. Ivarsson, U. Litzén and G. M. Wahlgren, Phys. Scr., **64,** 455 (2001)
46. Li Maosheng, Ma Hongliang, Chen Miaohua, Chen Zhijun, Lu Fuquan, Tang Jiayong and Yang Fujia, Hyp. Inter., **128,** 417 (2000)
47. Ma Hongliang, Chinese Phys., **11,** 905 (2002)
48. R. C. Rivest, M. R. Izawa, S. D. Rosner, T. J. Scholl, G. Wu and R. A. Hol, Canadian J. of Phys., **80,** 557 (2002)
49. T. J. Scholl et al., Canadian J. Phys., **80,** 713 (2002)
50. B. Furmann, D. Stefańska, E. Stachowska, J. Ruczkowski and J. Dembczyński, Eur. Phys. J. D, **17,** 275 (2001)
51. B. Furmann, D. Stefańska, J. Dembczyński and E. Stachowska, Phys. Scr., **72,** 300 (2005)
52. B. Furmann, D. Stefańska, J. Dembczyński and E. Stachowska, Atomic Data and Nuclear Data Tables, **93,** 127 (2007)
53. R. Li et al., Phys. Scr., **76,** 577 (2007)
54. N. Akhtar et al., submitted 2012
55. N. Akhtar et al., to be published.
56. N. J. Spector, Opt. Soc. Am., **54,** 1359 (1964)
57. J. Reader, J. Sugar, J. Phys. Rev., **137,** 784 (1965)
58. S. Feneuille, N. A. Pelletier, Physica (Utrecht), **40,** 347 (1968)
59. W. M. Glenn, Phys. Scr., **T100,** 22 (2002)
60. H. J. Andrä, A. Gaupp and W. Wittmann, Phys. Rev. Lett., **31,** 501 (1973)

61. H. J. Andrä, 4th Int. Conf. Atomic Physics, Atomic Physics vol 4, (New York: Plenum), p. 365 (1975)
62. S. L. Kaufman, Opt. Comm., **17,** 309 (1976)
63. W. H. Wing, G. A. Ruff, W. E. Lamb and J. J. Spezewski, Phys. Rev. Lett., **36,** 1488 (1976)
64. M. Dufay, M. Carré, M. L. Gaillard, G. Meunier, H. Winter and A. Zgainski, Phys. Rev. Lett., **37,** 1678 (1976)
65. Th. Meier, H. Hühnermann and H. Wagner, Opt. Comm., **20,** 376 (1977)
66. C. Höhle, H. Hühnermann, Th. Meier and H. Wagner, Zeitschrift für Phys. A, **284,** 261 (1978)
67. H. Hühnermann, H. Valentin and H. Wagner, Zeitschrift für Phys. A, **285,** 229 (1978)
68. C. Höhle, H. Hühnermann and M. Elbel, Zeitschrift für Phys. A, **295,** 1 (1980)
69. C. Höhle, H. Hühnermann and H. Wagner Zeitschrift für Phys. A, **304,** 279 (1982)
70. K. Dörschel, H. Hühnermann, E. Knobl, Th. Meier and H. Wagner, Zeitschrift für Phys. A, **302,** 359 (1981)
71. S. Beiersdorf, W. Heddrich, K. Kesper, H. Hühnermann, W. Möller and H. Wagner, J. Phys. G, **21,** 215 (1995)
72. K. Dörschel, W. Heddrich, H. Hühnermann, E. W. Peau, H. Wagner, G. D. Alkhazov, E. Ye. Berlovich, V. P. Denisov, V. N. Panteleev and A. G. Poyakov, Zeitschrift für Phys. A, **312,** 269 (1983)
73. G. D. Alkhazov, Leningrad Nuclear Physics Institute Preprints, **1004,** (1984)
74. K. Dörschel, W. Heddrich, H. Hühnermann, E. W. Peau, H. Wagner, G. D. Alkhazov, E. Ye. Berlovich, V. P. Denisov, V. N. Panteleev and A. G. Poyakov, Zeitschrift für Phys. A, **317,** 233 (1984)
75. G. D. Alkhazov, E. Ye. Berlovich, V. P. Denisov, V. N. Panteleev, V. I. Tikhonov, K. Dörschel, W. Heddrich, H. Hühnermann, E. W. Peau and H. Wagner, Zeitschrift für Phys. A, **316,** 123 (1984)
76. J. Bauche, H. Hühnermann, D. N. Stacey, V. Stacey and M. Wilson, Zeitschrift für Phys. A, **320,** 157 (1985)
77. G. D. Alkhazov, A. E. Barzakh, H. Hühnermann, K. Kesper, A. Mazumdar, W. Möller, R. Otto, V. N. Panteleev, A. G. Poljakov, C. Reese and H. Wagner, J. of Phys. B: At. Mol. Opt. Phys., **25,** 571 (1992)

78. R. Otto, H. Hühnermann, J. Reader and J. F. Wyart, J. of Phys. B: At. Mol. Opt. Phys., **28,** 3615 (1995)
79. A. E. Barzakh et al., Rev. Sci. Instrum., **83,** 02B306 (2012)
80. W. L. Guang et al., Jpn. J. App. Phys., **40,** 2508 (2001)
81. P. Schef et al., Phys. Scr., **73,** 217 (2006)
82. P. Villemoes et al., J. Phys. B: At. Mol. Opt. Phys., **26,** 4289 (1993)
83. W. Wollaston, Phil. Trans. Roy. Soc., **II,** 365 (1802)
84. J. Fraunhofer, Gilbert's Ann., **56,** 264 (1817)
85. L. Foucault, Ann. Chim. et Phys., **68,** 476 (1860)
86. G. Kirchhoff, Ann. chim. et phys., **58,** 254 (1860)
87. A. Ångström, Uppsala and W. Schultz, (1868)
88. N. Bohr, Phil. Mag., **26,** 476 (1913)
89. H. N. Russell and F. A. Saunders, Astrophys. J., **61,** 38 (1925)
90. A. A. Michelson, Phil. Mag., **31,** 338 (1891)
91. C. Fabry and A. Perot, Ann. de chim. et phys., **12(7),** 459 (1897)
92. H. Schüler and T. Schmidt, Z. Phys., **99,** 717 (1936)
93. H. Dorgelo, Z. Phys., **26,** 756 (1925)
94. L. S. Orstein and H. C. Burger, Z. Phys., **40,** 403 (1926)
95. H. N. Russel, F. A. Saunders, Astrophys. J., **61,** 38 (1925)
96. P. Dirac, Pro. Roy. Soc. A, **114**, 281 (1926)
97. Operating and Maintenance Manual, Radiant dyes CW-Ring Dye Laser.
98. F. M. Penning, Physica, **8,** 137 (1928)
99. C. Kenty, Phys. Rev., **80**, 95 (1950)
100. K. W. Meissner and W. F. Miller, Phys. Rev., **896**, 92 (1953)
101. B. Green et al., Appl. Phys. Lett., **29,** 727 (1976)
102. J. C. Travis, "Analytical optogalvanic spectroscopy in flames" In Analytical Laser, spectroscopy (1985)
103. J. F. Grandin and X. J. Husson, Phys. B., **14,** 433 (1981)
104. J. E. Lawler et al., Ser. Opt. Sci., **21,** 188 (1979)
105. M. L. Skolnick, J. Quantum Electron., **6,** 139 (1970)
106. W. H. Thomason and D. C. Elbers, Rev. Sci. Instrum., **46,** 409 (1975)
107. I. A. Siddiqui, Ph D thesis, Technical University Graz (2010)
108. W. E. Lamb, Theory of an Optical maser, Phys. Rev. A, **134(1),** 1429 (1964)

109. R. W. Bennet., Phys. Rev., **126,** 580 (1962)
110. B. Arcimowicz et al., Eur. Phys. J. D, **13,** 187 (2001)
111. R. Peck and K.Reeder, J. Opt. Soc. Am., **62,** 958 (1972)
112. L. Windholz and G. H. Guthöhrlein, Phys. Scr., **T105,** 55 (2003)
113. T. Quiering et al., Universitat der Bundeswehr, Hamburg diploma thesis, (1984)
114. G. R. Harrison et al., Wavelengths tables, The M.I.T press, (1969)
115. H. O. Behrens and G. H.Guthöhrlein, J. Phys., **C7-44**, 149 (1983)
116. H. O. Behrens, G. H. Guthöhrlein and A. Kasper, J. Phys., **C7-44**, 239 (1983)
117. N. Akhtar et al., 75th Annual Meeting of the DPG, 13th - 18th of March 2011, Dresden, Germany, POS A-26.58 (2011)
118. C. Salomon, D. Hills and J. L. Hall, J. Opt. Soc. B, **5**, 1576 (1988)
119. V. Bernard et al., J. Quantum Electronics, **33**, 1288 (1997)
120. H. Hühnermann et al., Nuclear Inst. and Methods in Physics Research B, **26(1),** 435-439 (1987)
121. K. Dörschel, Dissertation, Phillips-Universität Marburg/Lahn, p. 34, (1983)
122. Th. Win, Diplomarbeit, Phillips-Universität Marburg/Lahn, p. 24 (1993)
123. P. G. Johnson, A. Bolson and C. M. Henderson, Nuclear Instruments and Methods, **106(1),** 83-87 (1973)
124. G. N. Plass, J. of App. Phys., 49 (1942)
125. H. Hintenberger, Z. Naturforschung, **6a,** 275 (1951)
126. M. Kowalska, D. Yordanov, K. Blaum, D. Borremans, P. Himpe, P. Lievens, S. Mallion, R. Neugart, G. Neyens and N. Vermeulen, Hyp. Inter., **162,** 109-114 (2005)
127. http://www.physics.nist.gov/PhysRefData/Handbook/Tables/bariumtable6.htm.
128. B. K. Sahoo, B. P. Das, R. K. Chaudhuri and D. Mukherjee, Phys. Rev. A., **75,** 032507 (2007)
129. M. V. Hove, G. Borghs, P. D. Bisschop and R. E. Silverans, Z. Phys. A., **321,** 215 (1985)
130. N. Anjum, N. Akhtar, H. Hühnermann and L. Windholz, 60th ÖPG annual meeting, University of Salzburg, Austria, POS-AMP-4 (2010)